이학박사 학위 논문

Synthesis of Titania-based Nanostructures and Their Applications

타이타니아를 기반으로 한 나노구조의 합성과 응용

2015 년 2 월

서울대학교 대학원

화학부 무기화학전공

임 주 현

Ph. D. Dissertation

Synthesis of Titania-based Nanostructures and Their Applications

Supervisor : Professor Jin-Kyu Lee

Major : Inorganic Chemistry

February 2015

By Joohyun Lim

Department of Chemistry

The Graduate School

Seoul National University

`

Abstract

Synthesis of Titania-based Nanostructures and Their Applications

Joohyun Lim

Department of Chemistry, Inorganic Chemistry

The Graduate School

Seoul National University

Titania (TiO_2) nanostructures have been widely researched over the past several decades because of their outstanding properties and applications in various fields, in addition to their abundance and low-cost. In particular, titania nanostructures have been used for energy generation in solar-cells and energy storage in batteries.

In this thesis, three simple sol-gel synthetic methods for the preparations of titania of various sizes are reported. Spherical titania nanoparticles with sizes in the range of 60-300 nm could be obtained by changing the amount of reactants. Their size-dependent electrochemical properties are tested using Li-ion battery. Furthermore, simple preparation of hollow titania is also possible by using the soft-template method. Using this method, hollow (Sn,Ti) oxide and an iron oxide@titania yolk@shell structure could be obtained.

`

Furthermore, their electrochemical properties are tested.

Chapter 1 briefly describes the research background on titania nanostructures, including their synthesis methods, surface modifications, and their applications (photo-catalyst, solar-cells, and batteries).

Chapter 2 describes the preparation of spherical titania nanoparticles by using ethylene glycol in acetone solvent to reduce the reactivity of the titania source. The size of obtained titania nanoparticles is approximately between 70 nm and 300 nm; this size variation is obtained by varying the amount of water and the titania source. Reaction conditions including the kind of solvents and chelating agents are investigated.

Chapter 3 describes the preparation of spherical titania nanoparticles by using KCl in ethanol solvent to reduce the reactivity of titania source. The size of titania nanoparticles is controlled by the concentration of KCl and titania source, and the type of solvents. The prepared titania nanoparticles have similar or more powerful photo-catalytic property than that of very small and commercialized titania (P25).

Chapter 4 describes the preparation of spherical titania nanoparticles using a mixed solvent of ethanol and acetonitrile. The size of titania nanoparticles is varied by varying the amount of reactant, especially the water. The size-dependent electrochemical properties of titania are examined by evaluating the Li-ion capacity of about 60 nm, 120 nm, and 280 nm. These properties are related with the surface area measured using both gas- and liquid- based methods.

Chapter 5 describes the preparation of (Sn,Ti) oxide with a hollow structure

`

by the soft-template method under various conditions such as different calcination temperatures and atomic ratio of Sn in the composite oxide. The electrochemical properties of (Sn,Ti) oxide for use as an anode for Li-ion battery are investigated by comparing them with those of hollow titania nanoparticles.

Chapter 6 describes the preparation of an iron oxide@titania yolk@shell structure by the soft-template method. The ratio of the iron oxide core and titania shell could be controlled by changing the amount of the titania source. The electrochemical properties of a yolk@shell anode are compared with those of a just-mixed anode composed of iron oxide and hollow titania nanoparticles, by using Li-ion battery.

Keywords: titania, nanoparticle, size control, hollow, yolk@shell, electrochemical property, Li-ion battery

Student Number: 2009-20313

`

Contents

`

`

`

`

`

`

`

List of Figures

Chapter 1

Chapter 2

Chapter 3

Chapter 4

Chapter 5

`

Chapter 6

Appendix/Chapter 1

Appendix/Chapter 2

Appendix/Chapter 3

`

Appendix/Chapter 4

`

Appendix/Chapter 5

`

Appendix/Chapter 6

`

Appendix/Chapter 7

Appendix/Chapter 8

`

Appendix/Chapter 9

`

List of Scheme

Chapter 3

Appendix/Chapter 2

Appendix/Chapter 3

Appendix/Chapter 7

`

List of Tables

Chapter 4

Appendix/Chapter 2

Appendix/Chapter 7

`

Chapter 1.

Research Background

`

1.1 Titania

Titania (titanium dioxide, TiO_2) is one of the most widely used materials due to its outstanding properties as the white pigment, photo-catalyst, and electrodes of solar-cells and batteries. Especially, there have been many researches on the photo-active character of titania after the water splitting ability of titania under ultraviolet (UV) light was discovered by Fujishima and Honda in 1972.[1] The basic characters, synthetic methods, and applications of titania are discussed as below.

The most stable crystal structure of titania is tetragonal rutile (Figure 1.1). There are also two meta-stable crystal structures of titania such as tetragonal anatase and orthorthombic brookite and they transform to rutile phase under high temperature over 650 °C.[2] Anatase phase titania has the best photo-catalytic property due to the more reactive surface condition.[3]

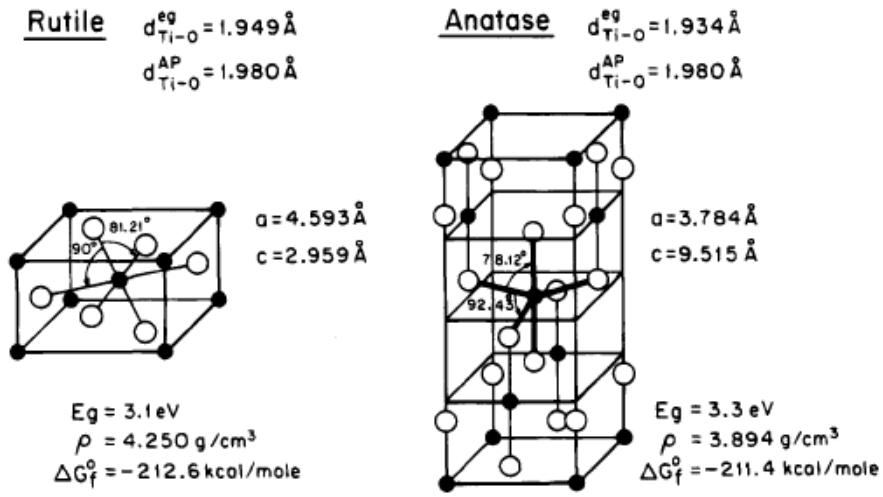

Figure 1.1. Crystal structures of titania.[2]

`

1.2 Synthesis of titania nanostructures

Materials in nanostructure have more powerful properties than in their bulk-state due to the high surface area, enhanced reactivity, size-dependent properties like band gap tuning, etc.

There are various methods to prepare titania nanostructures such as sol-gel method, emulsion using method, template using method, hydrothermal or solvothermal method, electrospray method, etc.[4-6]

Sol-gel method is easy and general method to get metal oxide nanoparticles through hydrolysis and condensation of metal alkoxide (brief equations represented below).

$$Ti(OR)_4 + 4H_2O \rightarrow Ti(OH)_4$$

$$Ti(OH)_4 \rightarrow TiO_2 + 2H_2O$$

In case of titania, the reactivity of titanium alkoxide have to be reduced to prepare mono-dispersed nanostructures and control their size due to the high reactivity to water. In this thesis, simple size control of titania nanoparticle is possible under the reactivity control of titanium precursor with several methods (from chapter 2~4). Using these methods, titania based hollow structures titania nanoparticles could be prepared (chapter 5 and 6).

Emulsion using method is preparing titania nanostructures in emulsions such as micelles and inverse-micelles. Template using method is using template like silica or polystyrene to make well-ordered structure of titania such as photonic crystal arrays or mesoporous (pore size about over several nanometers and under 50 nanometers) electrodes.

Hydrothemal or solvothermal methods are generally done with high temperature and high pressure by using autoclave (steel pressure vessels with

`

Teflon reactor). Various shapes of titania nanostructure such as very small nanoparticle, nanorod, wire, and hierarchical structures could be obtained using these methods.

Electrospray method is spraying the mixture of titania source or nanoparticle with solvent and binder from nozzle to the substrate. During the spraying, electric field is introduced between nozzle and substrate to make droplets including titania source. As a result, specific nanostructures could be generated after the solvent of droplets is evaporated.

The crystal structure of titania could be differed with various synthetic methods, reaction temperature, and other reactants. If the obtained titania has amorphous structure (has no crystal structure), calcination process is needed to get anatase (generally over 450 °C) and rutile (generally over 650 °C) phase. Although crystal structure is already obtained from as-prepared titania, further calcination process could enhance the crystallinity of titania.

1.3 Surface modification of titania

Surface modification of nanoparticles is very important because of high surface energy of small nanoparticle and potential to further application. Various functional groups including alkoxy silane, carboxylic acid, phosphonic acid, etc. could be attached on the surface of titania like presented image in Figure 1.2.[7-10]

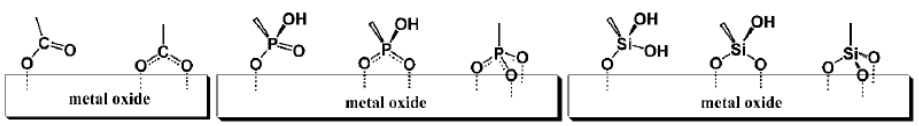

Figure 1.2. Surface binding modes of various functional groups on titania.[7]

`

Among them, carboxylic acid is the most widely used functional group especially in solar-cells so that most dye molecule is coupled with titania electrode *via* carboxylic acid group in dye sensitized solar-cells.[11] High adsorption ability of phosphonic acid group is also used for selective enrichment of phospho-peptide or proteins recently.[12, 13]

1.4 Titania as a photo-catalyst

When titania absorbs light (> about 3.0 eV, band gap of anatase), electrons are excited from valence band to conduction band and reactive holes are also generated in valence band (Figure 1.3). Both photo-generated electrons and holes have high reduction and oxidation property. Using this, titania is being widely used as a photo-catalyst in water splitting, degrading organic pollutant like dye, and various useful redox reactions.[14-22]

Meanwhile, photo-catalytic property of titania is powerful under the UV region, not in visible or near-IR region. But UV is too narrow part of entire sunlight (under 5 %) to get high efficient applications. To enhance photo-catalytic property of titania in visible region, doping of metallic and nonmetallic atom have been tried and preparation of composite with other semiconductors have been also investigated for the use of light which has much longer wavelength.[23] Very recently, metal nanoparticles such as Au and Ag are co-used with titania due to their visible-near IR light sensitivity from surface plasmon resornance.[24]

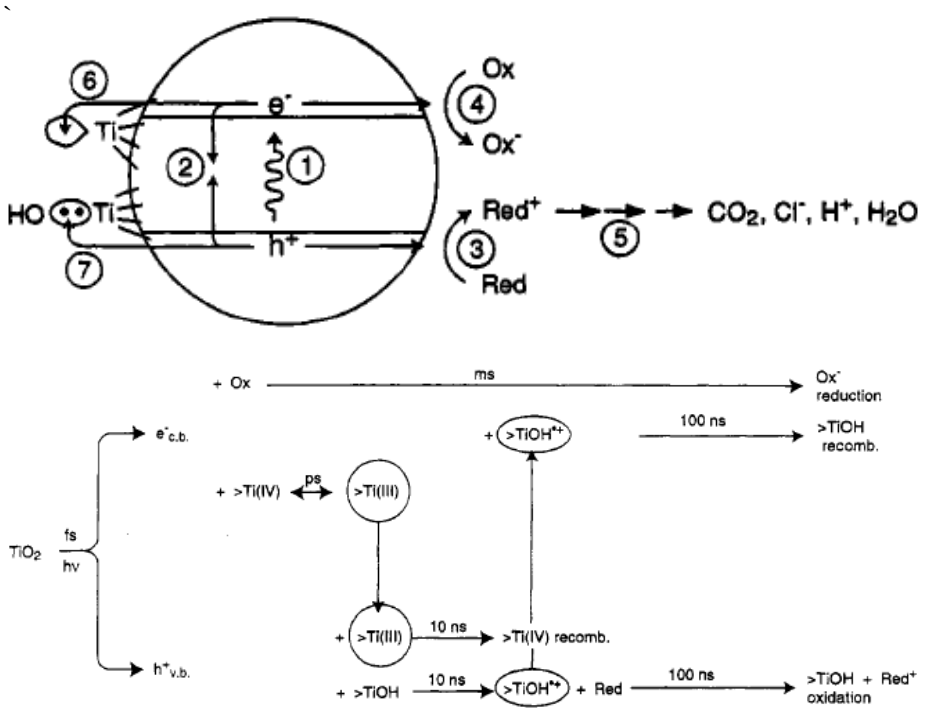

Figure 1.3. Photo-generated species in titania and their life-time.[17]

1.5 Titania in solar-cells

Titania acts as an electrode accepting electrons from donor group (dye, quantum dot, etc.) and transferring electrons to substrate, fluorine-doped tin oxide (FTO), generally. In order to load high amount of dye molecules to the titania surface, mesoporous titania film composed of small crystals about 20 nm is widely used in dye-sensitized solar-cell (Figure 1.4).[11]

Titania in several hundreds nm or sub-micron scale is also used as a scattering material in solar-cells. In presence of large titania particles, light path is lengthened and more efficient use of light is possible.[25] But with increasing size of titania, the surface area decrease, which makes low loading amount of donor materials. Large size having hierarchical structure of titania is widely used for their scattering advantage with large surface area.

`

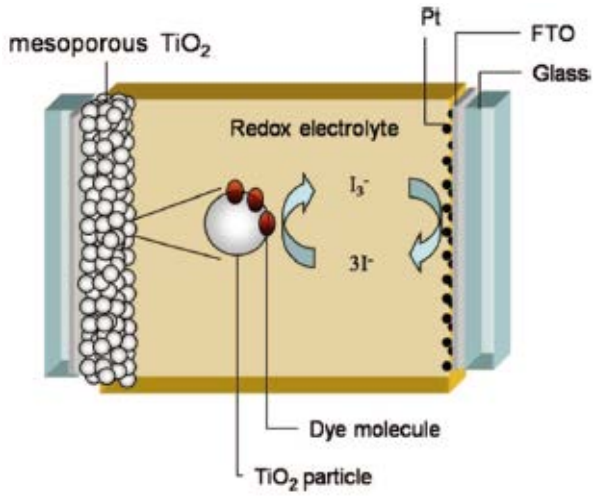

Figure 1.4. Titania in dye-sensitized solar cell.

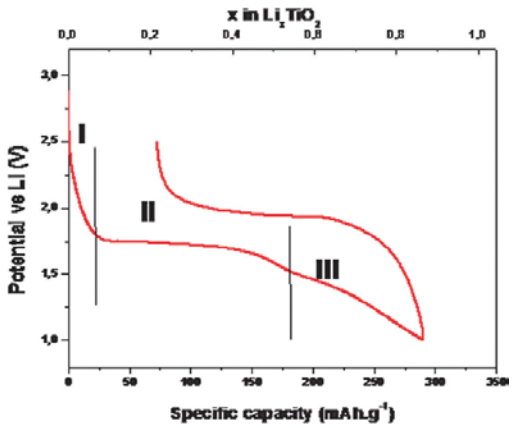

Figure 1.5. First galvanostatic Li-ion insertion and desertion of anatase titania.[28]

`

1.6 Titania as an energy storage material

Titania has been recognized as a potential anode material especially in Li-ion battery due to their high-rate performance, safety, stability, etc.[4, 26-30]

The intercalation mechanism of Li ion to the crystal of titania without huge volume change (< 4 %) makes safe and stable battery performance. Furthermore, redox potential between Li ion and titania is in about 1.5 V-1.8 V (general operating voltage of titania is 1 V-3 V). In this voltage region, the formation of solid electrolyte interface (SEI) layers that is the reason of low stable and unsafe batteries is inhibited. Li-ion insertion to anatase titania composed of first region of Li_xTiO_2 solid-solution formation, second region of two-phase intercalation, and third region of surface adsorption (Figure 1.5).

In spite of many advantages of titania, its low theoretical capacity (about 336 mAh/g or practically 168 mAh/g due to the high repulsion stress) limits their practical application in battery. The detailed explanation and application of titanina nanostructures would be represented in following chapters about Li-ion battery application (chapter 4~6).

`

1.7 References

[1] Fujishima, A.; Honda, K., *Nature* **1972**, *238*, 37-38.

[2] Linsebigler, A. L.; Lu, G.; Yates, J. T., *Chem. Rev.* **1995**, *95*, 735-758.

[3] Augustynski, J., *Electrochim. Acta* **1993**, *38*, 43-46.

[4] Chen, D.; Caruso, R. A., *Adv. Funct. Mater.* **2013**, *23*, 1356-1374.

[5] Chen, X.; Mao, S. S., *Chem. Rev.* **2007**, *107*, 2891-2959.

[6] Cushing, B. L.; Kolesnichenko, V. L.; O'Connor, C. J., *Chem. Rev.* **2004**, *104*, 3893-3946.

[7] Brennan, B. J.; Llansola Portoles, M. J.; Liddell, P. A.; Moore, T. A.; Moore, A. L.; Gust, D., *Phys. Chem. Chem. Phys.***2013**. *15*, 16605-16614.

[8] Zhao, J.; Milanova, M.; Warmoeskerken, M. M. C. G.; Dutschk, V., *Colloids Surf. A* **2012**, *413*, 273-279.

[9] Qu, Q.; Geng, H.; Peng, R.; Cui, Q.; Gu, X.; Li, F.; Wang, M., *Langmuir* **2010**, *26*, 9539-9546.

[10] Queffelec, C.; Petit, M.; Janvier, P.; Knight, D. A.; Bujoli, B., *Chem. Rev.* **2012**, *112*, 3777-3807.

[11] Hagfeldt, A.; Boschloo, G.; Sun, L.; Kloo, L.; Pettersson, H., *Chem. Rev.* **2010**, *110*, 6595-6663.

[12] Ma, W.-F.; Zhang, Y.; Li, L.-L.; You, L.-J.; Zhang, P.; Zhang, Y.-T.; Li, J.-M.; Yu, M.; Guo, J.; Lu, H.-J.; Wang, C.-C., *ACS Nano* **2012**, *6*, 3179-3188.

[13] Lu, Z.; Ye, M.; Li, N.; Zhong, W.; Yin, Y., *Angew. Chem. Int. Ed.* **2010**, *49*, 1862-1866.

[14] Schneider, J.; Matsuoka, M.; Takeuchi, M.; Zhang, J.; Horiuchi, Y.; Anpo, M.; Bahnemann, D. W., *Chem. Rev.* **2014**, *114*, 9919-9986.

[15] Chen, H.; Nanayakkara, C. E.; Grassian, V. H., *Chem. Rev.* **2012**, *112*, 5919-5948.

`

[16] Chen, X.; Shen, S.; Guo, L.; Mao, S. S., *Chem. Rev.* **2010**, *110*, 6503-6570.

[17] Hoffmann, M. R.; Martin, S. T.; Choi, W. Y.; Bahnemann, D. W., *Chem. Rev.* **1995**, *95*, 69-96.

[18] Kamat, P. V., *Chem. Rev.* **1993**, *93*, 267-300.

[19] Linsebigler, A. L.; Lu, G. Q.; Yates, J. T., *Chem. Rev.* **1995**, *95*, 735-758.

[20] Chen, C.; Ma, W.; Zhao, J., *Chem. Soc. Rev.* **2010**, *39*, 4206-4219.

[21] Chen, H. M.; Chen, C. K.; Liu, R.-S.; Zhang, L.; Zhang, J.; Wilkinson, D. P., *Chem. Soc. Rev.* **2012**, *41*, 5654-5671.

[22] Mills, A.; Davies, R. H.; Worsley, D., *Chem. Soc. Rev.* **1993**, *22*, 417-425.

[23] Asahi, R.; Morikawa, T.; Irie, H.; Ohwaki, T., *Chem. Rev.* **2014,** *114*, 9824-9852.

[24] Kochuveedu, S. T.; Jang, Y. H.; Kim, D. H., *Chem. Soc. Rev.* **2013**, *42*, 8467-8493.

[25] Deepak, T. G.; Gs, A.; Thomas, S.; A, A. T.; Nair, S. V.; Nair, S., *RSC Adv.* **2014**, *4*, 17615-17638.

[26] Chen, Z.; Belharouak, I.; Sun, Y. K.; Amine, K., *Adv. Funct. Mater.* **2013**, *23*, 959-969.

[27] Reddy, M. V.; Subba Rao, G. V.; Chowdari, B. V., *Chem. Rev.* **2013**, *113*, 5364-5457.

[28] Froschl, T.; Hormann, U.; Kubiak, P.; Kucerova, G.; Pfanzelt, M.; Weiss, C. K.; Behm, R. J.; Husing, N.; Kaiser, U.; Landfester, K.; Wohlfahrt-Mehrens, M., *Chem. Soc. Rev.* **2012**, *41*, 5313-5360.

[29] Jiang, C. H.; Zhang, J. S., *J. Mater. Sci. Technol.* **2013**, *29*, 97-122.

[30] Yang, Z.; Choi, D.; Kerisit, S.; Rosso, K. M.; Wang, D.; Zhang, J.; Graff, G.; Liu, J., *J. Power Sources* **2009**, *192*, 588-598.

`

Chapter 2.

Facile Preparation of Mono-dispersed Spherical Titania Nanoparticles by Using Ethylene Glycol with Precise Size Control

2.1 Abstract

Mono-dispersed spherical titania nanoparticles (TNPs) were obtained by using ethylene glycol (EG) as a chelating agent to reduce the reactivity of $Ti(OBu)_4$ (TB). The size of TNPs can be changed from ~70 nm to 300 nm by varing the amount of titania precursor and water. Increasing water content can reduce the size of TNPs, which is expected the generation of a large number of small seeds in the initial reaction state to form final small-sized TNPs. Synthesis of TNPs can be also possible in other solvents and chelating agents such as 1,4-dioxane and catechol, respectively.

`

2.2 Introduction

TNPs have been used as an UV-active photo-catalyts,[1-3] electrodes for dye-sensitized solar cells (DSSCs),[4] and in recent perovskite solar cells.[5] TNPs have also been widely used as a scattering material in DSSCs,[6] Li intercalating anode material in Li-ion batteries,[7-10] electrophoretic or photonic crystal materials,[11-14] and even as a carrier material for recent biotechnology.[15-19] The preparation of mono-dispersed TNPs with various sizes is very important in these applications. First, TNPs with a narrow size distribution are especially important in the formation of regular photonic crystal arrays[20] and the size of TNPs is one of the major factors in changing the reflection wavelength of the photonic band gap.[13] Size control of TNPs is also important for studying the size-dependent toxicity.[21, 22] Using small sized TNPs (less than 100 nm) is especially important for ensuring the colloidal stability for the electrophoretic or biological application. Hence, the synthesis of mono-dispersed and size controllable TNPs has been recognized as an important issue.

Meanwhile, the sol-gel method is a very simple and easy method for obtaining metal oxide nanoparticles, such as silica, from a silicon alkoxide precursor.[1, 23, 24] However, in contrast to silicon alkoxide, titanium alkoxide has a higher reactivity towards water because the electronegativity of titanium is lower than that of silicon and because of the coordination expansion of titanium.[25] Therefore, it is difficult to prepare TNPs with narrow size distribution. Several chemicals such as alkoxy- and amino-alcohols, have been used to reduce the reactivity of titanium alkoxide.[25] EG can also reduce the high reactivity of titanium alkoxide by chelating to the titanium atom; TNPs were prepared using this Ti-EG intermediate. Xia *et al*. prepared mono-dispersed spherical TNPs in the 200-500 nm range using the Ti-EG

`

intermediate in acetone solution.[26] Although this method has been used for preparing TNPs in many studies, small TNPs, below 200 nm, have rarely been prepared.[27-29]

Herein, the size control of TNPs, even below 200 nm, was performed using the Ti-EG intermediate in acetone solvent. The concentration of titania precursor and water were both varied for obtaining TNPs with different sizes. The formation and size control of TNPs were also possible in other solvents with chemical structure similar to that of acetone. Small TNPs below 100 nm with colloidal stability were functionalized for the further application.

2.3 Results and Discussion

EG was used to reduce the high reactivity of TB towards water. The formation of the Ti–EG complex, along with the generation of 1-butanol is expected during the reaction between TB and EG. The stability of TB in EG was tested by varying the molar ratio of TB and EG. Ideally, two EG molecules can react with one TB generating one Ti-EG intermediate and four molecules of 1-butanol as follows.

$$Ti(OBu)_4 + 2HOCH_2CH_2OH \rightarrow Ti(OCH_2CH_2O)_2 + 4BuOH$$

However, 0.05 mL of TB was reacted with 10 mL of EG (molar ratio of ~1:100) because the mixed solution had low stability at lower amounts of EG. The mixed solution of TB and EG was poured into the acetone solvent to obtain a white colloid of spherical nanoparticles. The size of nanoparticles could be reduced by decreasing the amount of the mixed solution of TB and EG. The range of obtained particle size was from about 300 nm (1.2 mM of TB in the acetone solvent) to 50 nm (0.05 mM of TB), as shown in Figure 2.1.

`

Although size control of TNPs was possible even below 200 nm, because of the limited amount of titania precursor, the amount of obtained product was too small for the characterization and application of TNPs.

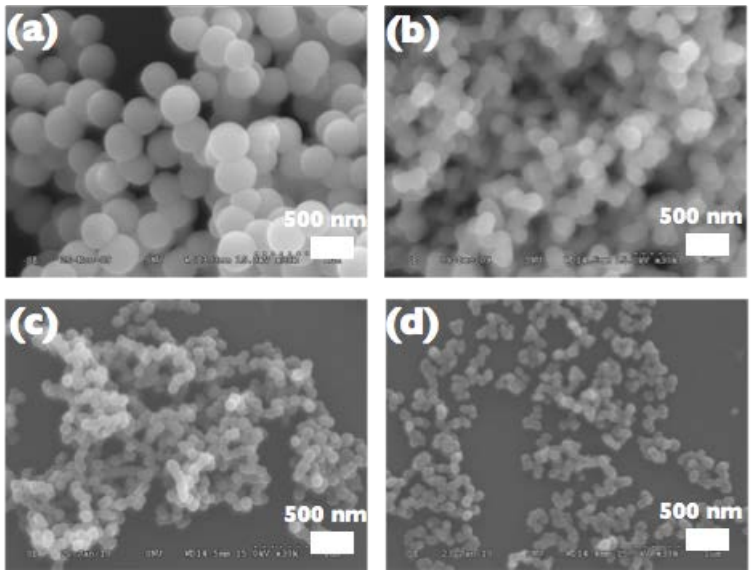

Figure 2.1. FE-SEM images of TNPs using (a) 1.2 mM, (b) 0.6 mM, (c) 0.3 mM, and (d) 0.05 mM of TB.

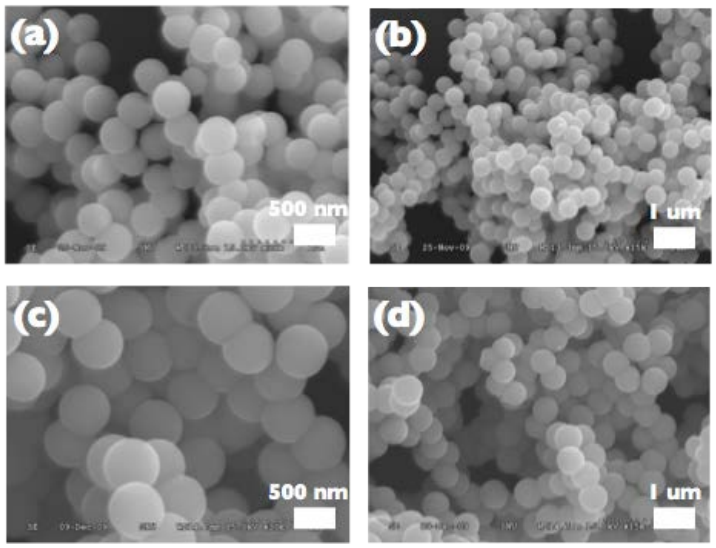

Figure 2.2. FE-SEM images of TNPs with (a) and (b) normal acetone solvent and (c) and (d) water-removed acetone solvent.

`

Additional water was introduced to control the size of nanoparticles without changing the titania precursor. When the small amount of water present in acetone was removed by $MgSO_4$, the obtained particle size was increased from about 300 nm to 500 nm (Figure. 2.2) indicating that a small amount of water can reduce particle size.

More water was added to the acetone solvent in order to reduce the size of TNPs without decreasing the amount of titania precursor. TNPs about 200 nm in size were prepared in acetone solvent using 0.6 mM of TB (Figure 2.3a). When the water to TB ratio was 5:1 (v/v), the size of TNPs decreased to 100 nm. Increasing the water content induced the preparation of smaller TNPs shown in Figure 2.3. TNPs below 100 nm were also obtained at a water : TB ratio (v/v) of 50:1 (Figure 2.3d). The decrease in particle size with increasing water content can be explained by the rapid formation of seeds in the initial reaction state.

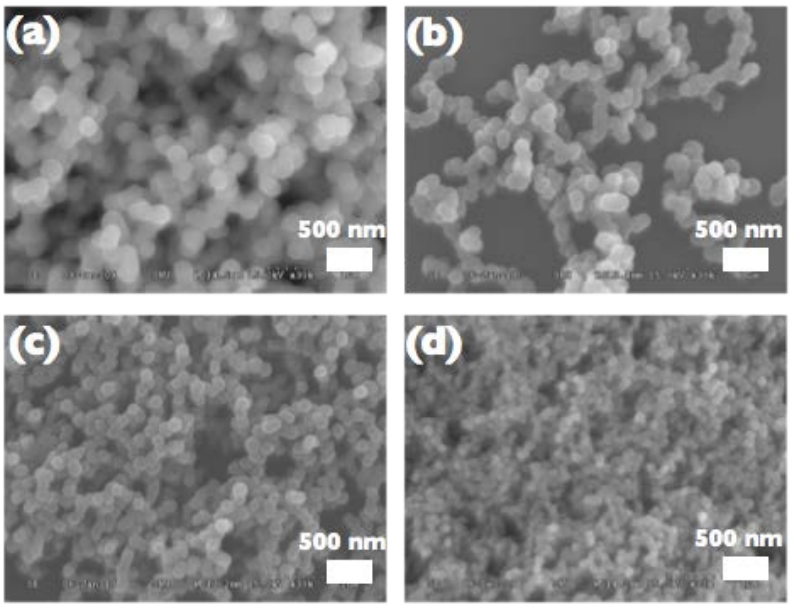

Figure 2.3. FE-SEM images of TNPs (a) without water, using water : TB (v/v) ratio of (b) 5:1, (c) 10:1, and (d) 50:1.

`

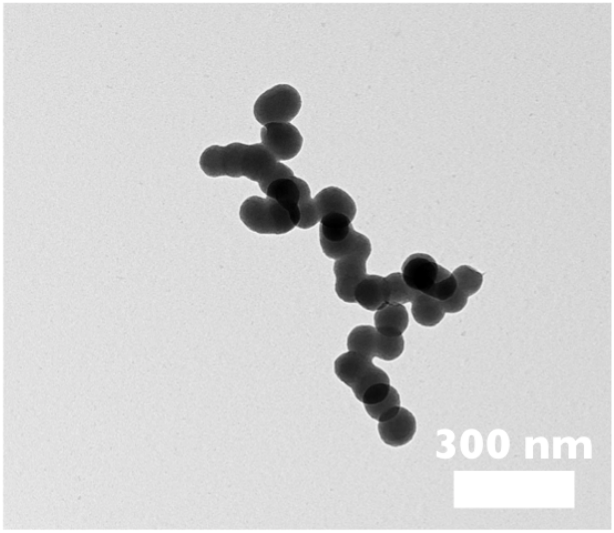

Figure 2.4. TEM image of aggregated TNPs.

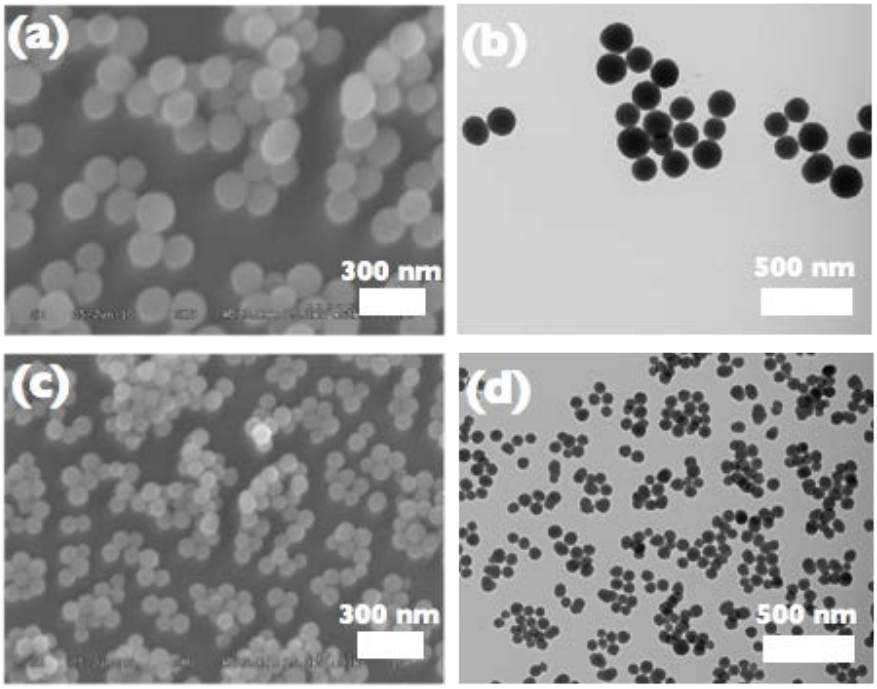

Figure 2.5. (a) FE-SEM and (b) TEM images of TNPs using Tween 20, (c) FE-SEM and (d) TEM images of TNPs using Tween 20 and water.

`

Although the size of TNPs was controlled by varying the amount of titania precursor and water, the prepared TNPs had a tendency to form aggregates and were not stabilized as individual particles, as shown in the TEM image in Figure 2.5, indicating poor colloidal stability in ethanol solvent. Tween 20 was used as a surface stabilizing agent to prepare TNPs without aggregation. [28] TNPs prepared with Tween 20 are shown in Figure 2.5; FE-SEM images in Figure 2.5 and TEM images in Figure 2.5b show mono-dispersed spherical TNPs without aggregation. When additional water was used in this system (water : TB (v/v) ratio = 10:1), ~70 nm TNPs were obtained without any aggregation (Figure 2.5c and 2.5d).

TNPs were also synthesized in other solvents. Although the formation of TNPs, from TB and EG, in acetone solvent is not fully understood yet, the preparation of TNPs in other solvent has rarely been studied before. In the reaction conditions used herein, any precipitation was observed on using other solvents such as methanol, ethanol, 2-propanol, ethyl acetate, and acetyl anhydride. Synthesis of TNPs in alcohol solvents was also attempted. Increasing the amount of water and making the reaction conditions acidic or basic using hydrochloric acid or ammonia, respectively also did not lead to the formation of particles in alcohol solvents.

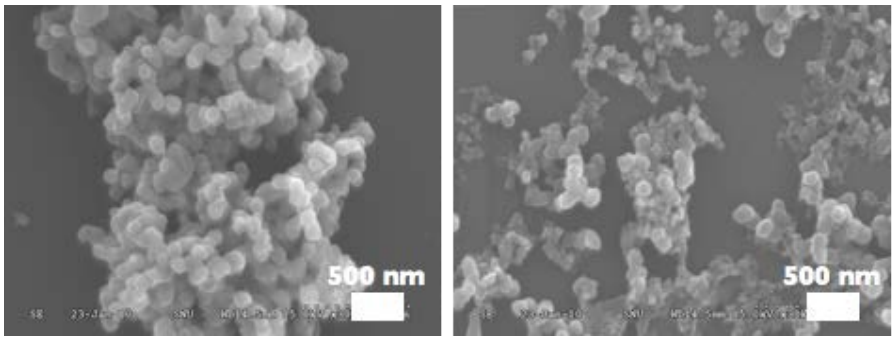

Figure 2.6. FE-SEM images of TNPs prepared in cyclohexanone solvent.

`

Meanwhile, in spite of not having perfect spherical morphology, particles were precipitated in cyclohexanone solvent, as shown in Figure 2.6. Because of the common characteristics in the chemical structure of acetone and cyclohexanone (aprotic and presence of oxygen with two lone-pair electrons), 1,4-dioxane and tetrahydrofuran were also tested as solvents for preparing TNPs. More spherical TNPs were obtained in both solvents and the method of decreasing the particle size by increasing the water content also worked in these solvents (Figure 2.7).

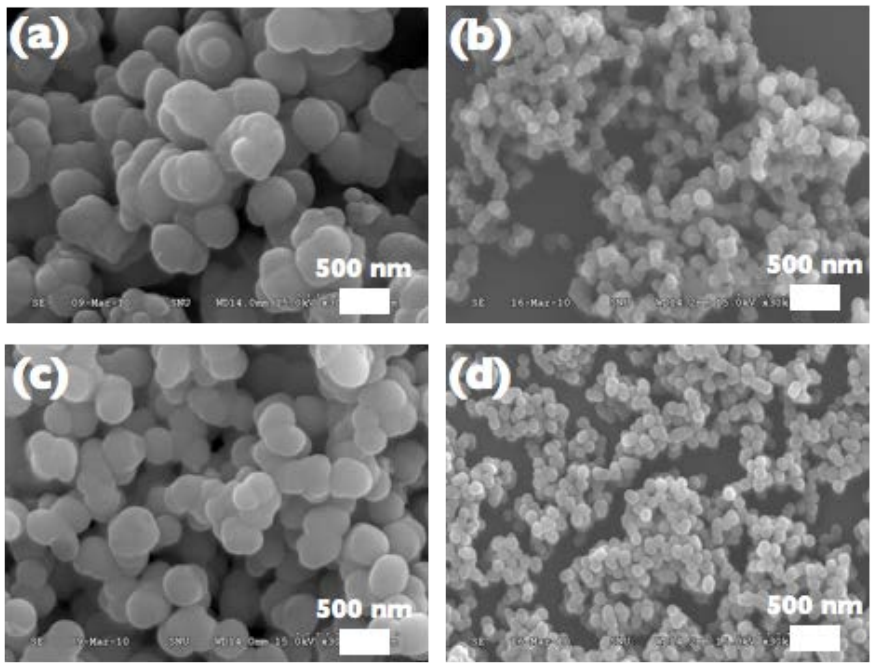

Figure 2.7. FE-SEM images of TNPs prepared (a) without and (b) with additional water in 1,4-dioxane and (c) without and (d) with additional water in THF.

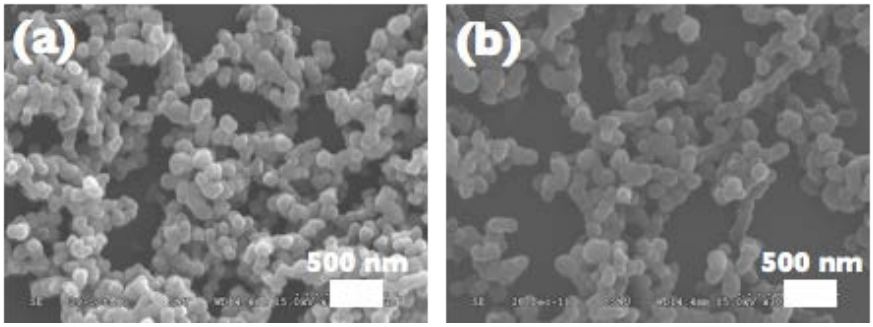

Figure 2.8. FE-SEM images of TNPs prepared using (a) TG and (b) catechol as chelating agent.

Chelating molecules, other than EG, were also used to reduce the high reactivity of TB. For this purpose, triethyleneglycol and catechol were used to make TNPs via stabilized intermediates. Spherical nanoparticles were successfully obtained using both chelating molecules (Figure 2.8). In the case of catechol, not only the mixed solution of TB and catechol but also the prepared TNPs showed a brownish-red color, because of their increased visible light absorbance due to charge transfer from catechol to titanium. [32, 33]

The obtained TNPs, from TB and EG, were characterized by thermogravimetric analysis (TGA), as shown in Figure 2.9a. As reported previously, the as-prepared TNPs showed a large weight loss of ~32 wt%, which was attributed to their glycol units.[26] X-ray diffraction patterns (XRD) were also obtained for the further characterization of the TNPs (Figure 2.9b). Although any crystalline peaks were observed for TNPs annealed at 350 °C for 2 hr, anatase (JCPDS File No. 21-1272) and rutile (JCPDS File No. 21-1276) crystallinity was observed for TNPs, annealed at 500 °C and 950 °C, respectively. These results were similar to those of the reported TNPs obtained from TB and EG precursors.[26, 34]

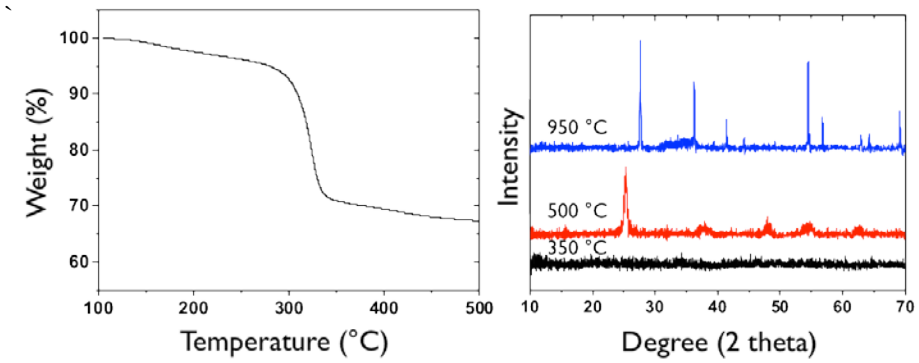

Figure 2.9. (a) Weight loss of the as-prepared TNPs in TGA and (b) XRD patterns of TNPs annealed under different temperatures.

Finally, as the scheme of Figure 2.10a, the surface of as-prepared TNPs about 70 nm was modified for the further applications such as preparing hybrid materials with other material, bio labeling and the carrier of bio-materials.

Amine groups were introduced on the surface of TNPs by using 3-(trimethoxysilylpropyl)diethylenetriamine (DETAS) which have alkoxy-silane coupling group. Hydrolysis of DETAS and condensation with the surface of prepared TNPs were confirmed by the change of surface charge from (-) 35.8 mV of Ti-O^- to (+) 25.4 mV of $–NH_3^+$ by zeta-potential (DET-TNPs). Additional experiment was performed to confirm the surface modification through coupling reaction between rhodamine B isothiocyanate (RITC) and DETAS-TNPs. Amine groups on the surface of TNPs could attack to the NCS group of RITC *via* nucleophilic addition. The coupling of RITC on the DET-TNPs was confirmed by comparing the color of TNPs having or not having functional amine group. In the left vial of Figure 2.10b, as-prepared TNPs were well dispersed as white colloid in ethanol with good colloidal stability. The middle vial of Figure 2.10b shows RITC adsorbed on TNPs without functional amine group by charge-charge interaction between positive

`

ammonium ion in RITC and negative surface of TNPs. But pink color was well monitored in the right vial of Figure 2.10b, which shows that RITC was coupled with DETAS-TNPs by chemical bonding. As a result, it could be concluded that functional TNPs with small size and good colloidal stability have potential for various application especially biotechnology.

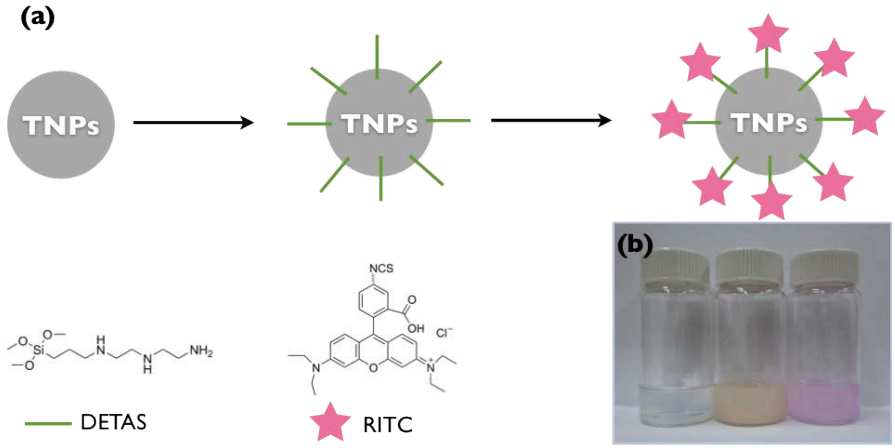

Figure 2.10. (a) Schematic image of the surface modification of TNPs and (b) digital photograph showing TNPs with colloidal dispersity in ethanol (left-as prepared TNPs, middle-RITC adsorbed TNPs, and right-RITC coupled TNPs).

`

2.4 Conclusions

The spherical TNPs were obtained from stable precursor mixture of TB and EG in acetone solvent. The size of TNPs was controlled by the concentration of titania precursor and water and colloidal stability of TNPs was obtained using Tween 20 as a surfactant in reaction condition. TNPs also could be prepared in other solvents or chelating agents for their similar chemical structure with acetone or EG. Functionalization of TNPs was tested with introducing RITC for the further applications such as bio-imaging or drug delivery.

2.5 Experimental Section

Materials and Instruments Titanium butoxide (TB), Tween 20, and rhodamine B isothiocyanate (RITC) were purchased from Aldrich. 3-(trimethoxysilylpropyl)diethylenetriamine (DETAS) was purchased by Gelest. All solvents were purchased by Samchun (Korea) and used without any purification.

Field-Emission Scanning Electron Microscopy (FE-SEM) and Transmission Electron Microscopy (TEM) images were acquired by Hitachi S-4300 and Hitachi-7600 instrument, respectively. X-Ray Diffraction patterns (XRD) were obtained by powder X-Ray diffractometry (D8 Advance, Bruker). The surface charge of TNPs was monitored using a Dynamic Light Scattering Spectrophotometer (DLS-7000).

`

Synthesis of TNPs To prepare ~70 nm TNPs, TB (0.05 mL) was dissolved in 5 mL of EG and stirred for 8 hr. This mixed solution was injected into an acetone solution (120 mL) containing 1.0 mL water and 0.1 mL of Tween 20 at room temperature. After 2 hr, the white product was washed by centrifugation (thrice at 17000 rpm for 10 min in ethanol) and re-dispersed in ethanol. TNPs of different sizes can be prepared by controlling the concentration of TB and water, as presented above. TNPs were also prepared using other solvents and chelating agents instead of ethanol and EG.

Surface modification of TNP DETAS (0.05 mL) was injected to TNPs (5 mg/mL in 10 mL of ethanol) and stirred over 2 hr under room temperature. The product was washed by centrifugation (thrice at 17000 rpm for 10 min in ethanol) and re-dispersed in ethanol. To introduce RITC, RITC (10 mg) was dissolved in DET-TNPs and stirred over 2 hr. The product was washed by centrifugation (thrice at 17000 rpm for 10 min in ethanol) and re-dispersed in ethanol. To confirm the electrostatic adsorption between TNPs and RITC, TNPs without amine group was mixed with RITC and purified in the same way of DET-TNPs.

`

2.6 References

[1] Chen, X.; Mao, S. S., *Chem. Rev.* **2007**, *107*, 2891-2959.

[2] Chen, H.; Nanayakkara, C. E.; Grassian, V. H., *Chem. Rev.* **2012**, *112*, 5919-5948.

[3] Schneider, J.; Matsuoka, M.; Takeuchi, M.; Zhang, J.; Horiuchi, Y.; Anpo, M.; Bahnemann, D. W., *Chem. Rev.* **2014**, *114*, 9919-9986.

[4] Hagfeldt, A.; Boschloo, G.; Sun, L.; Kloo, L.; Pettersson, H., *Chem. Rev.* **2010**, *110*, 6595-6663.

[5] Kazim, S.; Nazeeruddin, M. K.; Grätzel, M.; Ahmad, S., *Angew. Chem. Int. Ed.* **2014**, *53*, 2812-2824.

[6] Deepak, T. G.; Anjusree, G. S.; Thomas, S.; Arun, T. A.; Nair, S. V.; Sreekumaran Nair, A., *RSC Adv.* **2014**, *4*, 17615-17638.

[7] Chen, Z.; Belharouak, I.; Sun, Y. K.; Amine, K., *Adv. Funct. Mater.* **2013**, *23*, 959-969.

[8] Reddy, M. V.; Subba Rao, G. V.; Chowdari, B. V., *Chem. Rev.* **2013**, *113*, 5364-5457.

[9] Su, X.; Wu, Q.; Zhan, X.; Wu, J.; Wei, S.; Guo, Z., *J. Mater. Sci.* **2012**, *47*, 2519-2534.

[10] Yang, Z.; Choi, D.; Kerisit, S.; Rosso, K. M.; Wang, D.; Zhang, J.; Graff, G.; Liu, J., *J. Power Sources* **2009**, *192*, 588-598.

[11] Luo, Y.; Zhang, J.; Sun, A.; Chu, C.; Zhou, S.; Guo, J.; Chen, T.; Xu, G., *J. Mater. Chem. C* **2014**, *2*, 1990-1994.

`

[12] Shim, H.; Gyun Shin, C.; Heo, C.-J.; Jeon, S.-J.; Jin, H.; Woo Kim, J.; Jin, Y.; Lee, S.; Lim, J.; Gyu Han, M.; Lee, J.-K., *Appl. Phys. Lett.* **2014**, *104*, 051104.

[13] Shim, H.; Lim, J.; Shin, C. G.; Jeon, S.-J.; Han, M. G.; Lee, J.-K., *Appl. Phys. Lett*. **2012**, *100*, 063113.

[14] Wijnhoven, J. E. G. J.; Vos, W. L., *Science* **1998**, *281*, 802-804.

[15] Wu, S.; Weng, Z.; Liu, X.; Yeung, K. W. K.; Chu, P. K., *Adv. Funct. Mater*. **2014**, *24*, 5464-5481.

[16] Paunesku, T.; Rajh, T.; Wiederrecht, G.; Maser, J.; Vogt, S.; Stojicevic, N.; Protic, M.; Lai, B.; Oryhon, J.; Thurnauer, M.; Woloschak, G., *Nat. Mater*. **2003**, *2*, 343-346.

[17] Tachikawa, T.; Asanoi, Y.; Kawai, K.; Tojo, S.; Sugimoto, A.; Fujitsuka, M.; Majima, T., *Chem. Eur. J.* **2008**, *14*, 1492-1498.

[18] Jana, B.; Mondal, G.; Biswas, A.; Chakraborty, I.; Ghosh, S., *RSC Adv.* **2013**, *3*, 8215-8219.

[19] Zhang, X.; Wang, F.; Liu, B.; Kelly, E. Y.; Servos, M. R.; Liu, J., *Langmuir* **2014**, *30*, 839-845.

[20] Xia, Y. N.; Gates, B.; Yin, Y. D.; Lu, Y., *Adv. Mater*. **2000**, *12*, 693-713.

[21] Rancan, F.; Gao, Q.; Graf, C.; Troppens, S.; Hadam, S.; Hackbarth, S.; Kembuan, C.; Blume-Peytavi, U.; Ruhl, E.; Lademann, J. R.; Vogt, A., *ACS Nano* **2012**, *6*, 6829-6842.

[22] Pan, Y.; Neuss, S.; Leifert, A.; Fischler, M.; Wen, F.; Simon, U.; Schmid, G.; Brandau, W.; Jahnen-Dechent, W., *Small* **2007**, *3*, 1941-1949.

[23] Hench, L. L.; West, J. K., *Chem. Rev.* **1990**, *90*, 33-72.

`

[24] Chen, D.; Caruso, R. A., *Adv. Funct. Mater.* **2013**, *23*, 1356-1374.

[25] Schubert, U., *J. Mater. Chem.* **2005**, *15*, 3701-3715.

[26] Jiang, X. C.; Herricks, T.; Xia, Y. N., *Adv. Mater.* **2003**, *15*, 1205-1209.

[27] Wang, P.; Xie, T.-F.; Li, H.-Y.; Peng, L.; Zhang, Y.; Wu, T.-S.; Pang, S.; Zhao, Y.-F.; Wang, D.-J., *Chem. Eur. J.* **2009**, *15*, 4366-4372.

[28] Yu, H. K.; Yi, G.-R.; Kang, J.-H.; Cho, Y.-S.; Manoharan, V. N.; Pine, D. J.; Yang, S.-M., *Chem. Mater.* **2008**, *20*, 2704-2710.

[29] Wang, L.; Cai, Y.; Song, L.; Nie, W.; Zhou, Y.; Chen, P., *Colloids Surf. A* **2014**, *461*, 195-201.

[30] Chen, S.-L.; Dong, P.; Yang, G.-H.; Yang, J.-J., *Ind. Eng. Chem. Res.* **1996**, *35*, 4487-4493.

[31] Mine, E.; Hirose, M.; Nagao, D.; Kobayashi, Y.; Konno, M., *J. Colloid Interface Sci.* **2005**, *291*, 162-168.

[32] Duncan, W. R.; Prezhdo, O. V., *J. Phys. Chem. B* **2005**, *109*, 365-373.

[33] Rajh, T.; Chen, L. X.; Lukas, K.; Liu, T.; Thurnauer, M. C.; Tiede, D. M., *J. Phys. Chem. B* **2002**, *106*, 10543-10552.

[34] Jiang, X. C.; Wang, Y. L.; Herricks, T.; Xia, Y. N., *J. Mater. Chem.* **2004**, 14, 695-703.

`

Chapter 3.

Synthesis of Spherical Titania Nanoparticles with KCl Salt and Simple Size Control under Various Conditions

Accepted from *Bull. Korean Chem. Soc.* (2014.12.04)

3.1 Abstract

In this chapter, spherical titania nanoparticles are prepared with KCl. KCl salt could reduce the reactivity of titanium alkoxide due to their strong affinity with water. The size of titania nanoparticles is tuned from under 100 nm to several hundreds nanometer by changing various reaction conditions. The amount of titania source and KCl salt, reaction temperature, and the kind of solvent were systematically investigated in this chapter.

`

3.2 Introduction

Titania nanoparticles (TNPs), which are already in widespread used in our daily lives as white pigments and sunscreen materials, have attracted much attention for their possible applications in various fields, such as photonic band materials, gas sensing, solar cells, batteries, and photo-catalysts.[1-10] Among other properties, the great photo-catalytic properties of TNPs have been actively investigated to remove organic pollutants.[10,11] The photo-catalytic properties of TNPs come from their wide band-gap of approximately 3.4 eV and band position. Under UV irradiation, an electron of the valence band is excited to the conduction band, generating an electron-hole pair. The electron and hole migrate to the surface of the TNPs to participate in possible chemical reactions. Typically, the water absorbed on the surface of titania can participate in a redox reaction to generate reactive oxygen species (ROS), including hydroxyl radicals. Finally, organic pollutants can be easily degraded by the ROS. Very recently, reduced titania with oxygen vacancies has also attracted researcher attention for its increased visible light absorption and conductivity.[12,13]

It is known that the size of TNPs significantly affects all the properties of TNPs, including specific surface area, life-time of the electron-hole pair, conductivity, etc.[14] The sol-gel method was investigated to control the size of TNPs because of its simple, inexpensive, and low temperature characteristics; titanium alkoxides are typical starting materials in the sol-gel method for hydrolysis and condensation to produce TNPs. However, because of the high reactivity of titanium alkoxides with water, it is usually necessary to reduce their reactivity via the addition of a chelating agent or salt.[15-17] After Look and Zukoski initially used NaCl or HCl to reduce the reactivity between titanium alkoxide and water, various salts were used to prepare TNPs.[17] Eiden-

`

Assmann *et al.* used eight types of salts to obtain TNPs in the size range of a few hundred nanometers.[18] Although the preparation of TNPs in the size range of 10 nm to 300 nm by controlling the concentration of $CaCl_2$ has recently been reported,[19] there are few studies regarding the size control of TNPs with other salts. Therefore, we have employed KCl salt to prepare TNPs of approximately 100 nm in size for application in electrophoretic devices.[3] However, other reaction conditions, such as reaction temperature and various solvents, were not thoroughly investigated.

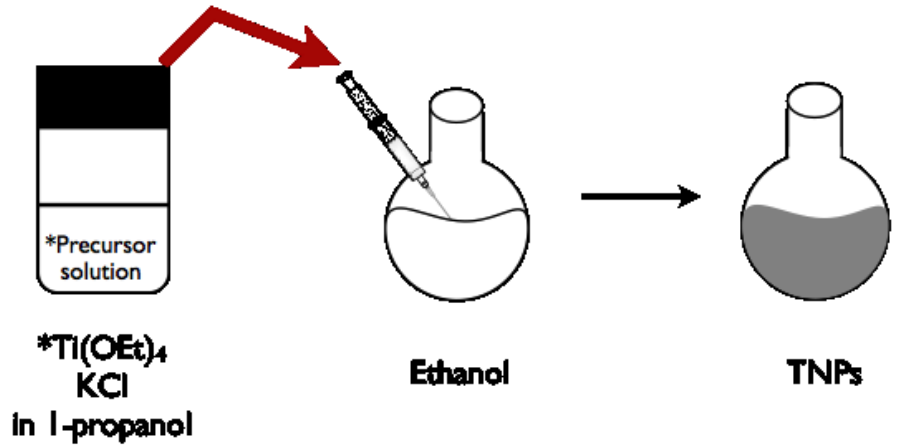

Scheme 3.1. Synthetic process for preparing TNPs.

`

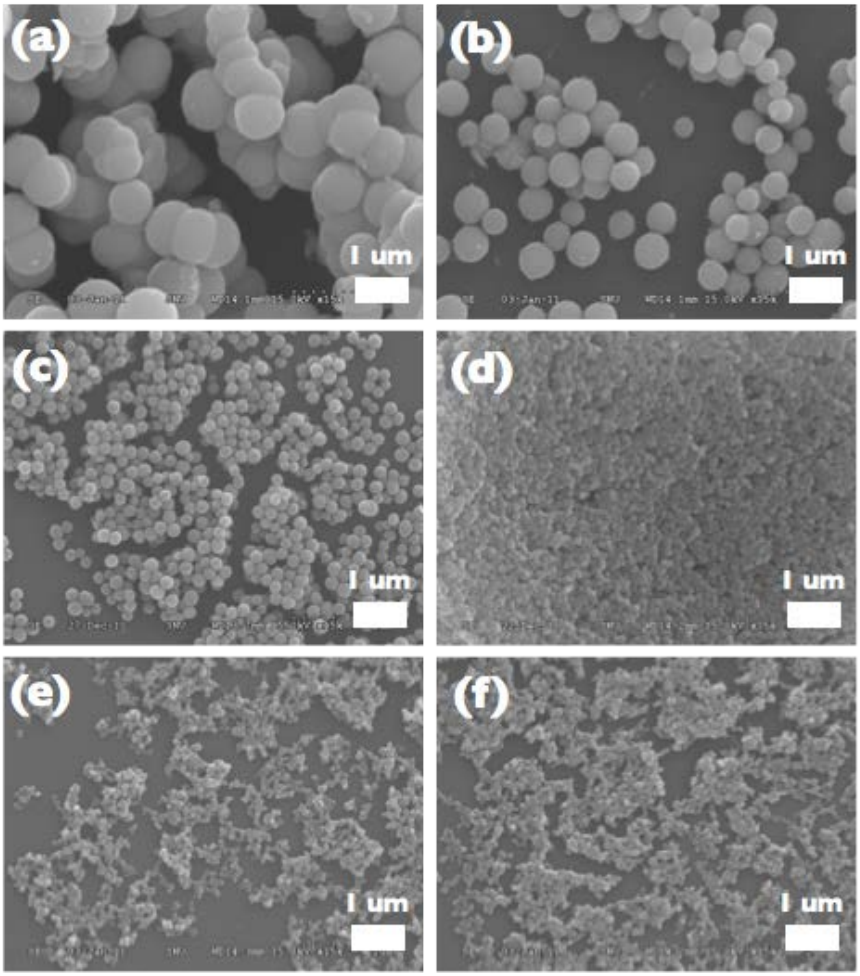

Figure 3.1. FE-SEM images of prepared TNPs using different concentration of KCl ((a) and (b): 0.16 M, (c) and (d): 0.32 M, (e) and (f): 0.48 M) and precursor solution ((a), (c), and (e): 6 mL, (b), (d), and (f): 12 mL).

3.3 Results and Discussion

The synthetic method to control the size of TNPs using KCl was represented by reducing the reactivity of titanium alkoxide as represented scheme 3.1. First, titanium ethoxide was diluted in 1-propanol with KCl salt. This mixed precursor solution was clear and stable over several weeks without any

`

precipitation because of the high solubility of the partially hydrolyzed titanium precursor in 1-propanol with KCl.[20] When the precursor solution was diluted by injection into an excess amount of ethanol, white spherical colloids were generated as a result of the lower solubility of the partially hydrolyzed titanium precursor in ethanol. Further hydrolysis and condensation of the colloids progressed to afford dense nanoparticles.

Representative field-emission scanning electron microscopy (FE-SEM) images of the generated TNPs at various conditions are shown in Figure 3.1. The size of the TNPs could be controlled from approximately 100 to 800 nm by varying the concentration of KCl and titanium alkoxide as well as the amount of precursor solution. When the concentration of KCl was increased (0.16, 0.32, and 0.48 M), the size of the resulting TNPs decreased. The formation of TNPs can be described as the aggregation of smaller particles[18,21] rather than the seed-growth method of the Lamer model.[22] Therefore, a large number of smaller TNPs at the high KCl concentration could be explained by the high colloidal stability of the primary particles with less aggregation. When the concentration of titanium ethoxide was increased, the size of the TNPs also increased, as shown in Figure 3.2. The amount of precursor solution also affected the size of the TNPs (6 mL and 12 mL). However, contrary to the typical tendency, a large number of smaller TNPs were obtained upon increasing the amount of precursor solution; the particle size typically tends to increase with increasing amounts of precursor solution. Under our synthetic conditions, when the amount of the precursor solution was increased, the concentrations of both KCl and titanium ethoxide were also increased, which competitively affected the size of the generated TNPs. As a result, a stabilizing effect for primary particles at high concentrations of KCl seemed to be a major driving force for the generation of smaller sized TNPs.

`

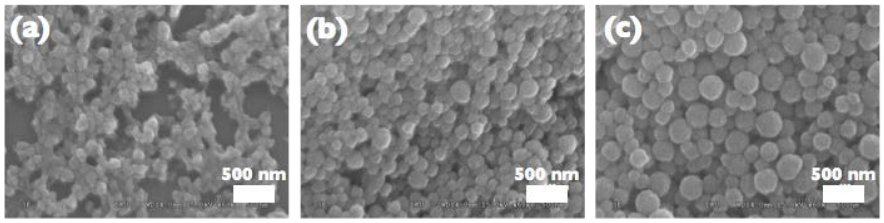

Figure 3.2. FE-SEM images of TNPs using (a) 0.4 mL, (b) 0.8 mL, and (c) 1.2 mL of titanium ethoxide in precursor solution.

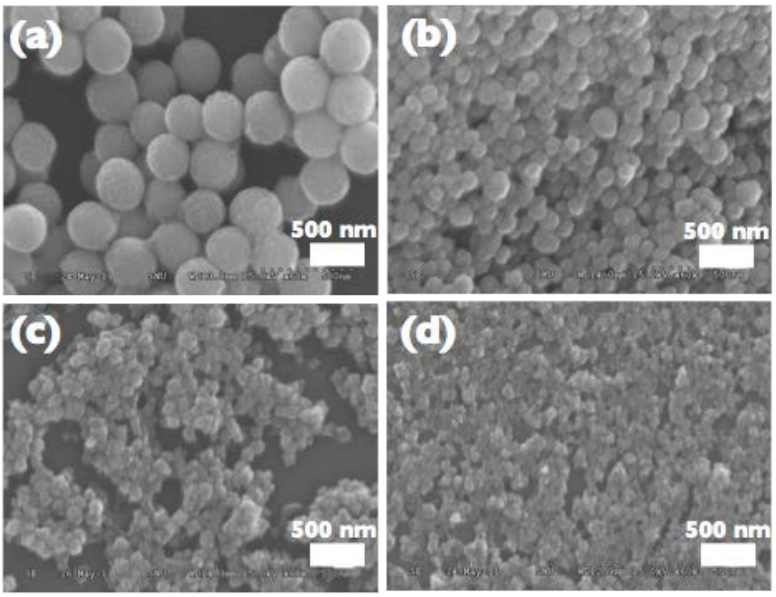

Figure 3.3. FE-SEM images of prepared TNPs at various reaction temperatures; (a) 0 °C, (b) room temperature, (c) 60 °C, and (d) 80 °C.

`

The size of the TNPs was also affected by the reaction temperature, as shown in Figure 3.3. When a 0.48 M KCl solution was used, approximately 100 nm TNPs (Figure 3.3b) were obtained at room temperature, whereas much larger TNPs (approximately 300 nm, Figure 3.3a) were obtained at 0 °C, and much smaller TNPs (Figure 3.3c and 3.3d) were obtained at 60 °C and 80 °C, respectively. These results are consistent with the suggested explanation in the literature that the reaction rate of the hydrolysis-condensation of metal alkoxides increases at higher temperatures to generate more small particles Generally, many seed particles are generated at high temperatures that grow into small particles, whereas at low temperatures, fewer seed particles are generated that grow into larger particles.[23]

To precisely understand the size-control mechanism of TNPs under our synthetic conditions, the growth of TNPs was monitored by transmission electron microscopy (TEM).

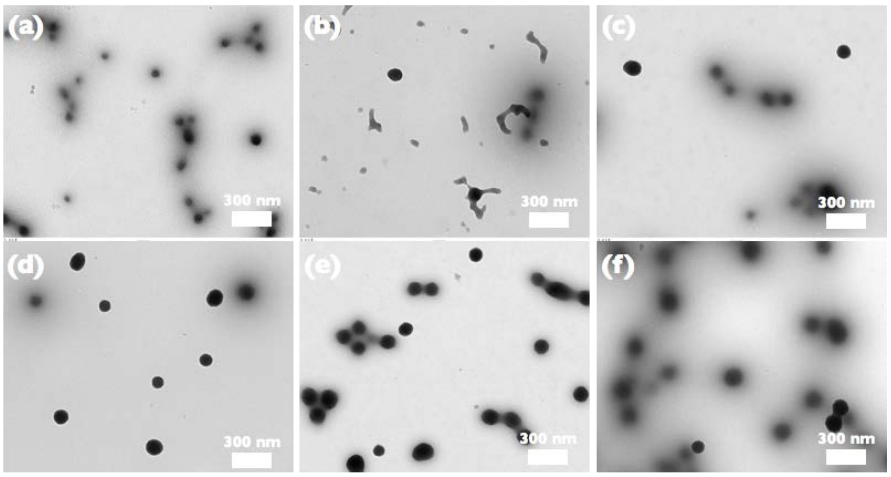

Figure 3.4. TEM images of aliquots of TNPs extracted at (a) 5 min, (b) 10 min, (c) 15 min, (d) 20 min, (e) 25 min, and (f) 30 min after reaction under 0 °C.

`

Aliquots of the reaction mixture were collected at 0 °C and characterized using TEM (Figure 3.4). After 5 min, particles approximately 50 nm in size were already observed, and the particle size continuously increased to approximately 130 nm after 30 min. Gel-like materials were also observed in the image of the reaction mixture at 10 min, which seemed to be condensed onto the spherical particles, suggesting that these phenomena were explained by neither the aggregation of primary particles nor the seed-growth method. Therefore, it appears that both methods might co-exist under our synthetic conditions.

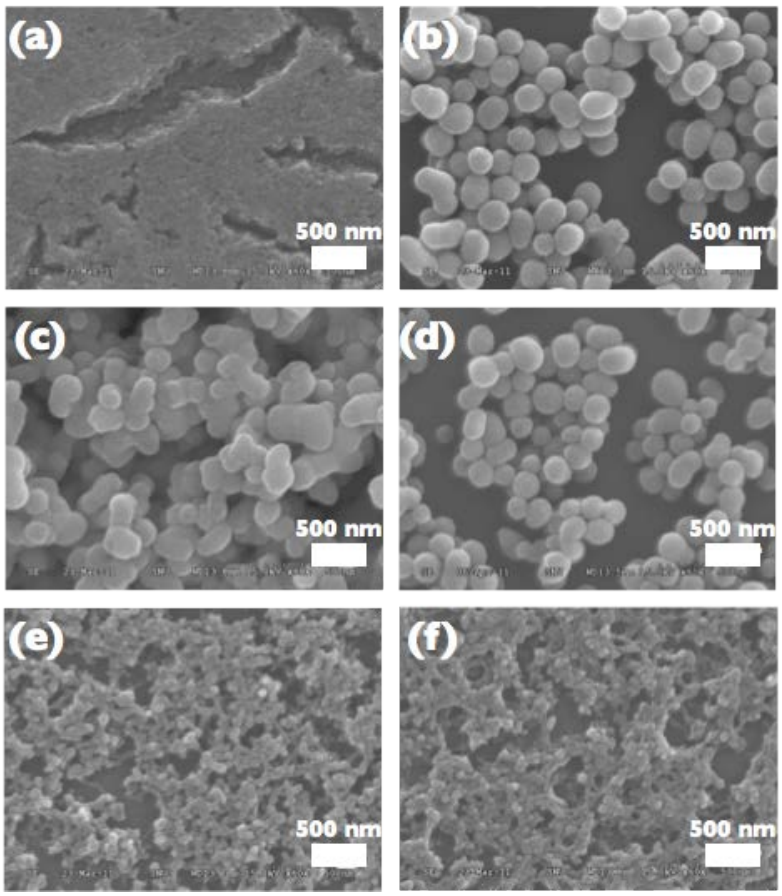

Figure 3.5. FE-SEM images of TNPs prepared in (a) THF, (b) 1,4-dioxane, (c) methanol, (d) acetone, (e) acetonitrile, and (f) DMSO.

`

The synthesis of TNPs was also tested in other solvent systems. The polarity of the solvent seemed to play an important role in the preparation of TNPs because polar solvents can have a strong interaction with water, in addition to salt. TNPs produced from various solvents with different polarities showed different sizes (Figure 3.5). A gel-like material, rather than well-developed spherical particles, was produced in the less polar tetrahydrofuran (THF, polarity index= 4.0) compared to ethanol (polarity index= 5.2). Because of the relatively weak interaction of THF with water, there may be too much water inhibiting the effective condensation of the titania precursor.

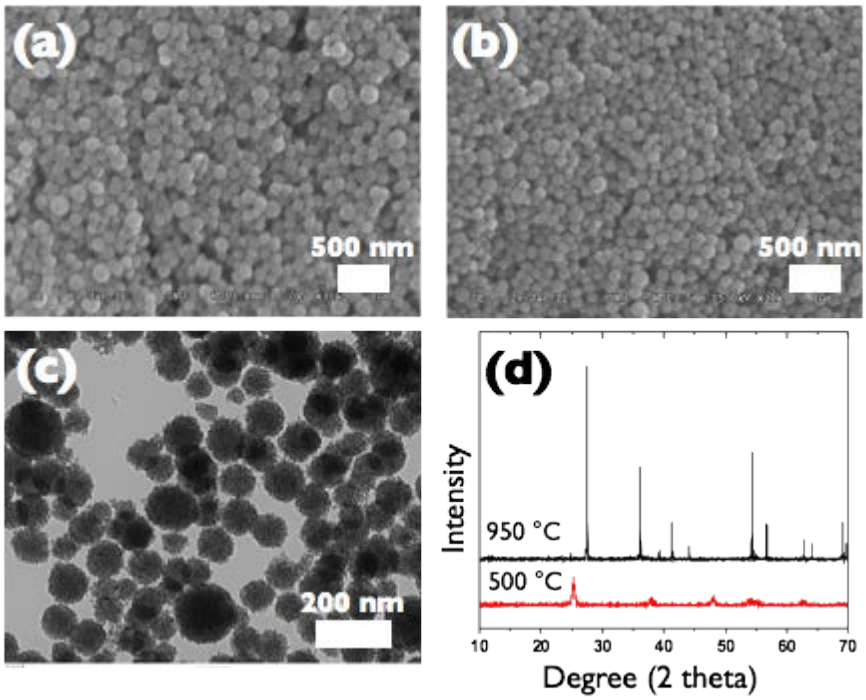

Figure 3.6. FE-SEM images of TNPs (a) as-prepared and (b) after annealed at 500 °C. (c) TEM image of annealed TNPs at 500 °C and (d) XRD patterns of annealed TNPs.

`

However, when 1,4-dioxane (polarity index= 4.8) was used as the solvent, spherical particles of approximately 250 nm in size were obtained. Furthermore, polar solvents with similar polarities (methanol and acetone, 5.1; acetonitrile, 5.8) produced nearly the same size TNPs, even though their shape seemed to be dependent on other factors. The smallest TNPs (approximately 50 nm in size) were obtained from dimethyl sulfoxide (DMSO, polarity index = 7.2), which has the highest polarity among the solvents tested. Based on these results, although more detailed investigations are needed to fully understand the polarity effect, the reactivity of titanium alkoxide in the presence of KCl may also be controlled by the polarity of the solvent.

For further characterization of the TNPs prepared at room temperature, approximately 100 nm size TNPs were annealed and monitored by FE-SEM and X-ray diffraction (XRD) patterns (Figure 4). The spherical shape of the TNPs remained after calcination at 500 °C with little shrinkage observed. According to XRD, the peaks of the TNPs annealed at 500 °C and 950 °C could be assigned to anatase (JCPDS File No. 21-1272) and rutile (JCPDS File No. 21-1276) crystalline phases, respectively, indicating that the titania was well prepared. Using 100 nm anatase TNPs, the photo-catalytic properties were investigated by the degradation of an organic dye, methylene blue, under UV irradiation (Figure 3.7a). The photo-catalytic properties of the anatase TNPs synthesized by our method were very similar to those obtained from the commercially optimized photo-catalyst P25.

Surface modification of the prepared TNPs was performed to increase their adaptability for various applications. 3-(trimethoxysilylpropyl)diethylenetriamine (DETAS) was coupled onto the surface –OH groups of the TNPs via hydrolysis and condensation with the methoxy groups of DETAS, which was confirmed by measuring the change in

`

zeta potential (from – 15.7 mV of Ti-O^- to + 32.9 mV of $–NH_3^+$). The weight loss difference from the non-modified TNPs was measured by thermo-gravimetric analysis (TGA) (1 wt% difference, Figure 3.7b). When carboxylic acid groups were introduced by treating with 3-mercaptopropionic acid (MPA), a weight loss of 4 wt% was measured, clearly indicating the possibility of surface modification of the prepared TNPs.

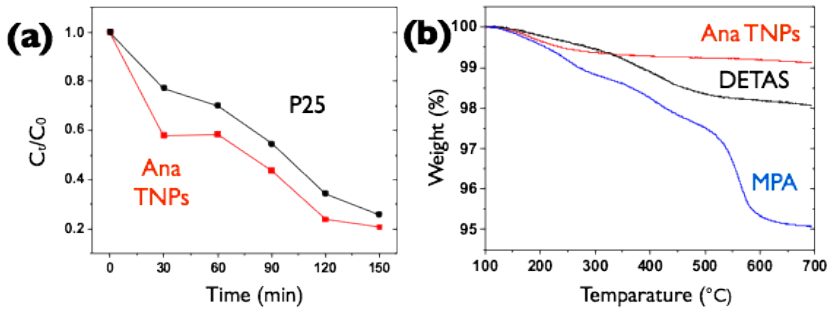

Figure 3.7. (a) Photo-catalytic degradation of methylene blue with anatase TNPs and P25. (b) Weight loss monitoring of TNPs and surface modified TNPs using TGA.

`

3.4 Conclusions

In this chapter, the factors controlling the size of TNPs in the presence of KCl were systemically investigated. The amount of titanium precursor, the concentration of KCl, the reaction temperature, and the polarity of the solvent were all shown to affect the kinetics of the hydrolysis/condensation and to dictate the resulting particle size. It was also shown that the prepared TNPs at room temperature could be effectively phase-transformed to anatase nanocrystals, which exhibited very effective photo-catalytic activity comparable to that of commercialized TiO_2 photo-catalysts. This simple preparation method, which allows for size control of our particles, along with easy surface modification could expand the usage of TNPs to various applications.

3.5 Experimental Section

Materials and Instruments Titanium ethoxide, methylene blue, 3-mercaptopropionic acid (MPA), and commercial titania P25 were purchased from Aldrich. KCl was purchased from Samchun (Korea), and 3-(trimethoxysilylpropyl)diethylene-triamine (DETAS) was purchased from Gelest. All solvents were purchased from Samchun (Korea) and used without any further purification.

FE-SEM and TEM images were acquired on Hitachi S-4300 and Hitachi-7600 instrument, respectively. XRD patterns were monitored by powder X-ray diffraction (D8 Advance, Bruker). The TGA was performed using an SDT Q600 (TA Instruments Inc.). The TGA samples were preheated at 100 °C for 30 min, after which the temperature was raised to 800 °C at a rate of 10

`

°C/min in a N_2 atmosphere. UV irradiation was provided by a UV lamp at 254 nm and 15 W.

Synthesis of TNPs To prepare the TNPs approximately 100 nm in size, titanium ethoxide (0.85 mL) was diluted in 25 mL of 1-propanol with 0.64 M KCl (0.2 mL). This mixed solution (12 mL) was injected into the ethanol solvent (50 mL) at room temperature, and a white collide was generated. After 2 h, the white product was washed by centrifugation (three times at 17000 rpm for 10 min in ethanol) and re-dispersed in ethanol. TNPs of other sizes could be prepared as presented above with various concentrations of KCl. TNPs were also prepared by this method in various solvents by changing the reaction solvent from ethanol to another solvent.

Degradation of methylene blue A total of 20 mg of photo-catalyst was dispersed in 20 mL of water containing 20 ppm methylene blue. The mixed solution was stabilized in a dark room for 30 min and irradiated using UV light. The remaining methylene blue solution was extracted by removing the photo-catalyst by centrifugation. The absorbance at 666 nm was used to determine the amount of methylene blue in the solution.

Surface modification of TNP A total of 100 mg of TNPs was dispersed in 20 mL of ethanol containing 0.05 mL of DETAS. After 6 hr under room temperature, modified TNPs were obtained after washing via centrifugation. Surface modification using MPA was performed by a method similar to that used for DETAS, except reflux conditions were utilized rather than room temperature.

`

*** Contributions**

Synthesis of TNPs in the various solvents was done with Yun Ji Park in Department of Chemistry, Seoul National University (current in Department of Chemistry, University of Illinois at Urbana-Champaign).

3.6 References

[1] Xia, Y. N.; Gates, B.; Yin, Y. D.; Lu, Y., *Adv. Mater.* **2000**, *12*, 693-713.

[2] Moon, J. H.; Cho, Y.-S.; Yang, S.-M., *Bull. Korean Chem. Soc* **2009**, *30*, 2245-2248.

[3] Shim, H.; Lim, J.; Shin, C. G.; Jeon, S.-J.; Han, M. G.; Lee, J.-K., *Appl. Phys. Lett.* **2012**, *100*, 063113.

[4] Chen, X.; Mao, S. S., *Chem. Rev.* **2007**, *107*, 2891-2959.

[5] Chen, D.; Caruso, R. A., *Adv. Funct. Mater.* **2013**, *23*, 1356-1374.

[6] Bai, J.; Zhou, B., *Chem. Rev.* **2014**, *114*, 10131-10176.

[7] Hagfeldt, A.; Boschloo, G.; Sun, L.; Kloo, L.; Pettersson, H., *Chem. Rev.* **2010**, *110*, 6595-6663.

[8] Bai, Y.; Mora-Sero, I.; De Angelis, F.; Bisquert, J.; Wang, P., *Chem. Rev.* **2014**, *114*, 10095-10130.

[9] Jiang, C. H.; Zhang, J. S., *J. Mater. Sci. Technol.* **2013**, *29*, 97-122.

[10] Chen, H.; Nanayakkara, C. E.; Grassian, V. H., *Chem. Rev.* **2012**, *112*, 5919-5948.

[11] Schneider, J.; Matsuoka, M.; Takeuchi, M.; Zhang, J.; Horiuchi, Y.; Anpo, M.; Bahnemann, D. W., *Chem. Rev.* **2014**, *114*, 9919-9986.

[12] Tan, H.; Zhao, Z.; Niu, M.; Mao, C.; Cao, D.; Cheng, D.; Feng, P.; Sun, Z., *Nanoscale* **2014**, *6*, 10216-10223.

[13] Shahid, M.; Choi, S.-Y.; Liu, J.; Kwon, Y.-U., *Bull. Korean Chem. Soc* **2013**, *34*, 2271-2275.

`

[14] Xu, N.; Shi, Z.; Fan, Y.; Dong, J.; Shi, J.; Hu, M. Z. C., *Ind. Eng. Chem. Res.* **1999**, *38*, 373-379.

[15] Schubert, U., *J. Mater. Chem.* **2005**, *15*, 3701-3715.

[16] Jiang, X. C.; Herricks, T.; Xia, Y. N., *Adv. Mater.* **2003**, *15*, 1205-1209.

[17] Look, J. L.; Zukoski, C. F., *J. Am. Ceram. Soc.* **1992**, *75*, 1587-1595.

[18] Eiden-Assmann, S.; Widoniak, J.; Maret, G., *Chem. Mater.* **2003**, *16*, 6-11.

[19] Han, C.; Luque, R.; Dionysiou, D. D., *Chem. Commun.* **2012**, *48*, 1860-1862.

[20] Sugimoto, T.; Kojima, T., *J. Phys. Chem. C* **2008**, *112*, 18760-18771.

[21] Bogush, G. H.; Zukoski Iv, C. F., *J. Colloid Interface Sci.* **1991**, *142*, 19-34.

[22] Lamer, V. K.; Dinegar, R. H., *J. Am. Chem. Soc.* **1950**, *72*, 4847-4854.

[23] Hong, M. P.; Kim, J. Y.; Vemula, K.; Kim, H. S.; Yoon, K. B., *Chem. Commun.* **2012**, *48*, 4250-4252.

`

Chapter 4.

Preparation of Titania Nanoparticles with Various Sizes and Their Size-dependent Electrochemical Properties

4.1 Abstract

The particle size (composed of small crystallites) effect of titania nanoparticles (TNPs) on Li ion storage is very basic and important subject, which is related to the surface area, porosity, diffusion length, etc. However, size control of TNPs under 200 nm has been limited by using simple sol-gel method due to the high reactive precursor; titanium alkoxide. TNPs with various sizes even under the 100 nm are obtained controlling the concentration of reactants in mixed solvent of ethanol and acetonitrile.

Among them, three different sizes of TNPs are prepared to compare the Li storage and 60 nm TNPs have the best reversible capacity of 182 mAh/g during 50 cycles at 1 C and a remarkable rate performance of 130 mAh/g at 10 C, which is attributed to its high surface area, well-developed porosity, and enhanced Li ion diffusivity. Interestingly, increasing capacity upon cycling is observed and the reason of this phenomenon is proposed to the enhanced contact between TNPs and liquid electrolyte from lattice volume expansion of TNPs during insertion/extraction of Li ion. Furthermore, the capacity of TNPs at high current density is more closely related to the surface area from Hg porosimetry than from general N_2 adsorption/desorption method.

`

4.2 Introduction

TNPs have been one of the most useful materials in various fields especially in energy applications like photo-catalysts, solar cells, and Li ion batteries (LIBs).[1-4] Among these, TNPs as the anode material for LIBs have very attractive characteristics of good cycling life, rapid discharge/charge rate, safety, etc.[5-10] The insertion/extraction of Li ion into/from the titania could be expressed as the reversible intercalation reactions according to the following reaction:

$$TiO_2 + xLi^+ + xe^- \leftrightarrow Li_xTiO_2$$

TNPs with relative high operation voltage are free from the formation and decomposition of solid-electrolyte interface (SEI) layer over that of most anode materials such as graphite, Si, and Sn (below 0.5 V),[5, 8] which makes batteries unstable and unsafe. Good stability or long lasting cycling property of titania are thanks to the small volume changes (less than 4 %) during insertion/extraction of Li ion because stability problems are usually comes from large volume expansion and contraction of active materials like Si, Sn, etc.[8] These properties are gaining more and more importance in the present needs of emerging automobile such as hybrid or full electric vehicles (EVs) because of more advantages over the conventional anode materials for accomplishing higher stability and safety.[5-10]

In case of the nanoparticles used as anode for LIBs, the size of nanoparticles is a very important consideration factor for expectation of battery property due to the different surface area, contact condition with electrolyte, ion diffusion length, etc. Although there were some reports about the crystal size effect of TNPs for LIBs anode,[9] the polycrystalline particle size effect (not the

`

crystal grain size but entire particle size composed of small crystal grains) was not systemically studied yet. The size effect of crystal grain to Li ion insertion was studied and crystal grains as small as 7 nm could fully uptake Li ion.[11]

However the titania crystal grains used in this study were commercial products, different synthetic methods were used to obtain them, and the electrochemical battery cell test was not performed. Increasing Li ion capacity with decreasing crystal grain size from 30 nm to 6 nm was reported with battery cell test but used TNPs were still from different commercial products.[12] Kim group also researched the crystal grain size effect of TNPs from the same synthetic procedure using different annealing temperature to control the crystal grain size.[13, 14] However, annealing at different temperature could not only vary the size of TNPs but also change crystal structure, which determined electrochemical properties of particles such as electric conductivity[15, 16] and Li ion insertion mechanism.[10, 17]

However, researches on the size effect of TNPs were limited on the crystal grain size. Moreover, other factors like crystalline structure and electric properties resulted from different synthetic route were not controlled. Therefore, more methodical investigation for Li ion insertion of TNPs is still important subject under synthetically controlled condition.

One reason of still-limited research on the TNPs size effect on LIBs could be addressed to the difficult preparation of various sized TNPs by the same method. In terms of nanoparticle synthesis, size control of TNPs is very challenging for their high reactive precursor; titanium alkoxide generally. In the sol-gel process, size tunable synthesis of spherical silica nanoparticles is very easy though mild hydrolysis-condensation of silicon alkoxide.[18] But titanium alkoxide has much high reactivity toward water[19] than silicon alkoxide, so not only size control but also preparation nanoparticles with

`

narrow size distribution is difficult. Reactivity of titanium alkoxide has been reduced by several methods. First, bidentate ligands such as ethylene glycol could stabilize the reactivity of titanium precursor to water by chelation.[19, 20] But the size control could be only possible upper 200 nm and the amount of titanium source in reaction condition was too small to get enough amounts of product for various applications.[21] Ionic salts or polymers[22] also could reduce the reactivity of titanium alkoxide *via* ionic interaction of salts with water or surfactant effect of polymers but size control under 200 nm was also restricted. In the last, the reactivity of titanium alkoxide could be reduced by low solubility of hydrolyzed intermediates of titania precursor to reaction solvent. Sugimoto *et al*. deeply studied synthesis and mechanism of titania in mixture of alcohol and acetonitrile and showed the possibility of changing particle size in their series reports.[23-25] By using the similar method, various sized TNPs were obtained by changing reactants or solvent but the size range of TNPs was still limited (>143 nm).[26] So the size control of TNPs smaller than 200 nm, especially smaller than 100 nm, is still the challenging subject.

In this chapter, TNPs with various sizes from about 60 nm to 300 nm were prepared by using mixed solvent of alcohol and acetonitrile. Electrochemical properties were investigated with anatase TNPs assembled by aggregation of crystallites about 11.8 nm, 12.1 nm, and 12.6 nm, respectively. Anatase TNPs having the size of 60 nm showed Li ion capacity over ideal capacity at 1 C and high rate performance without any additional process or materials.

Capacity activation derived from lattice expansion was reported even though fairly reversible intercalation reaction. Furthermore, Li ion storage at high rate was more related to surface area detected by Hg porosimetry analysis than commonly used N_2 adsorption/desorption analysis, which provided more understanding of the actual contact area between solid active materials and

`

liquid electrolyte especially at high current density.

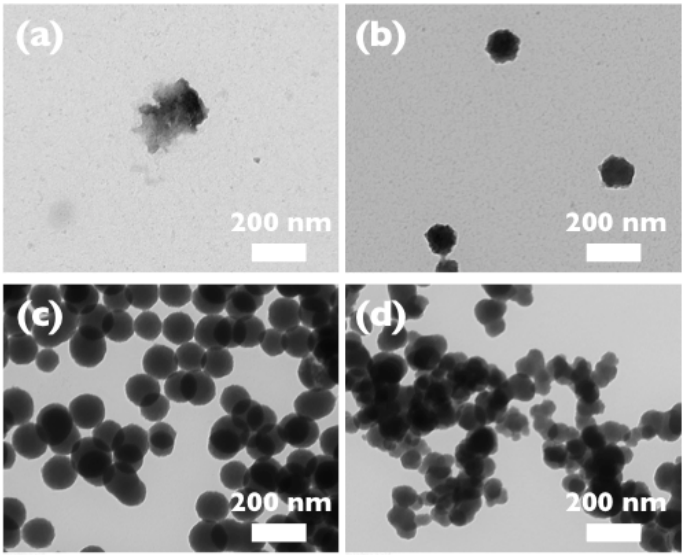

Figure 4.1. TEM images of TNPs using various ratio of ethanol and acetonitrile (v/v). (a) 9:1, (b) 3:1, (c) 1:3, and (d) 1:9. Other reaction condition was the same as follows; 2 mL of diluted $Ti(OBu)_4$ solution, 0.05 mL of ammonia solution.

4.3 Results and Discussion

Synthesis of TNPs TNPs were prepared *via* hydrolysis and condensation of titanium butoxide in mixture solvent composed of ethanol and acetonitrile in presence of ammonia solution. During the initial reaction step, hydrolyzed titanium source is precipitated due to the reduced solubility toward acetonitrile and condensed fabricating spherical nanoparticles.[23-25]

First, the effect of mixed solution was confirmed by varing the volume ratio of ethanol and acetonitrile in Figure 4.1 and an appropriate mixing ratio is needed to make spherical particles because different solubility of hydrolyzed titanium precursor with changing mixing ratio of solvent. Irregular particles

`

or no particles were formed from incomplete precipitation-condensation in excess ethanol and large aggregation was major particle morphology in excess acetonitrile. About 1:1 volume ratio of ethanol and acetonitrile seemed appropriate to prepare non-aggregated spherical TNPs with relatively narrow size distribution and the following synthesis of TNPs was proceeded using this condition.

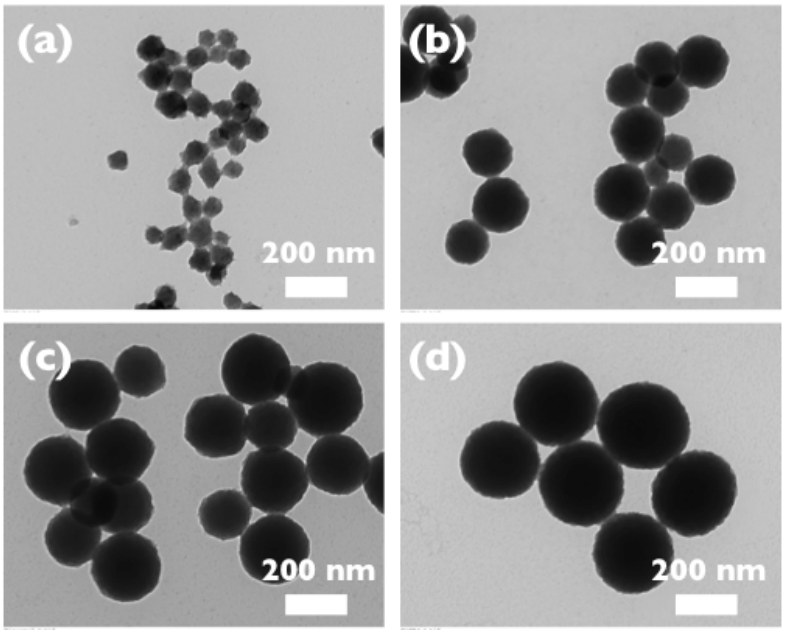

Figure 4.2. TEM images of TNPs using various amount of diluted $Ti(OBu)_4$ solution such as (a) 0.025 mL, (b) 0.05 mL, (c) 0.1 mL, and (d) 0.2 mL. Other reaction condition was the same as follows; 2 mL of diluted $Ti(OBu)_4$ solution, 0.05 mL of ammonia solution in 1:1 (v/v) mixture of ethanol : acetonitrile solution (10 mL).

`

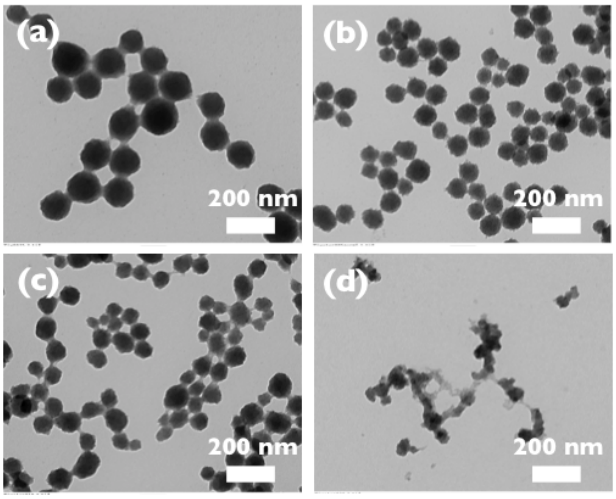

Figure 4.3. TEM images of TNPs using various amount of water such as (a) 0.025 mL, (b) 0.05 mL, (c) 0.1 mL and (d) 0.2 mL. Other reaction condition was the same as follows; 2 mL of diluted $Ti(OBu)_4$ solution, 0.05 mL of ammonia solution in 1:1 (v/v) mixture of ethanol : acetonitrile solution (10 mL).

Size control of TNPs from 60 nm to 300 nm was possible by varying the concentration of reactants. Main factors changing the size of TNPs are concentration of titanium source, water, ammonia solution and each reaction conditions were investigated as follows. First, increasing particle size with the more amount of titania precursor is general result and TNPs from 60 nm to 300 nm could be fabricated (Figure 4.2).

The smaller TNPs were synthesized with the higher amount of water to be as small as 60 nm (Figure 4.3). It is because when the water concentration in reaction is increased, solubility of hydrolysis product from titanium butoxide to acetonitrile is much lowered and it produces the smaller TNPs.[25]

`

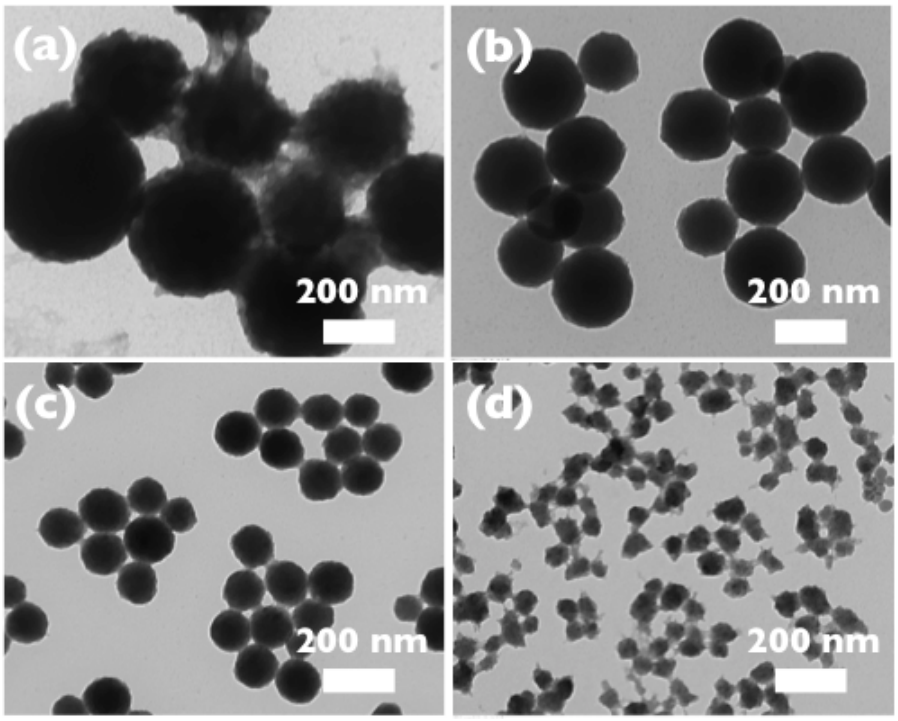

Figure 4.4. TEM images of TNPs using various amount of ammonia solution such as (a) 0.025 mL, (b) 0.05 mL, (c) 0.1 mL, and (d) 0.2 mL. Other reaction condition was same as follows; 2 mL of diluted $Ti(OBu)_4$ solution, in 1:1 (v/v) mixture of ethanol : acetonitrile solution (10 mL).

However in case of using too much water, insufficient condensation of titanium source could fabricate not fully spherical particles but attached particles each other or some irregular aggregates like an aerogel structure. Figure 4.4 shows the effect of ammonia solution, which has the same size change tendency with water from similar mechanism.

In order to investigate the electrochemical property of TNPs under 100 nm first, about 60 nm of TNPs were prepared and annealed under 500 °C (60A).

`

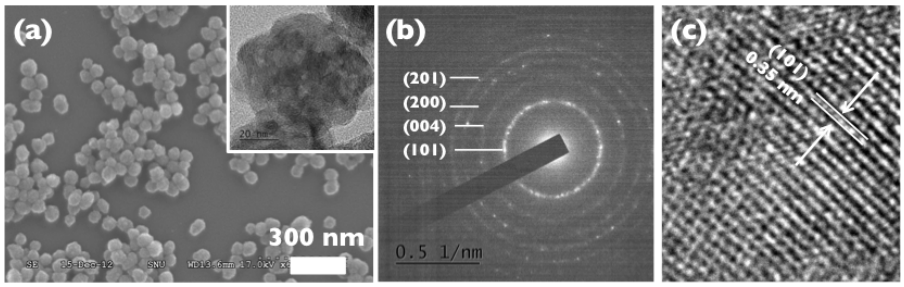

Figure 4.5. (a) SEM image with the inset of HR-TEM image, (b) electron diffraction patterns, and (c) lattice fringe in HR-TEM of 60A.

In Figure 4.5, SEM image and HR-TEM image of inset shows about 60 nm of crystalline titania was prepared and retain their own spherical structure. The diffraction patterns and lattice fringe of (101) (0.35 nm) indicate anatase crystal structure was formed in 60A. Anatase is well-known for the most suitable Li ion insertion/extraction host in point of its higher Li ion storage capability than rutile phase and better structural stability than brookite phase.[7, 27, 28]

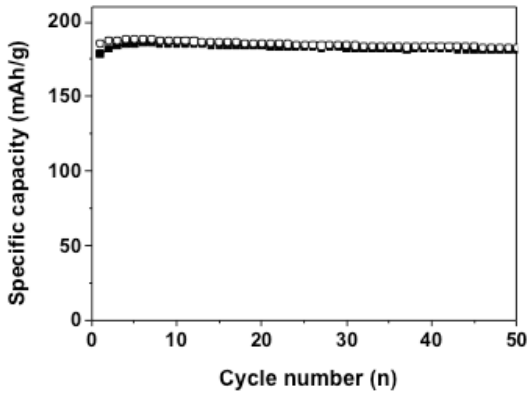

Figure 4.6. Cyclic performance of 60A at a current density of 168 mA/g (1 C) for 50 cycles.

`

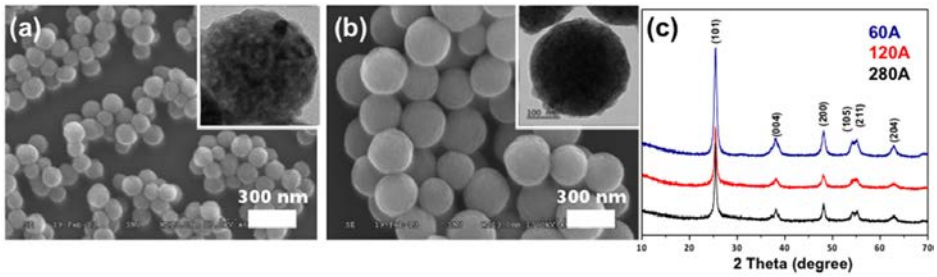

Figure 4.7. SEM images with the inset of HR-TEM images of (a) 120A and (b) 280A. (c) XRD patterns of TNPs.

The electrochemical property of 60A anode was simply tested by making Li-ion battery coin-cell (Figure 4.6). Under the current density of 168 mA/g, Li capacity over 180 mAh/g was obtained with high stability. To study the size effect on the electrochemical properties, two bigger TNPs of 120 nm and 280 nm were annealed under 500 °C (120A and 280A).

SEM images of Figure 4.7a and 4.7b with the inset of HR-TEM images show the spherical crystalline structure of 120A and 280A. XRD patterns of three annealed TNPs also could be indexed to pure anatase phase (Figure 4.7.c).

Moreover, from the (200) peak, crystal domain size of each anatase TNPs was calculated as 11.8 nm, 12.1 nm and 12.6 nm by Scherrer equation, where the particle size from 60 nm, 120 nm and 280 nm, respectively.

Surface area and porosity of TNPs The surface area and pore distribution of the size-controlled anatase TNPs were investigated by using both nitrogen adsorption/desorption isotherms and mercury intrusion porosimetry. By using nitrogen based BET first, surface area of 60A was confirmed as 73.1 m^2/g, which is higher than 45.8 m^2/g from 120A and 40.9 m^2/g from 280A. All TNPs showed the isotherms of type IV patterns with distinct H_1 and H_2

`

hysteretic loops around 0.9 P/P_0 and 0.5 P/P_0, respectively (Figure 4.8a).[27]

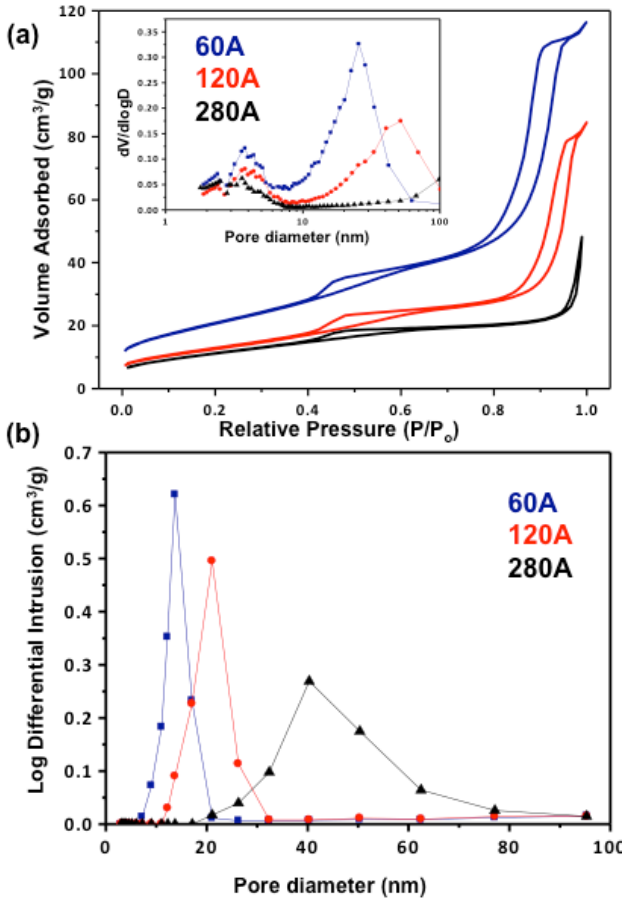

Figure 4.8. (a) Nitrogen adsorption/desorption isotherms of anatase TNPs with the inset of BJH pore size distribution and (b) pore size distribution from mercury porosimetry.

The presence of H_1 loop character is very interesting because it is expected to come from almost uniform TNPs spheres in fairly regular array and H_2 indicate the pores of typical ink-bottle type of mesopores inside TNPs. It could be related to the pore size distribution from BJH method (the inset of Figure 4.8a); all TNPs have pores as small as 4 nm and the smaller TNPs have more quantity of the small sized pore. 60A and 120A have another large pore

`

with 26 nm and 52 nm, respectively which is believed that it is originated from densely packed gap between each entire particles; ideally, hexagonal close packed identical 60 nm spheres have cavity radius about 27 nm and 120 nm sphere have 54 nm,[28] which means that the size of inter-particle pores in this chapter is very close to the calculated value. 280A did not show any another large pore under 100 nm but the bigger pore over 100 nm (about 116 nm) is expected due to the similar reason with other two TNPs. Because bimodal pores are well known to have advantages to the adsorption of reactant molecules from fast diffusion with this porous structure,[29] 60A which has the widest surface area and well developed bimodal pore are expected to have good contact with LIBs electrolyte.

Very similar characterizations were also done by using mercury (Hg) porosimetry. Although N_2 based detection of surface area and porosity is generally used and accepted methodology, materials characters from this method could not explain liquid based contact between solid anode and liquid electrolyte in LIBs exactly. For example, gas can penetrate closed pore or small pore which liquid electrolyte has difficulty to enter. Even though Hg based method has disadvantages such as less sensitivity of nanometer region from limited range of detection (from about 3~4 nm to 400~500 μm),[30, 31] Hg liquid based monitoring could explain the contact between solid and liquid to support N_2 gas based method. Hg intrusion has been used to investigate the porous character of materials[31] and changed porosity of Si anode before and after lithiation LIBs[32] but Li ion capacity of materials was rarely explained with this methodology. Surface area of TNPs was calculated with Hg method to have lower numerical value than N_2 based Brunauer, Emmett and Teller (BET) method; 32.4 m^2/g and 17.4 m^2/g for 60A and 120A, respectively. Especially, surface area of 280A was very low as 6.3 m^2/g and these lower

`

surface area than N_2 based BET indicates that Hg liquid could not intrude into small pores with the range of small mesopore to micropore or closed pore that only gas could penetrate. Furthermore, large pore from well-packed TNPs aggregate was also obtained with the smaller size to have 14 nm of 60A and 21 nm of 120A than N_2 based method demonstrating hard intrusion of Hg liquid than N_2 gas (Figure 4.8b). The large pore of 280A was also detected as 40 nm that was not detected from N_2 based Barrett–Joyner–Halenda (BJH) method. But small pores about 4 nm by N_2 based BJH was not detected, which might be due to the less sensitivity on several nanometer region from limited detection range of Hg porosimeter itself (could not detect small pores under 3~4 nm) or non-wetting character of Hg droplet.[30]

Electrochemical properties of TNPs Li ion capacity of the size-controlled TNPs at a current density of 1 C (1 C = 168 mA/g) was evaluated in Figure 4.9a. 60A shows the best capacity and superior cycling stability with almost no fading up to 50 cycles. Moreover, the first discharge and charge capacity of 60A deliver 186 mAh/g and 179 mAh/g, which corresponding to only a 3.7% irreversible capacity loss (ICL). It is known that the ICL is possibly caused by side reactions as the electrolyte decomposition or by irreversible trapping of Li ion over the defects of anatase polymorph.[33] Without any additional materials enhancing conductivity or stability, the discharge capacity of 60A is comparable to recent researches which had applied pure titania to anode material.[14, 33, 34] Figure 4.9b shows the discharge/charge capacities of TNPs with the increasing C-rate from 0.5 C to 30 C.

`

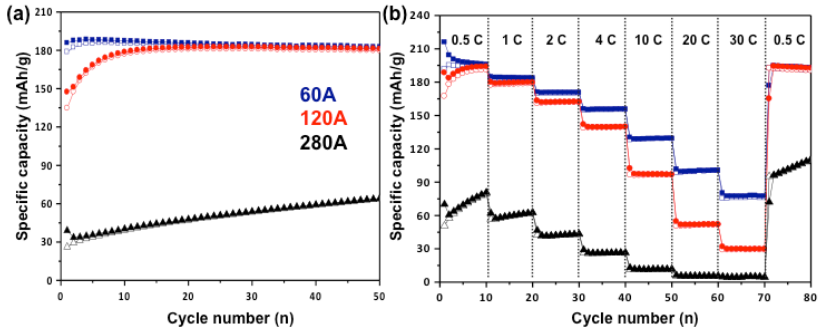

Figure 4.9. (a) Cycle performance of the size-controlled TNPs at a current density of 168 mA/g at 1 C for 80 cycles and (b) rate performance of the size-controlled TNPs at different current densities.

Clearly, 60A indicates the best rate performance not only with regard to capacity retention up to 80 cycles but also with regard to recovered capacity at 0.5 C after increase to 30 C: The discharge capacity of 60A is 196 mAh/g and 193 mAh/g at 10th and 80th, which presents an almost 100% recovered capacity from even though at 30 C.

Furthermore, the discharge capacity of 60A at 10 C is 120 mAh/g, which is comparable to recent researches used defects or carbons[35, 36] or even better.[37, 38] It is well known that crystal grain size strikingly impacts on the Li ion insertion behavior and storage capability.[11, 13, 14, 39] From the electrochemical performance in Figure 4.9, the entire particle size composed of small crystal as well as small crystal grain size affects the Li ion storage capability; smaller grain of 60A and 120A showed higher capacity than larger grain 280A and despite of similar grain size, larger entire particle size of 120A could not showed their highest capacity until 30th cycle.

`

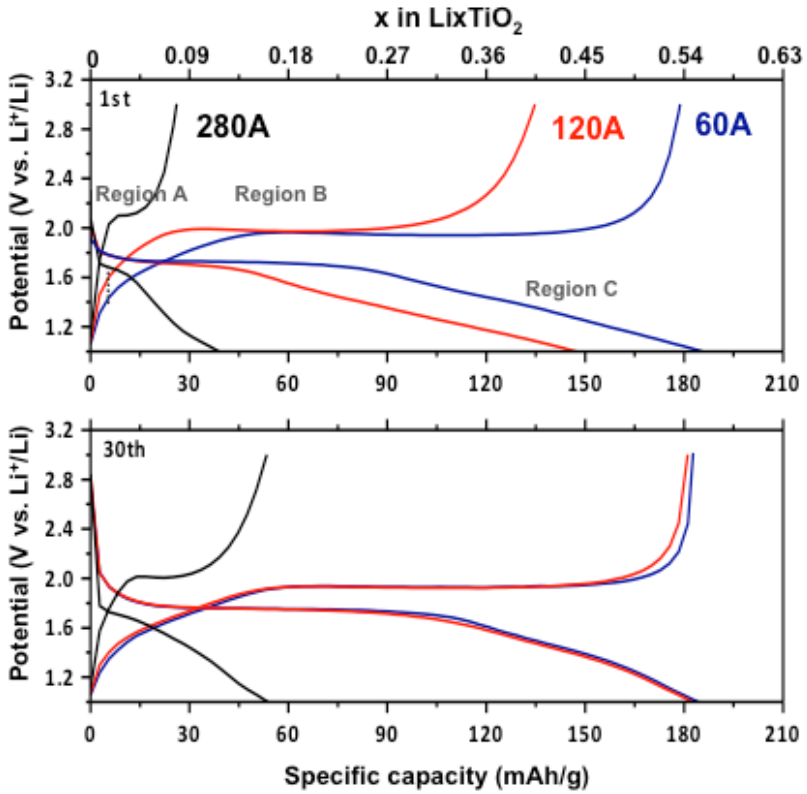

Figure 4.10. Voltage profiles of TNPs at 1st and 30th cycle.

Interestingly, the increase of capacity was observed for all the TNPs in Figure 4.9. This increasing capacity character of TNPs was further evaluated because it was rarely reported and not well understood yet. To find the origin of enhanced capacity, first and 30th discharge/charge profiles of each TNP were investigated in Figure 4.10. It has been accepted that the insertion of Li ion into anatase titania is divided into three different regions;[7, 40] solid-solution, intercalation, and surface adsorption (Region A, Region B, and Region C in Figure 4.10a, respectively). The first region of the discharge curve

`

characterized by a potential drop (> 1.78 V) is attributed to the formation of the conductive Li_xTiO_2 in solid-solution domain. The second region exhibits a plateau at 1.78 V, which is ascribed to a well-known two phase electrochemical reactions.

The third region (< 1.5 V) shows a sloped curve associated with further Li ion insertion into $Li_{0.5}TiO_2$. A significant difference in the voltage profiles between 1st and 30th cycles shown in Figure 4.10 is that plateau potential gap between discharge and charge decreases considerably at 30th cycle for all the TNPs. Furthermore, the discharge capacity of 120A and 280A is increased from 147.3 mAh/g and 38.9 mAh/g to 182.5 mAh/g and 53.8 mAh/g, respectively at 30th cycle. From the comparison between 1st and 30th voltage profile, the degree of polarization of the electrode upon cycling decreases for all the TNPs, which indicates that Li ion insertion/extraction is easier upon cycling.[41]

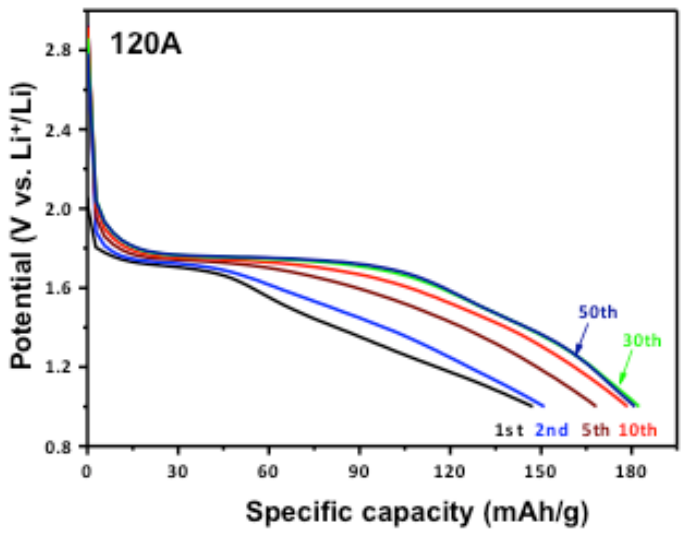

Figure 4.11. Li-ion insertion curves of 120A from 1st to 50th discharge at 1 C.

`

Among the all TNPs, the capacity of 120A showed the most dramatic increase and Li ion insertion was further investigated from 1st to 50th insertion curve as shown in Figure 4.11. The Region B is developed upon cycling, which implies facilitated Li ion intercalation reaction through the repeated discharge/charge process. Increasing capacity upon cycling is not just strange phenomenon but rarely reported. Although the mechanism of increasing capacity is also not well known but there are some proposals. The first is reversible growth of a polymer/gel-like thin film layer resulted from decomposition of electrolyte on the surface of anode materials. However, this layer is usually formed at low voltage around 0.8 V and titania is well known as hardly forming of the decomposed thin layer due to a relatively high operating voltage of 1.5-1.8 V.[5, 42-44]

The second proposal is the recovered capacity from irreversibly reacted and unused portion of anodes at initial cycles. Yu *et al.*[45] and Lian *et al.*[46] insisted that the initial irreversible capacity *via* conversion reaction was becoming partially reversible with repeated cycling. It could explain active materials that react with Li ion by conversion reaction such as SnO_2 and other metal oxide systems,[45, 46] hence this proposal also could not be the answer of increasing capacity of titania which takes Li ion by intercalation mechanism. Until now, the increasing capacity of titania upon cycling was rarely reported and was just mentioned as fast activation of electrodes[14] or explained *via* enhancement of contact between electrode and electrolyte upon cycling.[34] Gaining the more contact opportunity of unexposed portion of TNPs over repeated cycling is an acceptable proposal. Titania is well known for very stable materials of LIBs anode mainly from little volume change during discharging/charging process, however, the lattice volume of titania could be expanded with small degree upon repeated intercalation reaction[39, 40, 47].

`

Moreover, Li ion diffusivity could be increased by one order of magnitude even with 1% lattice expansion.[48] From the reported researches and gradually increased intercalation reaction shown in Figure 6.11, the possibility that electrolyte could penetrate into TNPs to reach inner crystal grains owing to the enhanced Li ion diffusivity through the lattice expansion is proposed in here. Also, the faster increasing capacity of 120A than 280A might come from both higher surface area and more porous structure providing sufficient electrode/electrolyte contact and facile Li ion transport. The degree of increasing capacity of 60A is insignificant compared to both 120A and 280A. This result probably comes from the 1st discharge capacity of 186 mAh/g was already over ideal capacity of 168 mAh/g without strong Li-Li repulsions in the Li_xTiO_2 lattice[49, 50] *via* high surface area and the best-developed porous structure among the TNPs.

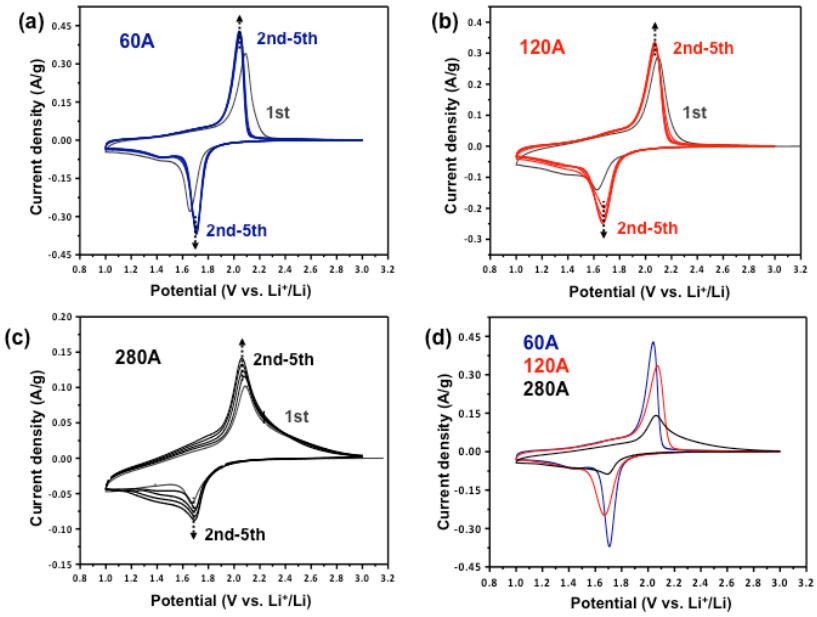

Figure 4.12. First and 2nd-5th cyclic voltammograms (CVs) of (a) 60A, (b) 120A, (c) 280A, and (d) comparison representation of the TNPs on 5th CV.

`

To further clarify the electrochemical process of the TNPs, cyclic voltammogram (CV) measurements were carried out. Figure 4.12a, b, and c depict the CVs of the TNPs for the first five cycles at a scan rate of 0.1 mV/s in the potential window of 1 to 3 V. The striking differences in the CVs at 5th cycle among the TNPs are clearly displayed in Figure 4.12d. For all the TNPs, the intensities of redox peak currents corresponding to Li ion insertion/extraction peak currents are slightly increasing upon cycling.

Moreover, the degree of polarization of each TNP decreases upon cycling as the same trend in the galvanostatic discharge/charge curves of Figure 4.11. In Figure 4.12d the CV of 60A clearly exhibits less gap between the redox peak positions, which means better kinetics than 120A. Also, the larger intensities of the redox peak currents imply development of high surface area present the higher capacity, which agrees well with the Li ion storage performance in Figure 4.9.[34, 41]

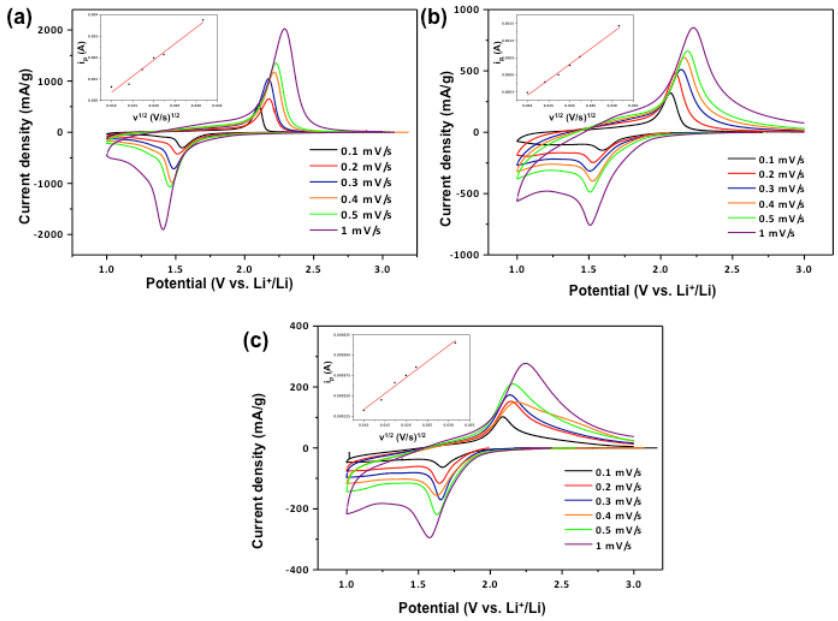

Figure 4.13. SSCVs of (a) 60A, (b) 120A, and (c) 280A with the inset of correlation line of i_p vs $v^{1/2}$.

`

To investigate Li ion diffusion both in active material and in electrolyte near the interface of electrolyte/electrode, scan rates for slow-scan cyclic voltammetry (SSCV) measurements with varying scanning rates of 0.1, 0.2, 0.3, 0.4, 0.5, and 1 mV/s were conducted as shown in Figure 4.13. By using Randles – Sevcik equation for the reversibly diffusion controlled system at room temperature, diffusion coefficient (*D*) could be obtained *via* the slope from voltammetric current densities *vs*. square root of scan rate. The equation is displayed as

$$i_p = (2.69 \times 10^5) n^{3/2} A D^{1/2} C v^{1/2}$$

,where i_p is the peak current; n is the number of electrons transferred in the electrode reaction; A is the surface area of the electrode (cm^2); D is diffusion coefficient of Li ion (cm^2/s); C is the concentration of Li ion (mol/cm^3); v is the CV scan rate (V/s). As discussed above, because the detected surface area of the TNPs has different value according to the physical phase of medium (e.g. gas and liquid) for analysis, plausible surface area of the TNPs is necessary to obtain the effective D_{Li+}. As shown in Table 4.1, the determined D_{Li+} of 60A from BET surface area based on N_2 adsorption/desorption isotherms is 8.12×10^{-20} cm^2/s in accordance with the recently reported value estimated by the SSCV method.[51, 52] Moreover, the determined D_{Li+} of 60A from Hg intrusion surface area is 5.04×10^{-19} cm^2/s which is about six times higher than that from BET surface area. It was also observed that the D_{Li+} by both the BET surface area and the Hg intrusion surface area were increased with decreasing the particle size of TNPs. Generally, the mobility of electron is faster than that of Li ion, hence Li ion diffusion has practical importance for

`

achieving high LIBs performance. Therefore, the results attribute the best electrochemical performance of 60A among TNPs to fast Li ion diffusion kinetics.

Table 4.1. Li ion diffusion coefficients by using surface area from N_2 and Hg methods.

TNPs	D_{Li+} (SSCV-BET)[a] [cm^2/s]	D_{Li+} (SSCV-Hg)[b] [cm^2/s]
60A	8.12×10^{-20}	5.04×10^{-19}
120A	1.60×10^{-20}	2.87×10^{-19}
280A	1.32×10^{-21}	2.75×10^{-19}

[a]SSA = specific surface area obtained from N_2 adsorption/desorption analysis
[b]SSA = specific surface area obtained from Hg intrusion porosimetry analysis

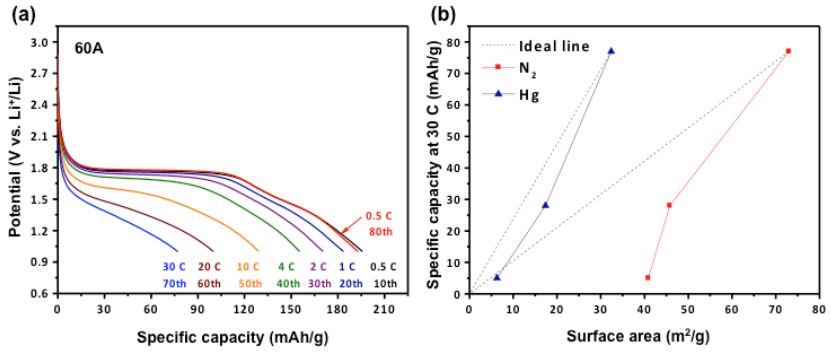

Figure 4.14. (a) The 1st insertion curves of 60A at the rates from 0.5 C to 30 C and (b) relation between discharge capacity at 30 C and surface area from N_2 method and Hg method compared with ideal line.

`

Surface area dependent high-rate performance of TNPs Figure 4.14a presents the last discharge curves of each cycle set in Figure 4.10b of 60A at various rates. It is well known that the extent of both Region A and C depends on the surface area of the material[5, 14, 34, 53] and the proportion of Region C in the overall discharge capacity significantly increased as the C-rate increased. This result implied that the reaction kinetics of surface adsorption (i.e. interfacial storage process) is much faster than those of intercalation reactions, and thus, high rates might provide more emphasis on the surface area dependent storage mechanisms.[43, 55] Based on discussions and references above, the capacity at high rate is related with the surface area of TNPs. From N_2 adsorption/desorption analysis, the highest surface area was obtained in 60A and comparatively similar surface area was developed in 120A and 280A. But the capacity gap between each TNP is similar showing stair-like differences and it is more related with the surface area characterized *via* Hg intrusion porosimetry. The relation between the discharge capacity at 30 C and the surface areas characterized by both N_2 adsorption/desorption analysis and Hg intrusion porosimetry analysis was depicted in Figure 4.14b. If TNPs with very small surface area could be assumed to have no Li ion storage at high current density of 30 C, the black dotted line might indicate the ideal linear-relation between Li ion capacity with surface area of TNPs for each analysis. The plot from Hg liquid analysis shows more similar relation with ideal line than from N_2 gas analysis, proposing that it is another helpful tool understanding the contact area between solid active materials and liquid electrolytes especially at high current density.

`

4.4 Conclusions

A simple sol-gel method under mixture solvent of ethanol and acetonitrile had been introduced to prepare size-controlled TNPs even with the size of particles under 100 nm, which was hardly reported by using similar methods. Changing the various reactants especially the amount of water, the size of TNPs could be controlled from about 60 nm to 300 nm. Three anatase TNPs with diameter of 60 nm, 120 nm, and 280 nm (notated as 60A, 120A, and 280A, respectively), assembled by aggregation of crystallites of 11.8 nm, 12.1 nm, and 12.6 nm, respectively, were synthesized and the development of uniform spherical particles and mesoporous arrangement with bimodal porosity were confirmed. The effect of polycrystalline particle size composed of small crystal grains on LIBs performance was comfirmed; Li ion storage capability and electrochemical kinetic of the electrode increased as the particle size decreased. The 60A electrode exhibited good Li ion storage performance showing a large reversible capacity of 182 mAh/g during 50 cycles at 1 C and a remarkable rate performance of 130 mAh/g at 10 C, which was attributed to its high surface area, well-developed porosity, and enhanced Li ion diffusivity. All the TNPs presented capacity activation and the proportion of intercalation reaction in the overall discharge capacity was increased upon cycling, therefore, we proposed the enhancement of contact between active materials and electrolyte resulted from the lattice expansion upon cycling. It was demonstrated that the surface area from Hg porosimetry analysis was more related to high rate capacity of TNPs than from N_2 adsorption/desorption analysis, suggesting that Hg porosimetry analysis could more accurately described the actual contact area between solid active materials and liquid electrolyte especially at high rate.

`

4.5 Experimental Section

Materials and Instruments Titanium tetrabutoxide, anhydrous ethanol and acetonitrile were purchased from Aldrich. Absolute ethanol and absolute acetonitrile were prepared from J.T. Baker and Aldrich, respectively. Ammonia solution (29 % in water) was purchased from Samchun and deionized (DI) water purified by Milli-Q purification system was used for all the experiments. All solvents and reagents used in this study were commercially available and used as received.

The size and morphology of products were analyzed by field-emission scanning electron microscopy (FE-SEM, Hitachi S-4300, 4.2 kV) and transmission electron microscopy (TEM, Hitachi-7600, 100 kV). More detailed image, lattice space and diffraction pattern were obtained using TEM with more accelerating voltage (JEM-2100F, JEOL, 200 kV). The crystallinity of the samples were evaluated by powder X-ray diffraction (XRD) analyses on Bruker New D8 Advance Diffractometer with Cu Ka radiation (λ = 1.5418 Å). The scanning rate was 0.02 ° per second and range was from 10 to 70 °. The surface area and porosity of the products was measured using the nitrogen adsorption–desorption isotherm and BJH methods on a Micromeritics ASAP 2420. Mercury porosimeter (Micromeritics, AutoPore IV 9500) was also use to investigate surface area and porosity based on liquid phase.

Synthesis of TNPs In general synthesis of 60A, 0.5 mL of titanium butoxide was dissolved to 1:1 (v/v) mixture of anhydrous ethanol and acetonitrile (20 mL) in glove box. In round-bottom flask (RBF), 1:1 (v/v) mixture of ethanol and acetonitrile mixture (100 mL) with 1 mL of ammonia

`

solution (29 % aqueous solution) and 0.5 mL of water was prepared. And then, prepared titanium butoxide solution was injected to RBF and the reaction was done under room temperature. Synthesis of 120A was the same condition of 60A synthesis except additional water. In case of 280A, synthetic condition is as follows; 0.5 mL of titanium butoxide was dissolved to 1:1 (v/v) mixture of anhydrous ethanol and acetonitrile (20 mL) in glove box. In round-bottom flask, 1:1 (v/v) mixture of ethanol and acetonitrile mixture (100 mL) with 1 mL of ammonia solution (29 % aqueous solution) was prepared. And then, prepared titanium butoxide solution was injected to RBF and the reaction was done under room temperature (RT). All TNPs - after 2 hr reaction, the whole milky solution of particles was purified and washed with ethanol using centrifugation/re-dispersion (17,000 rpm, 10 min, 3 times). The white product was well dried in room temperature for overnight, following annealed at 500 °C under air for 2 hr.

Electrochemical test Working electrodes were fabricated by mixing the size-controlled TNPs, Super P as a conductive agent, and PVDF as a binder in N-methyl-2-pyrrolidone (NMP) solvent at a weight ratio of 80:10:10. The mixed slurry was uniformly plastered on an aluminum foil current collector *via* doctor blade processing. The electrodes were dried under vacuum at 120 °C overnight and then pressed. A 2016 type coin cell consisted of a working electrode and lithium metal as a counter and reference electrode separated by a polypropylene separator (Celgard2400) was assembled in a glove box under a dry argon atmosphere. The organic electrolyte used was 1.0 M $LiPF_6$

`

dissolved in a mixture of ethylene carbonate (EC) and diethyl carbonate (DEC) with a volume ratio of 1 : 1. Galvanostatic testing (WBCS3000 cycler, WonA tech, Korea) was carried out on the coin cell in the voltage range of 3.0 to 1.0 V (vs. Li^+/Li) at room temperature. The cyclic voltammetry (CV) was conducted at a scan rate of 0.1 mV/s. Scan rates for slow-scan cyclic voltammetry (SSCV) were varied from 0.1 to 1 mV/s to determine effective diffusion coefficient of Li^+.

*** Contributions**

Electrochemical properties of TNPs were tested with Ji Hyun Um and Prof. Yung-Eun Sung in School of Chemical & Biological Engineering, Seoul National University.

`

4.6 References

[1] Chen, X.; Mao, S. S., *Chem. Rev.* **2007**, *107*, 2891-2959.

[2] Chen, D.; Caruso, R. A., *Adv. Funct. Mater.* **2013**, *23*, 1356-1374.

[3] Zhang, Q.; Uchaker, E.; Candelaria, S. L.; Cao, G., *Chem. Soc. Rev.* **2013**, *42*, 3127-3171.

[4] Li, W.; Wu, Z.; Wang, J.; Elzatahry, A. A.; Zhao, D., *Chem. Mater.* **2014**, *26*, 287-298.

[5] Chen, Z.; Belharouak, I.; Sun, Y. K.; Amine, K., *Adv. Funct. Mater.* **2013**, *23*, 959-969.

[6] Reddy, M. V.; Subba Rao, G. V.; Chowdari, B. V., *Chem. Rev.* **2013**, *113*, 5364-5457.

[7] Froschl, T.; Hormann, U.; Kubiak, P.; Kucerova, G.; Pfanzelt, M.; Weiss, C. K.; Behm, R. J.; Husing, N.; Kaiser, U.; Landfester, K.; Wohlfahrt-Mehrens, M., *Chem. Soc. Rev.* **2012**, *41*, 5313-5360.

[8] Su, X.; Wu, Q.; Zhan, X.; Wu, J.; Wei, S.; Guo, Z., *J. Mater. Sci.* **2012**, *47*, 2519-2534.

[9] Jiang, C. H.; Zhang, J. S., *J. Mater. Sci. Technol.* **2013**, *29*, 97-122.

[10] Yang, Z.; Choi, D.; Kerisit, S.; Rosso, K. M.; Wang, D.; Zhang, J.; Graff, G.; Liu, J., *J. Power Sources* **2009**, *192*, 588-598.

[11] Wagemaker, M.; Borghols, W. J. H.; Mulder, F. M., *J. Am. Chem. Soc.* **2007**, *129*, 4323-4327.

[12] Jiang, C.; Wei, M.; Qi, Z.; Kudo, T.; Honma, I.; Zhou, H., *J. Power Sources* **2007**, *166*, 239-243.

[13] Kang, J. W.; Kim, D. H.; Mathew, V.; Lim, J. S.; Gim, J. H.; Kim, J., *J. Electrochem. Soc.* **2011**, *158*, A59-A62.

[14] Rai, A. K.; Anh, L. T.; Gim, J.; Mathew, V.; Kang, J.; Paul, B. J.; Song, J.; Kim, J., *Electrochim. Acta* **2013**, *90*, 112-118.

`

[15] Tighineanu, A.; Ruff, T.; Albu, S.; Hahn, R.; Schmuki, P., *Chem. Phys. Lett.* **2010**, *494*, 260-263.

[16] Fang, H.-T.; Liu, M.; Wang, D.-W.; Sun, T.; Guan, D.-S.; Li, F.; Zhou, J.; Sham, T.-K.; Cheng, H.-M., *Nanotechnology* **2009**, *20*, 225701.

[17] Deng, D.; Kim, M. G.; Lee, J. Y.; Cho, J., *Energy Environ. Sci.* **2009**, *2*, 818-837.

[18] Cushing, B. L.; Kolesnichenko, V. L.; O'Connor, C. J., *Chem. Rev.* **2004**, *104*, 3893-3946.

[19] Schubert, U., *J. Mater. Chem.* **2005**, *15*, 3701-3715.

[20] Jiang, X. C.; Herricks, T.; Xia, Y. N., *Adv. Mater.* **2003**, *15*, 1205-1209.

[21] Wang, P.; Xie, T.-F.; Li, H.-Y.; Peng, L.; Zhang, Y.; Wu, T.-S.; Pang, S.; Zhao, Y.-F.; Wang, D.-J., *Chem. Eur. J.* **2009**, *15*, 4366-4372.

[22] Eiden-Assmann, S.; Widoniak, J.; Maret, G., *Chem. Mater.* **2003**, *16*, 6-11.

[23] Sugimoto, T.; Kojima, T., *J. Phys. Chem. C* **2008**, *112*, 18760-18771.

[24] Sugimoto, T.; Kojima, T., *J. Phys. Chem. C* **2008**, *112*, 18437-18444.

[25] Kojima, T.; Sugimoto, T., *J. Phys. Chem. C* **2008**, *112*, 18445-18454.

[26] Mine, E.; Hirose, M.; Nagao, D.; Kobayashi, Y.; Konno, M., *J. Colloid Interface Sci.* **2005**, *291*, 162-168.

[27] Armstrong, A. R.; Armstrong, G.; Canales, J.; Bruce, P. G., *Angew. Chem. Int. Ed.* **2004**, *43*, 2286-2288.

[28] Kavan, L.; Grätzel, M.; Gilbert, S. E.; Klemenz, C.; Scheel, H. J., *J. Am. Chem. Soc.* **1996**, *118*, 6716-6723.

[29] Sing, K. S. W., *Pure Appl. Chem.* **1985**, *57*, 603-619.

[30] Avery, R. G.; Ramsay, J. D. F., *J. Colloid Interface Sci.* **1973**, *42*, 597-606.

[31] Chen, Y.; Dionysiou, D. D., *Appl. Catal., B* **2008**, *80*, 147-155.

`

[32] Giesche, H., *Part. Part. Syst. Charact.* **2006**, *23*, 9-19.

[33] Tzschichholz, G.; Steinborn, G.; Hentschel, M. P.; Lange, A.; Klobes, P., *J. Porous Mater.* **2011**, *18*, 83-88.

[34] Jo, M. R.; Heo, Y.-U.; Lee, Y. C.; Kang, Y.-M., *Nanoscale* **2014**, *6*, 1005-1010.

[35] Ma, Y.; Ji, G.; Ding, B.; Lee, J. Y., *J. Mater. Chem.* **2012**, *22*, 24380-24385.

[36] Kubiak, P.; Fröschl, T.; Hüsing, N.; Hörmann, U.; Kaiser, U.; Schiller, R.; Weiss, C. K.; Landfester, K.; Wohlfahrt-Mehrens, M., *Small* **2011**, *7*, 1690-1696.

[37] Bi, Z. H.; Paranthaman, M. P.; Guo, B. K.; Unocic, R. R.; Meyer, H. M.; Bridges, C. A.; Sun, X. G.; Dai, S., *J. Mater. Chem. A* **2014**, *2*, 1818-1824.

[38] Zhen, M. M.; Su, L. W.; Yuan, Z. H.; Liu, L.; Zhou, Z., *RSC Adv.* **2013**, *3*, 13696-13701.

[39] Jiao, W.; Li, N.; Wang, L.; Wen, L.; Li, F.; Liu, G.; Cheng, H.-M., *Chem. Commun.* **2013**, *49*, 3461-3463.

[40] Zhang, C. L.; Zhang, Q. Y.; Kang, S. F.; Li, X., *J. Mater. Chem. A* **2014**, *2*, 2801-2806.

[41] Wagemaker, M.; Kearley, G. J.; van Well, A. A.; Mutka, H.; Mulder, F. M., *J. Am. Chem. Soc.* **2002**, *125*, 840-848.

[42] Wang, J.; Zhou, Y.; Hu, Y.; O'Hayre, R.; Shao, Z., *J. Phys. Chem. C* **2011**, *115*, 2529-2536.

[43] Lei, J. F.; Du, K.; Wei, R. H.; Ni, J.; Li, L. B.; Li, W. S., *RSC Adv.* **2013**, *3*, 13843-13850.

[44] Ban, C.; Wu, Z.; Gillaspie, D. T.; Chen, L.; Yan, Y.; Blackburn, J. L.; Dillon, A. C., *Adv. Mater.* **2010**, *22*, E145-E149.

`

[45] Lee, J. E.; Yu, S.-H.; Lee, D. J.; Lee, D.-C.; Han, S. I.; Sung, Y.-E.; Hyeon, T., *Energy Environ. Sci.* **2012**, *5*, 9528-9533.

[46] Taberna, P. L.; Mitra, S.; Poizot, P.; Simon, P.; Tarascon, J. M., *Nat. Mater.* **2006**, *5*, 567-573.

[47] Yu, Y.; Chen, C. H.; Shi, Y., *Adv. Mater.* **2007**, *19*, 993-997.

[48] Lian, P.; Zhu, X.; Liang, S.; Li, Z.; Yang, W.; Wang, H., *Electrochim. Acta* **2011**, *56*, 4532-4539.

[49] Zukalová, M.; Kalbáč, M.; Kavan, L.; Exnar, I.; Graetzel, M., *Chem. Mater.* **2005**, *17*, 1248-1255.

[50] Song, K.; Seo, D.-H.; Jo, M. R.; Kim, Y.-I.; Kang, K.; Kang, Y.-M., *J. Phys. Chem. Lett.* **2014**, *5*, 1368-1373.

[51] Kavan, L.; Kratochvilová, K.; Grätzel, M., *J. Electroanal. Chem.* **1995**, *394*, 93-102.

[52] Kavan, L.; Rathouský, J.; Grätzel, M.; Shklover, V.; Zukal, A., *J. Phys. Chem. B* **2000**, *104*, 12012-12020.

[53] Bousa, M.; Laskova, B.; Zukalova, M.; Prochazka, J.; Chou, A.; Kavan, L., *J. Electrochem. Soc.* **2010**, *157*, A1108-A1112.

[54] Shin, J.-Y.; Joo, J. H.; Samuelis, D.; Maier, J., *Chem. Mater.* **2011**, *24*, 543-551.

[55] Shin, J.-Y.; Samuelis, D.; Maier, J., *Adv. Funct. Mater.* **2011**, *21*, 3464-3472.

`

Chapter 5.

Hollow Nanoparticles of (Sn,Ti) Oxide Solid-solution as a High-rate Performance Anode for Lithium Ion Battery

5.1 Abstract

Hollow structured nanoparticles of (Sn,Ti) oxide solid-solution were prepared by a simple soft template method and used as the anode material for lithium ion batteries. The hollow (Sn,Ti) oxide nanoparticles (HSTs) exhibited a higher and more stable capacity than hollow titania nanoparticles because the Sn atom is well distributed in titania without formation of separated SnO_2 grains. Moreover, the effect of calcination temperature and Sn content for electrochemical performance of HSTs are systematically investigated.

`

5.2 Introduction

Due to the limited Li-ion capacity of widely used carbon-based anode, metal oxides of Sn, Fe, Mn, Co, etc. having relatively high capacity with low cost have been considered as the anode material for Li-ion battery. Among them, tin oxide (SnO_2) has the theoretical Li-ion capacity of 790 mAh/g and actually showed high capacity when used as an anode material.[1-4] However, the practical use of SnO_2 is still limited because the high initial capacity decreases during repeated charging/discharging cycles. The main reason of capacity fading is huge volume change during conversion reaction with Li-ion expressed as below.

$$SnO_2 + 4Li+ + 4e^- \rightarrow Sn + 2Li_2O$$

$$Sn + xLi+ + xe^- \leftrightarrow Li_xSn\ (0 \leq x \leq 4.4)$$

First, SnO_2 is reduced by Li-ion forming metallic Sn, which is believed as irreversible or partially reversible. Second, metallic Sn makes alloy with Li-ion to form Li_xSn changing its volume over 200 % and physical stress from volume change induce degradation of anode reducing capacity. To overcome this problem, preparation of hollow SnO_2 and coating of carbon material were tried.[4-6] Especially, void space of hollow SnO_2 structures released the physical stress from volume change and gave stable cycling performance of SnO_2 anode.

Meanwhile, formation of composite oxide with titania (TiO_2) was also investigated for enhancing capacity stability.[4, 7-9] In spite of relatively low theoretical Li-ion capacity about 168 mAh/g, titania has been regarded as potential replacement anode for their high stability and safety even under the high current density. Preparing composite oxide of solid-solution using Sn

`

and Ti were reported to get synergy effect of high capacity of Sn part and high stability of Ti part.[10-15] For example, wide range composition of $Ti_xSn_{1-x}O_2$ solid solutions were prepared and showed their anode property under the voltage range of 1.2 V-3.5 V to avoid the structure collapse to metallic Sn.[14] Very recently, $(Sn,Ti)O_2$ solid-solution nanorod showed the initial capacity about 300 mAh/g under the voltage range of 0.1 V-3.0 V.[15] But the researches on the structure as well as the electrochemical property of Sn with Ti oxide are still limited.

Here, (Sn,Ti) oxide hollow nanoparticles (HSTs) were prepared to get stable anode material with high rate-performance *via* both void space and solid-solution structure. The hollow structure was obtained by simple soft template method with polyacrylic acid (PAA) and the composition of solid-solution was controlled by the ratio of metal precursors. The effect of atomic composition and calcination temperature on electrochemical performance was systemically monitored. The best anode performance was obtained by HST composed of 26 % Sn atom and 74 % Ti atom annealed at 500 °C (HST2_500), which showed the initial capacity of 450 mAh/g and 50th capacity of 380 mAh/g under the current density of 100 mA/g and even showed 260 mAh/g under the high current density of 3 A/g.

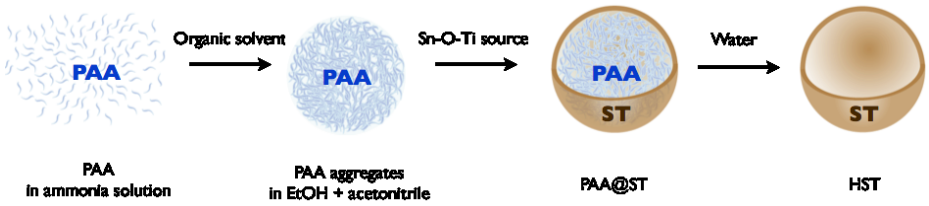

Figure 5.1. Schematic image of preparing HSTs.

`

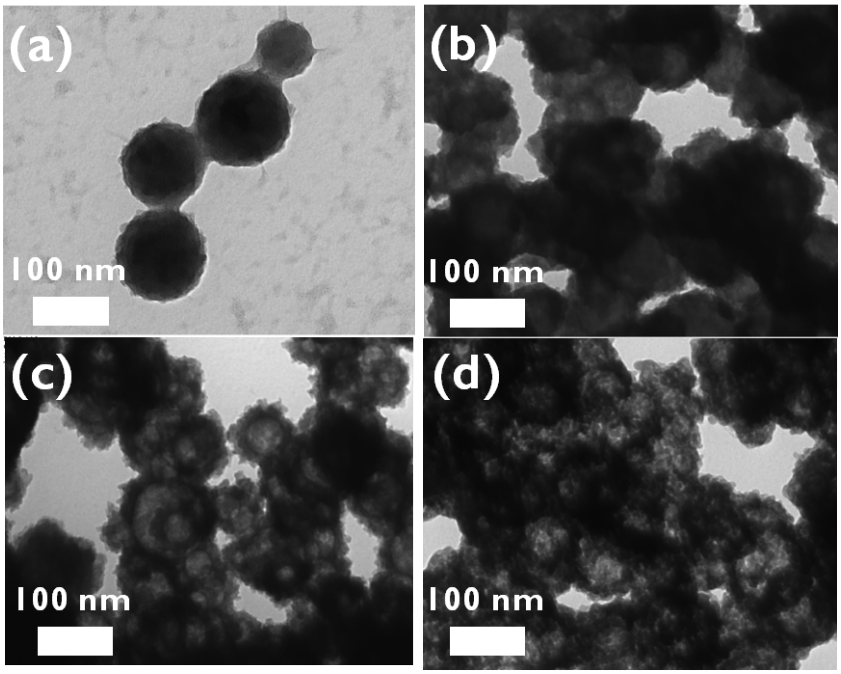

Figure 5.2. TEM images of (a) aggregated PAA, (b) PAA@ST, (c) HST2, and (d) HST2_500.

5.3 Results and Discussion

Synthesis of HSTs The synthesis scheme for HSTs is presented in Figure 5.1. To get HSTs, simple soft template method preparing hollow SiO_2 nanoparticles using PAA was modified[16] due to more simple and easy process than hard template method. First, PAA in ammonia solution was poured into the mixed solvent of ethanol and acetonitrile then PAA-ammonium salt precipitate into around 100 nm sized spherical aggregates for their low solubility to the organic solvent (Figure 5.2a). The precursor of tin tetrachloride pentahydrate (300 mg for HST2) was co-dissolved with titanium butoxide (1.0 mL) in ethanol and acetonitrile and injected to form the composite shell on the surfaces of the PAA-ammonium aggregates *via*

`

hydrolysis and condensation (Figure 5.2b). Hollow structure of HST2 was obtained after simply removing the PAA-ammonium cores with water. (Figure 5.2c). The extraction of PAA was also confirmed by comparing the remained weight after TGA experiment. Figure 5.3 showes that 15 wt% was decreased from PAA@ST and 39 wt% was decreased from HST until 800 °C in air. It indicates the PAA was clearly removed by washing with water. In case of HTNPs, the same method was used except precursor; only titanium butoxide (1.0 mL) used as titania precursor.

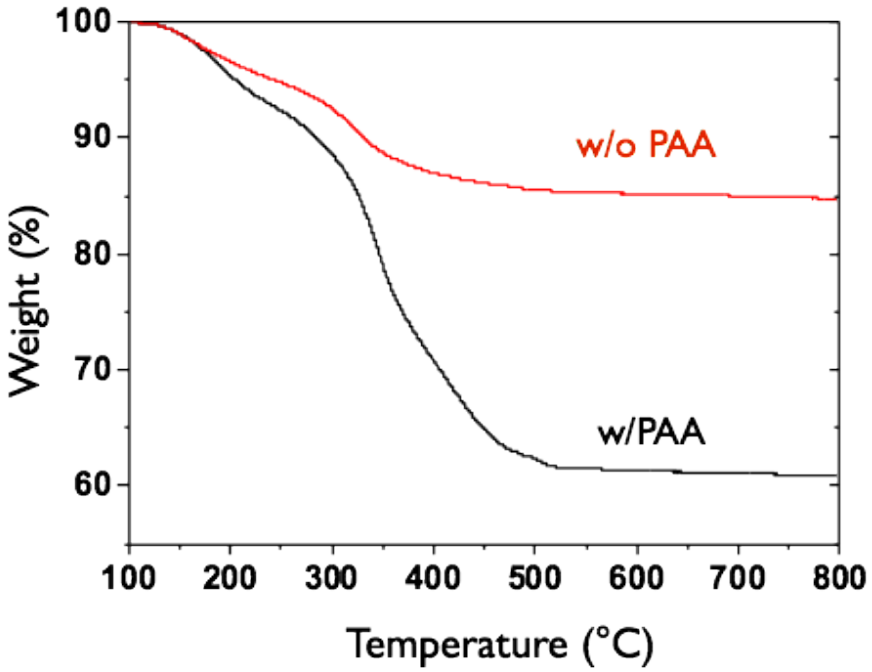

Figure 5.3. TGA experiment of PAA@ST (w/PAA) and HST (w/o PAA).

`

HST2 was annealed under 500 °C for 2 hr (HST2_500) and monitored by HR-TEM with EDS. First, high-angle annular dark-field (HAADF) image of Figure 5.4a shows hollow structure of HST2_500. In the EDS mapping of Figure 5.4b, c, and d, all three components of HST2_500 (Ti, Sn, and O) were well distributed in hollow structure. HR-TEM image of Figure 5.4e shows well-developed crystal phase of HST2_500 having lattice fringe of 3.27 Å, which is larger than 3.25 Å of typical (110) lattice fringe of rutile titania.

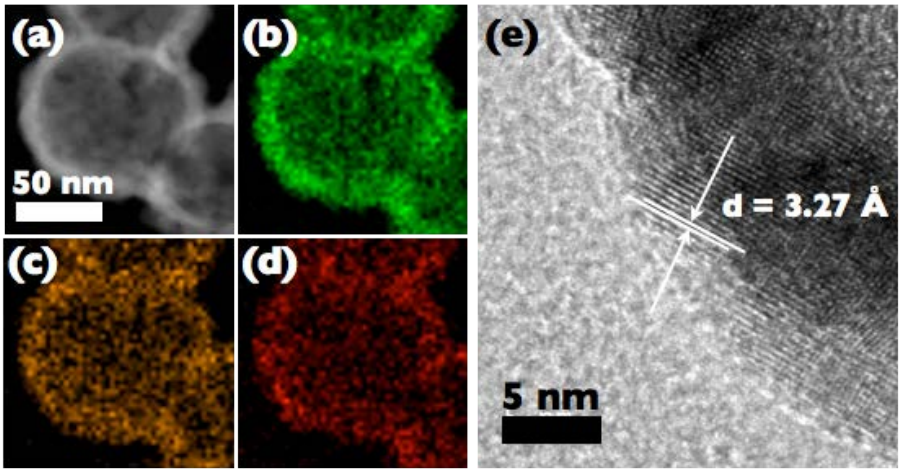

Figure 5.4. (a) HAADF image and EDS mapping (b-Ti, c-Sn, d-O), and HR-TEM image with lattice fringe of HST2_500.

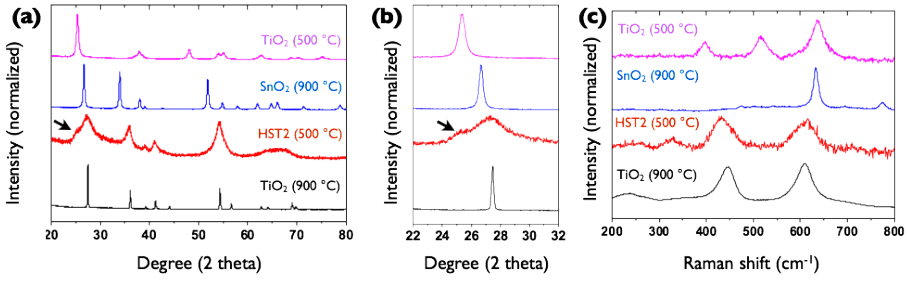

Figure 5.5. (a) and (b) XRD patterns and (c) Raman monitoring of HST2_500.

`

The crystal phase of HST2_500 was investigated by XRD (Figure 5.5a and b). Generally, at 500 °C, titania forms anatase and tin oxide forms rutile phase. The higher temperature over 650 °C is needed to form rutile phase with titania.[17-19] Although HTNP showed typical anatase phase at 500 °C, the main crystal phase of HST2_500 was rutile. In Figure 5.5b, the intense (110) peak of HST2_500 was laid between the rutile peak of SnO_2 and TiO_2, which represented the solid-solution formation of Sn and Ti oxide.[10, 20] The early formation of rutile phase with Sn cation was reported because Sn could act as seed for the growth of rutile phase.[21, 22] A little shoulder (see the arrow of Figure 5.5a and 5.5b) was monitored in front of (110) peak and expected to be (101) peak due to the excess Ti atom of HST2_500 (24 % of Sn and 76 % of Ti by ICP-AES). From XRD data, lattice fringe of HST2_500 could be calculated using Bragg's law, $d_{(hkl)} = \lambda/2sin\theta$, where $d_{(hkl)}$ is the crystal plane distance of (hkl), λ is the wavelength of X-ray used in the XRD experiment, and θ is the diffraction angle of (hkl) crytal plane.[23] The plane distance of intense (110) peak of HST2_500 is Calc. 3.27 Å, which is the same value with the distance that was monitored using HR-TEM in Figure 5.4e. The lattice fringe of 3.27 Å is larger than rutile TiO_2 and smaller than rutile SnO_2 (Calc. 3.25 Å and 3.34 Å, respectively from (110) data of Figure 5.5b). This enlarged lattice fringe of HST2_500 resulted from introducing slightly larger Sn^{4+} ion into crystal structure of smaller Ti^{4+}.[21]

To get more information of HST2_500, Raman spectroscopy monitoring was carried out (Figure 5.5c). First, raman spectra of HTNP showed the bands of B1g (396 cm^{-1}), A1g + B1g (516 cm^{-1}), and Eg (639 cm^{-1}), which assigned to the anatase lattice.[22, 24] But HST2_500 have no bands of anatase but rutlile; little shifted from rutile bands of Eg and A1g at 449 cm^{-1} and 610 cm^{-1}, respectively,[24] which confirms solid-solution of (Sn,Ti) oxide again.

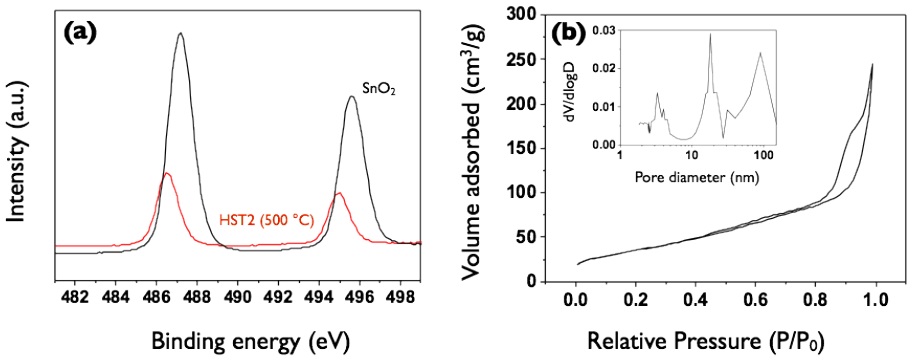

Figure 5.6. (a) XPS spectra of Sn 3d and (b) nitrogen adsorption/desorption isotherms of the HST2_500. Inset shows corresponding pore size distribution.

The presence of Sn in HST2_500 was also confirmed by XPS (Figure 5.6a). Two peaks corresponding to $Sn3d_{5/2}$ (487.2 eV) and $Sn3d_{3/2}$ (495.6 eV) were monitored in the SnO_2 sample due to the spin-orbit coupling, which could be assigned to the reported binding energy of Sn.[12, 25] In case of HST2_500, binding energy of Sn was shifted about negative 0.6 eV to the value of 486.6 eV and 495.0 eV, respectively. It results from electronegativity change when Sn is incorporated to TiO_2 than SnO_2 (electronegativity of Ti=1.54 and Sn=1.96).[26] The obtained XPS spectra confirmed again the solid-solution structure of HST2_500.

`

Using nitrogen adsorption/desorption isotherm, the surface area and porosity of HST2 were also investigated. The isotherm plot of HST2_500 showed type IV patterns with H_3 hysteretic loops[27] (Figure 5.6b) and a Brunauer-Emmett-Teller (BET) surface area of 53.5 m^2/g. The size of mesopores was calculated about 3.3 nm by the Barrett-Joyner-Halenda (BJH) in the inset of Figure 5.6b, which indicated the porous structure of HST2_500 shell. The larger pore could be assigned to the inner void space of HST2_500 with well-developed hollow structure.

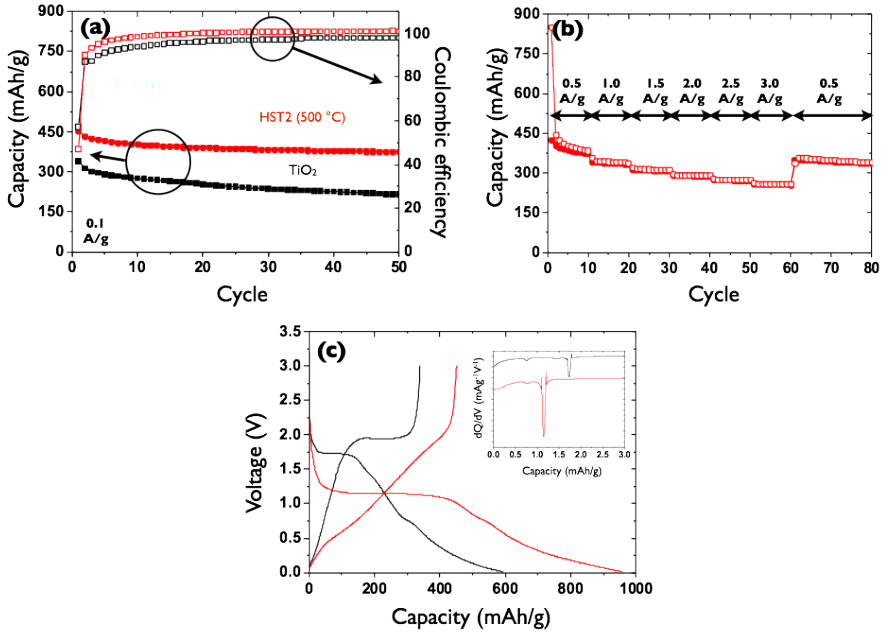

Figure 5.7. (a) Cycling performances at a current density of 0.1 A/g for 50 cycles with the corresponding coulombic efficiencies of HST2_500 and HTNP. (b) Rate performance of HST2_500 at various current densities and (c) charge and discharge voltage profiles of HST2_500 and HTNP.

`

Electrochemical properties of HST2_500 Figure 5.7a shows the cycling performances of the HST2_500 and HTNP in the voltage range of 0.01 V-3.0 V to use not only Ti but also Sn component. The first de-lithiation capacity of HST2_500 was about 450 mAh/g and showed stable capacity until 50th cycles of 375 mAh/g. Although first de-lithiation capacity of HTNP was 340 mAh/g, which is higher than theoretical capacity of titania (168 mAh/g), it decreased to about 200 mAh/g at 50th cycle. It may result from the structure collapse under the over-potential because titania is well-known as very stable anode material in the voltage of 1.0 V-3.0 V.[7, 8]

In Figure 5.7b, the rate performance of HST2_500 was displayed with increasing current density from 0.5 A/g to 3.0 A/g. When the current density of 0.5 A/g was applied, the initial capacity of 420 mAh/g was decreased to 380 mAh/g at 10th capacity. After 11th cycle under the current density of 1.0 A/g, the Li-ion capacity of HST2_500 was stabilized and showed the capacity of 250 mAh/g even in the high current density of 3.0 A/g. After 61th cycles, the capacity was almost recovered under the current density of 0.5 A/g again. The highest capacity and high-rate performance of HST2_500 with stability are similar or better than those of recent reports which used composite oxide of Sn and Ti.[10, 12, 15, 28]

The voltage profile of HST2_500 and HTNP was represented in Figure 5.7c. The first litiation of HST2_500 shows similar voltage profile with general intercalation profile of anatase titania, which composed of three steps; solid-solution, intercalation and surface adsorption.[2, 29, 30] But the voltage plateau of HST2_500 was in the voltage at 1.2 V in contrast to 1.7 V of anatase titania (inset of Figure 5.7c) and the similar plateau was reported by solid solution of $(Sn,Ti)O_2$ nanorods.[15]

`

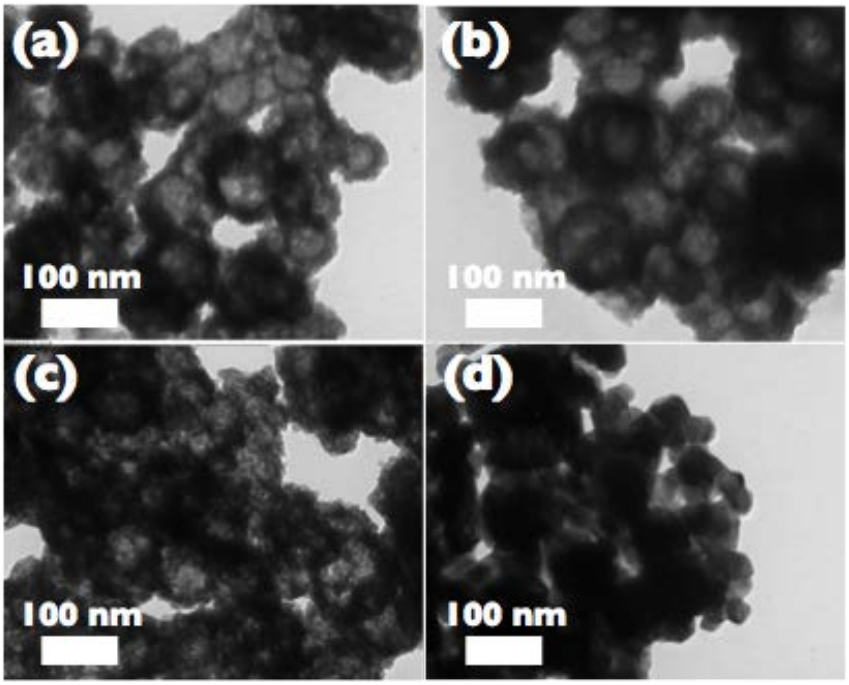

Figure 5.8. TEM images of (a) as-prepared HST2, (b) HST2_400, (c) HST2_500, and (d) HST2_900.

Effect of calcination temperature HST2 was annealed under the different temperature to investigate the relation between calcination temperature and electrochemical properties. Annealed HST2s under 400 °C, 500 °C and 900 °C were prepared, denoted as HST2_400, HST2_500 and HST_900, respectively and monitored by TEM (Figure 5.8). First, as-prepared HST2 shows well-developed hollow structure before calcination and HST2_400 still have similar hollow structure. In case of HST2_500, small crystalline was generated in the hollow shell, which indicates polycrystalline nature. But more harsh calcination condition of HST2_900 made larger crystalline without hollow structure.

`

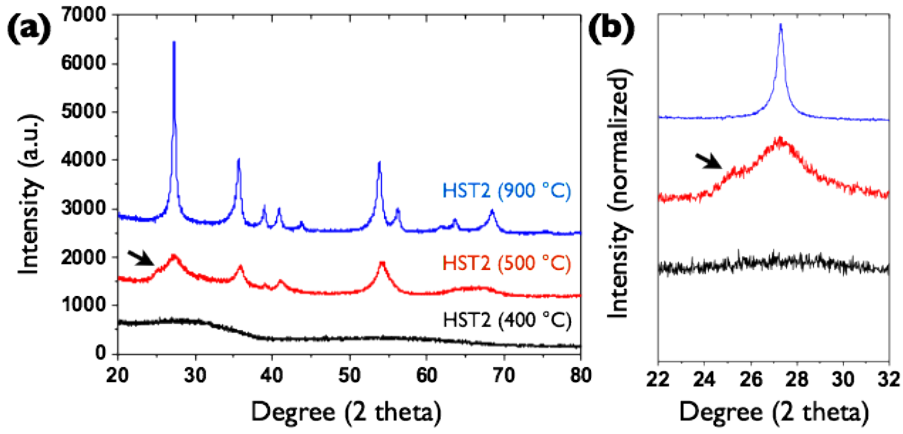

Figure 5.9. XRD patterns of HST2s from various calcination temperatures.

The HST2s annealed at different temperatures were confirmed by XRD and displayed in Figure 5.9. First, HST2_400 showed no specific diffraction patterns, which indicate the amorphous structure. HST2_500 could be assigned to rutile as mentioned before and HST2_900 also have rutile phase with more sharp peaks due to the larger crystal size. Furthermore, the small peak of HST2_500 expected to small portion of anatase titania was disappeared in the HST2_900 due to the phase transformation of anatase titania to rutile.

Figure 5.10 shows the electrochemical properties of the HST2s annealed at different temperatures. First, Figure 5.10a presents the cycling performance of HST2s at a current density of 0.1 A/g with the plot of coulombic efficiency. The discharge capacity was enhanced with increasing calcination temperature and it might results from increased conductivity of HST2 with decreasing defect site. Although HST2_900 showed the highest Li-ion capacity of ~550 mAh/g at the first cycle, it rapidly decreased with repeated cycle to 350 mAh/g, lower than HST2_500. The low stability of HST2_900 could result

`

from collapsed structure without hollow morphology.

The voltage profiles of HST2s were also displayed in Figure 5.10b. HST2_400 showed amorphous character without plateau regions in comparison to the rutile character of HST2_500 and HST2_900 with similar plateau region.[31] Therefore, among HST2s, HST2_500 seemed the best anode sample for their rutile crystalline with hollow structure.

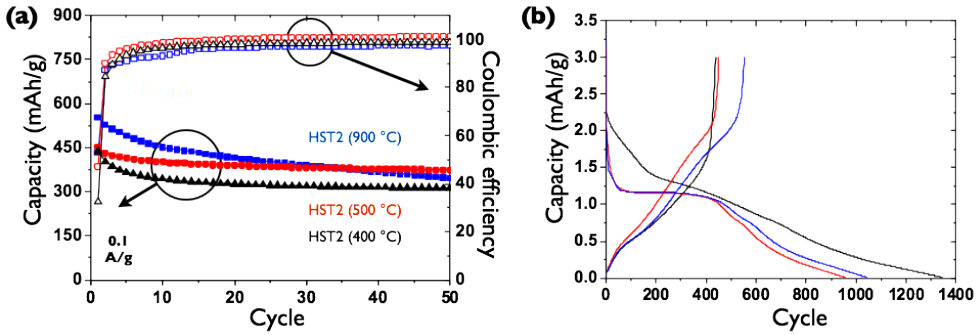

Figure 5.10. (a) Cyclic performances and (b) charge and discharge voltage profiles of HST2 from various calcination temperatures.

`

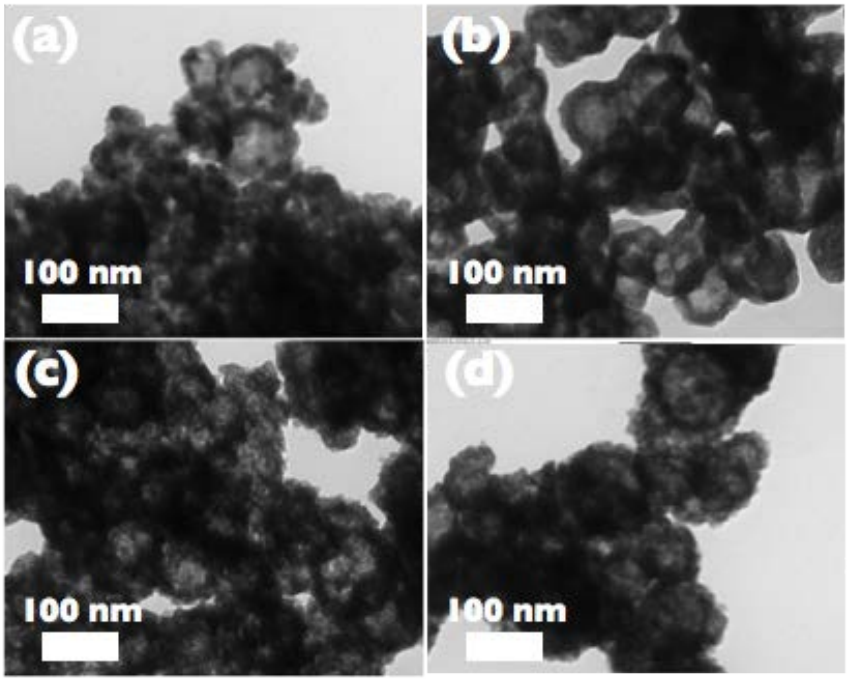

Figure 5.11. TEM images of (a) HTNP, (b) HST1_500, (c) HST2_500, and (d) HST3_500.

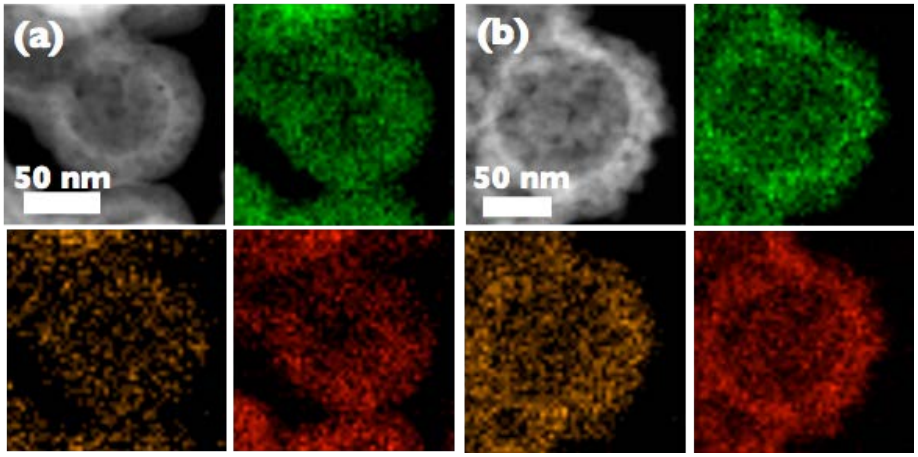

Figure 5.12. HAADF and EDS mapping images of (a) HST1_500 and (b) HST3_500. Green-Ti, yellow-Sn, and red-O.

`

Effect of Sn content. HSTs were prepared by varying the composition of Sn and Ti under the same calcination temperature of 500 °C. The atomic composition was controlled by changing the amount of metal precursors and the prepared HSTs confirmed to have the ratio of 10:90, 24:76, and 26:74 (Sn:Ti), respectively (ICP-AES). The ratio of Sn was not increased by using more amount of Sn precursor (saturated to 26:74) and HSTs were denoted as HST1_500, HST2_500 and HST3_500 with increasing ratio of Sn. Figure 5.11 displays the morphology of HSTs composed of different Sn ratio. HSTs have well-developed hollow structure with crystalline grains. Interestingly, increased Sn ratio made the surface morphology of HST rough and a little phase separation between Sn and Ti could be expected with the high concentration of Sn source in reaction condition. The atomic distribution of HSTs was also confirmed by EDS mapping in Figure 5.12. All atoms of Ti, Sn, and O were well-distributed overall structure of HST1_500 and HST3_500.

Crystal structure of HSTs was monitored by XRD. The similar rutile phase was confirmed with HST1_500 and HST3_500 (Figure 5.13a). In Figure 5.13b, in spite of less amount of excess Ti in HST3_500, tiny shoulder expected to (101) of anatase titania was small in HST1_500 and more definite in HST3_500. It could be expected that high concentration of Sn source induces more non-homogeneous structure of composite, which limits perfect transformation to homogeneous rutile phase.

Figure 5.13 shows the electrochemical properties of the HSTs with different Sn content. First, Figure 5.13a presents the cycling performance of HSTs at a current density of 0.1 A/g with the plot of coulombic efficiency. The initial discharge capacity was enhanced with increasing Sn content and it might results from increased both theoretical capacity and conductivity.

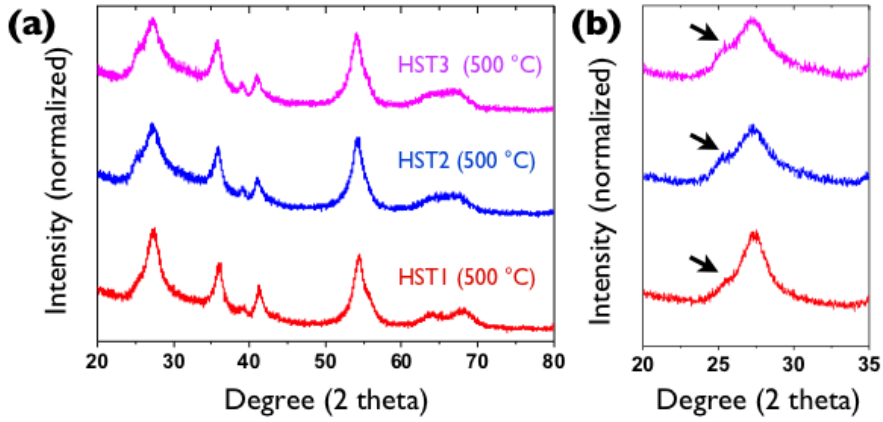

Figure 5.13. (a) and (b) XRD patterns of HSTs.

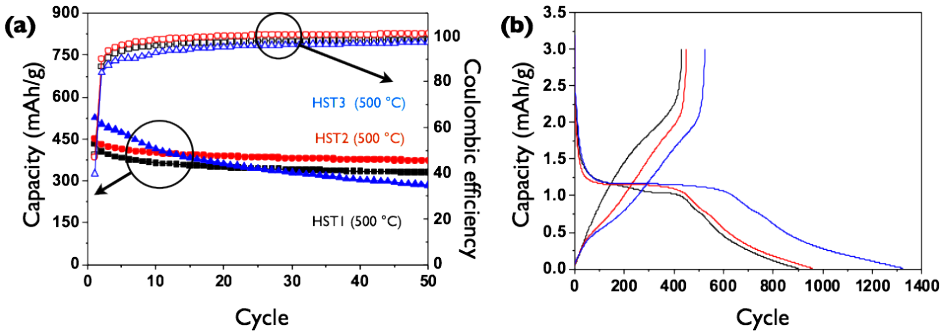

Figure 5.14. (a) Cyclic performances and (b) charge and discharge voltage profiles of HSTs from various Sn content.

In case of HST3_500, the Li-ion capacity rapidly decreased from about 530 mAh/g of first cycle to 300 mAh/g of 50th cycle. From TEM image of Figure 5.11 and and XRD pattern in Figure 5.13, this unstable electrochemical performance of HST3_500 could result from not enough stabilization of Sn content in the TiO_2 as (-Sn-O-Ti-) due to the non-homogeneous structure (increased -Sn-O-Sn- portion). As a result, HST2_500 is the best anode materials due to their high content of Sn with homogeneous -Sn-O-Ti- formation in the hollow structure.

`

5.4 Conclusions

Solid-solution of (Sn,Ti) oxide with hollow structure was successfully prepared by a simple soft template method. The presence and structure of Sn in the composite oxide were confirmed by EDS, XRD, XPS, ICP, and Raman. The effect of calcination temperature and Sn content to the electrochemical properties of HSTs were also investigated. The highest Li ion capacity of HST2_500 was 450 mAh/g with high stability due to the enough content of Sn and hollow structure. Moreover, high rate-performance of HST2_500 was monitored as 280 mAh/g even at a current density of 3.0 A/g.

5.5 Experimental Section

Materials and Instruments Titanium tetrabutoxide, poly(acrylic acid) (PAA, MW 1,800), anhydrous ethanol, absolute acetonitrile and tin tetrachloride pentahexahydrate were purchased from Aldrich. Absolute ethanol was prepared from J.T. Baker. Ammonia solution (29 % in water) and acetonitrile were purchased from Samchun and deionized (DI) water purified by a Milli-Q purification system was used for all of the experiments. All solvents and reagents used in this study were commercially available and used as received.

The atomic ratio of the HSTs was confirmed by using inductively coupled plasma atomic emission spectrometry (ICP-AES, Optima-4300 DV). The sizes and morphologies of products were analyzed by using transmission electron microscopy (TEM, Hitachi-7600, 100 kV). More detailed images and information about the atomic distributions in HSTs were obtained using TEM with a higher accelerating voltage (Tecnai F20, FEI, 200 kV) and an energy

`

dispersive spectroscopy (EDS) system. Thermogravimetric analysis (TGA) was performed using an SDT Q600 (TA Instruments Inc.) to confirm the extraction of the PAA cores. The samples for TGA were preheated at 100 °C for 30 min and then the temperature was raised to 800 °C at 10 °C/min in the air. The crystallinity of the samples was evaluated by powder X-ray diffraction (XRD) analysis on a Bruker New D8 Advanced Diffractometer with Cu K radiation (λ = 1.5418 Å). The scanning rate was 0.02 ° per second and the range was from 20 to 80 °. The surface areas and porosities of the products were measured using the nitrogen adsorption-desorption isotherm and Barrett-Joyner-Halenda (BJH) methods on a Micromeritics ASAP 2420. Raman analyses in pellet state were performed with the Renishaw inVia microscope equipped with Leica microscope.

Synthesis of HSTs Hollow solid-solution of Sn and Ti oxide could be prepared by co-condensation of Sn precursor and Ti precursor. First, PAA (200 mg) was dissolved in 2 mL of ammonia solution. This PAA/ammonia solution was injected into a mixture of absolute ethanol and acetonitrile (1:1 v/v, V_{tot} = 200 mL) with vigorous mechanical stirring and white colloids were formed. $SnCl_4 \cdot 5H_2O$ (200 mg or 300 mg or 350 mg for HST1, 2, and 3, repectively) and $Ti(OBu)_4$ (1.0 mL) were diluted with a mixture of absolute ethanol and acetonitrile (1:1 v/v, V_{tot} = 40 mL) and poured into the PAA colloids. This turned to the milky colloids of PAA-ammonium aggregates into PAA/ST core/shell particles and after a reaction for 2 hr, the products were purified and washed with water and ethanol using centrifugation/re-dispersion

`

(17,000 rpm, 10 min, 3 repetitions). White product was well dried at room temperature overnight, followed by annealing at 400 °C for 8 hr or 500 °C for 4 hr or 900 °C for 4 hr under air. In case of HTNP, only titania source was used without Sn salt. SnO_2 was prepared without both titania source and PAA and annealed for comparative monitoring of XRD and Raman.

Electrochemical tests Working electrodes were fabricated by mixing the anode materials synthesized for this study, Super P as a conductive agent, and PVDF as a binder at a weight ratio of 70:15:15 in *N*-methyl-2-pyrrolidone (NMP) solvent. The mixed slurry was uniformly plastered onto a copper foil current collector *via* doctor blade processing. The electrodes were dried under vacuum at 120 °C overnight and then pressed. A 2032 type coin cell consisting of a working electrode and lithium metal as a counter and reference electrode separated by a polypropylene separator (Celgard 2400) was assembled in a glove box under a dry argon atmosphere. The organic electrolyte was 1.0 M $LiPF_6$ dissolved in a mixture of ethylene carbonate (EC) and diethyl carbonate (DEC) with a volume ratio of 1:1. Galvanostatic testing (WBCS3000 cycler, WonA Tech, Korea) was carried out on the coin cell over the voltage range of 3.0 to 0.01 V (vs. Li^+/Li) at room temperature (25 °C).

`

*** Contributions**

Electrochemical properties were tested with Ji Hyun Um and Prof. Yung-Eun Sung in School of Chemical & Biological Engineering, Seoul National University. Raman spectroscopy monitoring was done with Jae-Ho Hwang and Prof. Jwa-Min Nam in Department of Chemistry, Seoul National University.

5.6 References

[1] Wang, Z.; Zhou, L.; Lou, X. W., *Adv. Mater.* **2012**, *24*, 1903-1911.

[2] Reddy, M. V.; Subba Rao, G. V.; Chowdari, B. V., *Chem. Rev.* **2013**, *113*, 5364-5457.

[3] Scrosati, B., *Electrochim. Acta* **2000**, *45*, 2461-2466.

[4] Chen, J. S.; Archer, L. A.; Wen Lou, X., *J. Mater. Chem.* **2011**, *21*, 9912-9924.

[5] Hong, Y. J.; Son, M. Y.; Kang, Y. C., *Adv. Mater.* **2013**, *25*, 2279-2283.

[6] Yuan, C.; Wu, H. B.; Xie, Y.; Lou, X. W., *Angew. Chem. Int. Ed.* **2014**, *53*, 1488-1504.

[7] Chen, Z.; Belharouak, I.; Sun, Y. K.; Amine, K., *Adv. Funct. Mater.* **2013**, *23*, 959-969.

[8] Su, X.; Wu, Q.; Zhan, X.; Wu, J.; Wei, S.; Guo, Z., *J. Mater. Sci.* **2012**, *47*, 2519-2534.

[9] Yang, Z.; Choi, D.; Kerisit, S.; Rosso, K. M.; Wang, D.; Zhang, J.; Graff, G.; Liu, J., *J. Power Sources* **2009**, *192*, 588-598.

[10] Chang, C.-C.; Chen, Y.-C.; Huang, C.-W.; Su, Y. H.; Hu, C.-C., *Electrochim. Acta* **2013**, *99*, 69-75.

`

[11] Issac, I.; Scheuermann, M.; Becker, S. M.; Bardají, E. G.; Adelhelm, C.; Wang, D.; Kübel, C.; Indris, S., *J. Power Sources* **2011**, *196*, 9689-9695.

[12] Kyerematen, N. A.; Vacandio, F.; Sougrati, M. T.; Martinez, H.; Jumas, J. C.; Knauth, P.; Djenizian, T., *J. Power Sources* **2013**, *224*, 269-277.

[13] Yan, J.; Song, H.; Zhang, H.; Yan, J.; Chen, X.; Wang, F.; Yang, H.; Gomi, M., *Electrochim. Acta* **2012**, *72*, 186-191.

[14] Uchiyama, H.; Hosono, E.; Zhou, H.; Imai, H., *Solid State Ionics* **2009**, *180*, 956-960.

[15] Chen, Y.-C.; Hung, T.-F.; Hu, C.-W.; Chiang, C.-Y.; Huang, C.-W.; Su, H.-C.; Liu, R.-S.; Lee, C.-H.; Chang, C.-C., *Nanoscale* **2013**, *5*, 2254-2258.

[16] Wan, Y.; Yu, S.-H., *J. Phys. Chem. C* **2008**, *112*, 3641-3647.

[17] Jiang, X. C.; Herricks, T.; Xia, Y. N., *Adv. Mater.* **2003**, *15*, 1205-1209.

[18] Jiang, X. C.; Wang, Y. L.; Herricks, T.; Xia, Y. N., *J. Mater. Chem.* **2004**, *14*, 695-703.

[19] Joo, J. B.; Lee, I.; Dahl, M.; Moon, G. D.; Zaera, F.; Yin, Y., *Adv. Funct. Mater.* **2013**, *23*, 4246-4254.

[20] Hirata, T.; Ishioka, K.; Kitajima, M.; Doi, H., *Physical Review B* **1996**, *53*, 8442-8448.

[21] Cao, Y.; He, T.; Zhao, L.; Wang, E.; Yang, W.; Cao, Y., *J. Phys. Chem. C* **2009**, *113*, 18121-18124.

[22] Majrik, K.; Tálas, E.; Pászti, Z.; Sajó, I.; Mihály, J.; Korecz, L.; Drotár, E.; Tompos, A., *Appl. Catal., A* **2013**, *466*, 169-178.

[23] Lin, J.; Yu, J. C.; Lo, D.; Lam, S. K., *J. Catal.* **1999**, *183*, 368-372.

`

[24] Fresno, F.; Tudela, D.; Coronado, J. M.; Fernandez-Garcia, M.; Hungria, A. B.; Soria, J., *Phys. Chem. Chem. Phys.* **2006**, *8*, 2421-2430.

[25] Zhou, X.; Fu, W.; Yang, H.; Ma, D.; Cao, J.; Leng, Y.; Guo, J.; Zhang, Y.; Sui, Y.; Zhao, W.; Li, M., *Mater. Chem. Phys.* **2010**, *124*, 614-618.

[26] Duan, Y.; Fu, N.; Liu, Q.; Fang, Y.; Zhou, X.; Zhang, J.; Lin, Y., *J. Phys. Chem. C* **2012**, *116*, 8888-8893.

[27] Sing, K. S. W., *Pure Appl. Chem.* **1985**, *57*, 603-619.

[28] Liao, J.-Y.; Manthiram, A., *Adv. Energy Mater.* **2014**, *4*, 1400403.

[29] Froschl, T.; Hormann, U.; Kubiak, P.; Kucerova, G.; Pfanzelt, M.; Weiss, C. K.; Behm, R. J.; Husing, N.; Kaiser, U.; Landfester, K.; Wohlfahrt-Mehrens, M., *Chem. Soc. Rev.* **2012**, *41*, 5313-5360.

[30] Kubiak, P.; Fröschl, T.; Hüsing, N.; Hörmann, U.; Kaiser, U.; Schiller, R.; Weiss, C. K.; Landfester, K.; Wohlfahrt-Mehrens, M., *Small* **2011**, *7*, 1690-1696.

[31] Dambournet, D.; Belharouak, I.; Amine, K., *Chem. Mater.* **2009**, *22*, 1173-1179.

`

Chapter 6.

Synthesis of Iron Oxide@Titania Yolk@Shell Nanoparticles as a High-performance Anode for Lithium Ion Battery

6.1 Abstract

Yolk-shell structured nanoparticles with iron oxide core, voids, and a titania shell configuration are prepared by a simple soft template method and used as the anode material for lithium ion batteries. The iron oxide-titania yolk-shell nanoparticles (IO@void@TNPs) exhibit a higher and more stable capacity than simply mixed nanoparticles of iron oxide and hollow titania because of the unique structure obtained by the perfect separation between iron oxide nanoparticles (IONPs) in combination with the adequate internal void space provided by stable titania shells. Moreover, the structural effect of the IO@void@TNPs clearly demonstrates that the capacity retention value after 50 cycles is approximately four times that for IONPs under the harsh operating conditions, i.e. when the temperature is increased to 80 °C.

`

6.2 Introduction

Transition metal oxides have been regarded as one of the most promising materials for lithium ion battery (LIB) anodes because of a much higher theoretical capacity (~1000 mAh/g) than that of commercially used graphite (372 mAh/g).[1,2] Among various transition metal oxides, iron oxides have several advantages including high theoretical capacities (928 mAh/g for Fe_3O_4 and 1007 mAh/g for α-Fe_2O_3 assuming accommodation of eight and six Li ions per formula unit, respectively), high natural abundance, environmental friendliness, and relatively low cost.[3-5] However, their use in LIB anodes is hindered by poor capacity retention resulting from the inherently large volume expansion/contraction during conversion reactions and severe aggregation of iron oxide nanoparticles (IONPs).[2,6,7] To improve the capacity retention issue, many research groups have investigated the nanostructures of IONPs and their hybridization with other materials such as carbon or polymers.[8-11] Various nanostructured materials with structures such as hollow, porous, and yolk-shell have been explored in the effort to achieve high capacity, good cycle stability, and enhanced rate performance. These nanostructures were expected to shorten the Li ion diffusion length, increase the electrolyte-electrode contact area, and accommodate the strain attributed to large volume changes.[4,8,12-14] The hybridization of iron oxide with titania, which is well-known for its very stable character for Li ion storage by intercalation reactions, has been reported to show a synergistic effect between two different characters: the high theoretical capacity of iron oxide and the high cycle-stability of titania. Yu *et al*. prepared titania/Fe_2O_3 core-shell arrays on carbon textiles and demonstrated stability and high rate capability,[15] and titania nanotubes grafted with hollow Fe_2O_3 were also investigated to obtain anode materials with excellent capacity retention.[16] A yolk-shell structure has an

`

internal void space, which can effectively relax the strain on the core materials associated with volume changes during the Li ion insertion/extraction processes.[9,17-21] Recently, sulfur-titania yolk-shell structures were synthesized for Li-S batteries and exhibited high capacity retention due to the presence of the internal void spaces.[22] Based on these reports, it is expected that hollow titania can be used as a yolk-shell template to provide stability during charge/discharge processes with iron oxide core material providing the structural advantages of internal void space. However, no results based on yolk-shell IO@void@TNP structures for application to LIB anodes have been reported yet, even though a material having similar nanostructures was already reported.[23]

In this chapter, IO@void@TNPs were prepared and investigated the structural effect of core@void@shell on the performance of LIB anodes. The method for synthesizing the yolk-shell structures was very simple. Easily removable soft templates was used, in contrast to the previously reported yolk-shell synthetic method that used hard silica templates, which were relatively difficult to be etched out.[23] The hybridized yolk-shell structures of iron oxide and titania exhibited excellent cycle stability when they were compared with IONPs themselves or simply mixed nanoparticles of iron oxide and hollow titania. Moreover, the structural effect of the core@void@shell configuration was also confirmed under the harsh condition of an elevated cell operating temperature of 80 °C.

`

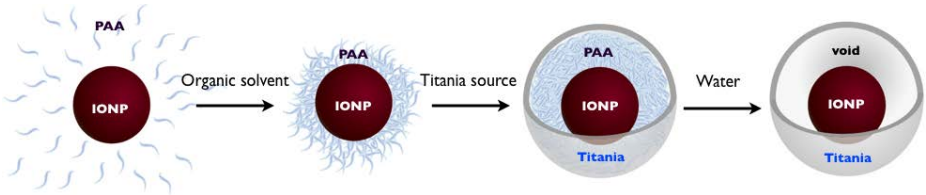

Figure 6.1. Schematic image of the method for synthesizing IO@void@TNPs.

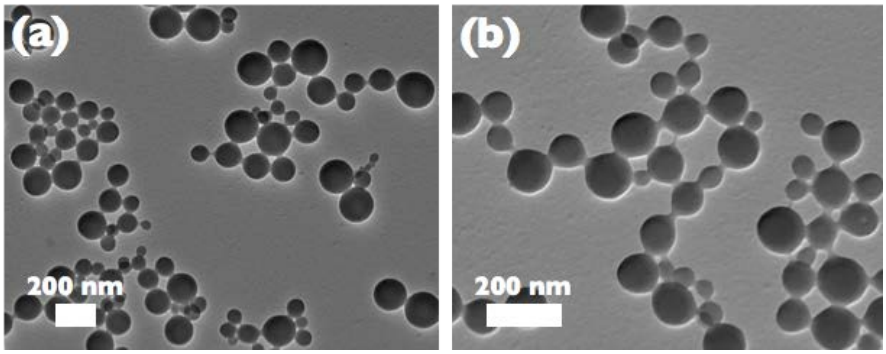

Figure 6.2. TEM images of PAA-ammonium aggregated particles.

6.3. Results and Discussion

Synthesis and Characterization of Particles The overall scheme for synthesizing IO@void@TNPs is illustrated in Figure 6.1. A previously reported preparation method for synthesizing hollow silica nanoparticles[24] by a polyelectolyte-controlled system was modified to obtain hollow titania structures. This method is a sort of soft template method for preparing hollow nanoparticles that is much simpler and easier than the hard template method using SiO_2, especially to prepare large amounts of the desired product.[27] First, PAA in ammonia solution was precipitated as spherical nano-aggregates with particle sizes of around 100 nm in a mixture of ethanol and acetonitrile because of the low solubility of the PAA-ammonium salt (Figure 6.2).

Titanium butoxide was used as the precursor of the titania shells to be formed on the surfaces of the PAA-ammonium aggregates *via* hydrolysis and

`

condensation. Hollow titania nanoparticles (TNPs) were then obtained after dissolving the PAA-ammonium cores with water, and the empty inner spaces were clearly observed (Figure 6.3a). The removal of the PAA-ammonium cores was clearly confirmed by TEM; even though the PAA-ammonium core/titania shell structures were well characterized before the extraction of the cores, the empty inner spaces of the hollow titania nanoparticles were clearly observed after the extraction (Figure 6.3). Furthermore, the difference of the remaining weight after thermal decomposition at up to 800 °C in air by TGA indicated that the PAA-ammonium cores removed by the extraction with water corresponded to 21 wt% (Figure 6.4).

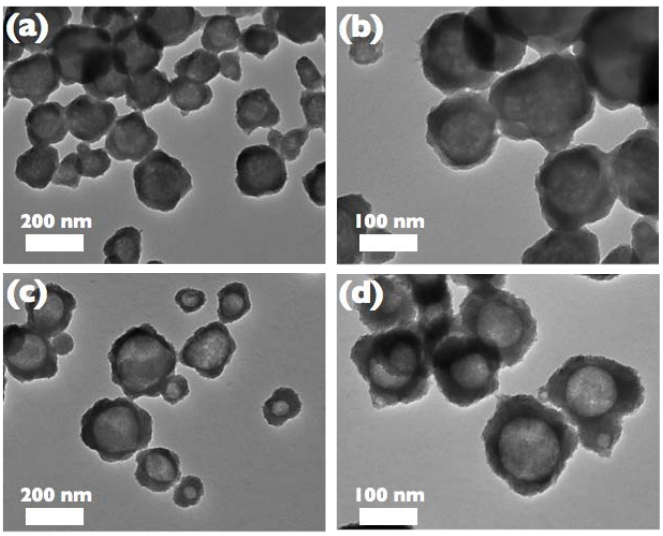

Figure 6.3. (a) and (b) TEM images of PAA-ammonium aggregated cores/titnaia shells and (c) and (d) corresponding hollow titania particles.

`

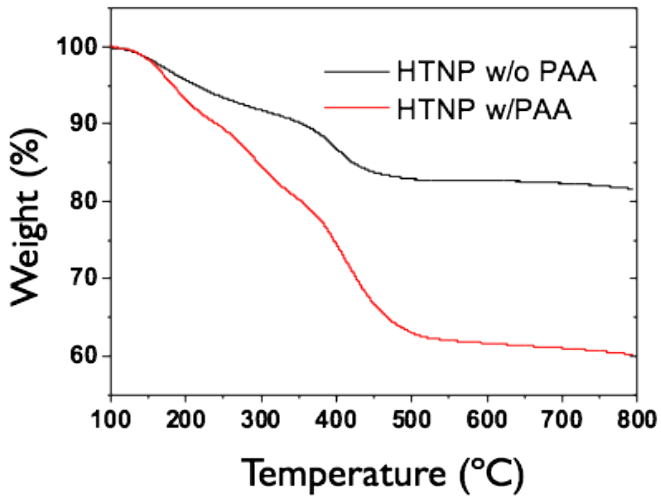

Figure 6.4. Thermogravimetric analysis of PAA-ammonium/titania core/shell and hollow titania.

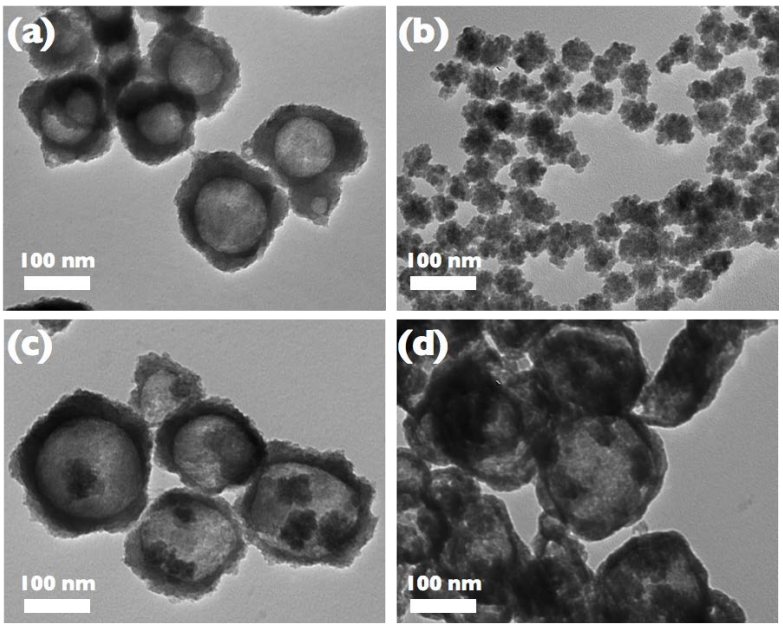

Figure 6.5. TEM images of (a) hollow titania nanoparticles, (b) IONPs, (c) IO@void@TNPs, and (d) IO@void@TNPs after calcination.

`

Figure 6.6. Photographs showing the dispersability of PAA and PG-IONPs in polar ammonia solution and non-polar organic solvent mixture of ethanol and acetonitrile.

IONPs having ~40 nm sizes were obtained by the hydrolysis/condensation of iron chloride hexahydrate, followed by partial reduction in hot ethylene glycol (Figure 6.5b).[25] To make sure that IONPs were well-dispersed in the ammonia solution, PG groups were grafted onto the surfaces of the IONPs by the polymerization of glycidol.[26] PG grafted IONPs were well-dispersed in the ammonia solution containing PAA and co-precipitated with PAA to generate IONP/PAA core-shell structures in a mixture of ethanol and acetonitrile (Figure 6.5). Successive injection of titanium butoxide and extraction of the PAA-ammonium layer generated IO@void@TNPs as shown in Figure 6.5c. After isolation from the hollow titania nanoparticles that did not contain IONPs by using an external magnet, IO@void@TNPs were annealed at 500 °C for 2 h in air to remove any residual organic compounds and transform

`

titania from the amorphous to the anatase phase, which is well-known as the electrochemically most active crystalline phase of TiO_2 in order to use them as the anode material of LIBs.[28] The yolk-shell structures of the IO@void@TNPs were well maintained after the calcination (Figure 6.5d). The HR-TEM images of the IO@void@TNPs in Figure 6.7a also clearly show the yolk-shell structure, and one selected particle of IO@void@TNP was investigated with a higher magnification (Figure 6.7b). The same particle was scanned by EDS to confirm the atomic distribution of IO@void@TNP (Figure 6.7c). First, titanium was detected only in the shell of the IO@void@TNP and is presented in green. Iron, in red, was located only in the small core spheres, and oxygen was detected from the whole area of the IO@void@TNP, which indicated that both the core and shell materials were in the oxide form.

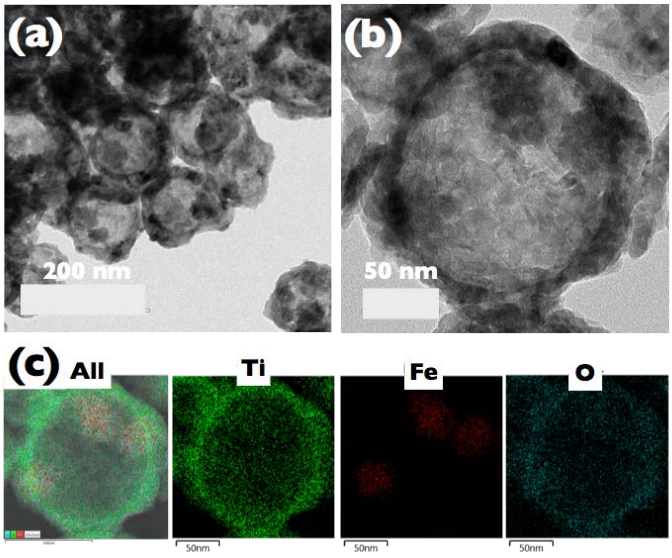

Figure 6.7. (a) and (b) HR-TEM images and (c) corresponding EDS elemental mapping images of the IO@void@TNPs (green-Ti, red-Fe, and sky blue-O).

`

The composition of IO@void@TNPs was confirmed to comprise 24 wt% iron oxide cores and 76 wt% titania shells by ICP-AES (data is not shown). The crystalline phase of IO@void@TNPs was characterized by XRD (Figure 6.8a), and the diffraction patterns show peaks for both titania and iron oxide, that can be assigned to anatase and magnetite, respectively. Notably, as-prepared IONPs have been characterized as magnetite,[24] but during the annealing process in air, they might be oxidized to maghemite. However, from the viewpoint of LIB applications, both iron oxide phases are effective in terms of Li ion capacity,[5] and a detailed characterization was not carried out after the annealing process. The surface area and porosity of IO@void@TNPs and the hollow titania nanoparticles were measured by using nitrogen absorption/desorption isotherms. They exhibited type IV patterns with H_3- and H_2-like hysteretic loops[39] with the specific surface areas of 75.4 and 53.8 m^2/g, respectively (Figure 6.8b), confirming the presence of mesopores in the hollow titania shells.[30] Pore sizes of approximately 3.6 and 7.2 nm, respectively, were calculated by the Barrett-Joyner-Halenda (BJH) pore distribution method, which also indicated the mesoporous titania shells within the well-developed nanostructures of IO@void@TNP.

`

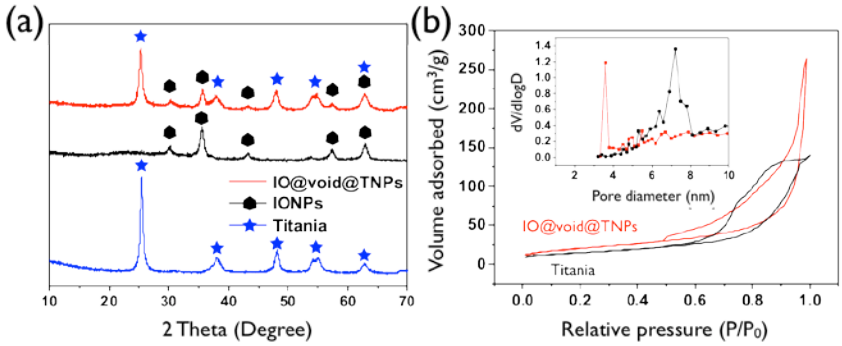

Figure 6.8. (a) XRD patterns and (b) nitrogen adsorption/desorption isotherms of the IO@void@TNPs and the hollow titania nanoparticles. Inset shows corresponding pore size distribution.

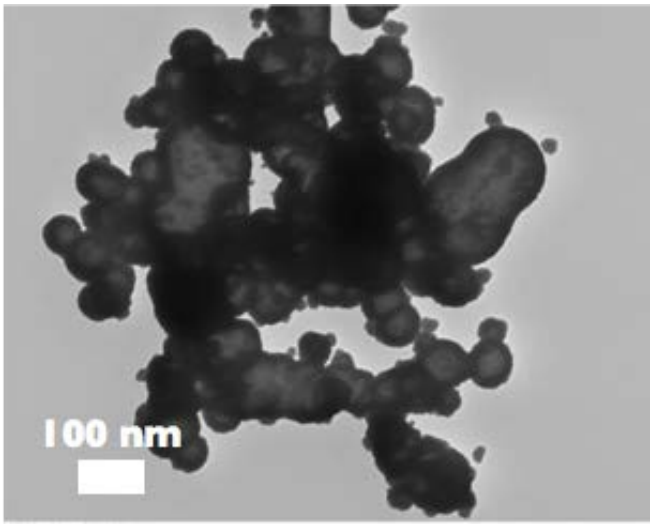

Figure 6.9. TEM image of the yolk-shell structures using twice the amount of IONPs used in the normal preparation method for IO@void@TNPs.

`

Attempts to Control the Ratio of Iron Oxide Core to Titania Shell Attempts were made to control the ratio of iron oxide core to titania shell of the yolk-shell structure due to the relatively low 24 wt% of the iron oxide cores (calculated from the ICP-AES measurement). If the weight percentage of iron oxide can be increased, the amount of Li ion storage will also be increased because of the larger ideal capacity of iron oxide than that of titania. For this purpose, a larger amount of IONPs was used to increase the entire weight ratio of iron oxide cores in the IO@void@TNPs. However, when twice amount of the IONPs was used, the yolk-shell structure with titania could also be formed but many IONPs were included in the large interconnected titania structure and there were not as many well-defined spherical IO@void@TNPs (Figure 6.9). On the other hand, when the smaller amount of titania precursor was used to decrease the weight ratio of titania in the IO@void@TNPs, thinner or less dense titania shells were formed with well incorporated IONP cores (Figures 6.10a, 6.10c, and 6.10e). In that case, however, the thermal stability of the titania shells caused problems. When the 66 % of the titania precursor was used, compared to the normal amount, to prepare IO@void@TNPs, even though some yolk-shell structure particles were formed, most of the structures were collapsed and separated into IONPs and many tiny pieces of titania (Figure 6.10b). Furthermore, any yolk-shell particles prepared by using 33 % and 17 % of the titania precursor compared to the normal amount could not retain their structures after calcination (Figures 3.10d and f). Therefore, in our study IO@void@TNPs of 24 wt% iron oxide cores and 76 wt% titania shells were determined to be the best model structures for attaining high capacity with stable structures.

`

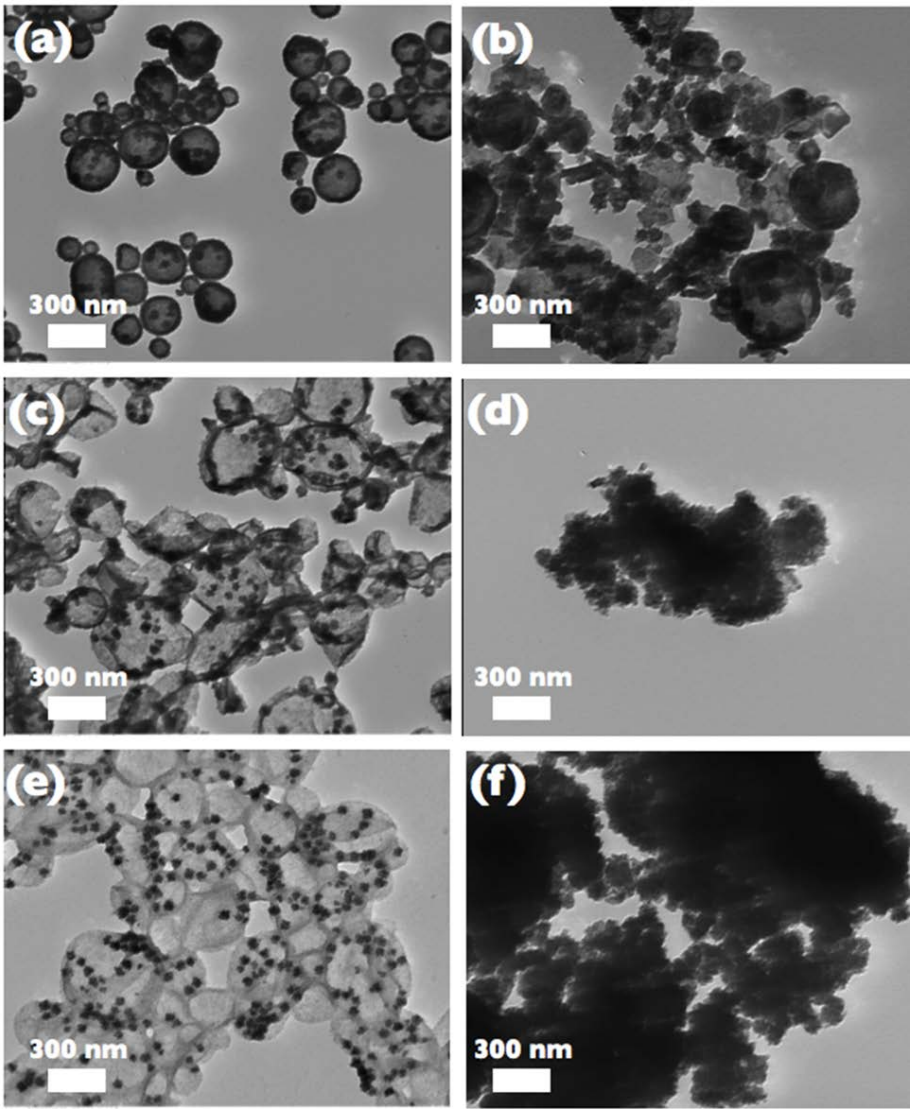

Figure 6.10. TEM images of IO@void@TNPs using 66% of the titania precursor (a) before and (b) after calcination, 33% of the titania precursor (c) before and (d) after calcination, and 17% of the titania precursor (e) before and (f) after calcination, used in the normal preparation method for IO@void@TNPs.

`

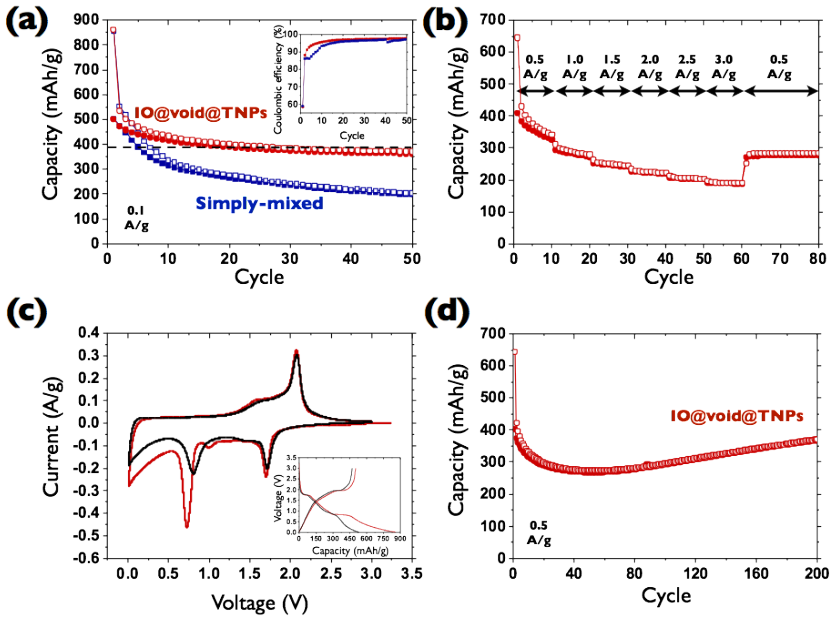

Figure 6.11. (a) Cycling performances of IO@void@TNPs and simply-mixed nanoparticles at a current density of 0.1 A/g for 50 cycles. Inset shows corresponding coulombic efficiencies, (b) rate performance of IO@void@TNPs at various current densities, (c) cyclic voltammograms of IO@void@TNPs at a scan rate of 0.1 mV/s for initial two cycles. Inset shows charge and discharge voltage profiles, and (d) long-term cycling performance of IO@void@TNPs at a current density of 0.5 A/g for 200 cycles.

Electrochemical Properties Figure 6.11 shows the electrochemical properties of the IO@void@TNPs at room temperature (25 °C). Figure 5a presents the cycling performances of the IO@void@TNPs at a current density of 0.1 A/g. To confirm the effect of void on capacity retention, it was also tested on the coin cell prepared with simply (physically) mixed nanoparticles of iron oxide and hollow titania nanoparticles in the same weight ratio of IO@void@TNP s (IONPs:hollow TNPs = 24:76, w/w). The IO@void@TNPs

`

and simply mixed nanoparticles exhibited almost the same capacity in the first cycle because of the same composition ratio of titania and iron oxide.

However, as expected, the capacity of simply mixed nanoparticles degraded with repeated cycling in contrast to the superior performance of the yolk-shell type electrode. Moreover, the capacity of IO@void@TNPs was close to the calculated theoretical capacity of ~400 mAh/g from the weight ratio of titania and iron oxide in the yolk-shell nanoparticles, as shown with a dashed line in Figure 6.11a, and it was consistent with a recently reported result using titania tubes/hollow iron oxide with a similar weight ratio.[16] The inset of Figure 6.11a shows that the coulombic efficiencies of the IO@void@TNPs remained relatively stable after 10 cycles despite the high capacity loss in the first cycle mainly because of the formation of a solid electrolyte interface (SEI) layer,[31,32] whereas that of the simply mixed nanoparticles was much lower over the whole cycle and fairly unstable during the initial and last periods.

The rate capability of IO@void@TNPs cycled between 0.01 V and 3 V was evaluated stepwise by increasing the galvanostatic current from 0.5 A/g to 3 A/g and then returning to 0.5 A/g as shown in Figure 6.11b. When cycled at 0.5 A/g, the initial charge capacity of approximately 410 mAh/g decreased to 330 mAh/g for the subsequent 10 cycles. Afterward, the capacity became stable as the current density increases. At significant high rate (3.0 A/g), IO@void@TNPs had high stability with capacity of about 200 mAh/g, which was much higher capacity than that of titania and iron oxide composites in recent reports.[15,33] After 60 cycles, when the current density was reduced back to 0.5 A/g, the capacity of the IO@void@TNPs had almost recovered to the original value, thus showing good rate capability.

`

Cyclic voltammetry (CV) was conducted to further understand the reactions of IO@void@TNPs in the range of 0.01–3.0 V at a slow scan rate of 0.1 mV/s (Figure 6.11c). The first cathodic peak as shown with a red line at around 1.70 V can be attributed to the insertion of Li ions into the titania shells. Subsequent cathodic peaks were observed at 0.99 V, corresponding to the chemically intermediate reduction of Fe^{3+} to Fe^{2+}, and 0.72 V, indicating the complete reduction of Fe^{2+} to Fe^{0} and the formation of the SEI layer, as reported.[5,10] Meanwhile, the anodic peak with a shoulder at around 1.6 V was ascribed to the oxidation of Fe^{0} to Fe^{2+} and Fe^{3+} and the other anodic peak at 2.1 V indicated the extraction of Li ions from the titania shells.[2,7,16] In the second cycle as shown with a black line in Figure 6.11c, the cathodic and anodic peaks corresponding to the Li ion insertion to titania and extraction from the Li_xTiO_2 shells were nearly unchanged, implying a good reversibility of the Li ion insertion and extraction reactions. In addition, one broad peak at around 0.80 V was observed for the cathodic process, indicating irreversible phase transformation during the first cycle and the reduction peak was shifted from 0.72 V to a higher potential of 0.80 V, suggesting the activation process of Li ion insertion as previously reported in the literature.[34, 35] Similar features are also shown in the inset plot of the galvanostatic discharge-charge voltage profiles between 0.01 V and 3.0 V at a current density of 0.1 A/g.

To confirm the effect of the titania shells and void spaces, the capacity retention of the IO@void@TNPs was compared to those of only IONPs and simply mixed nanoparticles as shown in Figure 6.12. In contrast to the severe capacity decrement in the case of IONPs (under 30 % of initial capacity), IO@void@TNPs still maintained over 70% of their initial capacity.

`

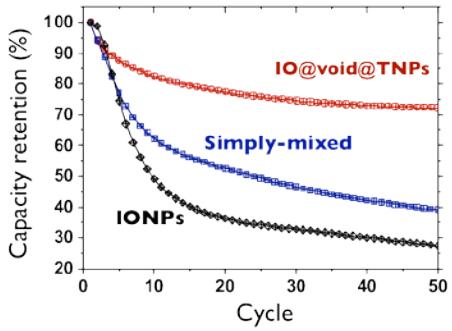

Figure 6.12. Capacity retentions of IO@void@TNPs, IONPs, and simply mixed nanoparticles.

Interestingly, simply mixed nanoparticles also retained their capacity better than IONPs, indicating that the attempt to mix them with hollow titania nanoparticles might help the IONPs to be more stable. However, the simply mixed nanoparticles maintained only 40 % of their initial capacity, which once again emphasizes that both the perfect separation of IONPs and adequate void space are required to obtain high capacity retention in IO@void@TNPs. In order to check the contribution of anatase titania shell to the capacity of the IO@void@TNPs, the capacities of the pure hollow titania nanoparticles shown in Figure 6.5a were measured at the different voltage ranges either between 0.01 to 3.0 V or 1.0 to 3.0 V. In general, the practically attainable capacity of anatase titania is reported to be about half of the theoretical capacity of 335 mAh/g.[36] However, the voltage ranging from 0.01 to 3.0 V (*vs.* Li/Li^+) was usually applied in the measurements to maximize the utilization of the iron oxide nanoparticles, and it was expected to cause the lower capacity retention for titania shell owing to the phase transformation from tetragonal TiO_2 toward orthorhombic $Li_{0.5}TiO_2$ and another phases upon further Li ion insertion.[38] The stable capacity retention of the hollow titania shell nanoparticles, as shown in Figure 6.13a, was clearly measured in the voltage

`

range of 1.0 to 3.0 V at about 180 mAh/g. As expected, in experiments with the wide voltage range of 0.01 to 3.0 V, the first discharge capacity of 243 mAh/g was continuously decreased to 120 mAh/g after the 50th discharge cycle. Also, the unstable cycle performance of the hollow titania nanoparticles showed clear distinction after continuous charge/discharge cycles between 1.0 and 3.0 V (Figure 6.13b). Therefore, the contribution of titania shell to the total capacities of the IO@void@TNPs is not significant, less than ~150 mAh/g after initial 10 cycles, even though the weight percentage of titania is about 76%. The cyclic stability of IO@void@TNPs was evaluated at a current density of 0.5 A/g during 200 cycles, as shown in Figure 6.12d. The reversible capacity was maintained during the entire cycles, and most importantly, the capacity initially decreased during 40 cycles and then slowly increased until 200 cycles towards the theoretical capacity of ~400 mAh/g, calculated from the weight ratio of titania and iron oxide in the yolk-shell nanoparticles.[16] This type of increment in capacity was often observed when iron oxide nanoparticles were used as an active material for lithium-ion batteries and an activation process was already proposed in the literatures.[2,7,38]

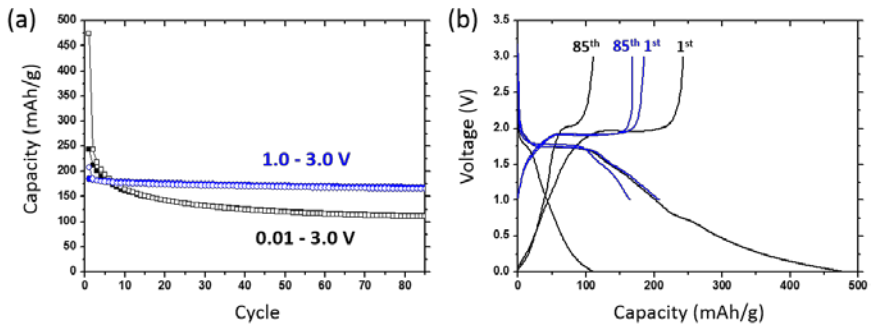

Figure 6.13. (a) Cycling performances of hollow titania with different voltage ranges of 3.0 to 1.0 V and 3.0 to 0.01 V at 0.1 A/g for 85 cycles and (b) corresponding charge and discharge voltage profiles at 1st and 85th cycle.

`

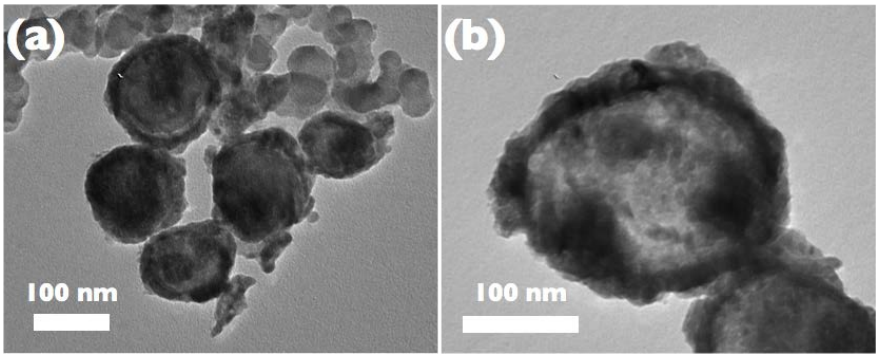

Figure 6.14. (a) and (b) TEM images of IO@void@TNPs after 50 cycles at a fully charged state.

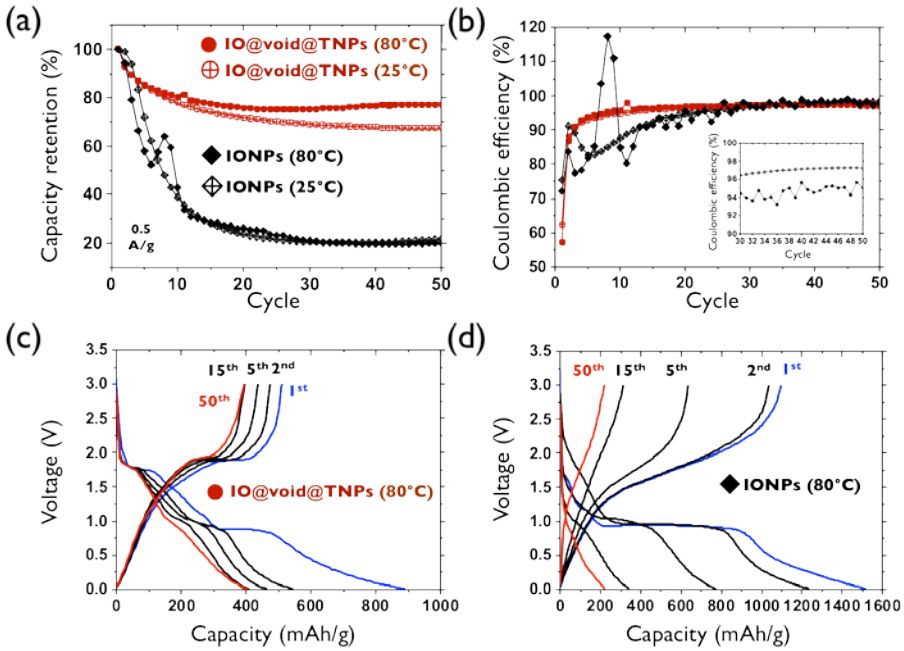

Figure 6.15. (a) Capacity retention of IO@void@TNPs and IONPs measured at room temperature of 25 °C and at an elevated temperature of 80 °C at a current density of 0.5 A/g for 50 cycles, (b) Coulombic efficiencies of IO@void@TNP and IONP electrodes operated at 25 °C and 80 °C. Galvanostatic charge and discharge voltage profiles of (c) IO@void@TNPs

`

and (d) IONPs operated at 80 °C at a current density of 0.5 A/g.

Figure 6.14 exhibits TEM images of IO@void@TNPs with the removal of the SEI layer after 50 cycles at a fully charged state. Obviously, most IO@void@TNPs showed a similar morphology to the as-prepared IO@void@TNPs shown in Figure 6.5d and Figure 6.7. Moreover, the yolk-shell structures of iron oxide cores and titania shells within the IO@void@TNPs was well maintained as shown in Figure 6.14a and 6.14b, and the size of the IONPs in Figure 6.14b was similar to that of the as-prepared IO@void@TNPs with no significant agglomeration, which demonstrated the stability of these structures during the lithiation and delithiation processes.

To further investigate the effects of a structure with a core@void@shell configuration on electrochemical properties, a cell test of the IO@void@TNPs and IONPs was performed at the elevated operating temperature of 80 °C. Figure 6.15a presents the cycling performance of IO@void@TNPs and IONPs measured at the operating temperatures of 25 and 80 °C at a current density of 0.5 A/g for 50 cycles. Except for the interval from 3rd to 6th cycle and the last few cycles, the capacity of the IONPs at 80 °C was higher than that at 25 °C since the Li ion diffusivity in the electrolyte increased and the cell resistance decreased with the increased cell temperature.[39,40] However, the cyclability of IONPs at 80 °C was quite unstable over the entire cycle, including the large initial fluctuation, which was commonly observed in other cells in that condition. This feature may have resulted from the harsh operating temperature condition compared to the reported results from other groups (usually at 60 °C).[20,40] However, high cycle stability of IO@void@TNPs was obtained at both 25 and 80 °C, and a 100 mAh/g higher capacity was obtained for the IO@void@TNPs at 80 °C.

`

These results were in good agreement with the effects of both the perfect separation of IONPs and adequate void space to obtain the high capacity retention as shown in Figure 6.12d. In addition, the effects were more obviously demonstrated when the operating temperature was increased to the harsh condition of 80 °C. The coulombic efficiencies of the IO@void@TNPs increased steadily after several cycles and reached 97.8% and 95.8% when operated at 25 and 80 °C, respectively. In contrast, the coulombic efficiency of the IONPs was considerably fluctuated over the whole cycle. Clearly, the coulombic efficiency of the IONPs at 80 °C repeated up and down from the 1st to the 50th cycle, as shown in Figure 6.15b and the inset plot enlarged after the 30th cycle, indicating their lower stability of IONPs compared to that of the IO@void@TNPs. In addition to the cyclability shown in Figure 7a, the discharge-charge galvanostatic profiles of the IO@void@TNPs and IONPs at 80 °C are presented in Figure 6.15c and 6.15d. The charge capacity of the IO@void@TNPs achieved a stable state after the 15th cycle, maintaining it until 50th cycle, whereas that of the IONPs decreased very fast during the whole cycle.

In order to interpret the capacity increment of the IO@void@TNPs at 80 °C as being an effect of the shells and void spaces, the 50th cycle charge capacities of the IO@void@TNPs and the IONPs operated both at 25 and at 80 °C were examined in more detail. The 50th cycle charge capacity at 25 °C and the charge capacity difference between 25 and 80 °C on the 50th cycle are presented in Figure 6.16. According to the bar graph exhibited in Figure 6.16, an increase of approximately 100 mAh/g was observed in the 50th cycle charge capacity for the IO@void@TNPs at 80 °C compared to that at 25 °C, whereas in the 50th cycle, the charge capacity of IONPs at 80 °C was similar to that at 25 °C (it actually decreased about 1 mAh/g). Moreover, the capacity

`

at 80 °C of the IO@void@TNPs was about 33% higher than the capacity at 25 °C, which indicated that a considerable amount of improvement was observed in the 50th cycle charge capacity at 80 °C without any capacity loss, in contrast to IONPs, and the yolk-shell structure had an advantage under the harsh operating condition of 80 °C.

Therefore, these results imply that the core@void@shell configuration contributed significantly to capacity retention, and the effects of encapsulation of IONPs in titania shells with adequate void spaces between IONPs were manifested under the harsh operating condition.

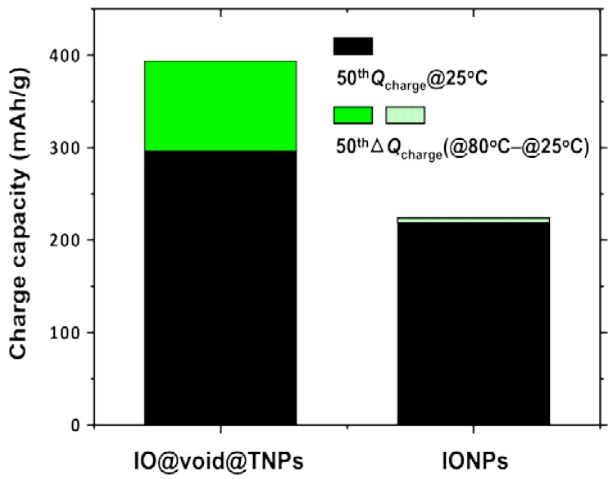

Figure 6.16. The 50th cycle charge capacity at 25 °C and the 50th cycle charge capacity difference between 80 °C and 25 °C for IO@void@TNPs and IONPs, respectively.

`

6.4 Conclusions

IO@void@TNPs were successfully prepared by a simple soft template method. After calcination, the yolk-shell structures composed of iron oxide cores, voids, and titania shells were confirmed by TEM, XRD, nitrogen adsorption/desorption analysis, etc. The excellent cycle stability of the IO@void@TNPs, compared to only IONPs and simply mixed nanoparticles of iron oxide and hollow titania, emphasized the core@void@shell structural effect due to the perfect separation between IONPs with the stable titania shells providing internal void spaces. The effect was more remarkable under the harsh condition of an elevated cell operating temperature of 80 °C than at the normal cell condition of 25 °C**.**

6.5 Experimental Section

Materials and Instruments Titanium tetrabutoxide, poly(acrylic acid) (PAA, MW 1,800), anhydrous ethanol, acetonitrile, absolute acetonitrile, ferric chloride hexahydrate, and glycidol were purchased from Aldrich. Absolute ethanol was prepared from J.T. Baker. Ammonia solution (29 % in water), ethylene glycol, ethanol, and sodium acetate were purchased from Samchun and deionized (DI) water purified by a Milli-Q purification system was used for all of the experiments. All solvents and reagents used in this study were commercially available and used as received.

The weights of the IONP cores and titania shells were confirmed by using inductively coupled plasma atomic emission spectrometry (ICP-AES, Optima-4300 DV) installed at the National Center for Inter-university Research Facilities (NCIRF) at Seoul National University. The sizes and morphologies of products were analyzed by using field-emission scanning electron microscopy (FE-SEM, Hitachi S-4300, 4.2 kV) and transmission electron

`

microscopy (TEM, Hitachi-7600, 100 kV). More detailed images and information about the atomic distributions in IO@void@TNPs were obtained using TEM with a higher accelerating voltage (JEM-2100F, JEOL, 200 kV) and an energy dispersive spectroscopy (EDS) system. Thermogravimetric analysis (TGA) was performed using an SDT Q600 (TA Instruments Inc.) to confirm the extraction of the PAA cores. The samples for TGA were preheated at 100 °C for 30 min and then the temperature was raised to 800 °C at 10 °C/min in nitrogen. The crystallinity of the samples was evaluated by powder X-ray diffraction (XRD) analysis on a Bruker New D8 Advanced Diffractometer with Cu K radiation (λ = 1.5418 Å). The scanning rate was 0.02 ° per second and the range was from 10 to 70 °. The surface areas and porosities of the products were measured using the nitrogen adsorption-desorption isotherm and Barrett-Joyner-Halenda (BJH) methods on a Micromeritics ASAP 2420.

Hollow Titania Nanoparticles PAA (2.0 g) was dissolved in 20 mL of ammonia solution. An aliquot of 4 mL of this solution was injected into a mixture of absolute ethanol and acetonitrile (1:1 v/v, V_{tot} = 400 mL) with vigorous mechanical stirring and white colloids were formed. Titanium butoxide (1.5 mL) was diluted with a mixture of absolute ethanol and acetonitrile (1:1 v/v, V_{tot} = 60 mL) and poured into the PAA colloids. This turned the milky colloids into PAA/titania core/shell particles, and after a reaction for 2 h, the products were purified and washed with water and ethanol using centrifugation/re-dispersion (17,000 rpm, 10 min, 3 repetitions), and hollow titania nanoparticles were obtained. The white product was well dried at room temperature overnight, followed by annealing at 500 °C in air for 2 h.

`

IONPs IONPs with an average size of 40 nm were prepared according to a previously published procedure.[25] $FeCl_3 \cdot 6H_2O$ (15.0 g) was dissolved in 750 mL of ethylene glycol and 100.0 g of sodium acetate was completely dissolved in a mixed solvent of water (100 mL) and ethylene glycol (750 mL). Then, the two solutions were mixed with vigorous mechanical stirring to form a turbid yellow-brown solution. The solution was stirred at 70 °C for 1 h and then refluxed for 24 h. After cooling to room temperature, the black sediment was purified by centrifugation and re-dispersed in ethanol three times to collect the IONP products. These IONPs, which were prepared for use as simply mixed anodes with hollow titania nanoparticles, were annealed at 500 °C in air for 2 h.

Surface Modification of IONPs with Polyglycidol Polyglycidol (PG) was grafted onto IONPs by using a method similar to that of a previously reported paper.[26] IONPs (200 mg) were dispersed in 15 mL of glycidol and the mixture was allowed to react at 140 °C for 6 h. After the reaction, the mixture was cooled to room temperature and 10 mL of DI water was added to dissolve the sticky product. Then, an excess amount of acetone was added until aggregates formed in the solution. The aggregates were centrifuged and re-dispersed in ethanol. Centrifugation and re-dispersion were repeated thrice to remove the free PG, which was not grafted onto the surfaces of the IONPs.

IO@void@TNPs The synthetic method used for the hollow titania nanoparticles was also used to prepare the IO@void@TNPs, except for using PG grafted IONPs. Prepared PG grafted IONPs were dispersed in 20 mL of ammonia solution containing 2.0 g of PAA. An aliquot of 4 mL of this solution was injected into a mixture of absolute ethanol and acetonitrile (1:1 v/v, V_{tot} = 400 mL) with vigorous mechanical stirring and dark colloids were formed. Titanium butoxide (1.5 mL) was diluted in a mixture of absolute

`

ethanol and acetonitrile (1:1 v/v, V_{tot} = 60 mL) and poured into the dark colloids of the PG grafted IONPs/PAA. After 2 h, much darker aggregates were collected by a magnet to remove any hollow titania nanoparticles that did not contain IONPs. The selected IO@void@TNPs were purified and washed with water and ethanol using centrifugation/re-dispersion (17,000 rpm, 10 min, 3 repetitions). The dark product was well dried at room temperature overnight, followed by annealing at 500 °C in air for 2 h.

Electrochemical Test Working electrodes were fabricated by mixing the anode materials synthesized for this study, Super P as a conductive agent, and PVDF as a binder at a weight ratio of 70:15:15 in N-methyl-2-pyrrolidone (NMP) solvent. The mixed slurry was uniformly plastered onto a copper foil current collector *via* doctor blade processing. The electrodes were dried under vacuum at 120 °C overnight and then pressed. A 2032 type coin cell consisting of a working electrode and lithium metal as a counter and reference electrode was assembled in a glove box under a dry argon atmosphere. The organic electrolyte was 1.0 M $LiPF_6$ dissolved in a mixture of ethylene carbonate (EC) and diethyl carbonate (DEC) with a volume ratio of 1:1. Galvanostatic testing (WBCS3000 cycler, WonA Tech, Korea) was carried out on the coin cell over the voltage range of 3.0 to 0.01 V (vs. Li+/Li) at room temperature (25 °C) and an elevated temperature (80 °C).

*** Contributions**

Synthesis of iron oxide nanoparticle was done with Jihoon Ahn in Department of Chemistry, Seoul National University. Electrochemical properties were tested with Ji Hyun Um and Prof. Yung-Eun Sung in School of Chemical & Biological Engineering, Seoul National University.

`

6.6 References

[1] Poizot, P.; Laruelle, S.; Grugeon, S.; Dupont, L.; Tarascon, J. M., *Nature* **2000**, *407*, 496-499.

[2] Lee, S. H.; Yu, S. H.; Lee, J. E.; Jin, A.; Lee, D. J.; Lee, N.; Jo, H.; Shin, K.; Ahn, T. Y.; Kim, Y. W.; Choe, H.; Sung, Y. -E.; Hyeon, T., *Nano Lett* **2013**, *13*, 4249-4256.

[3] Kim, J.; Chung, M. K.; Ka, B. H.; Ku, J. H.; Park, S.; Ryu, J.; Oh, S. M., *J. Electrochem. Soc.* **2010**, *157*, A412-A417.

[4] Ji, L.; Lin, Z.; Alcoutlabi, M.; Zhang, X., *Energy Environ. Sci.* **2011**, *4*, 2682-2699.

[5] Reddy, M. V.; Subba Rao, G. V.; Chowdari, B. V., *Chem. Rev.* **2013**, *113*, 5364-5457.

[6] Zhang, W.-M.; Wu, X.-L.; Hu, J.-S.; Guo, Y.-G.; Wan, L.-J., *Adv. Funct. Mater.* **2008**, *18*, 3941-3946.

[7] Lee, J. E.; Yu, S.-H.; Lee, D. J.; Lee, D.-C.; Han, S. I.; Sung, Y.-E.; Hyeon, T., *Energy Environ. Sci.* **2012**, *5*, 9528-9533.

[8] Zhang, L.; Wu, H. B.; Lou, X. W. D., *Adv. Energy Mater.* **2014**, *4*, 1300958.

[9] Yuan, C.; Wu, H. B.; Xie, Y.; Lou, X. W., *Angew. Chem. Int. Ed.* **2014**, *53*, 1488-1504.

[10] Wu, Y.; Zhu, P.; Reddy, M. V.; Chowdari, B. V. R.; Ramakrishna, S., *ACS Appl. Mater. Interfaces* **2014**, *6*, 1951-1958.

[11] Kim, J.-K.; Aguilera, L.; Croce, F.; Ahn, J.-H., *J. Mater. Chem. A* **2014**, *2*, 3551-3556.

[12] Osiak, M.; Geaney, H.; Armstrong, E.; O'Dwyer, C., *J. Mater. Chem. A* **2014**, *2*, 9433-9460.

[13] Li, Y.; Fu, Z.-Y.; Su, B.-L., *Adv. Funct. Mater.* **2012**, *22*, 4634-4667.

`

[14] Wang, Z.; Zhou, L.; Lou, X. W., *Adv. Mater.* **2012**, *24*, 1903-1911.

[15] Luo, Y.; Luo, J.; Jiang, J.; Zhou, W.; Yang, H.; Qi, X.; Zhang, H.; Fan, H. J.; Yu, D. Y. W.; Li, C. M.; Yu, T., *Energy Environ. Sci.* **2012**, *5*, 6559-6566.

[16] Yu, L.; Wang, Z.; Zhang, L.; Wu, H. B.; Lou, X. W., *J. Mater. Chem. A* **2013**, *1*, 122-127.

[17] Liu, J.; Qiao, S. Z.; Chen, J. S.; Lou, X. W.; Xing, X.; Lu, G. Q., *Chem. Commun.* **2011**, *47*, 12578-12591.

[18] Hong, Y. J.; Son, M. Y.; Kang, Y. C., *Adv. Mater.* **2013**, *25*, 2279-2283.

[19] Son, M. Y.; Hong, Y. J.; Lee, J.-K.; Chan Kang, Y., *Nanoscale* **2013**, *5*, 11592-11597.

[20] Choi, S. H.; Kang, Y. C., *ACS Appl. Mater. Interfaces* **2014**, *6*, 2312-2316.

[21] Liu, N.; Lu, Z.; Zhao, J.; McDowell, M. T.; Lee, H. W.; Zhao, W.; Cui, Y., *Nat. Nanotechnol.* **2014**, *9*, 187-192.

[22] Wei Seh, Z.; Li, W.; Cha, J. J.; Zheng, G.; Yang, Y.; McDowell, M. T.; Hsu, P.-C.; Cui, Y., *Nat. Commun.* **2013**, *4*, 1331-1336.

[23] Liu, J.; Xu, J.; Che, R.; Chen, H.; Liu, M.; Liu, Z., *Chem. Eur. J.* **2013**, *19*, 6746-6752.

[24] Wan, Y.; Yu, S.-H., *J. Phys. Chem. C* **2008**, *112*, 3641-3647.

[25] Cha, J.; Lee, J. S.; Yoon, S. J.; Kim, Y. K.; Lee, J.-K., *RSC Adv.* **2013**, *3*, 3631-3637.

[26] Zhao, L.; Chano, T.; Morikawa, S.; Saito, Y.; Shiino, A.; Shimizu, S.; Maeda, T.; Irie, T.; Aonuma, S.; Okabe, H.; Kimura, T.; Inubushi, T.; Komatsu, N., *Adv. Funct. Mater.* **2012**, *22*, 5107-5117.

[27] Lou, X. W.; Archer, L. A.; Yang, Z., *Adv. Mater.* **2008**, *20*, 3987-4019.

[28] Froschl, T.; Hormann, U.; Kubiak, P.; Kucerova, G.; Pfanzelt, M.; Weiss, C. K.; Behm, R. J.; Husing, N.; Kaiser, U.; Landfester, K.; Wohlfahrt-Mehrens, M., *Chem. Soc. Rev.* **2012**, *41*, 5313-5360.

`

[29] Sing, K. S. W., *Pure Appl. Chem.* **1985**, *57*, 603-619.

[30] Sasidharan, M.; Nakashima, K.; Gunawardhana, N.; Yokoi, T.; Inoue, M.; Yusa, S.-i.; Yoshio, M.; Tatsumi, T., *Chem. Commun.* **2011**, *47*, 6921-6923.

[31] Hang, B. T.; Doi, T.; Okada, S.; Yamaki, J.-i., *J. Power Sources* **2007**, *174*, 493-500.

[32] Liu, S.; Zhang, L.; Zhou, J.; Xiang, J.; Sun, J.; Guan, J., *Chem. Mater.* **2008**, *20*, 3623-3628.

[33] Chen, M.; Li, W.; Shen, X.; Diao, G., *ACS Appl. Mater. Interfaces* **2014,** *6*, 4514-4523.

[34] Wang, B.; Chen, J. S.; Wu, H. B.; Wang, Z.; Lou, X. W., *J. Am. Chem. Soc.* **2011**, *133*, 17146-17148.

[35] Wang, Z.; Luan, D.; Madhavi, S.; Hu, Y.; Lou, X. W., *Energy Environ. Sci.* **2012**, *5*, 5252-5256.

[36] Su, X.; Wu, Q.; Zhan, X.; Wu, J.; Wei, S.; Guo, Z., *J. Mater. Sci.* **2012**, *47*, 2519-2534.

[37] Deng, D.; Kim, M. G.; Lee, J. Y.; Cho, J., *Energy Environ. Sci.* **2009**, *2*, 818-837.

[38] Li, X.; Qiao, L.; Li, D.; Wang, X.; Xie, W.; He, D., *J. Mater. Chem. A* **2013**, *1*, 6400-6406.

[39] Masarapu, C.; Zeng, H. F.; Hung, K. H.; Wei, B., *ACS Nano* **2009**, *3*, 2199-2206.

[40] Hou, X.; Wang, X.; Liu, B.; Wang, Q.; Wang, Z.; Chen, D.; Shen, G., *ChemElectroChem* **2014**, *1*, 108-115.

`

Appendix/Chapter 1.

Precise Size-control of Silica Nanoparticles *via* Alkoxy Exchange Equilibrium of Tetraethyl Orthosilicate in the Mixed Alcohol Solution

Published as *Bull. Korean Chem. Soc.* **2012**, *33*, 1067-1070.

1.1 Abstract

Even though silica nanoparticles (SNPs) have been synthesized and used in various fields such as bioimaging, drug- and gene-delivery, and composite polymers, a solvent effect during the well-known Stöber method of hydrolysis-and-condensation of tetraethyl orthosilicate (TEOS) is not completely understood yet. It could be possible to control the size of silica nanoparticles in the range from 20 nm to few hundred nm by simple changes of solvent ratio and all the resulted SNPs was characterized by Transmission Electron Microscopy (TEM), and Field-Emission Scanning Electron Microscopy (FE-SEM). An alkoxy exchange reaction of TEOS in alcoholic solution seemed to play the major role of size control, and the several intermediates were characterized by GC-MS. In this chapter, the mechanistic understandings of the relationship between solvent ratio and size of SNPs will be discussed.

`

1.2 Introduction

SNPs are one of the most interesting materials with regard to their easy preparation, nontoxicity, and simple surface modification. Based on their various advantages, SNPs have been widely studied and used in various fields such as solid support materials in the column chromatography,[1] insulating layer and silica-polymer composite[2] in engineering fields, and bio-imaging and drug/gene delivery systems in nano-biotechnology.[3-5] To make SNP work effectively in all these applications, it is necessary to synthesize size-controllable and mono-dispersed silica particles. Since Stöber showed that spherical silica particles having narrow size distribution could be prepared from TEOS as silica source in alcohol solvent with water and aqueous ammonia as catalyst,[6] his method has been used and modified to prepare mono-dispersed and regular sized SNPs.[7] The size control of SNPs was possible by varying the concentration of reactants, the chain length of alkyl group in alcohol solvents and silica sources, base catalysts to primary amine instead of ammonia solution.[8] It was also reported that the usage of amino acids and the control of the mixing ratio of their optical isomers could change the size of SNPs.[9]

Although it is known that the basic formation mechanism of SNPs is the hydrolysis-and-condensation of TEOS, interestingly, the role of solvent during the formation of SNPs has not been systematically investigated yet. When alcohols with long alkyl chains were used as solvent, the size of SNPs was increased due to the different hydrolysis-and-condensation rate to generate seeds. As an example, it was reported that the different sized SNPs were synthesized in methanol (4 nm) and ethanol (8 nm) because the supersaturation ratio of the hydrolyzed silica sources in methanol was higher than that in ethanol.[10] In other words, many smaller seeds were generated in

`

fast reaction environment in methanol and could grow to produce many smaller SNPs compared to those produced in ethanol. The reason of different reaction rates in different solvents was mainly described as the consequence of the changes of polarity, degree of hydrogen bond, and viscosity;[11] the solvent having a low polarity, low hydrogen bonding ability, and high viscosity could retard the formation of seed leading to increase the final size of SNPs. It was also reported that silica sources with the long or bulky alkoxy groups resulted to generate the large sized SNPs due to the steric effect which decrease the rate of hydrolysis.[11] On the other hand, it was well known in silicon chemistry that the alkoxy groups of silicon compounds could be exchanged in alcohol solution, especially in the presence of acid or base catalysts, and the rate of hydrolysis and condensation reactions were also affected by the character of alkoxy groups.[12-14] Therefore, we investigated the alkoxy exchange reactions in the conditions where SNPs were usually synthesized and found a new factor to give simpler and more precise control over their size than conventional methods.

`

1.3 Results and Discussion

SNPs were prepared by the modified Stöber method; 0.6 mL of TEOS was hydrolysed and condensed to give SNPs in various mixed alcohol solutions with a basic catalyst of ammonia solution (1 mL of water and 3 mL of 30 % NH_4OH in 50 mL of total alcoholic solution). When the relative volume ratio of methanol:ethanol was varied as 10:0, 8:1, 4:1, 2;1, 1:1, and 0:10 while all the other factors were fixed, the size of produced SNPs increased from 20 to 300 nm as shown in Figure 1.1. The changes of the size of SNPs in the mixed alcohol solvent might come from the average effect of polarity, hydrogen bonding and viscosity of two alcohols as suggested in earlier reports, but the trend was not lineally related with the mixing ratios of two alcohols. Therefore we speculated the effect of alkoxy exchange of silica sources and deliberately designed the reactions of TEOS in the mixed alcohol solvents; it was important to analyse the early state of silica sources because the generation of seeds or nuclei was expected to be the key event to become nanoparticles.[15]

`

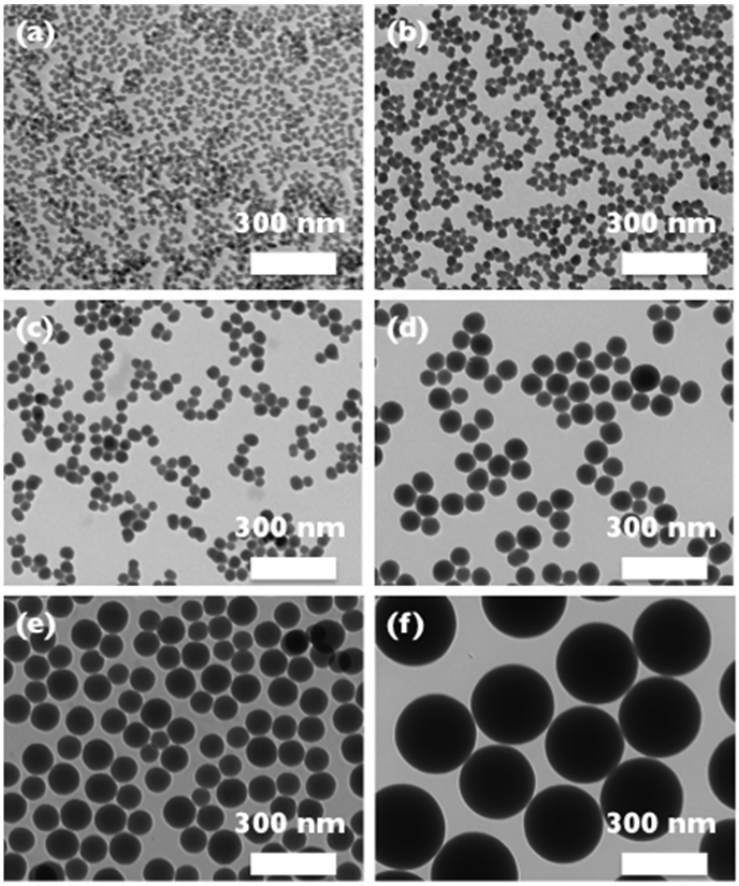

Figure 1.1. TEM images of SNPs prepared in the mixtures of methanol:ethanol (v/v); (a) 10:0, (b) 8:1, (c) 4:1, (d) 2:1, (e) 1:1, and (f) 0:10.

First, the early stage of the reaction was monitored by GC to understand the change of TEOS in a mild basic condition (20 μL of 30 % NH_4OH in 50 mL of total methanol solution); a small amount (1/150 times) of the base catalyst compared to the normal synthetic condition of SNPs was used to slow down the hydrolysis-and-condensation reaction. After treating with the diluted ammonia solution for 4 hr, TEOS in methanol changed to other compounds and these generated compounds were confirmed by GC (Figure. 1.2).

`

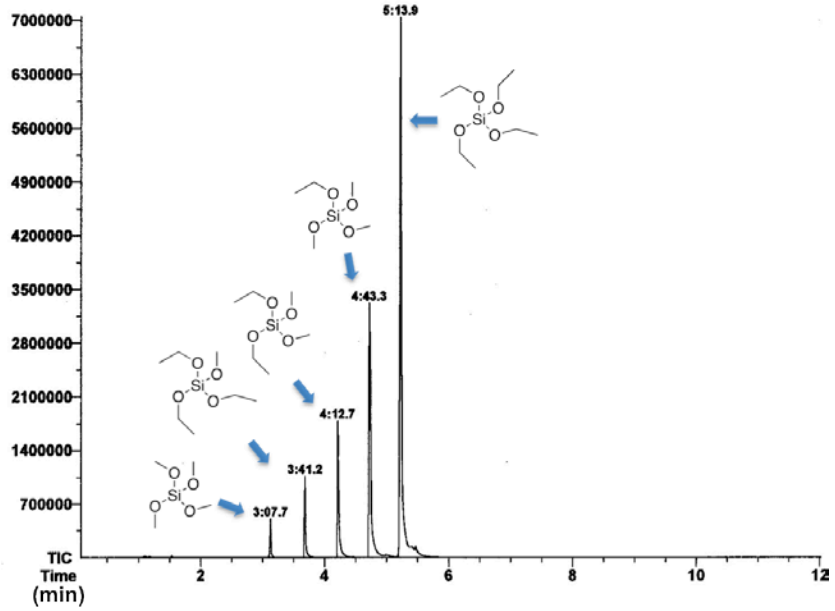

Figure 1.2. GC analysis of TEOS in methanol after stirring in the mild basic condition for 4 hr.

Based on the results of GC-MS analyses (see GC-MS data of the Experimental Section), these compounds were assigned as the methoxy exchanged TEOS with different numbers of the methoxy group from 0 to 4; $Si(OEt)_{4-n}(OMe)_n$. In order to trace the behavior of TEOS in more detail with time, further GC analyses at various times were tried and the change of TEOS was detected (Figure. 1.3). However the exchange rate to generate $Si(OEt)_{4-n}(OMe)_n$ did not show any significant changes and quantitative analysis was very complicated due to the characteristic reactivity of TEOS in basic condition; alkoxy exchange reaction always competed with hydrolysis reaction which went further to burst condensation. It was known that, with acidic catalyst, the hydrolysis rate of TEOS was relatively fast but the condensation rate was relatively slow, and the ultimately generated product

`

was not in a particle shape but generally in amorphous gel because a dense condensation could not occur.[12,16] Therefore, when an acid catalyst was employed, the fast alkoxy exchange and retarded hydrolysis-and-condensation could make it possible to monitor silicon species at the early stage of the reaction in the mixed alcohol solvent systems. Even though acidic catalyst condition is not the real reaction condition for preparing SNPs, we expect that it is possible to monitor the relative amounts of alkoxy exchanged products with time and to explain the size control of SNPs in different mixed alcohol solvent systems.

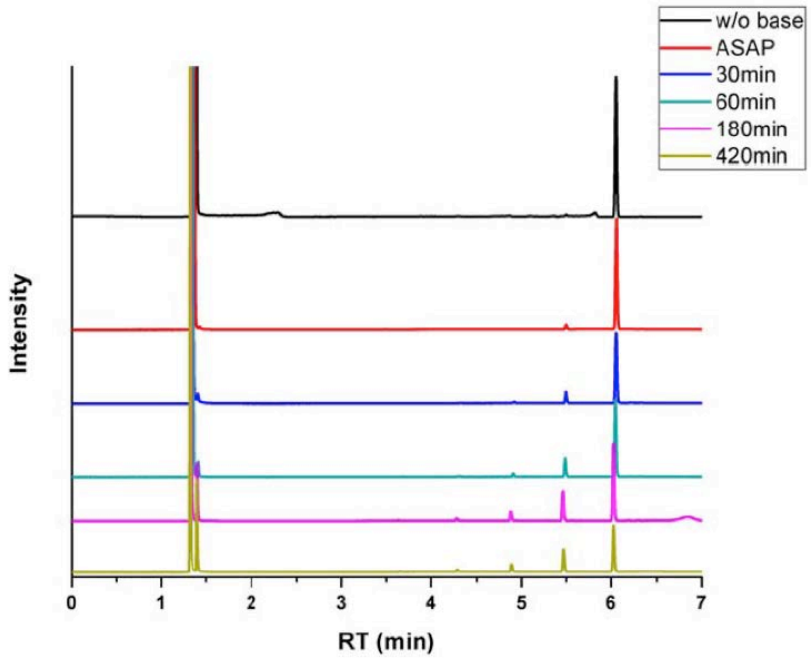

Figure 1.3. GC analysis of TEOS in methanol; before and after the addition of the base catalyst.

`

The exchange reaction of TEOS in methanol with a diluted hydrochloric acid as a catalyst was monitored and the generated silicon compounds were confirmed as exactly same as those from the basic condition (see GC-MS data of the Experimental Section). This experiment was carried out with a very small amount of acid (1/100 times) and within a short period of time (few minutes) compared to the case of basic condition shown in Figure 1.2. Therefore the detailed GC analyses of TEOS in methanol with the acid catalyst could be performed with time intervals and same peaks were observed as those from the basic condition in Figure 1.2 with slight differences of peak intensities (Figure. 1.4). When TEOS in methanol was characterized by GC, only two peaks of methanol solvent (1.3 min) and TEOS itself (6.0 min) were observed without the acid catalyst. With the acid catalyst, however, the intensity of TEOS peak was reduced and other new peaks appeared with time. Just after the addition of the acid catalyst, a new peak at 5.4 min at the left side of TEOS was detected, that was confirmed to have one methoxy group and three ethoxy groups by separated GC-MS experiment. With time, ethoxy groups in TEOS were sequentially changed to methoxy groups to show new peaks at 4.9, 4.3, and 3.6 min. All five peaks were clearly observed from the sample after 5 min of acid treatment, and the relative intensities were shifted towards the tetramethyl orthosilicate (TMOS) peak at 3.6 as time passed. Unlike to the case with the base catalyst, owing to the decreased speed of the hydrolysis-and-condensation reaction to generate Si-O-Si siloxane linkage, those mixed alkoxy silicon compounds, $Si(OEt)_{4-n}(OMe)_n$, generated by fast alkoxy exchange reaction could have a reasonable stability showing the accumulated species during the reaction. However, all those silicon species eventually reacted with water to form silica and no significant amounts of them were left after 60 min. Most of the hydrolysed compounds

`

and condensed oligomeric products were not observed in GC experiments probably due to the adsorption in the column because of their strong interaction through the polar Si-OH bonds. During the alkoxy exchange reaction from TEOS to TMOS, ethanol was generated but its retention time was so close to that of methanol in GC condition that these peaks were hard to be clearly distinguished.

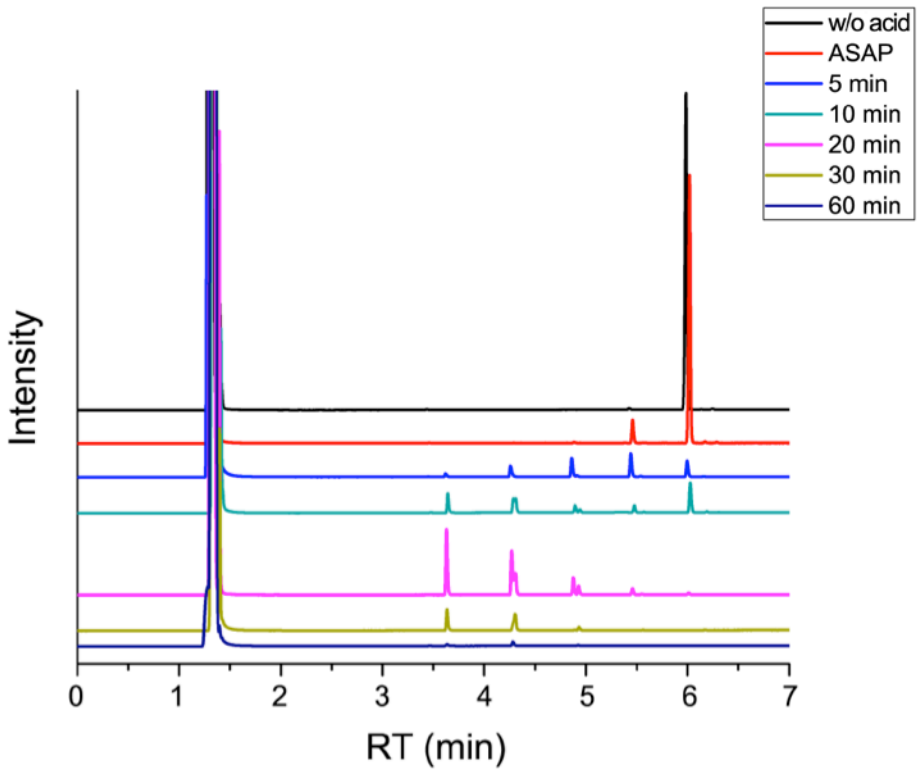

Figure 1.4. GC analysis of TEOS in methanol; before and after the addition of the acid catalyst.

`

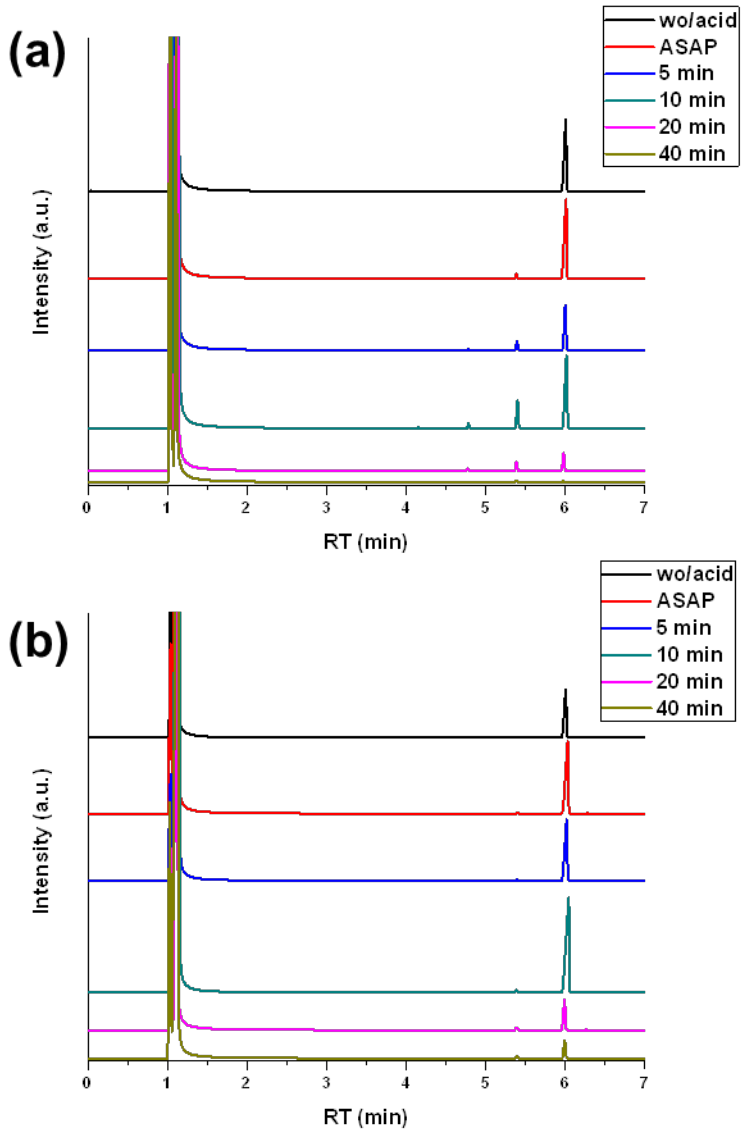

Figure 1.5. GC analysis of TEOS with the acid catalyst in the mixing ratio of methanol and ethanol; (a) 1:1 and (b) 1:9.

`

Based on the GC analyses, more than one silica source could exist in the methanol solution of TEOS with a catalyst while only TEOS peak was detected from the solution of TEOS in ethanol (result was not shown), corroborating that the reactivity difference of silica sources could have a relationship with the size of generated SNPs. The relative amounts of mixed alkoxy silicon compounds, $Si(OEt)_{4-n}(OMe)_n$, generated by a fast alkoxy exchange reaction at the different mixing ratio of methanol:ethanol (1:1 and 1:9) were monitored by GC in the acidic catalyst condition (Figure. 1.5). As expected, the methoxy exchange rate of TEOS was decreased when the ratio of ethanol in the mixed alcohol solution was increased. Therefore, the size of SNPs synthesized in the mixed alcohol solvent seemed to be determined by the effect of alkoxy exchange of TEOS and the averaged reactivity of generated silicon species in the early stage of the hydrolysis-and-condensation reaction.

The effect of alkoxy exchange reaction of TEOS in the early stage of the hydrolysis-and-condensation reaction can be simply explained as follows:

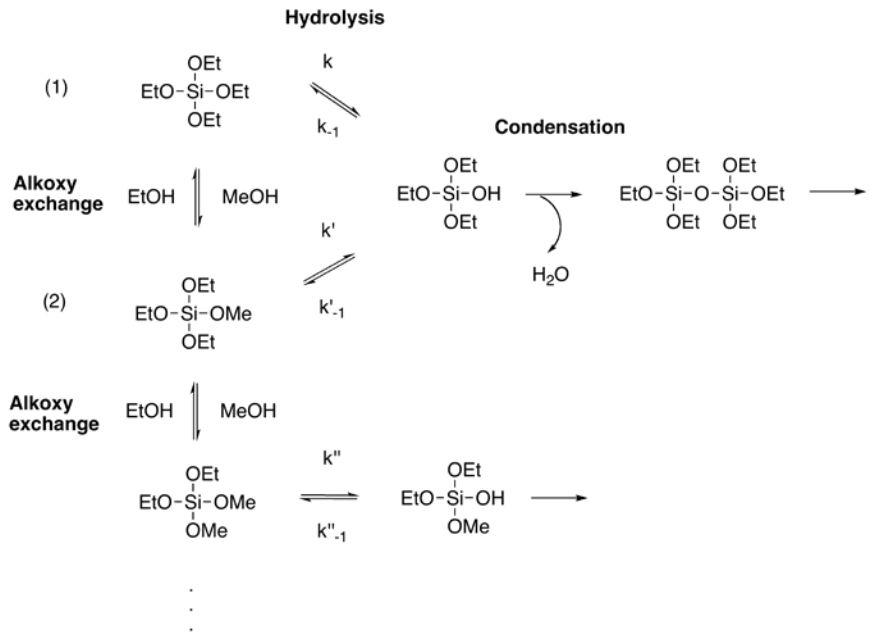

`

For the reaction of TEOS in ethanol, normal hydrolysis and condensation occurs as a major reaction route. When methanol exists as a co-solvent, the methoxy exchange reaction can compete to hydrolysis so some portion of TEOS is changed to $Si(OEt)_3(OMe)$. Since the hydrolysis rate constant of TMOS is known to be more than four times faster than TEOS,[17] this methoxy-exchanged silicon compound can also participate in hydrolysis and the hydrolysis rate of $Si(OEt)_3(OMe)$ should be faster than that of TEOS (k'>k).

Therefore, the more methoxy groups are exchanged on the Si site, the faster hydrolysis occurs, and the faster supersaturation point is reached starting to form seeds for SNPs; many small seeds are generated at the fast reaction environment in methanol and they can grow to generate many small sized SNPs compared to those from the ethanol solution.

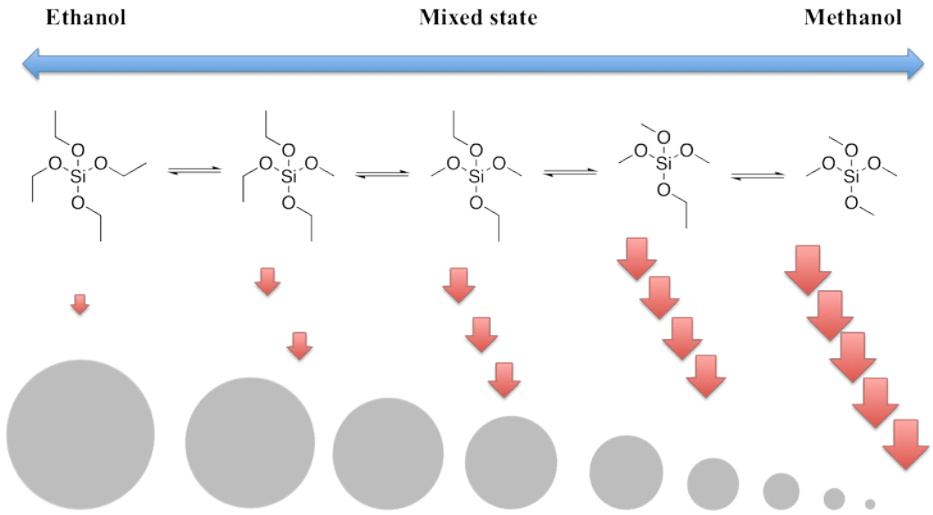

Figure 1.6. Schematic illustration of the size control of SNPs by generating various silicon compounds by alkoxy exchange equilibrium with different mixing ratios of solvents.

`

From the sizes of prepared SNPs when the mixed alcohol solvent was used (Figure. 1.1), the more methanol was mixed, the more reactive silicon compounds were formed, the faster hydrolysis-and-condensation occurred, and ultimately, the smaller SNPs was produced as illustrated in Figure 1.6. As an extension of the idea to control the size of SNPs by the alkoxy exchange equilibrium, 1-propanol having the longer alkyl chain compared to methanol was mixed with ethanol. However, all the SNPs prepared from ethanol, 1-propanol, and the 1:1 mixture of ethanol and 1-propanol showed almost same sizes and no dependency on the solvent ratio (Figure. 1.7). It was pretty similar to the result recently reported by Kang *et al*.; the solvent mixtures of ethanol and 1-butanol with different volume ratios did not actually change the size of SNPs.[18] These results might come from the concentration of TEOS and ammonia, which were already high enough to produce large size SNPs in the presence of ethanol. Therefore another condition to generate smaller size SNPs in ethanol was selected by decreasing the amount of the base catalyst. At this reaction condition, the size of SNPs was precisely controlled by the alkoxy exchange equilibrium. As shown in Figure 1.8, the size of SNPs was increased from 80 to 100, and finally to 200 nm when the volume ratio of ethanol and 1-propanol was varied from 10:0, 5:5, and 0:10, respectively.

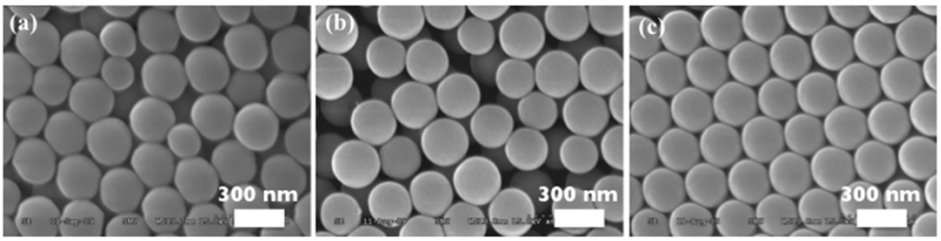

Figure 1.7. SEM image of SNPs prepared in (a) ethanol, (b) the mixed ratio of ethanol: 1-propanol, and (c) 1-propanol.

`

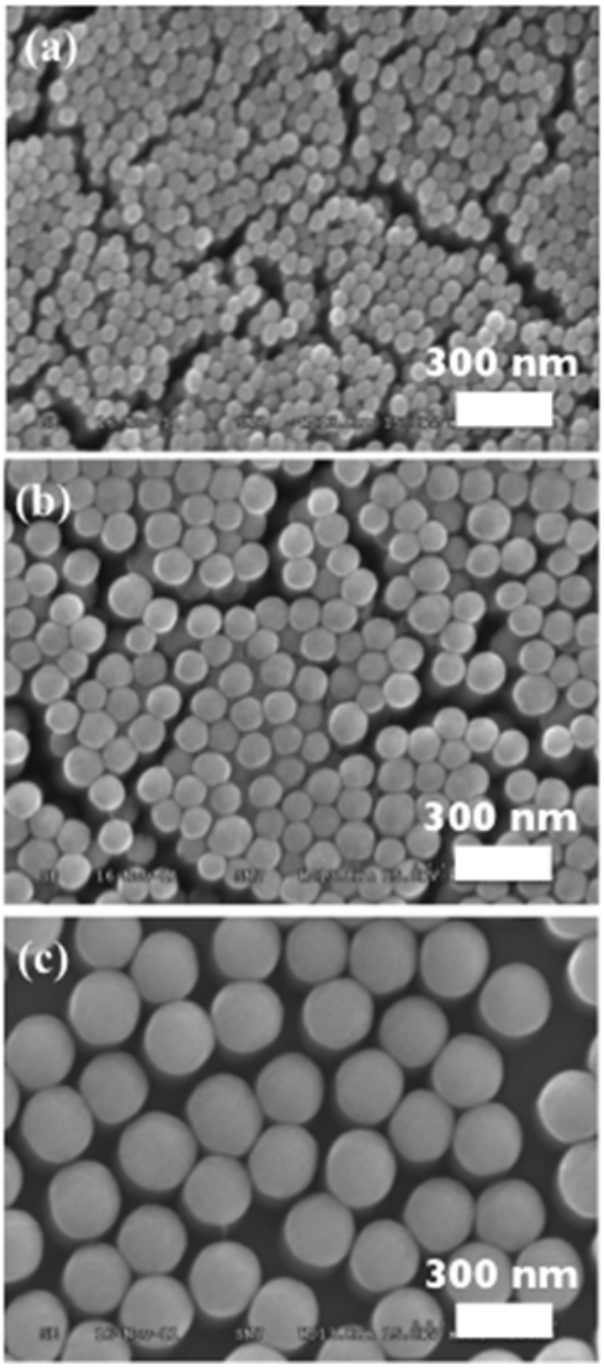

Figure 1.8. SEM images of SNPs synthesized from (a) ethanol, (b) the 1:1 mixture of ethanol:1-propanol, and (c) 1-propanol.

`

1.5 Conclusions

The solvent effect on the synthesis of SNPs were investigated and concluded that the fast equilibrium of alkoxy exchange at the early stage of the hydrolysis-and-condensation reaction of TEOS was very critical to determine the size of the resulted SNPs. From the deliberately designed GC and GC-MS experiments, it would be observed that the larger amount of alcohol having a short alkyl chain was employed, the more reactive silicon compound was generated. As the result, the rate of hydrolysis-and-condensation was increased to produce many small sized SNPs. Based on our finding of solvent effect, the size of produced SNPs could be precisely tuned in the ranges from 20 to 300 nm by simply varying the relative volume ratio of methanol:ethanol while all the other factors were fixed.

1.6 Experimental Section

Materials and Characterizations Methanol, ethanol, 1-propanol, ammonia solution, and hydrochloric acid were purchased from Samchun (Korea) and 99% ethanol was purchased from J.T. Baker. Tetraethyl orthosilicate (TEOS) was purchased from TCI and all solvent was used without any purification.
TEM and FE-SEM images were acquired using Hitachi-7600 (Hitachi) and Hitachi S-4300 (Hitachi) instruments, respectively. Gas chromatography (GC) analyses of TEOS in alcohol solvents were carried out by using Acme-3000 (Young Lin) and Gas Chromatography-Mass Spectrometry (GC-MS) used to analyze silicon compounds was JMS-600W (JEOL).

Synthesis of SNPs in the mixed alcohol solutions SNPs were synthesized from the condition of 0.6 mL of TEOS, 3 mL of ammonia, and 1 mL of water in the mixed alcohol solvent (methanol and ethanol, total volume was

`

maintained to be 50 mL). In case of using ethanol and 1-propanol, SNPs were synthesized from the condition of 0.6 mL of TEOS, 2 mL of ammonia in the mixed alcohol solvent (99% ethanol and 1-propanol, total volume was maintained to be 50 mL). The reaction mixture was stirred at the speed of 400 rpm for 12 h at room temperature. The SNP products were washed three times with ethanol by the centrifugation-redispersion at 15,000 rpm.

GC analyses The injection temperature was 200 °C and the detection temperature was 250 °C. The column temperature was programmed as the initial temperature (30 °C) was hold for 1 min., and increased to 75 °C by the speed of 30 °C/min, and finally increased to 150 °C by the speed of 10 °C/min. GC samples in the acid catalyst were prepared by adding 2.44 μmol of hydrochloric acid to 0.45 mmol of TEOS dissolved in 47 mmol of methanol, and samples in the base catalyst were prepared with the same composition except using 0.29 mmol of ammonia solution.

`

GC-MS data of TEOS

t: JEOL JMS600 Ionization mode: EI+

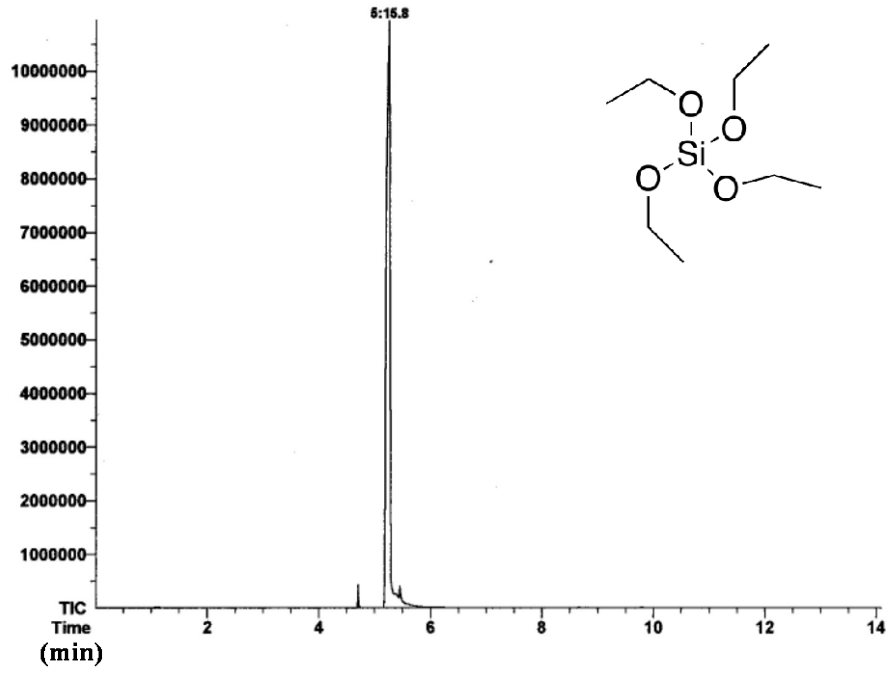

Instrument: JEOL JMS600
Inlet: GC

Ionization mode: EI+

Scan: 327
Base: m/z 193; 100%FS TIC: 5784536

R.T.: 5:12

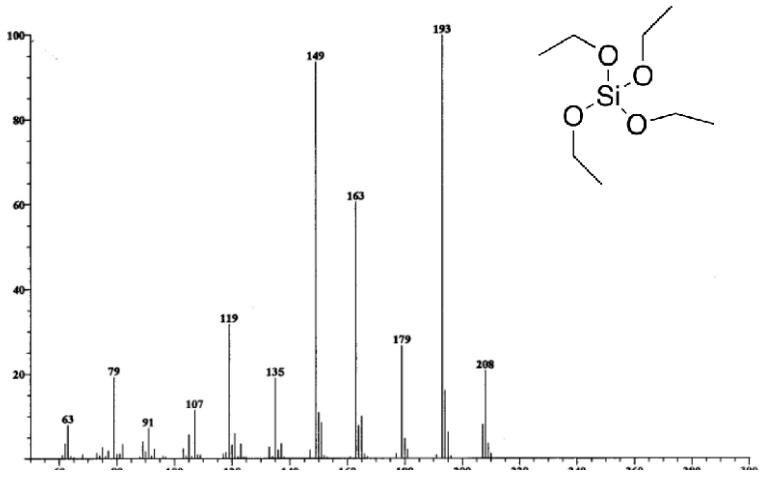

`

GC-MS data of TEOS with ammonia solution

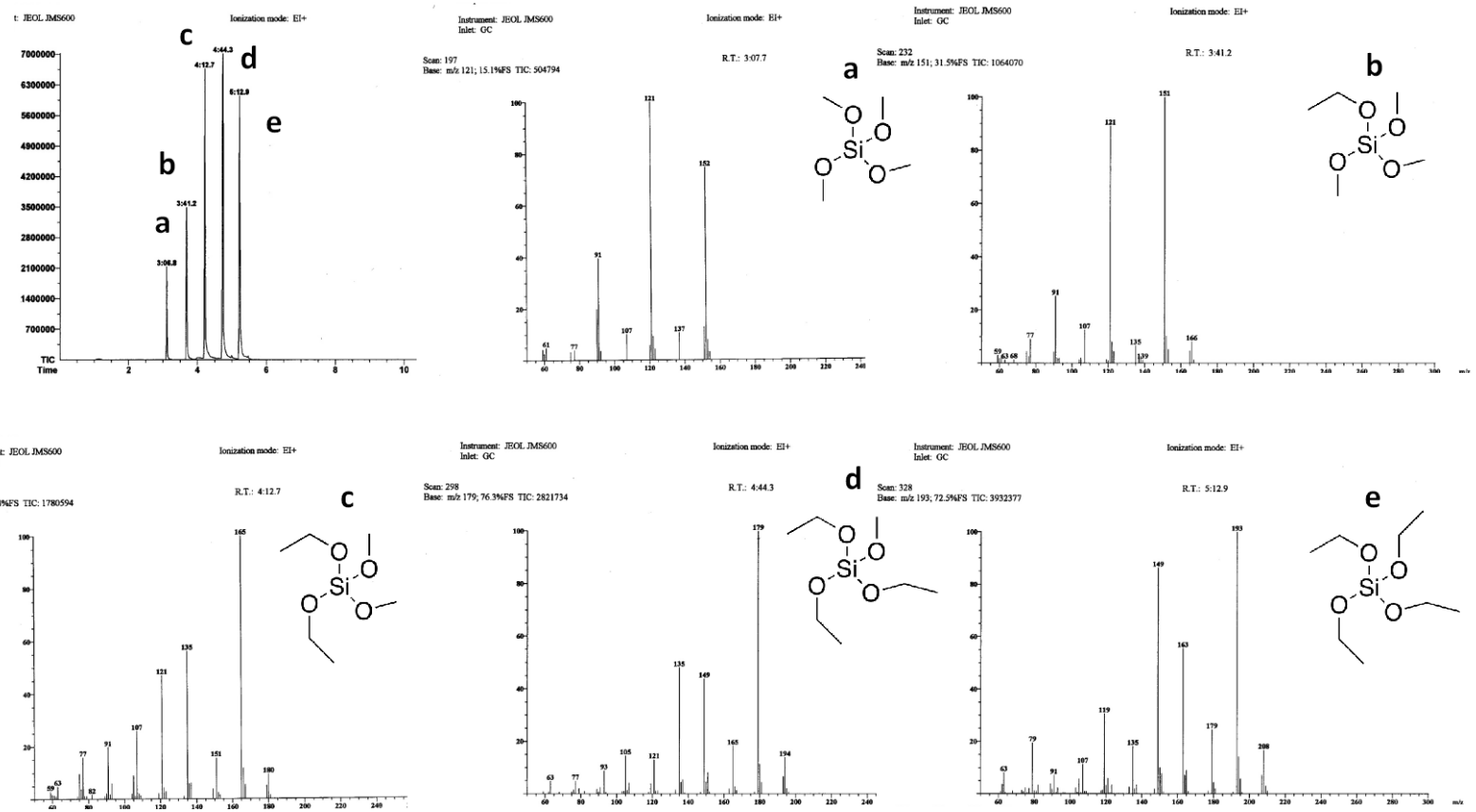

`

GC-MS data of TEOS with hydrochloric acid

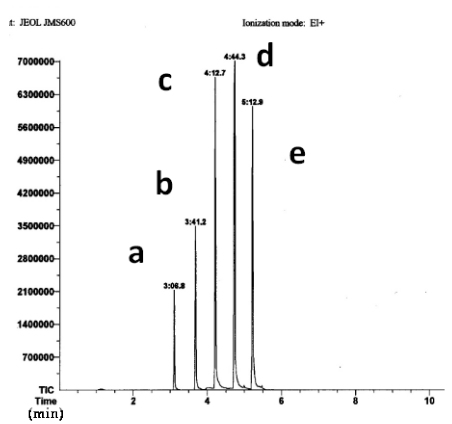

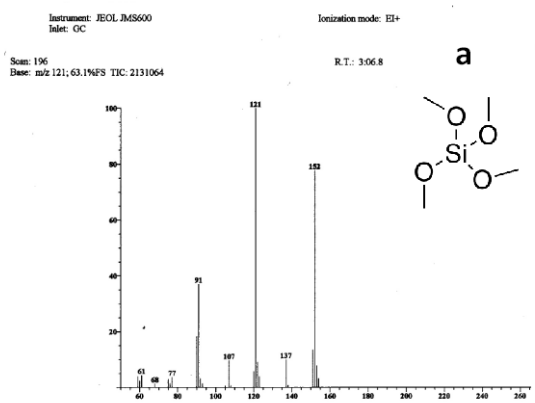

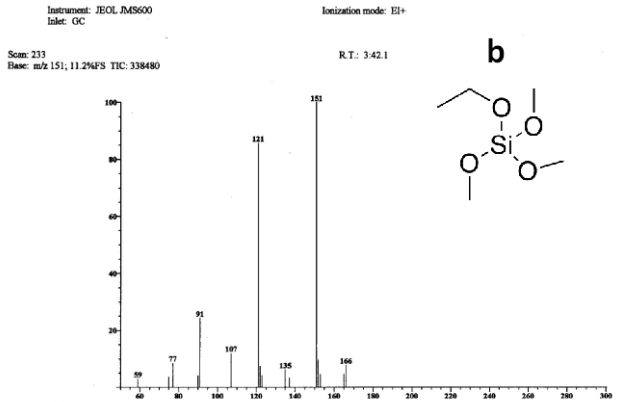

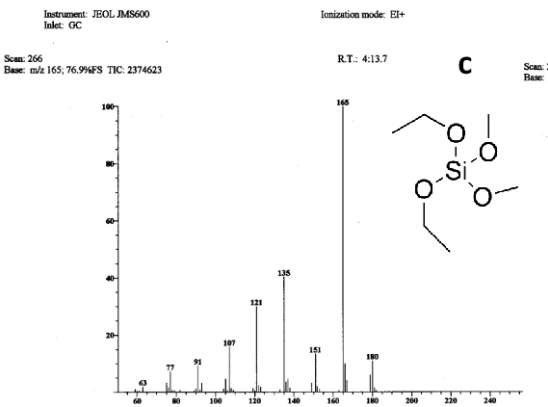

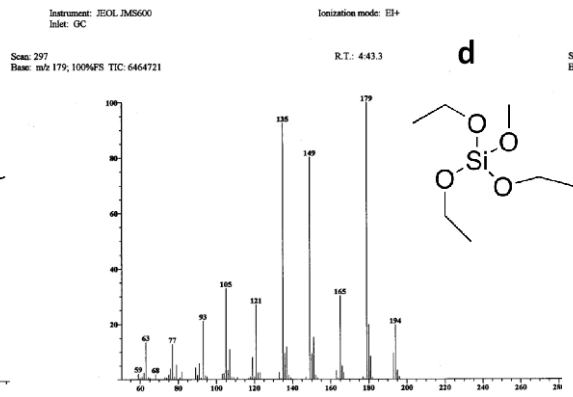

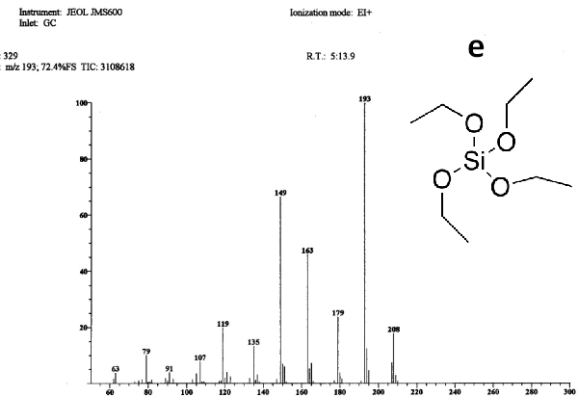

`

1.6 References

[1] Mesa, M.; Sierra, L.; Lopez, B.; Ramirez, A.; Guth, J. L., *Solid State Sci.* **2003**, *5*, 1303-1308.

[2] Zou, H.; Wu, S. S.; Shen, J., *Chem. Rev.* **2008**, *108*, 3893-3957.

[3] Bhakta, G.; Sharma, R. K.; Gupta, N.; Cool, S.; Nurcombe, V.; Maitra, A., *Nanomedicine* **2011**, *7*, 472-479.

[4] Bonacchi, S.; Genovese, D.; Juris, R.; Montalti, M.; Prodi, L.; Rampazzo, E.; Zaccheroni, N., *Angew. Chem. Int. Ed.* **2011**, *50*, 4056-4066.

[5] He, Q.; Shi, J., *J. Mater. Chem.* **2011**, *21*, 5845-5855.

[6] Stöber, W.; Fink, A.; Bohn, E., *J.Colloid Interf. Sci.* **1968**, *26*, 62-69.

[7] Kim, J. W.; Kim, L. U.; Kim, C. K., *Biomacromolecules* **2006**, *8*, 215-222.

[8] Venkatathri, N.; Yun, D. S.; Yoo, J. W., *Mater. Res. Bull.* **2009**, *44*, 1317-1322.

[9] Yokoi, T.; Sakamoto, Y.; Terasaki, O.; Kubota, Y.; Okubo, T.; Tatsumi, T., *J. Am. Chem. Soc.* **2006**, *128*, 13664-13665.

[10] Green, D. L.; Lin, J. S.; Lam, Y. F.; Hu, M. Z. C.; Schaefer, D. W.; Harris, M. T., *J. Colloid Interface Sci.* **2003**, *266*, 346-358.

[11] Brinker, C. J., *J. Non-Cryst. Solids* **1988**, *100*, 31-50.

[12] Brinker, C. J.; Keefer, K. D.; Schaefer, D. W.; Assink, R. A.; Kay, B. D.; Ashley, C. S., *J. Non-Cryst. Solids* **1984**, *63*, 45-59.

[13] Bernards, T. N. M.; van Bommel, M. J.; Boonstra, A. H., *J. Non-Cryst. Solids* **1991**, *134*, 1-13.

[14] Bernards, T. N. M.; Janssen, M. J. C. H.; van Bommel, M. J., *J. Non-Cryst. Solids* **1994**, *168*, 201-212.

[15] Lamer, V. K., *Ind. Eng. Chem.* **1952**, *44*, 1270-1277.

[16] Nogami, M.; Moriya, Y., *J. Non-Cryst. Solids* **1980**, *37*, 191-201.

[17] Chen, K. C.; Tsuchiya, T.; Mackenzie, J. D., *J. Non-Cryst. Solids* **1986**,

`

81, 227-237.

[18] Kang, S. J.; Kim, K. D.; Kim, H. T., *J Korean Ind. Eng. Chem.* **2000**, *11*, 216-219.

`

Appendix/Chapter 2.

Oligothiophene-modified Silver@Silica Core@Shell Nanoparticles for Inhibiting Open-circuit Voltage Drop and Aggregation in Polymer Solar Cells

Published as *J. Mater. Chem. A* **2014**, *2*, 15357-15364.

2.1 Abstract

Metal nanoparticles (NPs) have attracted much attention owing to their particular characteristics such as localized surface plasmon resonance (LSPR) and scattering properties, which can improve the light harvesting ability of photovoltaic cells. However, modification of the metal NP surface is needed to prevent particle aggregation and photoinduced charge trapping. Surface modification of silica-coated Ag NPs with oligothiophene (OT) provides silver/silica core-shell (Ag@SiO_2–OT) NPs, which are well dispersed in nonpolar organic solvents and miscible with the bulk-heterojunction (BHJ) layer of poly(3-hexylthiophene) (P3HT) and phenyl-C61-butyric acid methyl ester (PCBM) (P3HT:PCBM). Incorporation of the Ag@SiO_2–OT NPs into the P3HT:PCBM layers as the active layer of photovoltaic devices improves the light-harvesting ability and enhances the photo-conversion efficiency (PCE) by about 18 %. There is no significant change in the open-circuit voltage (V_{oc}) value even when up to 30 wt% of Ag@SiO_2–OT NPs are incorporated, confirming that the OT-modified silica layer on silver NPs contributes to improving light absorption and photo-current without causing

`

aggregation and photo-induced charge trapping. Moreover, the deliberately designed transmission electron microscopy (TEM) investigation of the composite films of P3HT:PCBM and Ag@SiO_2–OT NPs reveals that Ag@SiO_2–OT NPs are mainly located in the P3HT domain owing to the favorable interaction between the similar molecular structures of OT and P3HT.

2.2 Introduction

Because of the rapid depletion of fossil-fuel energy resources, photovoltaic cells have started to gain recognition as a potential alternative to conventional energy sources with the added benefit of environmental friendliness. Organic photovoltaic cells (OPVs) based on π-conjugated polymers and fullerene derivatives have attracted considerable attention owing to low cost, large-scale fabrication, lightweight, possible solution processing, and mechanical flexibility of the devices.[1] Many efforts have been made toward the development of low band-gap polymers for fabricating high power conversion efficiency (PCE) solar cells.[2, 3] Consequently, the maximum PCE achieved recently exceeded 7 %.[4, 5] However, the current PCE values are still low; in order to achieve mass production and practical applications, the device performance needs to be improved to attain a PCE of 10–15 %.[6] To attain high efficiency, polymer-based solar cells should fulfil several requirements such as efficient light-harvesting ability and excellent charge carrier separation and charge transport.[2] In general, the photoactive layer should be thick enough to sufficiently absorb the incident light; however, the organic active layer is intrinsically very thin because of the short diffusion length and low carrier mobility of most polymeric materials.[7]

Thus, achieving efficient light trapping in the active layer of polymer-based

`

solar cells is challenging without increasing the film thickness.

Ag and Au nanoparticles (NPs) have extraordinary characteristics such as light-scattering effects and localized surface plasmon resonance (LSPR).[8] These properties are expected to improve the efficiency of solar cells, and two major mechanisms have been proposed.[9] First, the light-scattering effect from small metal NPs increases the optical path length of light, which makes the active layer absorb the incident solar light more efficiently. Second, the LSPR of metal NPs induces the strong local electromagnetic fields around the NPs to in-crease the light absorption of organic materials. Several groups have reported that metal NPs increased the performance of bulk-heterojunction (BHJ) solar cells without changing the thickness of the active layer.[10-13] However, metal NPs prepared by a typical reduction process in a water or polyol solution are not well dispersed in nonpolar organic solvents.[14,15] Therefore, they cannot be embedded in the active layer (typically composed of P3HT and PCBM);[16-18] they tend to aggregate during the film casting of the active layer owing to their insufficient solubility in both chlorobenzene (CB) and *o*-dichlorobenzene (DCB) and generate defects in the entire cell structure.[19] Due to their solubility and miscibility problem, metal NPs are usually introduced into the hole injection layer with poly(3,4-ethylenedioxythiophene):poly(styrene sulfonate) (PEDOT:PSS), which is water-soluble.[20-22] The NPs prepared using long alkyl chain surfactants, showing good dispersion in nonpolar organic solvents, were expected to prevent aggregation during the coating process.[11] However, the metal NPs still tend to aggregate probably due to the miscibility problem with P3HT-PCBM.

A direct contact of the metal NPs with organic electron donor and/or acceptor molecules causes another problem; it can act as a center of photoinduced exciton quenching, and recently, this charge trapping

`

mechanism in the active layer has been reported.[23-25] These electron loss mechanisms and direct contact with the metal cathode reduce the open-circuit voltage (V_{oc}) with increasing concentration of metal NPs.[26] To prevent the exciton quenching on the surface of metal NPs, several groups recently introduced an insulating silica layer onto the surface of metal NPs.[27-29]

In this chapter, a polymer-based BHJ solar cell was prepared with the oligothiophene (OT)-modified silica-coated silver NPs (Ag@SiO_2−OT NPs) as an additive to enhance the photocurrent without the drop in V_{oc}. The silica coating on the Ag NPs plays the role of an insulator to prevent direct contact with other organic molecules in the active layer, as well as the role to provide the modification platform based on the well-known silicon chemistry. When the surface of silver@silica core-shell (Ag@SiO_2) NPs is modified with the OT, as expected, the NPs become sufficiently soluble in nonpolar organic solvents and achieve good dispersion in the active layer. Optimizing the amount of the OT-modified silver/silica core-shell NPs (Ag@SiO_2−OT) embedded in a blend of P3HT and PCBM resulted in approximately 18% enhancement of PCE (4.25 %) compared to that of the P3HT:PCBM reference cell (3.59 %) under the same conditions. There was no change in the V_{oc} even after the addition of 30 wt% of Ag@SiO_2−OT NPs in the active layer, while there was a large drop in V_{oc} as a function of the amount of introduced NPs for devices prepared with bare Ag NPs. The location of Ag@SiO_2−OT NPs was precisely investigated by deliberately designed TEM analyses. The cross sectioned TEM images of the Ag@SiO_2−OT NPs embedded in P3HT-PCBM layer revealed that the NPs were distributed in the middle of the active layer, and most of them were mainly found in the P3HT region owing to the favorable interaction between the similar molecular structures of OT and P3HT.

`

2.3 Results and Discussion

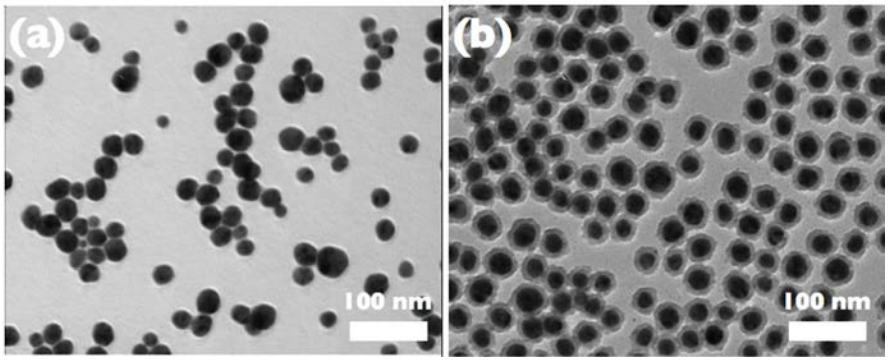

Figure 2.1. TEM images of (a) Ag NPs and (b) Ag@SiO_2 NPs.

Synthesis of Ag@SiO_2−OT NPs Ag NPs were synthesized by reducing silver nitrate in hot ethylene glycol (EG) in the presence of an excess amount of polyvinylpyrrolidone (PVP) as reported in the literature,[30] having a size in the range of 20−30 nm which was expected to be well introduced in a > 100 nm-thick P3HT-PCBM layer and to cause a sufficiently strong scattering effect (Figure 2.1a). An approximately 10-nm-thick silica shell was coated on the surface of Ag NPs by the controlled hydrolysis/condensation of tetraethyl orthosilicate (TEOS) in ethanol with a base catalyst as reported in the literature (Figure 2.1b),[31-33] which were expected to optimize the local electromagnetic field near the metal NPs without causing unwanted exciton quenching.[33] The surface of Ag@SiO_2 NPs were modified with (3-trimethoxysilylpropyl)diethylenetriamine (DETAS) having primary and secondary amine groups, as reported to reproducibly generate monolayer coating without using any additional basic catalyst in ethanol,[34] which were then connected to the OT derivative as shown in Scheme 1. The presence of amine groups on the silica layer was simply confirmed by the inversion of surface charges measured by the zeta potential in ethanol (−40 and +48 mV

`

for $Ag@SiO_2$ and $Ag@SiO_2$–DETAS NPs, respectively). The pristine surface of silica has negative charges due to the partial deprotonation of Si-OH into $Si\text{-}O^-$, while the surface functionalized with amine groups shows a positive charge owing to the partial protonation of amine groups to form $–NH^{3+}$ and $–NH^{2+}–$.

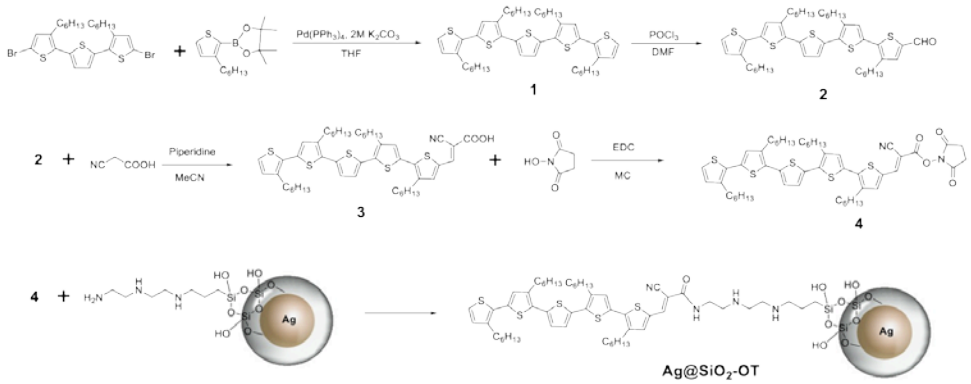

Scheme 2.1. Synthetic routes for oligothiophene derivatives and surface-modified Ag NPs.

Activated OT precursor molecule, 3, was synthesized by the consecutive palladium-catalyzed Suzuki reaction, Vilsmeier-Haack formylation reaction, and Knoevenagel condensation reaction, according to the reported procedures.[35-37] In order to attach the OT derivative to the amine groups on the surface of $Ag@SiO_2$–DETAS NPs, the terminal carboxyl group of compound 3 was transformed into the activated ester 4 by using N-hydroxysuccinimide with 1-ethyl-3-(3-dimethylaminopropyl)-carbodiimide (EDC). The coupling reaction of $Ag@SiO_2$–DETAS NPs and activated ester 4 to give $Ag@SiO_2$–OT NPs, was confirmed by the solubility change of nanoparticles. $Ag@SiO_2$–DETAS NPs were well dispersed in polar solvents such as ethanol owing to the hydrophilic character of the surface. However, after the modification by

`

OT, the hydrophobic nature of the attached OT groups made the NPs well-dispersed in nonpolar organic solvents such as chloroform and toluene, as shown in Figure 2a. The presence of OT groups on the particles was also confirmed by a thermogravimetric analysis (TGA, see Figure 2.2). When the temperature was raised from 100 to 800 °C, the weight loss of $Ag@SiO_2$ NPs was approximately 7 wt%, which could be caused by the elimination of water and decomposition of organic molecules such as the remaining ethoxy group and PVP. TGA analysis of $Ag@SiO_2$–DETAS also showed very similar weight loss to that of $Ag@SiO_2$, which is probably due to a relatively small weight portion of DETAS monolayer compared to heavy $Ag@SiO_2$ particle itself. However, in the case of $Ag@SiO_2$–OT, the total weight loss increased to 11 % showing 4 % point more weight loss from the attached oligomeric thiophene groups. Based on these TGA data, the number of the attached OT groups on each particle could be calculated (see experimental section). Each $Ag@SiO_2$–OT particle has ~5,700 OT groups on its silica surface with the packing density value of 0.9 ea/nm^2, which is in the reasonable range of packing density values from quantitative analysis of the surface amine groups using dye absorption (0.44 ea/nm^2) and back-titration (2.7 ea/nm^2) methods,[3,4] because only the primary amine groups can effectively react with a bulky activated ester 4, in our system. Introduced OT groups with the high packing density make the whole particle be well dispersed in nonpolar organic solvent and P3HT:PCBM active layer.

`

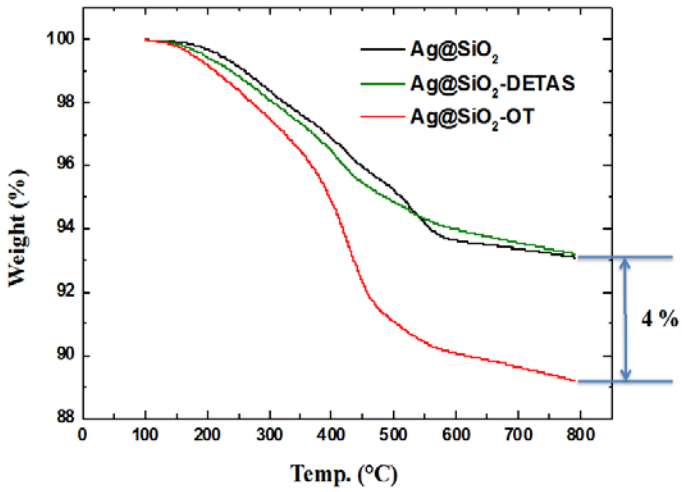

Figure 2.2. TGA results of surface modified silver nanoparticles.

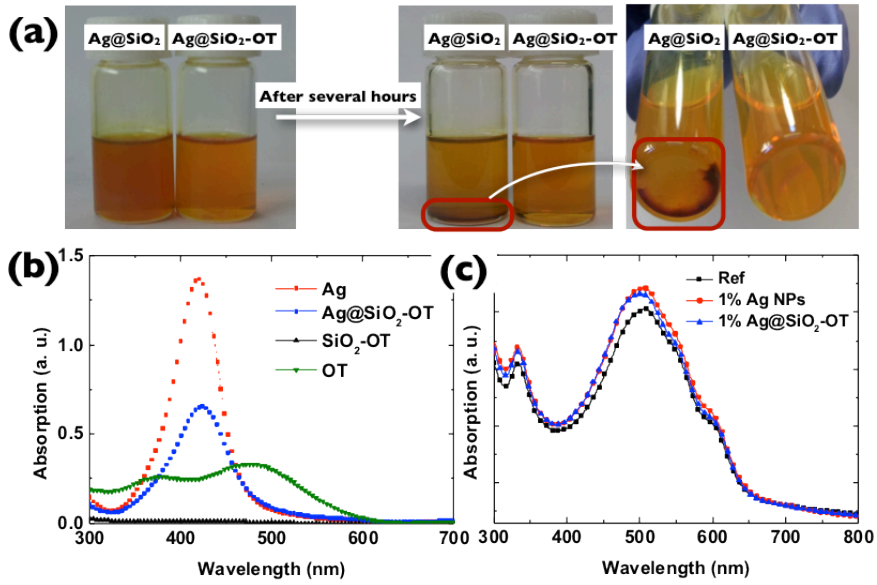

Figure 2.3. Photograph images of $Ag@SiO_2$ and $Ag@SiO_2$−OT in chloroform. (b) Absorption spectra of nanoparticles in 0.001 wt% (w/v) solution and 0.02 mM OT in chloroform and (c) a blended film with P3HT:PCBM = 1:0.8 (w/w).

`

Photophysical study UV-Vis absorption spectra of particles (0.001 wt%, w/v) in a chloroform solution and the blended P3HT:PCBM film with either Ag or Ag@SiO_2–OT NPs are presented in Figure 2.3b and 2.3c. As shown in Figure 2.3 b, the LSPR peak (λ_{max}) of the Ag NPs was observed with a general extinction characteristic at approximately 420 nm; in contrast, λ_{max} of the Ag@SiO_2 NPs was slightly red-shifted because of the high refractive index of the silica shell around Ag NPs as reported in the literature.[28, 38] Compound 4 showed the broad absorption spectrum in the range of 300–600 nm, attributed to the π–π* transition of the conjugated system. However, because most of the mass of SiO_2@OT comes from silica NPs and not from the organic moieties, the absorption intensity of the OT moieties in the SiO_2@OT NPs was almost negligible when the same amount of SiO_2@OT was used as that of compound 4. In other words, OT is more likely to act as a surface ligand rather than as a light-harvesting molecule, because the OT derivatives on the silica surface are much lighter than the silica NPs themselves.

The composite films were prepared by blending a solution of P3HT:PCBM with NPs at 1 wt% (w/w) ratios, fabricated by a spin-casting method, and followed by thermal annealing at 140 °C for 10 min. All samples showed a broad absorption in the wavelength range of 350−650 nm as shown in Figure 2.3c, where P3HT absorbed characteristically in 400−650 nm region and PCBM at <400 nm. The absorption spectra of the composite films indicated that the light-harvesting ability in the spectral range of 350−600 nm was improved when either Ag or Ag@SiO_2–OT NPs were added to the P3HT:PCBM matrix, compared with that of the film composed only of P3HT:PCBM.

`

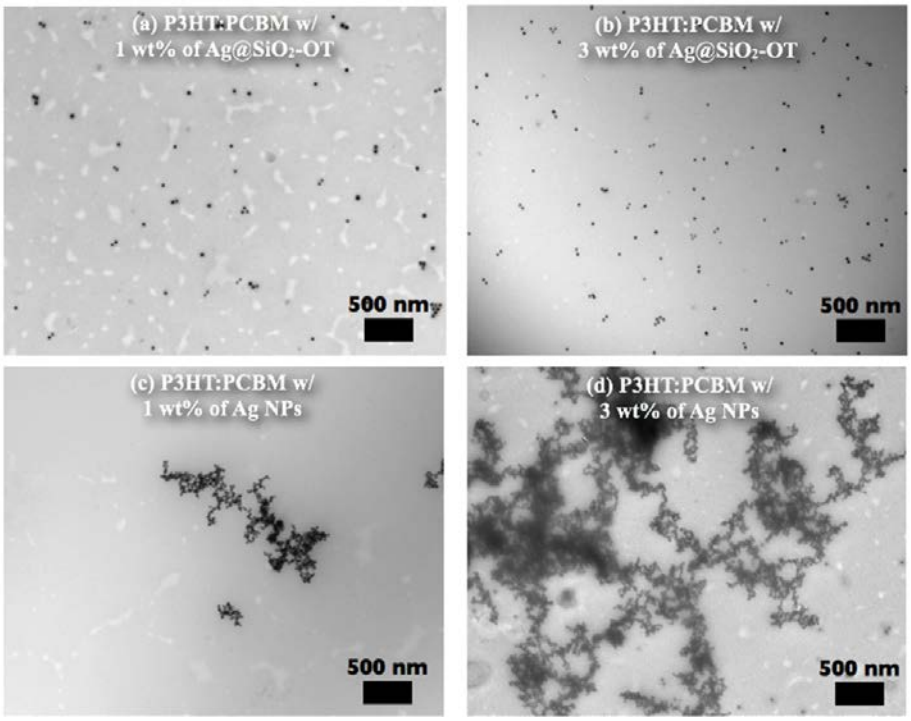

Figure 2.4. TEM images of composite films of NPs with P3HT:PCBM.

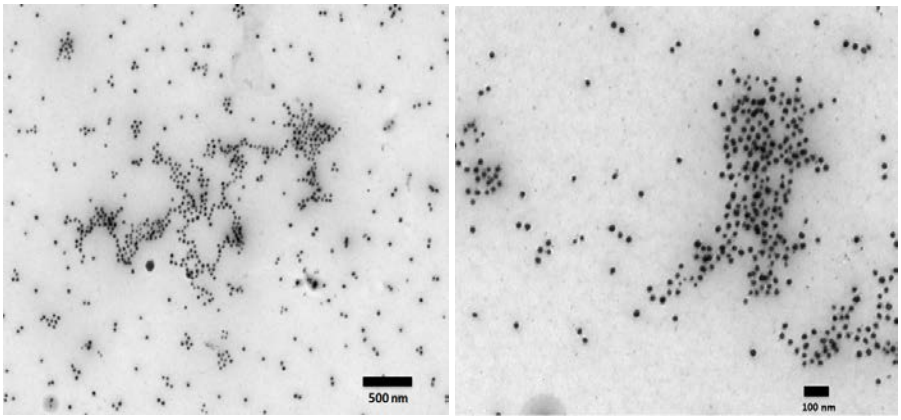

Figure 2.5. TEM images of P3HT:PCBM film with 3 wt% of $Ag@SiO_2$ composite films.

`

Morphology studies Figure 2.4 shows the TEM images of the various composite films of Ag or Ag@SiO_2–OT NPs with P3HT:PCBM. The individual Ag NPs significantly aggregated during the film casting process, which resulted in the formation of Ag NP aggregates (ca. >1 μm) even when only 1 wt% of Ag NPs were embedded in the active layer (Figure 2.4c and 2.4d). In addition, the aggregation was also observed from the composite film of Ag@SiO_2 NPs and P3HT:PCBM film. (see TEM images in Figure 2.5). On the other hand, as expected for the surface modified Ag@SiO_2–OT NPs, they are well dispersed in the active layer even at 3 wt% (Figure 2.4a and 2.4b), demonstrating that surface OT increased the miscibility with P3HT:PCBM to prevent the aggregation of Ag@SiO_2–OT NPs.

The surface morphology of the active layer could affect the photovoltaic performance, which should be closely related with the miscibility of metal NPs and organic components. Figure 2.6 shows the atomic force microscopy (AFM) images of composite films of P3HT:PCBM with various amounts of NPs. The roughness (R_{rms}) values increased only slightly from 0.548 to 0.635, 0.795, and 0.848 nm as the concentration of Ag@SiO_2–OT NPs increases to 1, 3, and 5 wt%, respectively (Figures 2.6a, 2.6b, and 2.6c compared to 2.6f). These smooth surfaces of composite films of P3HT:PCBM with Ag@SiO_2–OT NPs confirmed again the good miscibility, which would be expected to facilitate the photo-induced charge separation and transport.[27] In contrast, large aggregates (~200 nm diameter and ~50 nm height) were formed in the composite films of P3HT:PCBM with 3 wt% of as-prepared Ag NPs (Figure 4e): the aggregation of Ag NPs could generate charge-trapping sites and defects in the active layer, thus eventually reducing the V_{oc} and device performance as described in the next section.

`

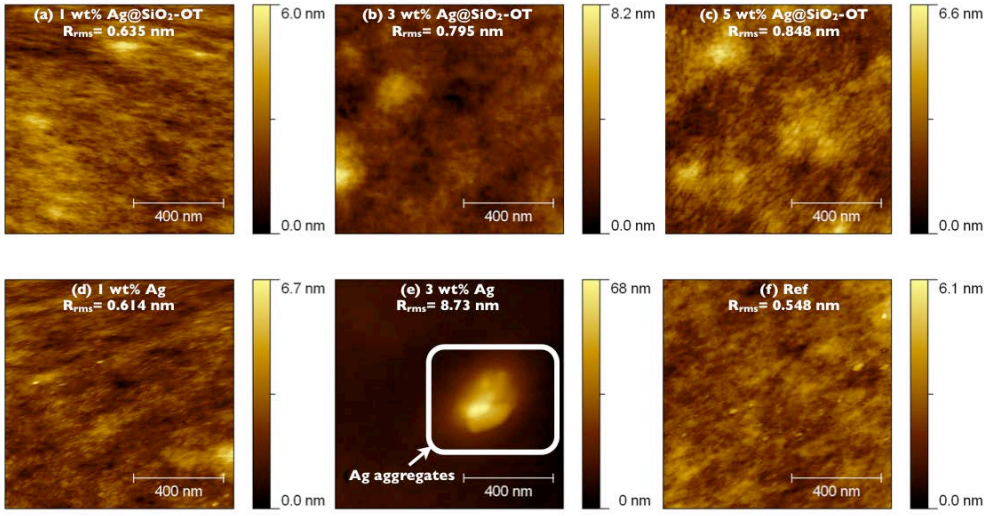

Figure 2.6. AFM images of composite films of P3HT:PCBM with nanoparticles: (a) 1 wt%, (b) 3 wt%, (c) 5 wt% of Ag@SiO_2–OT NPs, (d) 1 wt%, (e) 3 wt% of Ag NPs, and (f) without nanoparticles. Imaging area: 1 μm × 1 μm

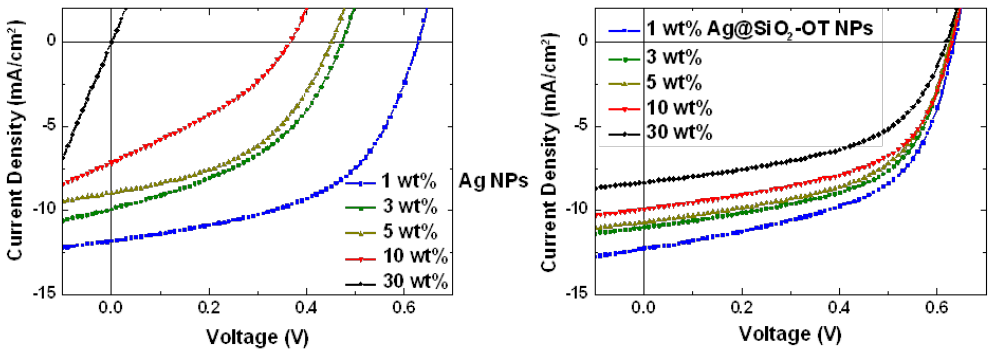

Figure 2.7. *I-V* curves of P3HT:PCBM (1:0.8) based solar cells with various amounts of Ag@SiO_2-OT NPs (left) and Ag NPs (right).

`

Table 2.1. The photovoltaic performance of polymer solar cells with various concentrations of nanoparticles.[a]

Types of NPs	NP ratio		V_{oc} (V)	J_{sc} (mA/cm^2)	FF	PCE (ave)	PCE (max)
	whole NPs (wt%)	Ag content (wt%)					
Ref	0	0	0.62 ± 0.01	10.28 ± 0.40	0.54 ± 0.02	3.44 ± 0.12	3.59
Ag@SiO_2-OT	1	0.66	0.63 ± 0.01	11.42 ± 0.45	0.55 ± 0.01	4.02 ± 0.17	4.25
	3	2	0.62 ± 0.01	10.71 ± 0.49	0.54 ± 0.01	3.57 ± 0.16	3.82
	5	3.33	0.62 ± 0.01	10.55 ± 0.35	0.54 ± 0.02	3.54 ±0.16	3.65
	10	6.6	0.62 ± 0.01	9.73 ± 0.35	0.54 ± 0.01	3.23 ± 0.10	3.38
	30	20	0.61 ± 0.01	7.98 ± 0.26	0.52 ± 0.01	2.56 ± 0.08	2.65
Ag	1	1	0.63 ± 0.01	11.37 ± 0.35	0.53 ± 0.01	3.78 ± 0.09	3.88
	3	3	0.47 ± 0.00	9.38 ± 0.54	0.42 ± 0.01	1.85 ± 0.14	2.01
	5	5	0.45 ± 0.01	8.72 ± 0.27	0.43 ± 0.02	1.70 ± 0.13	1.86
	10	10	0.35 ± 0.01	6.75 ± 0.56	0.34 ± 0.02	0.79 ± 0.08	0.88
	30	30	n.a.	n.a.	n.a.	n.a.	n.a.

[a]Photovoltaic performance parameters are the average values of at least 10 devices.

`

Photovoltaic device performance The photovoltaic devices were fabricated with various composite layers of P3HT:PCBM having different mixing ratios (1–30 wt%) of Ag NPs or Ag@SiO_2–OT NPs. The total concentration of all of devices are consistent (2 wt% w/v) to obtain a uniform, optimized active layer thickness (130~140 nm). The photovoltaic performances and *I-V* curves of these devices are shown in Table 2.1 and Figure 2.7. The short-circuit current (J_{sc}) values of the photovoltaic devices having the composite layers of P3HT:PCBM with Ag NPs (11.37 mA/cm^2) or Ag@SiO_2–OT NPs (11.42 mA/cm^2) at 1 wt% (w/w) were higher than those for the devices composed of P3HT:PCBM without NPs (10.28 mA/cm^2). This enhanced photocurrent was confirmed by the incident photon-to-current efficiency (IPCE) spectra. As displayed in Figure 2.8, the IPCE values for the photovoltaic devices having the composite layers with Ag@SiO_2–OT NPs were higher at all wavelengths than those for the device containing only pristine P3HT:PCBM; the IPCE values stayed higher than 60% in the range from 460 to 560 nm and reached the maximum of 75% at 520 nm. These results support that Ag@SiO_2–OT NPs increase the light-absorption ability due to their LSPR and scattering effects.

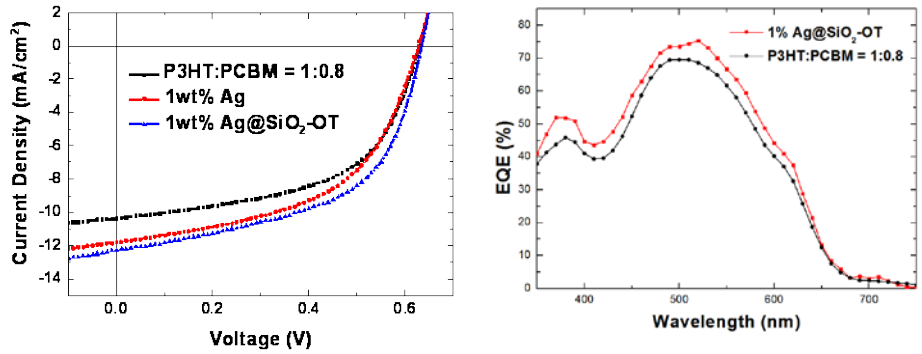

Figure 2.8. *I-V* curves (left) and IPCEs (right) of P3HT:PCBM based solar cells with nanoparticle components.

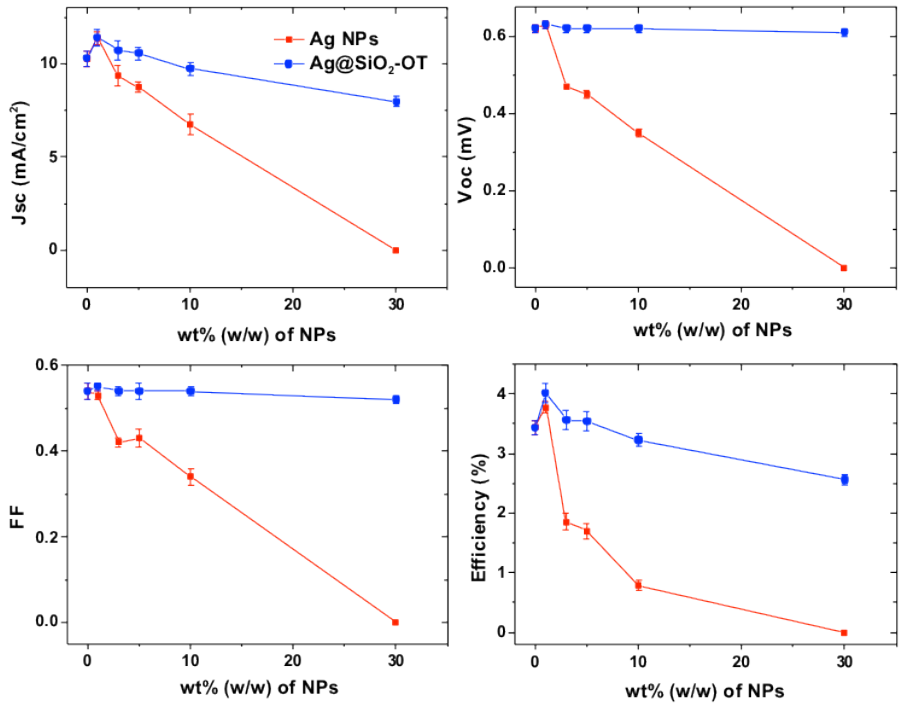

Figure 2.9. Dependence of the photovoltaic performance of nanoparticle-embedded devices on the concentration of nanoparticles.

`

For the devices having Ag NPs in the active layer, there was a significant drop in the V_{oc} after incorporating more than 3 wt% of Ag NPs (Figure 2.9b) in the active layer; similar results have also been reported in the literature.[10, 11] However, in the case of devices fabricated with Ag@SiO_2–OT NPs, the V_{oc} values were perfectly maintained even with a large amount of Ag@SiO_2–OT NPs (up to 30 wt%). This result confirms that the silica shell efficiently inhibits charge trapping on the surface of Ag NPs as expected and direct contact with a metal cathode, which would result in a change in the cathode work function.[26]

Furthermore, not only J_{sc} and FF but also PCE values for the devices having Ag@SiO_2–OT NPs embedded in the active layer were higher than those for the devices having Ag NPs, because the surface-modified NPs formed more uniformly dispersed active layers with low surface roughness values (Figure 2.6). Especially, the devices having an active layer with 30 wt% Ag@SiO_2–OT NPs showed PCE of 2.65 %, while the other with 30 wt% Ag NP showed ohmic contact *I-V* curve, as shown in Figure 2.8, which could be attributed to both the aggregation of Ag NPs and the damaged PEDOT:PSS layer caused by a high volume amount of ethanol used to introduce a large amount of Ag NPs.

For the devices having an active layer with Ag NPs, the photovoltaic performances were enhanced for the 1 wt% device but continuously deteriorated as the amount of Ag NPs increased, comparing to the device containing only pristine P3HT:PCBM (Table 1). These phenomena seemed to be consistent with reported results that an initial increase of the exciton generation in the hybrid plasmonic composite OPVs was observed and the high trapping rate of the generated polarons limited the amount of free carriers

`

in the hybrid systems.[40] Thus, as the surface of Ag NPs was modified by introducing SiO_2 layer and oligothiophene derivatives that are structurally similar to P3HT, Ag@SiO_2–OT NPs are efficiently incorporated into the P3HT:PCBM layers without aggregation, resulting in higher enhancement (18%) in the PCE value compared with that of the Ag NP-incorporated device (8%).

The location of NPs in the active layer The exact location of Ag@SiO_2–OT NPs within the BHJ layer is a critical issue because the increment of the light-absorption ability due to their LSPR and scattering effects is expected to affect significantly when they are closely located to (photoinduced) electron donor molecules, in this case, P3HT.[40] However, a phase separation within the BHJ layer could not be easily observed in the TEM experiment due to the similar electron densities of both organic components (P3HT and PCBM), only showing the existence of Ag@SiO_2–OT NPs within the BHJ layer (Figure 2.10).

In order to find the exact location of Ag@SiO_2–OT NPs within the BHJ layer, one of the components of the BHJ layer was selectively removed and the differences between the two TEM images were compared. Since diiodooctane (DIO) was well-known to dissolve selectively PCBM out of the BHJ layer without affecting P3HT,[41, 42] it was used to remove PCBM from the active layer sample on a TEM grid. The selective removal of PCBM by DIO was also monitored by a decrease in the absorbance of the active layer sample, particularly in the range of shorter than 400 nm (Figure 2.11), which corresponded to the characteristic absorption band of PCBM.[43] As shown in Figure 6a and 6b, TEM images of the active layer before and after the DIO treatment clearly showed distinguishable dark and bright regions; as the

`

PCBM region was removed by DIO, the darker region corresponded to the stacked P3HT and the brighter region represented the thinner or empty area.

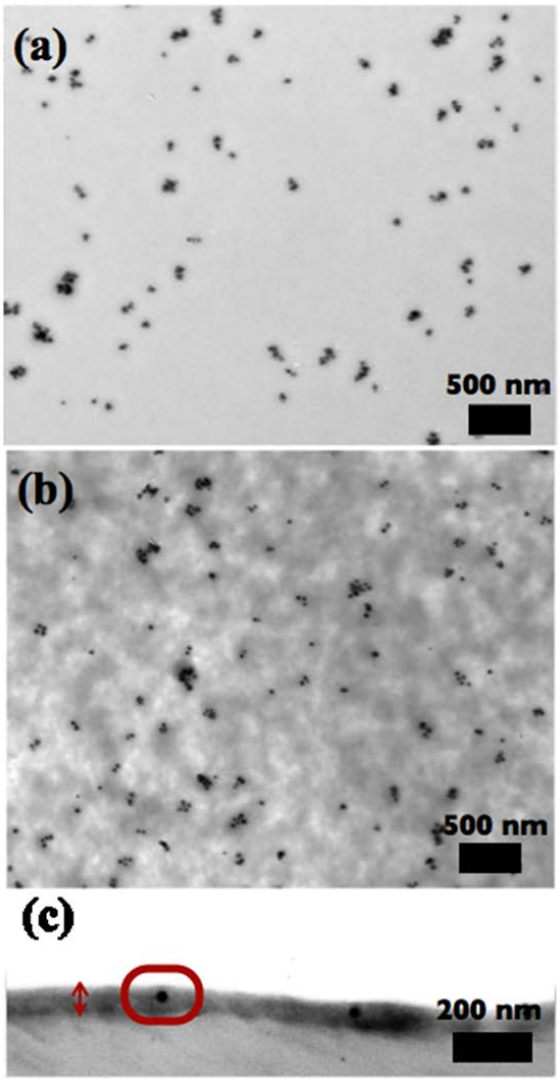

Figure 2.10. TEM images of blended P3HT:PCBM:Ag@SiO_2–OT = 1:1:0.03 (w/w/w) film (a) before and (b) after DIO treatment. (c) Cross-section of the film.

`

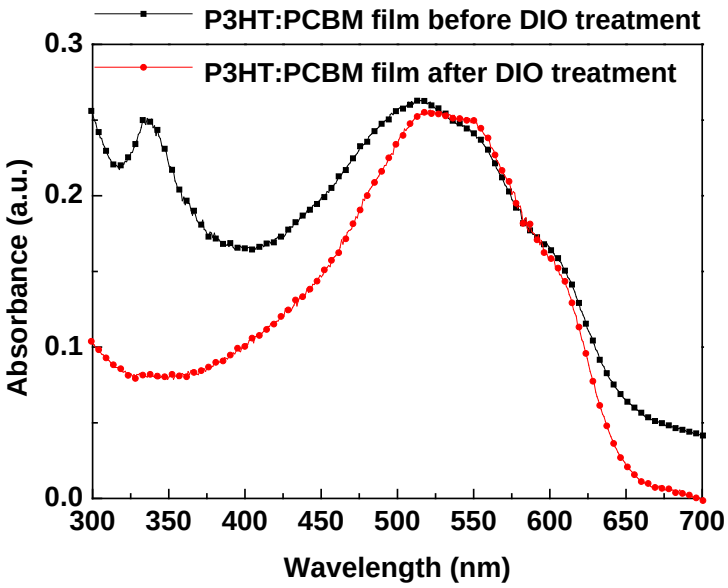

Figure 2.11. Absorption spectra of P3HT:PCBM blend film before and after DIO treatment.

The actual location of Ag@SiO_2–OT NPs was also checked using the TEM image of an ultramicrotomed cross section of a sample to show that they were all embedded inside the BHJ layer as shown in Figure 6c. Furthermore, from the results that the majority of NPs was in the dark region and the total number of NPs in the active layer seemed to be maintained after the DIO treatment, it could be concluded that most of Ag@SiO_2–OT NPs were located in the P3HT domain owing to their similar molecular structures of OT and P3HT; which increased the light-absorption ability due to LSPR and scattering effects of NPs and thus affected significantly the efficiency of photo-induced electron transfer (PET) from P3HT to PCBM.

`

2.4 Conclusions

In this chapter, silver@silica core@shell NPs were synthesized and deliberately modified their surface with OT in order to in-crease the light-harvesting ability in polymer solar cells. As the molecular structure of OT on the surface of Ag@SiO_2 NPs is similar to that of P3HT, the Ag@SiO_2–OT NPs are well dispersed in the organic solvents of processing and formed homogeneous composite layers of P3HT:PCBM with various mixing ratios.

Furthermore, as the silica shell on the surface of the Ag NPs protected them from the direct contact with organic materials such as P3HT and PCBM, it efficiently eliminated the trapping problem of initially generated polarons which caused serious limitation for the devices having an active layer with Ag NPs. The performance of the photovoltaic devices based on P3HT:PCBM:Ag@SiO_2–OT = 1:0.8:0.01 (w/w/w) showed nearly 12 % enhancement in the J_{sc} values compared with the pristine P3HT:PCBM device as well as the perfectly maintained V_{oc} values even with 30 wt% NPs, confirming the perfect miscibility of Ag@SiO_2–OT NPs with the P3HT:PCBM layer. Therefore, as the surface of Ag NPs was modified by introducing SiO_2 layer and oligothiophene derivatives, the resulting Ag@SiO_2–OT NPs became miscible with the P3HT:PCBM layer without aggregation, resulting in high enhancement (18 %) in the PCE values compared with the pristine P3HT:PCBM device. The TEM images of the active layer of P3HT:PCBM:Ag@SiO_2–OT in which PCBM was selectively washed with DIO solvent revealed that Ag@SiO_2–OT NPs were mainly located in the P3HT domain of the active layer because of the structural similarity between OT and P3HT. Further studies on the modification of the silica surface of metal NPs of different shapes and sizes with various organic molecules for efficient organic solar cells are underway.

`

2.5 Experimental Section

Materials and Instruments All organic chemicals were purchased from Aldrich and TCI. Solar cell materials P3HT and PCBM were purchased from Rieke Metals and Nano-C (USA), respectively. Poly(styrene sulfonate) doped poly(ethylenedioxythiophene) (PEDOT:PSS, Clevious PH) was purchased from Bayer. All solvents and reagents used in this study were commercially available and used without further purification unless otherwise specified.

^{1}H and ^{13}C NMR spectra were recorded using either an Advance 300 MHz Bruker spectrometer or 400 MHz Varian spectrometer. The UV-Vis spectra were recorded using a Beckman DU 650 spec-trophotometer. The mass spectra were obtained using a gas chromatograph-mass spectrometer (JEOL, JMS-AX505WA, HP 5890 Series II). The device performance was measured under AM 1.5G illumination (100 mW cm^{-2}) using a solar simulator (Peccell, Japan) and Solar Cell IPCE Measurement System (McScience, K3100). The light intensity at each wavelength was calibrated using a standard Si solar cell as a reference. Current density-voltage (*I*-*V*) curves were measured with a Kethley 2400 source measurement unit. The TEM images were acquired using Hitachi-7600 (Hitachi, Japan). For cross-sectional TEM images of the active layer, the films were sliced using the MTX ultramicrotome (RMC, USA). The AFM images were obtained using Nanoscope IV controller (Veeco Instruments, USA). Surface charge of NPs was monitored by zeta-potential (Zetasizer nano ZS90, Malvern). The thermo-gravimetric analysis (TGA) was performed using SDT Q600 (TA Instruments Inc.). The TGA samples were preheated at 100 °C for 30 min and then the temperature was raised to 800 °C at 10 °C/min in nitrogen.

`

Synthesis of Ag nanoparticles First, 10 g of polyvinylpyrrolidone (PVP; 10,000 g/mol; TCI) was dissolved in 50 mL of ethylene glycol (EG; Samchun). Then, the reaction temperature was increased to 120 °C. Next, 0.8 g of $AgNO_3$ (Aldrich) was dissolved in 5 mL of EG, and the mixture was added to the PVP solution. After 2 h, the brownish dark product was purified by centrifugation to remove the excess PVP (once at 4,000 rpm for 10 min in acetone, and thrice at 17,000 rpm for 10 min in ethanol), and the final Ag NPs were dispersed in ethanol.

Synthesis of Ag@SiO_2 nanoparticles First, 120 mg of Ag NPs was dispersed in 120 mL of ethanol. Then, 0.5 mL of tetraethyl orthosilicate (TEOS; TCI) was added to the Ag NP solution, after which 2.5 mL of ammonia solution (29 %; Samchun) and 2.5 mL of water were added. After 6 h, the product was purified by centrifugation (thrice at 17,000 rpm for 10 min in ethanol), and the final NPs were dispersed in ethanol. All processes were performed at room temperature.

Synthesis of SiO_2 nanoparticles First, 2 mL of TEOS was dissolved in 118 mL of ethanol, and 2.5 mL of ammonia solution and an equal volume of water were added. After the over-night reaction, the product was purified by centrifugation (20,000 rpm, 10 min), and the final NPs were dispersed in ethanol. All processes were performed at room temperature.

Surface modification of nanoparticles with amino-silane group First, 0.1 wt% of 3-trimethoxysilylpropyl)diethylenetriamine (DETAS; Gelest) was added to 3 mg/mL ethanol solution of NPs (silica-coated Ag NPs or silica NPs). After 6 h, the product was purified by centrifugation (thrice at 17,000

`

rpm for 10 min in ethanol), and the final NPs were dispersed in ethanol. All processes were performed at room temperature.

Synthesis of oligothiophene derivatives

3,3''',4',4''''-tetrahexyl-2,2':5',2'':5'',2''':5''',2''''-quinquethiophene (1): ^{1}H NMR (300 MHz, $CDCl_3$, δ): 7.19 (d, J=5.2 Hz, 2H), 7.12 (s, 2H), 6.99 (s, 2H), 6.96 (d, J=5.2 Hz, 2H), 2.82 (t, J=7.2 Hz, 8H), 1.72 (m, 8H), 1.37 (m, 24H), 0.93 (m, 12H). ^{13}C NMR (100 MHz, $CDCl_3$, δ): 139.86, 139.65, 135.75, 134.30, 130.48, 130.25, 130.10, 128.76, 125.86, 123.62, 31.72, 30.75, 30.69, 30.61, 30.33, 29.49, 29.32, 29.30, 29.25, 29.00, 22.67, 14.13; MS (MALDI-TOF) m/z: $[M + H]^+$ calcd. for $C_{57}H_{35}N_3OS_2$, 749.337; found, 749.324.

3,3''',3'''',4'-tetrahexyl-[2,2':5',2'':5'',2''':5''',2''''-quinquethiophene]-5-carbaldehyde (2): ^{1}H NMR (300 MHz, $CDCl_3$, δ): 9.84 (s, 1H), 7.60 (s, 1H), 7.20-7.11 (m, 3H), 6.98-6.92 (m, 3H), 2.88-2.79 (m, 8H), 1.77-1.63 (m, 8H), 1.47-1.25 (m, 24H), 0.93 (m, 12H). ^{13}C NMR (300 MHz, $CDCl_3$, δ): 182.52, 141.18, 140.28, 140.22, 140.09, 139.74, 139.10, 136.54, 134.89, 134.52, 132.78, 132.63, 130.44, 130.33, 130.12, 129.92, 128.76, 126.48, 125.95, 123.70, 31.67, 31.65, 31.60, 30.64, 30.56, 30.52, 30.23, 29.46, 29.42, 29.37, 29.28, 29.25, 29.22, 29.13, 22.62, 22.58, 14.10; MS (ESI-Mass) m/z: $[M + H]^+$ calcd. for $C_{45}H_{60}OS_5$, 777.325; found, 777.510.

(E)-2-cyano-3-(3,3''',3'''',4'-tetrahexyl-[2,2':5',2'':5'',2''':5''',2''''-quinquethiophen]-5-yl)acrylic acid (3): ^{1}H NMR (300 MHz, $CDCl_3$, δ): 8.04 (s, 1H), 7.60 (s, 1H), 7.46 (d, J=5.2 Hz, 1H), 7.25 (s, 1H), 7.24 (s, 1H), 7.22 (s, 1H), 7.06 (s, 1H), 7.04 (d, J=5.2 Hz, 1H), 2.88-2.79 (m, 8H), 1.77-1.63 (m, 8H), 1.47-1.25 (m, 32H), 0.93 (m, 12H); ^{13}C NMR (100 MHz, $CDCl_3$, δ): 173.85, 148.69, 143.97, 143.70, 143.45, 143.34, 140.05, 138.87, 138.20, 136.50, 136.32, 134.24, 133.92, 133.90, 133.79, 132.45, 129.85,

`

129.55, 127.63, 127.44, 122.31, 106.70, 35.54, 35.50, 35.41, 34.45, 34.31, 33.83, 33.39, 33.33, 33.25, 33.11, 33.05, 26.53, 26.50, 26.45, 17.86; MS (MALDI-TOF) m/z: $[M + H]^+$ calcd. for $C_{48}H_{61}NO_2S_5$, 844.338; found, 844.282.

(E)-2,5-dioxopyrrolidin-1-yl 2-cyano-3-(3,3''',3'''',4'-tetrahexyl-[2,2':5',2'':5'',2''':5''',2''''-quinquethiophen]-5-yl)acrylate (4): A mixture of (3) (0.178 g, 0.21 mmol), N-hydroxysuccinimide (1.05 mmol) and EDC (2.1 mmol) in dichloromethane (20 mL) was stirred at room temperature for 24 h. The mixture was extracted by dichloromethane and then the solvent was removed under reduced pressure. The residue was filtered by dichloromethane/hexane. Yield 74% (0.147 g). Dark red solid, ^{1}H NMR (300 MHz, $CDCl_3$, δ): 8.29 (s, 1H), 7.65 (s, 1H), 7.24-7.11 (m, 4H), 6.94-6.91 (m, 2H), 2.88-2.79 (m, 8H), 1.77-1.63 (m, 8H), 1.47-1.25 (m, 36H), 0.93 (m, 12H); ^{13}C NMR (100 MHz, $CDCl_3$, δ): 168.60, 159.42, 149.04, 145.76, 143.47, 140.87, 140.58, 140.22, 139.78,

137.00, 134.68, 134.59, 134.55, 132.28, 131.84, 131.68, 130.30, 130.13, 129.82, 128.77, 126.74, 125.99, 123.75, 114.59, 31.67, 31.65, 31.61, 31.55, 30.62, 29.92, 29.49, 29.43, 29.34, 29.29, 29.24, 29.19, 29.12, 25.59, 22.61, 22.56, 14.08, 14.05; MS (MALDI-TOF) m/z: $[M + H]^+$ calcd. for $C_{52}H_{64}N_2O_4S_5$, 941.354; found, 941.365.

Surface modification of nanoparticles with oligothiophene group First, 0.1 wt% of a pre-synthesized oligothiophene derivative in chloroform was added to 3 mg/mL ethanol:chloroform (1:1 v/v) mixed solution of NPs ($Ag@SiO_2$–DETAS or SiO_2–DETAS). After 6 h, the product was purified by centrifugation (once at 17,000 rpm for 10 min in ethanol, and twice at 17,000

`

rpm for 10 min in chloroform), and the final NPs were dispersed in chloroform. All processes were performed at room temperature.

Simple calculation of the number of attached OT group When 120 mg of Ag NPs were coated with SiO_2, about 180 mg of Ag@SiO_2 was obtained. It means the weight ratio of Ag:SiO_2 is 2:1 (density of Ag = 10.49 g/cm^2 , SiO_2 = 2.2 g/cm^2). Assuming Ag@SiO_2 has a perfect spherical core-shell structure, the diameter of Ag and thickness of SiO_2 could be approximated to 30 nm and 10 nm, respectively, from the weight ratio and TEM size. Using calculated size and thickness, the amount of OT in Ag@SiO_2–OT from TGA (4 %), and the molecular weight of OT (828.32 g/mol), other parameters in the following table could be calculated. (see Table 2.)

Table 2.2. The parameter for a calculation of the number of attached OT group

The weight of each particle	2.2×10^{-13} mg/ea
The surface area of each particle	6362 nm^2/ea
The number of OT in 1 mg of particle	4.8×10^{-8} mol
The number of the attached OT group on each particle	9.4×10^{-21} mol/ea or 5700/ea
The number of the attached OT on nm^2 (packing density)	0.89/nm^2

`

Device fabrication Indium tin oxide (ITO)-coated glass, which was cleaned by ultrasonication with detergent, followed by distilled water and 2-propanol sequentially, was used as a transparent electrode. The ITO surface was modified by spin-coating of a 40-nm-thick PEDOT:PSS layer after exposing the ITO surface to ozone for 10 min. The PEDOT:PSS layer was dried on a hot plate in air for 20 min at 140 °C. The reference solution consists of 20 mg/mL of P3HT and PCBM (1:0.8, w/w) in chlorobenzene (CB). To prepare the hybrid solutions, NPs were added to the reference solution at various ratios (1–30 wt%, w/w). The active layer was spin-coated from these solutions over the dried PEDOT:PSS layer at room temperature. The active layer was heated on a hot plate for 10 min at 140 °C. After drying the active layer, LiF (1 nm) and Al metal (100 nm) were deposited as the cathode under vacuum below 10^{-6} Torr, which yielded an active area of 4 mm^2 per pixel. Photovoltaic performance of all devices was investigated at one sun intensity (100 mW cm^{-2}) under simulated AM 1.5G illumination.

For the TEM images of the microtomed samples, the PEDOT:PSS layer was prepared on glass, and an active layer with 3 wt% (w/w) Ag@SiO_2–OT NPs was prepared on the PEDOT:PSS layer. After the entire layer was well dried, only the active layer with the Ag@SiO_2–OT NPs was obtained from the floating film on the water, because the PEDOT:PSS layer was dissolved out by water. Then, the floating film was introduced in an epoxy resin and sliced by an ultramicrotome.

`

*** Contributions**

Synthesis of OT derivatives and photovoltaic cell test were done by Dr. Woochul Lee and Prof. Jong-In Hong in Department of Chemistry, Seoul National University.

2.6. References

[1] Li, Y., *Acc Chem Res* **2012**, *45*, 723-733.

[2] Seo, J. H.; Gutacker, A.; Sun, Y.; Wu, H.; Huang, F.; Cao, Y.; Scherf, U.; Heeger, A. J.; Bazan, G. C., *J. Am. Chem. Soc.* **2011**, *133*, 8416-8419.

[3] Li, G.; Zhu, R.; Yang, Y., *Nat. Photon.* **2012**, *6*, 153-161.

[4] Liang, Y.; Xu, Z.; Xia, J.; Tsai, S. T.; Wu, Y.; Li, G.; Ray, C.; Yu, L., *Adv. Mater.* **2010**, *22*, E135-138.

[5] He, Z.; Zhong, C.; Su, S.; Xu, M.; Wu, H.; Cao, Y., *Nat. Photon.* **2012**, *6*, 591-595.

[6] Mishra, A.; Bauerle, P., *Angew. Chem. Int. Ed.* **2012**, *51*, 2020-2067.

[7] Shaw, P. E.; Ruseckas, A.; Samuel, I. D. W., *Adv. Mater.* **2008**, *20*, 3516-3520.

[8] Goesmann, H.; Feldmann, C., *Angew. Chem. Int. Ed.* **2010**, *49*, 1362-1395.

[9] Atwater, H. A.; Polman, A., *Nat. Mater.* **2010**, *9*, 205-213.

[10] Wang, D. H.; Park, K. H.; Seo, J. H.; Seifter, J.; Jeon, J. H.; Kim, J. K.; Park, J. H.; Park, O. O.; Heeger, A. J., *Adv. Energy Mater.* **2011**, *1*, 766-770.

[11] Chen, H. C.; Chou, S. W.; Tseng, W. H.; Chen, I. W. P.; Liu, C. C.; Liu, C.; Liu, C. L.; Chen, C. H.; Wu, C. I.; Chou, P. T., *Adv. Funct. Mater.* **2012**, *22*, 3975-3984.

[12] Wang, D. H.; Kim do, Y.; Choi, K. W.; Seo, J. H.; Im, S. H.; Park, J. H.; Park, O. O.; Heeger, A. J., *Angew. Chem. Int. Ed.* **2011**, *50*, 5519-5523.

[13] Xie, F.-X.; Choy, W. C. H.; Wang, C. C. D.; Sha, W. E. I.; Fung, D. D. S.,

`
Appl. Phys. Lett. **2011**, *99*, 153304-153303.

[14] Daniel, M.-C.; Astruc, D., *Chem. Rev.* **2003**, *104*, 293-346.

[15] Rycenga, M.; Cobley, C. M.; Zeng, J.; Li, W.; Moran, C. H.; Zhang, Q.; Qin, D.; Xia, Y., *Chem. Rev.* **2011**, *111*, 3669-3712.

[16] Kim, C. H.; Cha, S. H.; Kim, S. C.; Song, M.; Lee, J.; Shin, W. S.; Moon, S. J.; Bahng, J. H.; Kotov, N. A.; Jin, S. H., *ACS Nano* **2011**, *5*, 3319-3325.

[17] Li, X. H.; Choy, W. C. H.; Lu, H. F.; Sha, W. E. I.; Ho, A. H. P., *Adv. Funct. Mater.* **2013**, *23*, 2728-2735.

[18] Noh, H. S.; Cho, E. H.; Kim, H. M.; Han, Y. D.; Joo, J., *Org. Electron.* **2013**, *14*, 278-285.

[19] Gan, Q.; Bartoli, F. J.; Kafafi, Z. H., *Adv. Mater.* **2013**, *25*, 2385-2396.

[20] Wu, J. L.; Chen, F. C.; Hsiao, Y. S.; Chien, F. C.; Chen, P.; Kuo, C. H.; Huang, M. H.; Hsu, C. S., *ACS Nano* **2011**, *5*, 959-967.

[21] Chen, F.-C.; Wu, J.-L.; Lee, C.-L.; Hong, Y.; Kuo, C.-H.; Huang, M. H., *Appl. Phys. Lett.* **2009**, *95*, 013305-013303.

[22] Feng, Q.; Lu, X.; Zhou, G.; Wang, Z.-S., *PCCP* **2012**, *14*, 7993-7999.

[23] Salvador, M.; MacLeod, B. A.; Hess, A.; Kulkarni, A. P.; Munechika, K.; Chen, J. I.; Ginger, D. S., *ACS Nano* **2012**, *6*, 10024-10032.

[24] Xue, M.; Li, L.; de Villers, B. J. T.; Shen, H.; Zhu, J.; Yu, Z.; Stieg, A. Z.; Pei, Q.; Schwartz, B. J.; Wang, K. L., *Appl. Phys. Lett.* **2011**, *98*, 253302-253303.

[25] Topp, K.; Borchert, H.; Johnen, F.; Tunc, A. V.; Knipper, M.; von Hauff, E.; Parisi, J.; Al-Shamery, K., *J. Phys. Chem. A* **2009**, *114*, 3981-3989.

[26] Kim, K.; Carroll, D. L., *Appl. Phys. Lett.* **2005**, *87*, 203113-203113.

[27] Jankovic, V.; Yang, Y. M.; You, J.; Dou, L.; Liu, Y.; Cheung, P.; Chang, J. P.; Yang, Y., *ACS Nano* **2013**, *7*, 3815-3822.

[28] Choi, H.; Lee, J. P.; Ko, S. J.; Jung, J. W.; Park, H.; Yoo, S.; Park, O.;

`

Jeong, J. R.; Park, S.; Kim, J. Y., *Nano Lett* **2013**, *13*, 2204-2208.

[29] Xu, X.; Kyaw, A. K. K.; Peng, B.; Zhao, D.; Wong, T. K. S.; Xiong, Q.; Sun, X. W.; Heeger, A. J., *Org. Electron.* **2013**, *14*, 2360-2368.

[30] Silvert, P.-Y.; Herrera-Urbina, R.; Duvauchelle, N.; Vijayakrishnan, V.; Elhsissen, K. T., *J. Mater. Chem.* **1996**, *6*, 573-577.

[31] Arifin, E.; Lee, J.-K., *Bull. Korean Chem. Soc.* **2013**, *34*, 539-544.

[32] Yang, J.; Zhang, F.; Chen, Y.; Qian, S.; Hu, P.; Li, W.; Deng, Y.; Fang, Y.; Han, L.; Luqman, M.; Zhao, D., *Chem. Commun.* **2011**, *47*, 11618-11620.

[33] Graf, C.; Vossen, D. L. J.; Imhof, A.; van Blaaderen, A., *Langmuir* **2003**, *19*, 6693-6700.

[34] Jung, H.-S.; Moon, D.-S.; Lee, J.-K., *J Nanomater.* **2012**, *2012*, 8-15.

[35] Li, Z.; He, G. R.; Wan, X. J.; Liu, Y. S.; Zhou, J. Y.; Long, G. K.; Zuo, Y.; Zhang, M. T.; Chen, Y. S., *Adv. Energy Mater.* **2012**, *2*, 74-77.

[36] Lee, W.; Cho, N.; Kwon, J.; Ko, J.; Hong, J.-I., *Chem. Asian J.* **2012**, *7*, 343-350.

[37] Liu, Y.; Zhou, J.; Wan, X.; Chen, Y., *Tetrahedron* **2009**, *65*, 5209-5215.

[38] Jain, P. K.; El-Sayed, M. A., *Nano Lett.* **2008**, *8*, 4347-4352.

[39] Dang, M. T.; Hirsch, L.; Wantz, G.; Wuest, J. D., *Chem. Rev.* **2013**, *113*, 3734-3765.

[40] Wu, B.; Wu, X.; Guan, C.; Fai Tai, K.; Yeow, E. K.; Jin Fan, H.; Mathews, N.; Sum, T. C., *Nat. Commun.* **2013**, *4*, 2004.

[41] Gu, Y.; Wang, C.; Russell, T. P., *Adv. Energy Mater.* **2012**, *2*, 683-690.

[42] Lee, J. K.; Ma, W. L.; Brabec, C. J.; Yuen, J.; Moon, J. S.; Kim, J. Y.; Lee, K.; Bazan, G. C.; Heeger, A. J., *J. Am. Chem. Soc.* **2008**, *130*, 3619-3623.

[43] Cook, S.; Ohkita, H.; Kim, Y.; Benson-Smith, J. J.; Bradley, D. D. C.; Durrant, J. R., *Chem. Phys. Lett.* **2007**, *445*, 276-280.

`

Appendix/Chapter 3.

Fullerene Derivative-modified Silver@Silica Core@Shell Nanoparticles as an Acceptor for Polymer Solar Cells

3.1 Introduction

Recently, silica layer have been introduced on the metal nanoparticles (NPs) for inhibiting aggregation between metal NPs and charge trapping on the surface of metal NPs.[1-3] Furthermore, the surface modification of silica layer was the effective way of introducing metal NPs to the active layer of polymer solar cells because hydrophilic surface of silica was not soluble to non-polar solvent such as chloroform or chlorobenzene which are widely using solvent for donor and acceptor materials. Long alkyl chain like hexadecyl or octadecyl group was introduced on the surface of silica layer to give hydrophobic character to the NPs.[4, 5] Derivative of donor material, poly(3-hexylthiophene) (P3HT) was also introduced to the surface of NPs to prepare miscible NPs in active layer.[6] However, introducing acceptor materials on the silica layer for the polymer solar cells application was rarely reported.

Fullerene derivatives which are represented by phenyl-C61-butyric acid methyl ester (PCBM) have been widely used as the acceptor in polymer solar cells.[7] These fullerene family have been coupled with silica for the separation application such as chromatography[8, 9] but not for the solar cells.

In this chapter, silica layer of silver-silica core-shell NPs ($Ag@SiO_2$) was modified with the derivative of bis[60]PCBM (BP). BP was prepared from

`

bis[60]PCBM though two step reaction including acidification and EDC coupling. And than, BP was coupled with ammine-modified Ag@SNPs (Ag@SiO_2-BP). Finally, Ag@SiO_2-BP was used as donor material in the polymer solar cells.

3.2 Results and Discussion

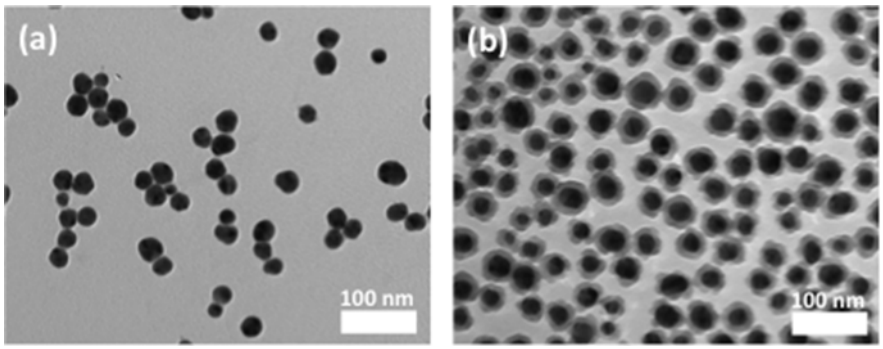

Figure 3.1. TEM images of (a) Ag NPs and (b) Ag@SiO_2 NPs.

Synthesis of Ag@SiO_2−BP NPs Ag@SiO_2-BP NPs were prepared using the same method with Ag@SiO_2-OT NPs in Appendix/Chapter 2 except using BP instead of OT derivative.[6] Figure 3.1 shows Ag NPs and Ag@SiO_2 NPs used in this chapter and the entire preparation scheme is represented in scheme 3.1. For the coupling with BP derivative, amine group was introduced using 3-trimethoxysilylpropyl)diethylenetriamine (DETAS).

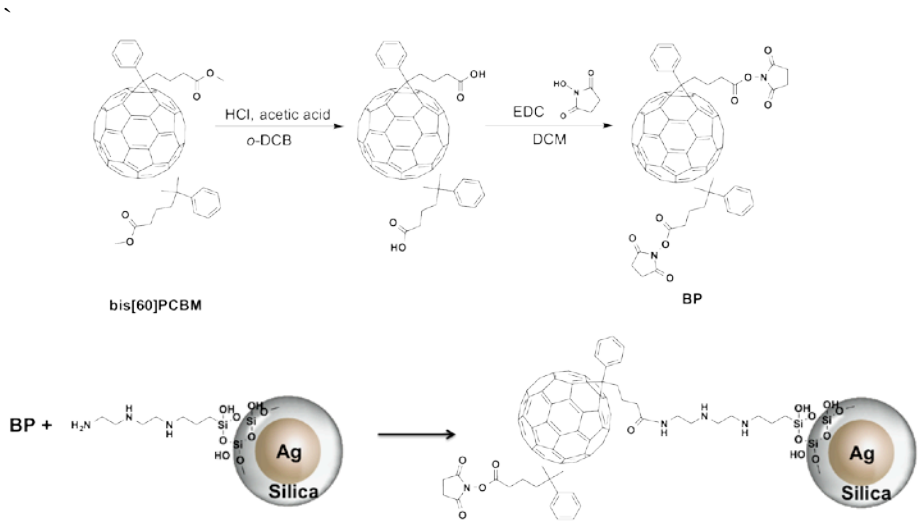

Scheme 3.1. Synthetic routes for BP and surface-modified Ag NPs.

For introducing bis[60]PCBM moiety on the surface of silica layer, bis[60]PCBM was modified to have good leaving group.[6,10] First, bis[60]PCBM was acidified to have carboxylic acid group instead of methyl ether group. And than, N-hydroxysuccinimide (NHS) as a good leaving group was introduced with 1-ethyl-3-(3-dimethylaminopropyl)-carbodiimide (EDC).

Final product of two-step reaction, BP, was confirmed using NMR and MALDI-MS. Figure 3.2 shows the ^{1}H NMR spectrum of bis[60]PCBM and BP. Synthesis of BP was well confirmed by the disappearing the peaks of methyl ether and increasing the alkyl peaks due to the introduced succinimide groups. MALDI-TOF also confirmed the successful preparation of BP. Mass from bis[60]PCBM, m/z: $[M + H]^{+}$ = 1102.4, was increased to have $[M + H]^{+}$ = 1267.4 of BP, which indicate succinimide groups was introduce to both two functional groups.

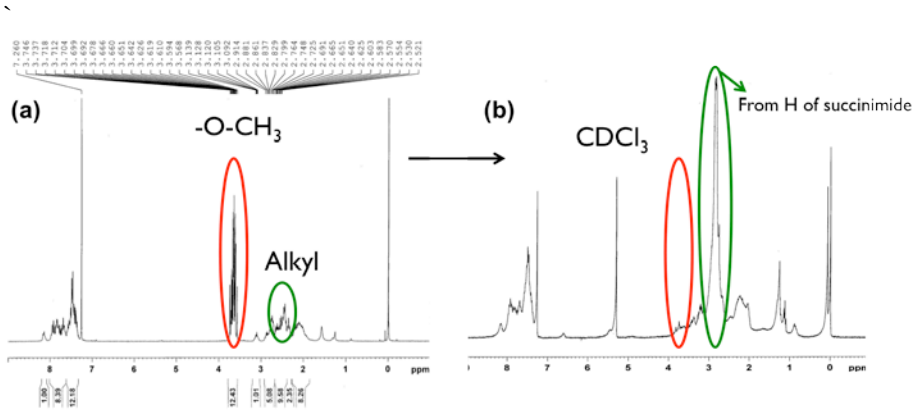

Figure 3.2. ^{1}H NMR spectum of (a) bis[60]PCBM and (b) BP.

BP was liked to the surface of silica layer by nucleophilic addition of amine in Ag@SiO_2-DETAS. The existence of organic group on the NPs was confirmed by using thermogravimetric analysis (TGA) in Figure 3.3.

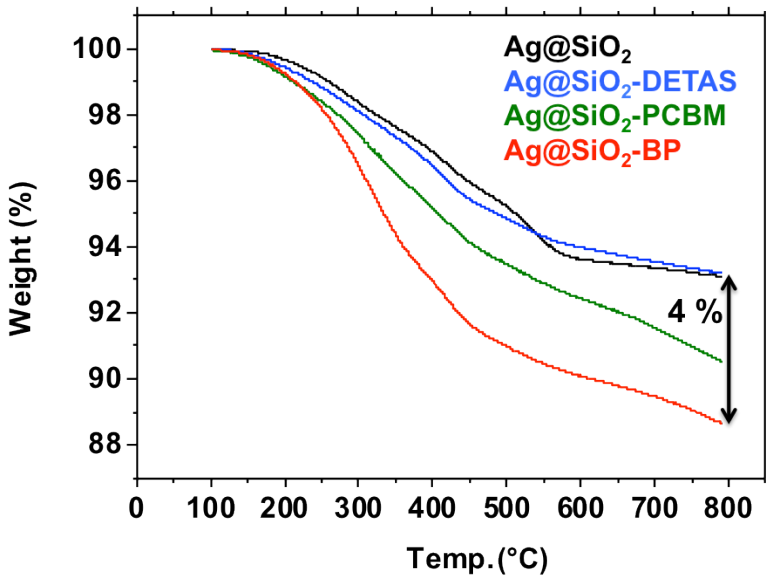

Figure 3.3. TGA resuls of surface modified Ag NPs.

`

When the temperature was raised from 100 to 800 °C, the weight loss of $Ag@SiO_2$ NPs was approximately 7 wt%, which could be caused by the elimination of water and decomposition of organic molecules such as the remaining ethoxy group and PVP. TGA analysis of $Ag@SiO_2$–DETAS also showed very similar weight loss to that of $Ag@SiO_2$, which is probably due to a relatively small weight portion of DETAS monolayer compared to heavy $Ag@SiO_2$ particle itself. However, in the case of $Ag@SiO_2$–BP, the total weight loss increased to 11 % showing 4 % point more weight loss from the attached BP groups. PCBM was also introduced but $Ag@SiO_2$-PCBM form big aggregate and not well dispersed in organic solvent such as chloroform and chlorobenzene.

In order to use $Ag@SiO_2$-BP as an acceptor with P3HT in polymer solar cells, well dispersable property in chloroform or chlorobenzene is very important. So the dispersability of $Ag@SiO_2$-BP was tested in chloroform for 24 hr (Figure 3.4).

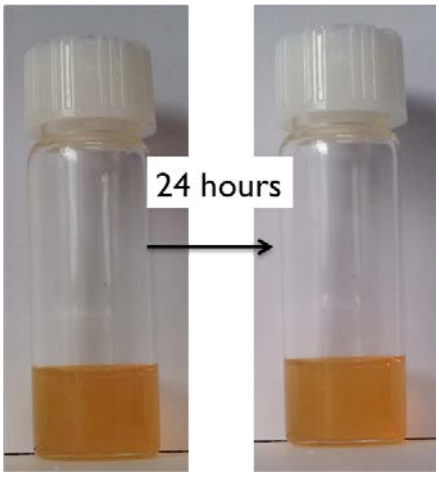

Figure 3.4. Well dispersable character of $Ag@SiO_2$-BP in chloroform solution.

`

In contrast to the low dispersity of Ag@SiO_2-PCBM, Ag@SiO_2-BP showed good dispersity in chloroform even after 24 hr. PCBM is typical and widely used soluble fullerene derivative for their functional group.[11] But in this case, functional group of PCBM was modified to coupling with NPs, which might the main reason of low dispersity of Ag@SiO_2-PCBM. However, bis[60]PCBM have two identical functional group and one of it could be still free after coupling with NPs giving well soluble property to Ag@SiO_2-BP.

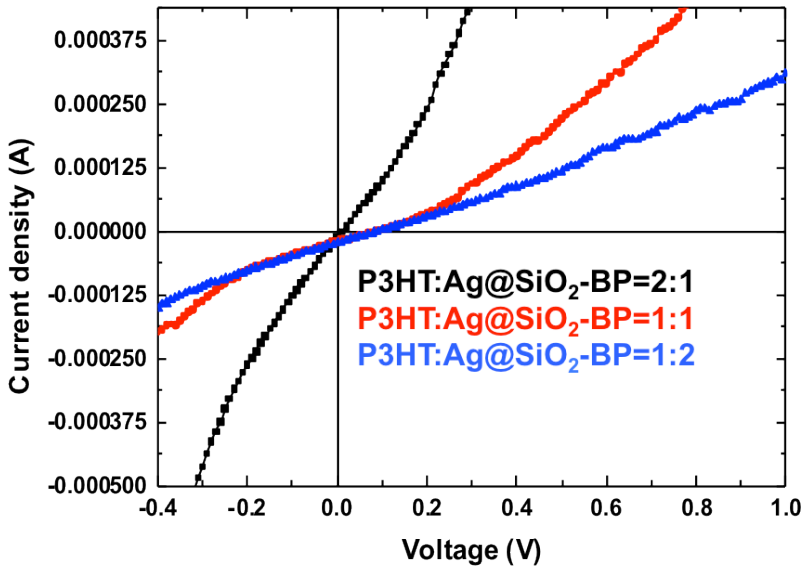

Figure 3.5. *I-V* curves of of P3HT: Ag@SiO_2-BP based solar cells.

`

Photovoltaic device performance In order to make polymer solar cells using Ag@SiO_2-PCBM as only acceptor material, the photovoltaic devices were fabricated with various composite layers of Ag@SiO_2-PCBM having different mixing ratios (2:1, 1:1, and 1:2 w/w) of P3HT to Ag@SiO_2-PCBM. The total concentration of all of devices was consistent (2 wt% w/v). The photovoltaic performances and *I-V* curves of these devices are shown in Figure 3.5.

But the short-circuit current (J_{sc}) and open circuit voltage (V_{oc}) values of the photovoltaic devices having the composite layers of Ag@SiO_2-PCBM was almost meaningless. Although the values were increased a little with increasing ratio of P3HT, all devices were not thought to work as photovoltaic cell. It seems that P3HT and Ag@SiO_2-PCBM could not form the effective bulk-heterojunction layer to extract electron and hole to external electrode.

3.3 Conclusions

In this chapter, silver-silica core-shell NPs were synthesized and deliberately modified their surface with BP in order to use as an accepter material in polymer solar cells. Ag@SiO_2–BP NPs were well dispersable in chloroform due to the additional functional group in fullerene unit. The photovoltaic cells using Ag@SiO_2–BP NPs as an acceptor material showed meaningless current and voltage. Further studies are needed to use Ag@SiO_2–OT NPs as acceptor materials.

`

3.4 Experimental Section

Materials and Instruments All organic chemicals were purchased from Aldrich and TCI. Solar cell materials P3HT and PCBM were purchased from Rieke Metals and Nano-C (USA), respectively. Bis[60]PCBM was purchased from Solenne BV (Netherlands). Poly(styrene sulfonate) doped poly(ethylenedioxythiophene) (PEDOT:PSS, Clevious PH) was purchased from Bayer. All solvents and reagents used in this study were commercially available and used without further purification unless otherwise specified.

^{1}H NMR spectra were recorded using either an Advance 300 MHz Bruker spectrometer. The mass spectra were obtained using a gas chromatograph-mass spectrometer (JEOL, JMS-AX505WA, HP 5890 Series II). The device performance was measured under AM 1.5G illumination (100 mW cm^{-2}) using a solar simulator (Peccell, Japan) and Solar Cell IPCE Measurement System (McScience, K3100). The light intensity at each wavelength was calibrated using a standard Si solar cell as a reference. Current density-voltage (*I-V*) curves were measured with a Kethley 2400 source measurement unit. The TEM images were acquired using Hitachi-7600 (Hitachi, Japan). Surface charge of NPs was monitored by zeta-potential (Zetasizer nano ZS90, Malvern). The thermo-gravimetric analysis (TGA) was performed using SDT Q600 (TA Instruments Inc.). The TGA samples were preheated at 100 °C for 30 min and then the temperature was raised to 800 °C at 10 °C/min in nitrogen.

Synthesis of Ag nanoparticles First, 10 g of polyvinylpyrrolidone (PVP; 10,000 g/mol; TCI) was dissolved in 50 mL of ethylene glycol (EG; Samchun). Then, the reaction temperature was increased to 120 °C. Next,

`

0.8 g of $AgNO_3$ (Aldrich) was dissolved in 5 mL of EG, and the mixture was added to the PVP solution. After 2 h, the brownish dark product was purified by centrifugation to remove the excess PVP (once at 4,000 rpm for 10 min in acetone, and thrice at 17,000 rpm for 10 min in ethanol), and the final Ag NPs were dispersed in ethanol.

Synthesis of Ag@SiO_2 nanoparticles First, 120 mg of Ag NPs was dispersed in 120 mL of ethanol. Then, 0.5 mL of tetraethyl orthosilicate (TEOS; TCI) was added to the Ag NP solution, after which 2.5 mL of ammonia solution (29 %; Samchun) and 2.5 mL of water were added. After 6 h, the product was purified by centrifugation (thrice at 17,000 rpm for 10 min in ethanol), and the final NPs were dispersed in ethanol. All processes were performed at room temperature.

Surface modification of nanoparticles with amino-silane group First, 0.1 wt% of DETAS (Gelest) was added to 3 mg/mL ethanol solution of NPs (silica-coated Ag NPs or silica NPs). After 6 h, the product was purified by centrifugation (thrice at 17,000 rpm for 10 min in ethanol), and the final NPs were dispersed in ethanol. All processes were performed at room temperature.

Synthesis of bis[60]PCBM derivatives

Acidification of bis[60]PCBM The concentrated hydrochloric acid (0.6 mL) and acetic acid (2.1 mL) were added to a 30 mg of bis[60]PCBM in 1 mL of 1,2 dichlorobenzene (*o*-DCB). The mixture was heated to 120 °C for 6 hr. The solvent was removed *in vacuo* and the precipitate was collected by

`

filtration. The crude product was washed with methanol and a solvent mixture of methanol:diethylether (1:1 v/v) several times and dried for further reaction.

BP Acidified bis[60]PCBM was dissolved in 20 mL of dichloromethane with 19.4 mg of NHS and 65.3 mg of EDC. The mixture was vigorously stirred at room temperature for 24 hr. The solvent was removed *in vacuo* and the precipitate was collected by filtration. The crude product was washed with methanol and several times and dried for further reaction. The course of the reaction was followed by TLC (after complete conversion, R_f is 0.0). MS (MALDI-TOF) m/z: [M + H]+ calcd. 1267.6; found, 1267.5.

Device fabrication Indium tin oxide (ITO)-coated glass, which was cleaned by ultrasonication with detergent, followed by distilled water and 2-propanol sequentially, was used as a transparent electrode. The ITO surface was modified by spin-coating of a 40-nm-thick PEDOT:PSS layer after exposing the ITO surface to ozone for 10 min. The PEDOT:PSS layer was dried on a hot plate in air for 20 min at 140 °C. The reference solution consists of 20 mg/mL of P3HT and Ag@SiO_2–BP NPs in chlorobenzene. To prepare the hybrid solutions, NPs were added to the reference solution at various ratios (2:1, 1:1 and 1:2 w/w, P3HT: Ag@SiO_2–BP). The active layer was spin-coated from these solutions over the dried PEDOT:PSS layer at room temperature. The active layer was heated on a hot plate for 10 min at 120 °C. After drying the active layer, LiF (1 nm) and Al metal (100 nm) were deposited as the cathode under vacuum below 10^{-6} Torr, which yielded an active area of 4 mm^2 per pixel. Photovoltaic performance of all devices

`

was investigated at one sun intensity (100 mW cm^{-2}) under simulated AM 1.5G illumination.

Mass (MALDI-TOF) data of bis[60]PCBM derivatives

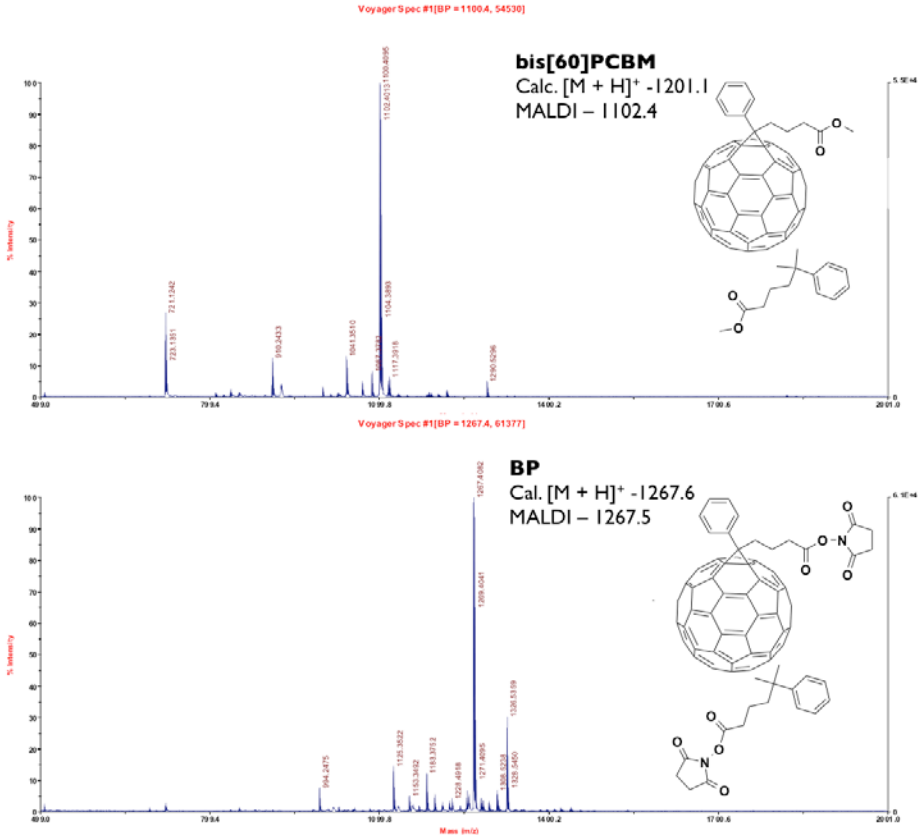

*** Contributions**

Photovoltaic cell test was done by Dr. Woochul Lee and Prof. Jong-In Hong in Department of Chemistry, Seoul National University.

`

3.5 References

[1] Choi, H.; Lee, J.-P.; Ko, S.-J.; Jung, J.-W.; Park, H.; Yoo, S.; Park, O.; Jeong, J.-R.; Park, S.; Kim, J. Y., *Nano Lett.* **2013**, *13*, 2204-2208.

[2] Wu, B.; Wu, X.; Guan, C.; Fai Tai, K.; Yeow, E. K.; Jin Fan, H.; Mathews, N.; Sum, T. C., *Nat. Commun.* **2013**, *4*, 2004.

[3] Salvador, M.; MacLeod, B. A.; Hess, A.; Kulkarni, A. P.; Munechika, K.; Chen, J. I. L.; Ginger, D. S., *Acs Nano* **2012**, *6*, 10024-10036.

[4] Xu, X.; Kyaw, A. K. K.; Peng, B.; Zhao, D.; Wong, T. K. S.; Xiong, Q.; Sun, X. W.; Heeger, A. J., *Org. Electron.* **2013**, *14*, 2360-2368.

[5] Jankovic, V.; Yang, Y.; You, J.; Dou, L.; Liu, Y.; Cheung, P.; Chang, J. P.; Yang, Y., *ACS Nano* **2013**, *7*, 3815-3822.

[6] Lee, W.; Lim, J.; Lee, J.-K.; Hong, J.-I., *J. Mater. Chem. A* **2014**, *2*, 15357-15364.

[7] Roncali, J., *Acc. Chem. Res.* **2009**, *42*, 1719-1730.

[8] Jinno, K.; Tanabe, K.; Saito, Y.; Nagashima, H., *Analyst* **1997**, *122*, 787-791.

[9] Vallant, R. M.; Szabo, Z.; Bachmann, S.; Bakry, R.; Najam-ul-Haq, M.; Rainer, M.; Heigl, N.; Petter, C.; Huck, C. W.; Bonn, G. K., *Anal. Chem.* **2007**, *79*, 8144-8153.

[10] Kim, B.; Yeom, H. R.; Choi, W.-Y.; Kim, J. Y.; Yang, C., *Tetrahedron* **2012**, *68*, 6696-6700.

[11] Hummelen, J. C.; Knight, B. W.; LePeq, F.; Wudl, F.; Yao, J.; Wilkins, C. L., *J. Org. Chem.* **1995**, *60*, 532-538.

`

Appendix/Chapter 4.

Colloidal Photonic Crystal Structure from Surface Modified TiO_2 Nanoparticles under the Electric Field.

Published as *Appl. Phys. Lett.* **2012**, *100*, 063113.

4.1 Abstract

The tunable photonic crystal behavior of highly concentrated, mildly charged TiO_2 nanoparticle colloids under external electric field is reported. Reflectance intensity change at the certain photonic bandgap and its irreversible switching characteristics are observed and discussed.

Through computer-aided numerical analysis, gradient spacing between charged particles is predicted under electric field, which is well coincidence with experimental results. Also, it is reported that the experimental evidence which the charged nanoparticle can play the role as a major charge carrier in non-aqueous liquid. Its short range moving and stacking on electrode cause the capacitive current flow and charge accumulation like ions in liquid state.

`

4.2 Introduction

Charged colloids are responsive to the electric field and exhibit electrophoretic movement to the direction of oppositely charged electrode. This concept has been used in many basic sciences to separate molecules,[1] to measure zetapotential of particle,[2] to deposit colloidal particle,[3] and even to applied engineering, i.e., e-ink display.[4] At a very high concentration, charged monodisperse colloid dispersed in preferentially polar solvent sometimes exhibits photonic stop band, which prohibits certain frequency range of light corresponding to the periodic structure composed of colloid and dispersion medium.[5–7] The long range self-assembly due to electrostatic repulsion is a main driving force to form periodic structure. Recently, there has been great attention to modulate lattice parameter of highly charged colloids through manipulating electric field in order to utilize them to create tunable photonic crystal for display application.[5,8] However, little has been reported on the behavior of highly concentrated, mildly charged colloids under electric field. To this end, the observation of unexpected behavior of positively charged TiO_2 nanoparticle dispersed in ethylene glycol at a very high concentration is reported. The reflection spectrum of colloidal dispersion has been monitored during switching potential to investigate the interesting phenomena of changing spectral reflectance and interpret the unusual short-range repulsive interactions of the colloid. A simulation work using numerical analysis method supports our interpretation of the experimental results.

`

4.3 Results and Discussion

TiO_2 nanoparticles were synthesized by using modified sol-gel synthesis.[9] Scanning electron microscopy (SEM), transmission electron microscopy (TEM), and dynamic light scattering (DLS) system were used to evaluate TiO_2 nanoparticles shape, diameter, and polydispersity index (PDI) (Figure 4.1). The average diameter and PDI of slightly lumpy sphere shape nanoparticles are about 103 nm and 0.1, respectively.

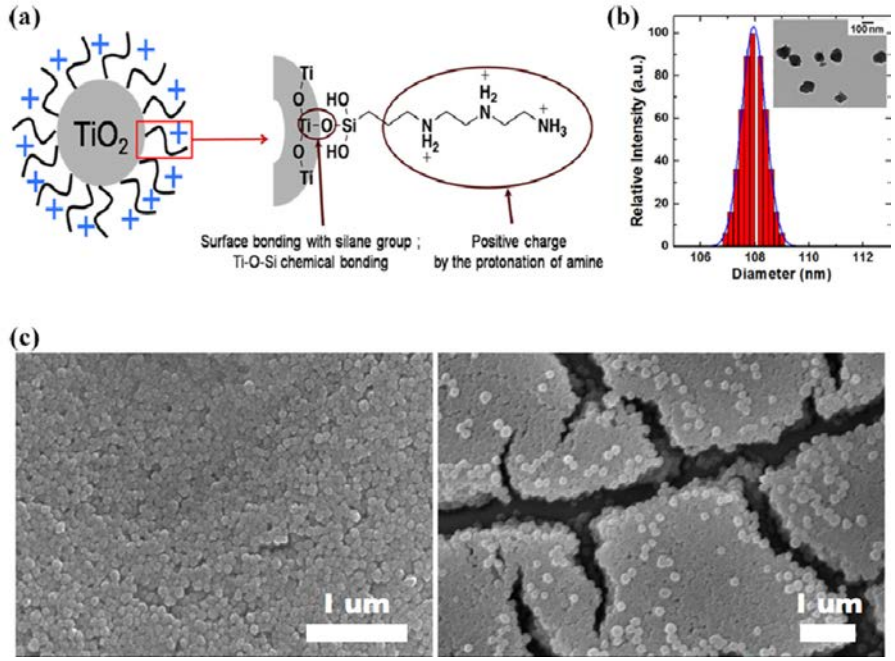

Figure 4.1. (a) A schematic view of positively charged TiO_2 nanoparticle; (b) Particle size distribution and TEM image (inset) of the synthesized TiO_2 nanoparticles; (c) SEM images of the colloidal layers after drying. Left one is formed by colloidal solution dropping on the glass in the air and the right one is formed on electrode surface in the test cell after applying voltage.

`

A silane coupling agent, (3-trimethoxysilylpropyl) diethylenetriamine (DETAS), was introduced to modify the surface charge of TiO_2 nanoparticles. Due to positively charged amine functional groups in DETAS (pKa values of three amino groups are 9.9, 9.1, and 4.3 respectively.10), modified nanoparticles have positive zeta potential of -56 mV. Positively modified TiO_2 nanoparticles were injected between two electrodes and the spectrophotometric setup was assembled similar to described elsewhere in the literature.[11]

Figure 4.2a shows the reflectance spectra of the test cell under external electric field. A reflection peak at 352 nm corresponding to certain lattice constant of Face Centered Cubic (FCC) structure is observed, which indicates a formation of a periodic dielectric structure. As is shown in Figure 4.1c, the nanoparticle assembles into a fairly periodic structure after applying electric field to the colloidal dispersion. Although photonic crystal properties are described exactly by Maxwell equations,[12] the reflectance spectral property of the normal incidence angle to FCC structure is simply approximated by combining the law of reflection with Snell's law and Bragg's law as follows:[13]

$$\lambda = 2 \cdot \sqrt{\frac{2}{3}} \cdot D \cdot n_{eff} \quad , (1)$$

where λ is the light wavelength of the fundamental frequency of reflection, D is pore spacing, and $n_{eff} = (\theta \cdot n_{sphere} + (1 - \theta) \cdot n_{background,}$ θ: solid fraction) is the effective refractive index of periodic FCC structure. For calculating wavelength of reflection maximum, the refractive index of TiO_2 nanoparticle was carefully decided as 2.3

`

considering several literatures which mentioned the refractive index of amorphous TiO_2[14–17] and its remarkably rising trend in the near UV region. The diameter of TiO_2 nanoparticle and refractive index of ethylene glycol are considered as 100 nm and 1.5, respectively. A 350 nm, which is very similar to the experimental result (352 nm), was predicted as peak position when inter particle distance is 10 nm. Figure 4.2a also shows a dramatic change of the reflection peak maximum value in response to applied electric field of ± 3 V along time. When upper ITO electrode is negatively biased, the peak optical density is gradually increased, whereas inversed electric field induces the degradation of peak intensity. The position of peak maximum is maintained during whole cycle, which means that the lattice constant of colloidal photonic crystal is not varied.

To understand and predict the behavior of charged particle movement in highly concentrated colloidal solution under the electric field, computer aided simulation was performed using numerical analysis. A part of simulation result and related schematic diagram are shown in Figure 4.2b. This figure illustrates a trend of the distance change between particles for z-coordinate projection along time under certain external electric field. The gap distances between adjacent particles are not even in the highly condensed colloidal system. As the particle is approached to the wall by electrostatic force, the gap distance is gradually narrowed due to the cumulated interactions from not only adjacent particle but several surrounding ones. This re-arrangement of the particles in response to the applied electrical potential is a time dependent process as is schematically described in Figure 4.2b.

`

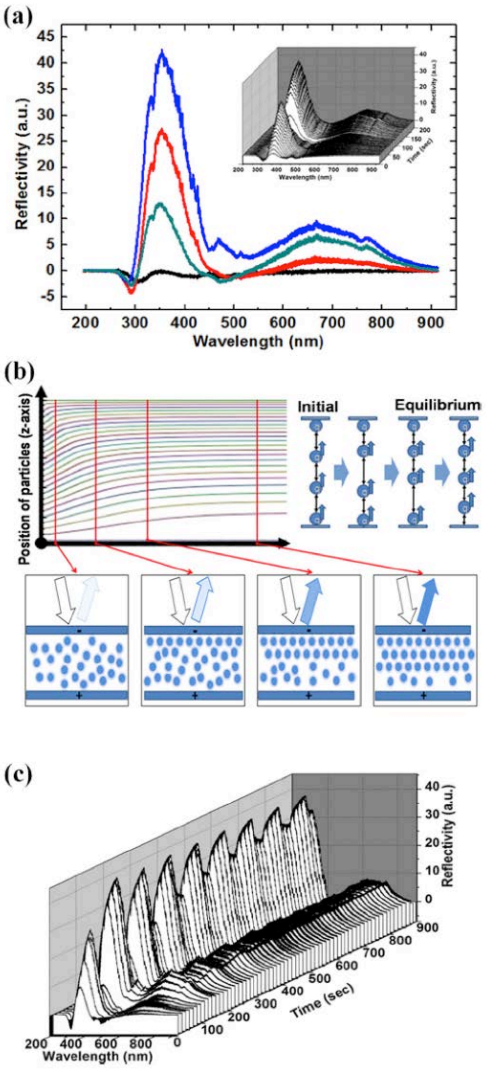

Figure 4.2. (a) Reflectance spectra of TiO_2 photonic crystal and the intensity tuning by applying external electric field; (b) A graph illustrates the simulation results about distance changing trend between particles and electrode by moving of charged particles for z-coordinate projection along time under certain external electric field; (c) A series of spectra recorded during switching between negative and positive potential.

`

This simulation result may offer the proper reason why the reflective peak intensity is gradually changed without peak position shift under the uniform external electric field. Because the minimum inter-particle distance is restricted by geometry, even excess field cannot lead to blue shift of reflected spectrum peak position.

However, the number of periodic colloidal layers stacked on electrode surface is varied proportional to the electric field gradient, and the thickness change directly affects the intensity of reflection at its photonic stop band.[18] When the electrostatic repulsion of the charged particle is comparably strong enough to allow field induced electrophoretic force, charged particles in solution exhibit long-range order self-assembly, and the geometric periodicity is able to be maintained under the external electric field, whereas the distance between particles is altered. The reflective peak position which represents the correlated lattice constant has been reported to be varied proportional to the electric field strength.[5,8] On the other hand, the mild repulsive force between particles in our system is not adequate to cause building spontaneous ordered structure by themselves as was reported by Yin et al. in one of their weakly charged sample.[19] As a result, a periodic structure is not observed until the distances between particles are sufficiently decreased by electric field support.

Interesting feature is observed in the Figure 4.2c, which reveals multi-cycle switching characteristics that exhibit periodic rising and falling as the electric field direction is reversed. While the maximum peak value of each cycle almost reaches its initial value, the minimum value is not recovered to its initial record, rather increased gradually with the number of cycles. This means that the thickness of the photonic crystal layer on the underside of

`

upper ITO electrode is increased with increasing number of cycles. This phenomenon implies that the release of charged particle is an irreversible process in this condition. As described above, the calculation of peak maximum wavelength suggests that the distance between particles comes to only a few nm. In such a case, unusually strong physical and chemical interactions between charged nanoparticles are able to take effect.

According to the Derjaguin and Landau, Verwey and Overbeek (DLVO) theory, the net energy is given by the sum of the double layer repulsion and the van der Waals attractive force. When the distance between particles is under several nm, the van der Waals interaction may be dominant.[20] Another possible interaction is chemical bonding between particles. Due to the long chain length of the coupling agent (Figure 4.1a), amino group ($-NH^{3+}$) of the end of the tail may have the opportunity to form hydrogen bonding with the residual hydroxyl group ($-OH^{-}$) on another particle's surface.[21,22] As a result, some of the closely approached particles have strong short-range interactions among them and are tightly packed to keep the hard contact, which is not released again in spite of applying reversed electric field. The thickness of residual structure increased as the number of cycles, and the peak minimum intensity does not go back to the initial value but rather gradually increased.

The variation of the peak intensity and the amount of charge passing through the test cell are plotted in Figure 4.3a. The charges were simply obtained by integrating the measured currents. The exponential behavior of charge variation is very similar to the peak intensity variation. This implies that the capacitive current is a major component rather than faradaic current, and the cumulated charge is occurred from stacking of the

`

nanoparticles on the electrode. To get more quantitative insights into this phenomenon, the peak to peak variations of both cumulated electric charge and reflective spectrum intensity from each repeated cycle are plotted for comparison. Figure 4.3b shows the increasing and decreasing form of corresponding charge changes and peak intensity changes, respectively.

If nanoparticle is the major charge carrying species, the charge variation should take the same form as the reflective spectrum intensity change, which means that the thickness of charged particle layer is varying. Electrical double layer capacitance of ITO electrode in pure ethylene glycol is measured by using electrochemical impedance spectroscopic analysis in order to confirm that assumption. Calculated double layer capacitance of ITO electrode, which can be charged by only small amount of ions in ethylene glycol, has the order of 10^{-11} F/cm^2 while that of test cell which contains charged nanoparticles dispersed in ethylene glycol has 10^{-6} order (refer to Figure 4.3a and formula F =C/V). From those results, in the case of highly condensed non-aqueous colloidal solution, we can conclude that the short-range movement of charged nanoparticle is the origin of capacitive current flow rather than ionic double layer forming by ions. In addition, the increasing trend of cumulated charge in Figure 4.3a reflects that the number of unreleased layers which contain charged particles is also increased during repeated charging/discharging cycles.

To increase the reversibility of the reflectance switching, some additional experiments of applied electric field were performed (Figure 4.3c). The maximum peak intensity is reduced with decreasing electric field, while the reproducibility of the peak reflectivity change is enhanced.

`

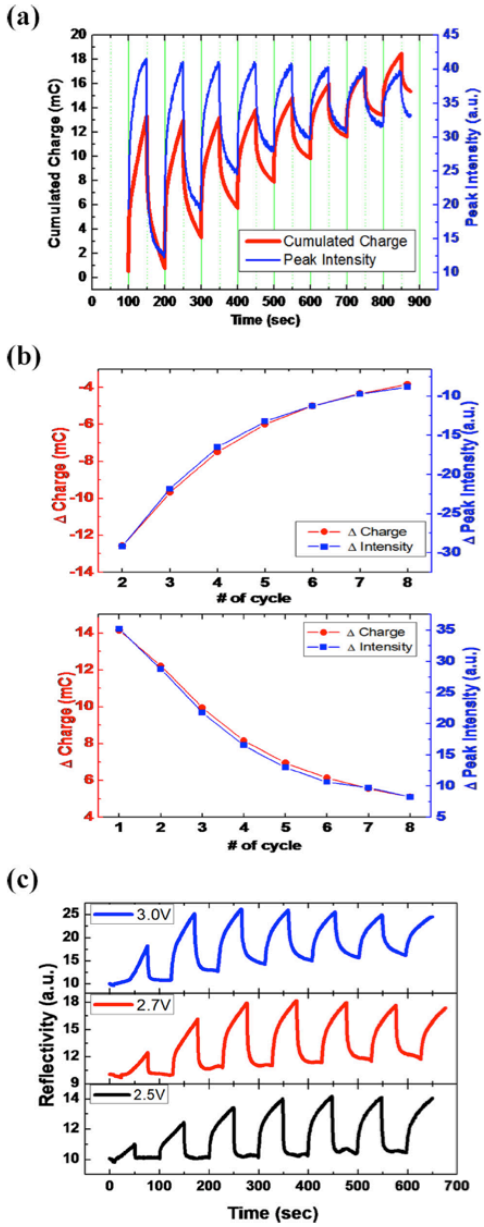

Figure 4.3. (a) Accumulated charges (thick, red line) and peak intensities (thin, blue line) *vs*. time, respectively, during switching between +3 V and -3 V; (b) The increasing form (up) and decreasing form (down) of the corresponding charge changes and the peak intensity changes with number of cycles; (c) Peak intensity switching behaviors under several different electric fields.

`

It is believed that the weaker electric field results in less probability of irreversible aggregation between the weakly charged particles when they are close enough to attract physically and/or chemically. These results suggest that the proper electric field strength control may be one of the useful methods to enhance the sustained tunability in order to open another avenue for the application of this technology to electrically tunable optical devices.

4.4 Conclusions

The spectroscopic and electrical properties of highly concentrated charge colloidal nanoparticle dispersion under external electric field were investigated in detail. A dramatic change of the reflection peak maximum in response to applied potential was observed. Through computer aided numerical analysis simulation, time-dependent re-arrangement of the charged particles under electric field is predicted, and this was verified by experimentally observed reflective intensity change. Also, It was shown that the experimental evidence that the charged nanoparticle can work as a major charge carrier instead of ions in non-aqueous liquid, and its short range movement also can be the origin of capacitive current flow. These results can pave a way for developing tunable optical device, especially switchable band pass filter or another type of capacitor.

`

4.5 Experimental Section

Materials and Instruments Titanium tetraethoxide was purchased from Aldrich and DETAS was purchased from Gelest. KCl, ethanol, 1-propanol was prepared in Samchun and all chemicals were used without any further purification.

Transmission Electron Microscopy (TEM) and Field-Emission Scanning Electron Microscopy (FE-SEM) images were acquired using Hitachi-7600 (Hitachi) and Hitachi S-4300 (Hitachi) instruments, respectively. The surface charge of TiO_2 was monitored using a zeta-potential analyzer (Zetasizer nano ZS90, Malvern).

Synthesis of TiO_2 100 nm sized TiO_2 was prepared by following method. $Ti(OEt)_4$ (0.43 mL) and 0.2 mL of 0.32 M KCl were added to 50 mL of 1-propanol. And then 60 mL of mixture was added to 200 mL of ethanol with vigorous stirring and reacted for 2 hr at room temperature. The white TiO_2 was collected using centrifuge for 10 min at 17,000 rpm. The precipitate was redispersed in ethanol, followed by centrifugation under the same conditions for washing the remained reactants. The washing procedure was repeated more than two times and TiO_2 was dispersed in ethanol for the next step.

Surface modification TiO_2 DETAS (0,1 wt% to TiO_2) was injected to TiO_2 dispersed in ethanol (3 mg/mL) and the mixed solution was stirred at room temperature over 2 hr. The mixture was centrifuged for 20 min at 20,000 rpm, and the precipitate was redispered in EtOH. This centrifugation-redispersion procedure was repeated more than two times to

`

obtain the dispersed solution of the DETAS-modified SiO_2 nanoparticles (DETAS-SiO_2). The DETAS modified TiO_2 nanoparticles (DETAS-TiO_2) was obtained as the same method.

Test device fabrication procedure and evaluation switching property The procedure for fabricating and evaluating switching property of the colloidal dispersion is as follows: the colloidal dispersion with final concentration of 6.05 v/v % prepared by proper centrifugation and re-dispersion to ethylene glycol was injected between two parallel Indium Tin Oxide (ITO) coated glasses to make the test cell. The UV-vis reflectance spectra of the test cell sample were taken with a spectrometer (Ocean Optics Inc, USB 4000). The spectrophotometric setup was assembled similar to described elsewhere in the literature.[11] All the spectra were obtained after subtracting the initial diffusive reflection spectrum from the measured data.

*** Contributions**

Dr. HongShik Shim, Dr. Chang Gyun Shin, Dr. Seog-Jin Jeon, and Dr. Moon Gyu Han in Samsung Advanced Institute of Technology did electrophoretic experiments and analysis.

`

4.6 References

[1] Hedrick, J. L.; Smith, A. J., *Arch. Biochem. Biophys.* **1968**, *126*, 155-164.

[2] Dukhin, A. S.; Goetz, P. J., *Ultrasound for Characterizing Colloids*, Elsevier, Amsterdam, **2002**.

[3] Gurrappa, I.; Binder, L., *Sci. Technol. Adv. Mater.* **2008**, *9*, 043001.

[4] Comiskey, B.; Albert, J. D.; Yoshizawa, H.; Jacobson, J., *Nature* **1998**, *394*, 253-255.

[5] Lee, I.; Kim, D.; Kal, J.; Baek, H.; Kwak, D.; Go, D.; Kim, E.; Kang, C.; Chung, J.; Jang, Y.; Ji, S.; Joo, J.; Kang, Y., *Adv. Mater.* **2010**, *22*, 4973-4977.

[6] Asher, S. A.; Holtz, J.; Liu, L.; Wu, Z., *J. Am. Chem. Soc.* **1994**, *116*, 4997-4998.

[7] Han, M. G.; Foulger, S. H., *Chem. Commun.* **2004**, 2154-2155.

[8] Shim, T. S.; Kim, S.-H.; Sim, J. Y.; Lim, J.-M.; Yang, S.-M., *Adv. Mater.* **2010**, *22*, 4494-4498.

[9] Eiden-Assmann, S.; Widoniak, J.; Maret, G., *Chem. Mater.* **2003**, *16*, 6-11.

[10] Koziol, T. R.; Grayeski, M. L., *J. Chromatogr. A* **1990**, *513*, 145-158.

[11] Shim, H.-S.; Yeo, I.-H.; Park, S.-M., *Anal. Chem.* **2002**, *74*, 3540-3546.

[12] Joannopoulos, J. D.; Johnson, S. G.; Winn, J. N.; Meade, R. D., *Photonic Crystals Molding the Flow of Light, 2nd ed.*, Princeton University Press, Princeton, **2008**.

[13] Aguirre, C. I.; Reguera, E.; Stein, A., *Adv. Funct. Mater.* **2010**, *20*, 2565-2578.

`

[14] Zhang, M.; Lin, G.; Dong, C.; Wen, L., *Surf. Coat. Technol.* **2007**, *201*, 7252-7258.

[15] Suzuki, N.; Tomita, Y.; Kojima, T., *Appl. Phys. Lett.* **2002**, *81*, 4121-4123.

[16] King, J. S.; Graugnard, E.; Summers, C. J., *Adv. Mater.* **2005**, *17*, 1010-1013.

[17] Jiang, K.; Zakutayev, A.; Stowers, J.; Anderson, M. D.; Tate, J.; McIntyre, D. H.; Johnson, D. C.; Keszler, D. A., *Solid State Sci.* **2009**, *11*, 1692-1699.

[18] Bertone, J. F.; Jiang, P.; Hwang, K. S.; Mittleman, D. M.; Colvin, V. L., *Phys. Rev. Lett.* **1999**, *83*, 300-303.

[19] Ge, J.; He, L.; Goebl, J.; Yin, Y., *J. Am. Chem. Soc.* **2009**, *131*, 3484-3486.

[20] Verwey, E. J. W.; Overbeek, J. Th. G., *Theory of the Stability of Lyophobic Colloids*, Elsevier, New York, **1948**.

[21] Kamisetty, N. K.; Pack, S. P.; Nonogawa, M.; Devarayapalli, K. C.; Kodaki, T.; Makino, K., *Chem. Lett.* **2007**, *36*, 322-323.

[22] Howarter, J. A.; Youngblood, J. P., *Langmuir* **2006**, *22*, 11142-11147.

`

Appendix/Chapter 5.

Synthesis of Polystyrene@Titania Core@Shell Nanoparticles and Their Tunable Reflectance of Colloidal Photonic Crystal Structure.

`

5.1 Introduction

Tuning photonic band gap by the electric field is an emerging field for device application such as display and sensor.[1-3] In order to make electric field-dependent photonic band gap materials, polystyrene and silica particles were used due to their simple synthesis with mono-dispersed size.[4] These materials showed good responsibility in electric field but their low refractive index limits the performance of device. Titania is effective material for photonic band due to their high refractive index and low absorbance in visible light.[1, 5] Although there have been a few efforts using titania to make photonic band gap materials, the difficulty to make homogeneously dispersible titania particles and their low electrophoretic mobility in electric field have restricted their usage in this interesting applications.[6-7]

In this chapter, the synthesis of polystyrene core/titania shell (PS@TiO_2) nanostructures with narrow size distribution and their tunable reflectance under the electric field was reported. PS@TiO_2 structure was prepared to make the materials with lower density, higher reflective index and narrow size distribution. A detailed synthetic method preparing PS@TiO_2 was shown. As a colloidal state in water, PS@TiO_2 showed reflectance in visible region and it was tunable by controlling the electric field. The reflectance by periodic arrays of PS@TiO_2 was also reversible under on/off voltage. For the more tuning range in visible region, surface modification of PS@TiO_2 to enhance surface charge needed.

`

5.2 Results and Discussion

Preparation of PS Nanoparticles (NPs) PS NPs about 130 nm were prepared by using surfactant free emulsion polymerization of styrene monomer[8] (Figure 5.1). Initiators are decomposed to radicals which could start the polymerization of styrene under heating condition. The surface charge of PS NPs was also determined by the charge of initiator; positive charge about (+) 30 mV by the ammine groups of 2,2'-azobis (2-methyl propionamidine) dihydrochloride (AIBA) and negative charge about (-) 30 mV by the sulfate group of potassium persulfate (KPS). PS NPs are well dispersed in water and polar organic solvent like ethanol due to their surface charge.

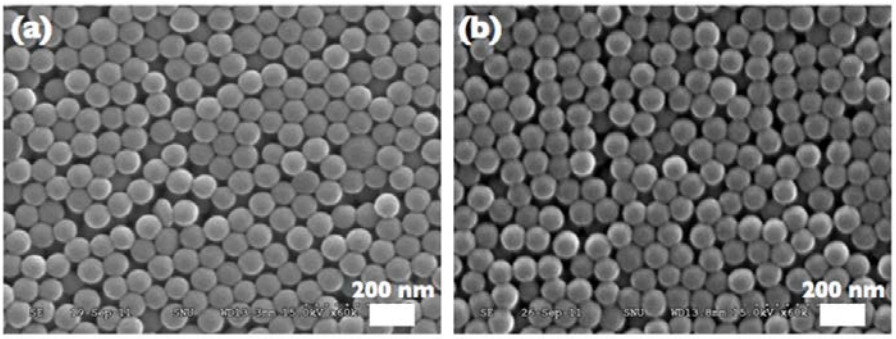

Figure 5.1. SEM images of PS NPs about 130 nm using (a) AIBA and (b) KPS as an initiator.

Preparation of PS@TiO_2 NPs using Ti-EG Two methods was used to obtain PS@TiO_2 NPs. First, both positive charged and negative charged PS NPs were dispersed in the mixed solution of ethanol and acetonitrile (1:11 v/v). And than, diluted titanium tetrabutoxide in ethylene glycol was added to the PS NPs without any base catalyst.

`

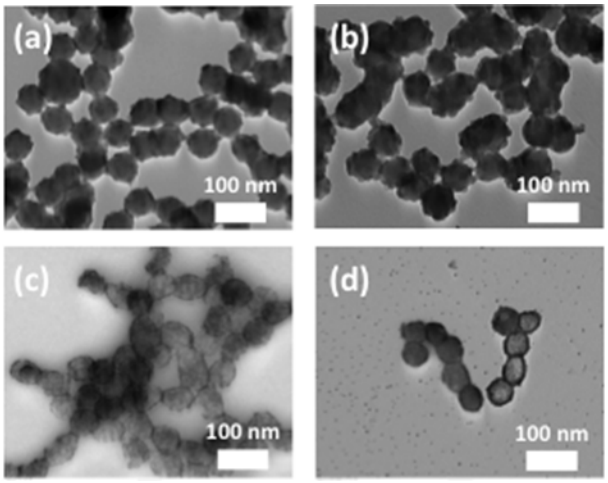

Figure 5.2. TEM images of PS@TiO_2 using (a), (b) negative charged PS NPs and (c), (d) positive charged PS NPs. (a) and (c) used 2 mL of titania precursor and (b) and (d) used 3 mL of titania precursor.

Titnaia was formed on negative charged PS NPs with not the perfect shell but island-like morphology which might results from the negative charge character of titania (Figure 5.2a and 5.2b). Using positive charged PS NPs like Figure 5.2c and 5.2d, titania layer was formed but the thickness was too thin.

For increasing the hydrolysis-condensation of titania precursor on the surface of PS NPs, PS NPs in water were added after the injection of titania precursor. The perfect titania shell was formed on the both charged PS NPs showing the surface water effect on the condensation of titania shell (Figure 5.3).

`

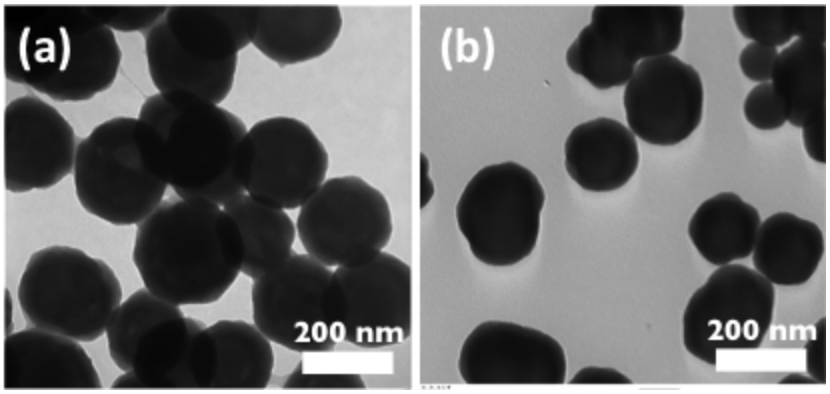

Figure 5.3. TEM images of PS@TiO_2 using (a) negative charged PS NPs and (b) positive charged PS NPs.

Interestingly, when hexadecyltrimethylammonium bromide (CTAB) was introduced to give the positive charge to negative charged PS NPs by the formation of bi layer, popcorn-like structure was prepared in acetone solvent. However, typical titania shell was formed in the mixed solvent of ethanol and acetonitrile (1:1 v/v). Because PS NPs are dissolved in acetone, slow dissolution of PS NPs and also slow formation of titania shell on the CTAB could make this popcorn-like titania structure.

`

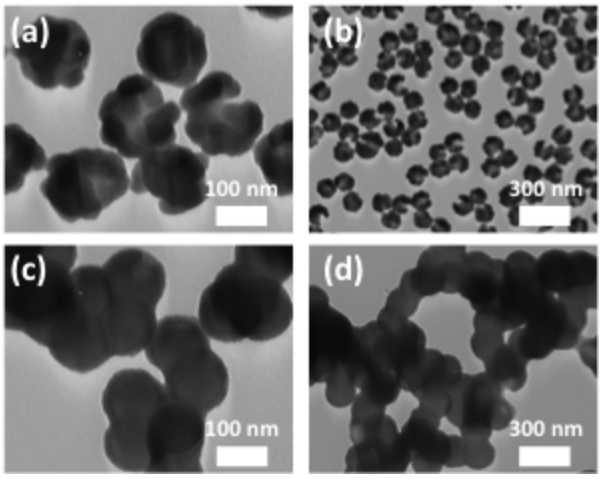

Figure 5.4. TEM images of PS@TiO_2 prepared by CTAB-modified negative PS NPs in (a) and (b) acetone and (c) and (d) mixed solvent of ethanol : acetonitrile (1:1 v/v).

Preparation of PS@TiO_2 NPs 2 The second method to prepare PS@TiO_2 NPs is using titania tetrabutoxide with base catalyst in the mixed solvent of ethanol and acetonitrile. When titania source was injected to the positive charged PS NPs without ammonia solution, very thin layer of titania was detected (Figure 5.5a). But using ammonia solution as the base catalyst for the hydrolysis-condensation of titania source, the perfect condensation of titania shell was possible with more thicker titania layer like Figure 5.5b.

`

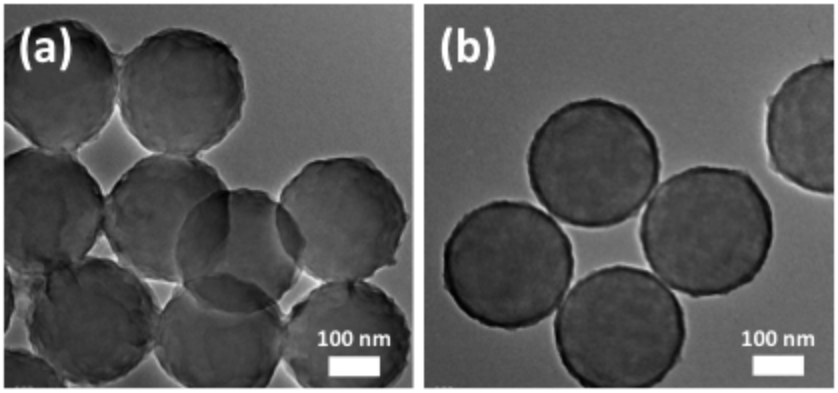

Figure 5.5. TEM images of PS@TiO_2 prepared by CTAB-modified negative charged PS NPs (a) without and (b) with ammonia solution in mixed solvent of ethanol : acetonitrile (1:3 v/v).

To control the thickness of titania shell, the ratio of PS NPs to titania source was decreased. Using more titania source to PS NPs, more thicker titnania shell was obtained (Figure 5.6).

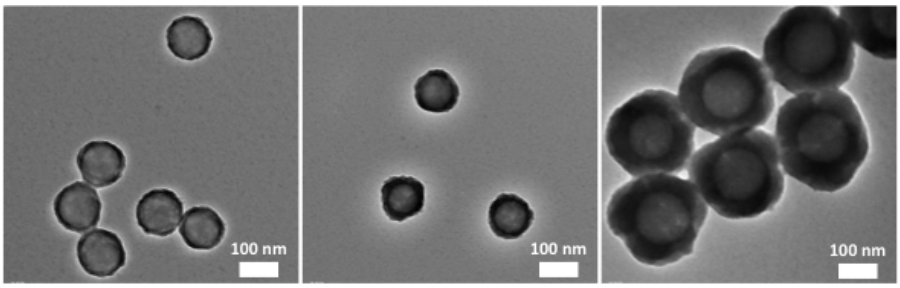

Figure 5.6. TEM images of PS@TiO_2 with increasing titania shell thickness.

`

Tunable reflectance of PS@TiO_2 NPs colloid photonic crystal PS@TiO_2 (zeta potential was -35.5 mV in water) about 150 nm with 130 nm PS core was prepared using base catalyst in mixed solvent of ethanol and acetonitrile to make photonic band gap upon the electric field. The images of NPs and their reflectance experimental system were shown in Figure 5.7.

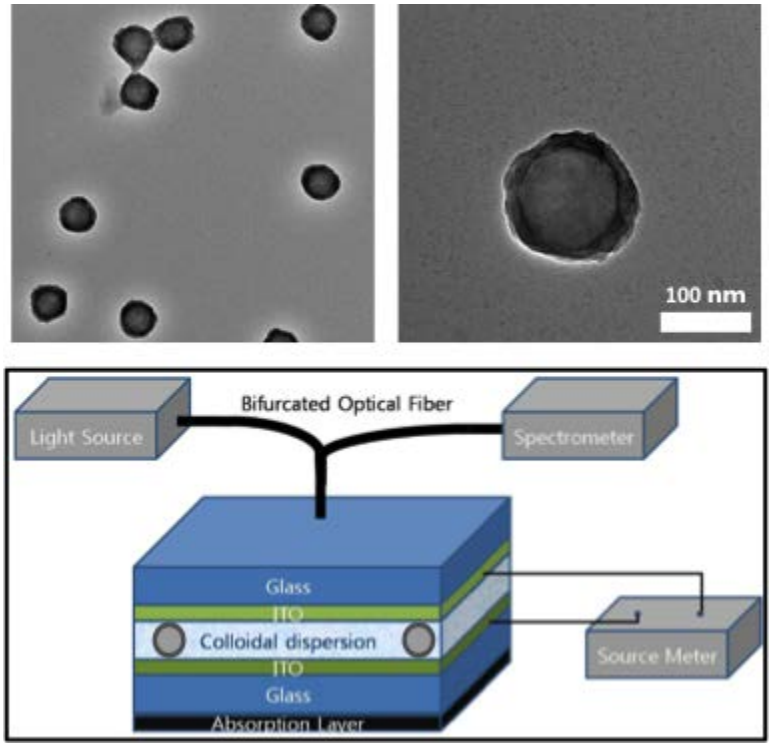

Figure 5.7. TEM images of PS@TiO_2 for colloidal photonic crystal and the image of reflectance experimental system.

`

Under the voltage of 3 V was applied to the PS@TiO_2 in water between two Indium tin oxide (ITO) glass, the reflectance of visible region about 600 nm was increased (left spectrum of Figure 5.8). It means that the NPs were formed periodic array near the ITO glass under the electric field. When the voltage was dropped to 0 V, the reflectance was red-shifted about 20 nm (right spectrum of Figure 5.8). The shifted reflectance indicates the distance between NPs was controlled by the external voltage but the tuning range was not wide.

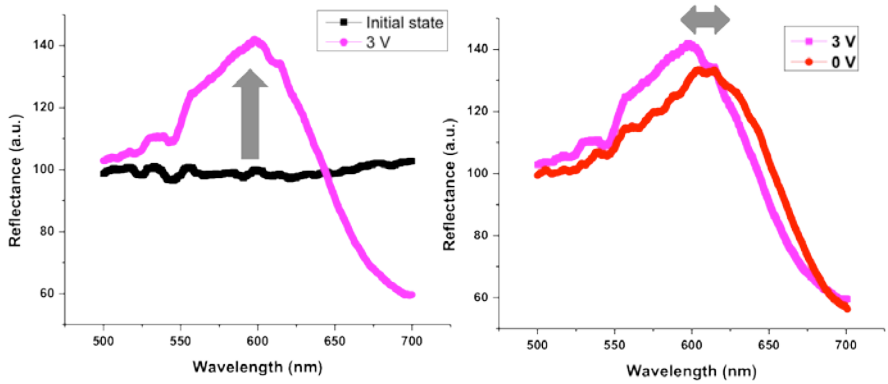

Figure 5.8. Reflectance of PS@TiO_2 in device under applying +3 V (left) and off voltage of 0 V (right).

Reversible reflectance of PS@TiO_2 with on-off voltage was displayed in Figure 5.9. The tuning range was stable but under the repeating on/off voltage, initial reflectance was red-shifted. It could be understood by the existence of remaining particle on the ITO surface which could not detached even the off voltage state. To get more wide controllable reflectance with stability, more strong surface charge might be introduced to the surface of PS@TiO_2.

`

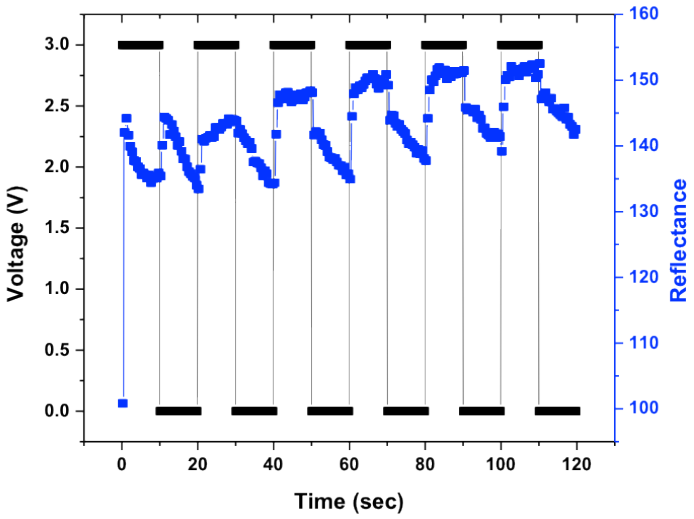

Figure 5.9. Reversible reflectance of PS@TiO_2 with on/off voltages.

5.3 Conclusions

Polystyrene core/titania shell (PS@TiO_2) was prepared by using 120 nm of PS particles as core and $Ti(OBu)_4$ as titania source in the mixed solvent of ethanol and acetonitrile. Prepared PS@TiO_2 was confirmed and characterized by using TEM, and zeta potential. PS@TiO_2 in water showed enhanced reflectance at visible region in electric field. Reflectance was tunable by varying applied voltage and it was reversible. For the wider tuning of reflectance, surface charge of the particle should be increased.

`

5.4 Experimental Section

Materials and Instruments Styrene, AIBA, KPS, polyvinyl pyrrolidione (PVP), titanium tetraethoxide, absolute ethanol, Tween 20 and CTAB were purchased from Aldrich and acetone, acetonitrile and ammonia solution (29 %) were prepared in Samchun. All chemicals were used without any further purification.

Transmission Electron Microscopy (TEM) and Field-Emission Scanning Electron Microscopy (FE-SEM) images were acquired using Hitachi-7600 (Hitachi) and Hitachi S-4300 (Hitachi) instruments, respectively. The surface charge of TiO_2 was monitored using a zeta-potential analyzer (Zetasizer nano ZS90, Malvern).

Synthesis of PS NPs 120 nm sized PS NPs was prepared by following method. PVP (MW=55,000) 0.4125 g, 4.8 mM of AIBA (or 9.6 mM of KPS), and 1 M of styrene were prepared in 25 mL of water and heated to 70 °C. After 24 hr, the white PS NPs was collected using centrifuge for 10 min at 17,000 rpm. The precipitate was re-dispersed in ethanol, followed by centrifugation under the same conditions for washing the remained reactants. The washing procedure was repeated more than two times and PS NPs were dispersed in ethanol for the next step.

Synthesis of PS@TiO_2 using Ti-EG PS NPs were dispersed in the 12 mL mixed solvent of ethanol and acetonitrile (1 mg/mL). Ti-EG solution (0.1 mL of titanium tetrabutoxide + 20 mL of ethylene glycol) was injected to the PS NPs and after 2 hr, PS@TiO_2 NPs were collected using centrifugation as PS NPs.

`

Synthesis of PS@TiO_2 using ammonia solution PS NPs were dispersed in the 12 mL mixed solvent of ethanol and acetonitrile (0.5 mg/mL) with the 0.05 mL of ammonia solution. Titanium butoxide (0.1 mL) injected to the PS NPs and after 2 hr, PS@TiO_2 NPs were collected using centrifugation as PS NPs.

Test device fabrication procedure and evaluation switching property The spectrophotometric setup was assembled similar to described elsewhere in the literature.[11] The photonic crystal dispersion was injected between two ITO glass separated by a 100 μm spacer. The optical properties of the photonic crystal layer were measured using an Ocean Optics USB 4000 photo-diode array spectrophotometer during potential application provided by a CHI 660D EC workstation. A Balanced Deuterium Tungsten Source (210-1700 nm) was used to illuminate samples through an optical fiber and the reflectance spectra were collected after calibrating the spectra against a STAN-SSH high reflectivity specular reflectance standard. The optical response was monitored every 12 ms and the stop-band peak position was simultaneously recorded using home-made software.

*** Contributions**

Dr. HongShik Shim, Dr. Chang Gyun Shin, Dr. Seog-Jin Jeon, and Dr. Moon Gyu Han in Samsung Advanced Institute of Technology did electrophoretic experiments and analysis.

`

5.5 References

[1] Han, M. G.; Shin, C. G.; Jeon, S.-J.; Shim, H.; Heo, C.-J.; Jin, H.; Kim, J. W.; Lee, S., *Adv. Mater.* **2012**, *24*, 6438-6444.

[2] Lee, I.; Kim, D.; Kal, J.; Baek, H.; Kwak, D.; Go, D.; Kim, E.; Kang, C.; Chung, J.; Jang, Y.; Ji, S.; Joo, J.; Kang, Y., *Adv. Mater.* **2010**, *22*, 4973-4977.

[3] Shim, T. S.; Kim, S.-H.; Sim, J. Y.; Lim, J.-M.; Yang, S.-M., *Adv. Mater.* **2010**, *22*, 4494-4498.

[4] Xia, Y. N.; Gates, B.; Yin, Y. D.; Lu, Y., *Adv. Mater.* **2000**, *12*, 693-713.

[5] Wijnhoven, J. E. G. J.; Vos, W. L., *Science* **1998**, *281*, 802-804.

[6] Luo, Y.; Zhang, J.; Sun, A.; Chu, C.; Zhou, S.; Guo, J.; Chen, T.; Xu, G., *J. Mater. Chem. C* **2014**, *2*, 1990-1994.

[7] Shim, H.; Lim, J.; Shin, C. G.; Jeon, S.-J.; Han, M. G.; Lee, J.-K., *Appl. Phys. Lett.* **2012**, *100*, 063113.

[8] Yun, D. S.; Lee, H.-S.; Jang, H. G.; Yoo, J. W., *Bull. Korean Chem. Soc.* **2010**, *31*, 1345-1348.

[9] Furusawa, K.; Norde, W.; Lyklema, J., *Kolloid Z Z Polym.* **1972**, *250*, 908-909.

`

Appendix/Chapter 6.

Synthesis of Au Rod@Titania Core@Shell Nanostructures and Their Photo-catalytic and Electron Dynamic Studies

6.1 Abstract

There have been the efforts to use visible light in photo-catalytic application due to the UV-limited property of semiconductor. Among various researches to use visible light, metal-semiconductor composite have efficient property with electron transfer. Recently electron transfers not only from semiconductor to metal but also metal to semiconductor were reported and many researches used this phenomenon to explain better property of metal-semiconductor in visible light than only semiconductor. But the electron transfer from metal to semiconductor is hardly understandable subject. Therefore, observing electron transfer and photocatalytic property with varying the absorbance of metal could give the evidence to understand metal-semiconductor system. In this chapter, Au rod@Titania core@shell nanostructures were prepared with different shell thickness. The photo-catalytic property of Au rod@Titania was monitored using degradation of organic dye. Furthermore, the electron dynamics of Au rod@Titania were also detected by using transient absorption spectroscopy (TA).

`

6.2 Introduction

Titania is not only used in the wide range of fields as white pigment or sunscreen[1] but also have attracted a lot of attention for their possible application in various fields such as gas sensing,[2] electronic device,[3] solar cell,[4] and photo-catalyst.[5, 6] Among them especially, titania as a photo-catalyst have been actively researched for their advantages to remove organic pollutants following the craze on recent green chemistry.

The photo-catalytic property of titania comes from its wide band-gap (3.2 eV for anatase phase). Under UV irradiation, electrons of the valence band are exited to the conduction band thus makes electron-hole pairs. The electron and hole migrate to the surface of titania to participate in possible chemical reactions. Usually, the water absorbed on the surface of titania could join to redox and hydroxyl radicals could be generated. Organic pollutants could easily degraded with hydroxyl radicals for their highly reactive property. But because UV region is only under 5 % of solar light, the main problem of titania is the limited used of the major part of light; visible and near-IR.[7]

To solve this problem, titania has been used with other semiconductor,[8] doped with other metal or non-metal atom for controlling the band-gap,[9] coupled with visible light antenna like quantum dot[10], or used with metal nanoparticle like Pt.

Typically, the longer life-time of exciton by electron transfer from titania to metal nanoparticle under UV light has been recognized as the main reason of increasing photo-catalytic property of titania with metal nanoparticle. Recently however, using metal nanoparticle like Au to enhance the photo-catalytic property of titania under visible and near-IR

`

light have been reported.[11, 12] To explain the metal nanoparticle effect, helping titania active under visible light, two major factors were suggested.

First, the localized surface plasmon resonance (LSPR) of metal nanoparticle could increase the absorbance of titania itself even under visible light.[13] Second, excited electrons of metal nanoparticle under visible light could move to the conduction band of titania. Actually, the charge transfer from Au sphere (SPR extinction around 520 nm) to titania was monitored by laser instrument.[14]

In this chapter, the core@shell structures of Au rod@Titania nanostructures were prepared for the more abundant visible and near IR light responsible photo-catalyst. The electro dynamics was also conducted to monitor the electron transfer between Au rod and titania, which was limited to the Au sphere of 520 nm extinction in the former studies. The photo-catalytic property of Au rod@Titania was compared with commercial titania (P25) and only titania prepared in this chapter by degradation of methylene blue (MB).

6.3 Results and Discussion

Synthesis and photo-catalytic property of Au rod@Titania First, Au rod was prepared using well-known seed-growth method (Figure 6.1a).[15, 16] Briefly, gold precursor is reduced on the specific crystal phase of Au seed preferentially and anisotropic growth proceed to form rod shape under mild reductive condition in presence of surfactant like CTAB.

Au rod@Titania was prepared using mixed solution of titanium butoxide, KCl, and 1-propanol as stabilized titania precursor. In ethanol solvent, titania precursor was added following rapid injection of Au rod in small

`

amount of water. Hydrolysis and condensation of titania precursor could proceed the surface of Au rod with water and spherical core@shell structure was obtained like in TEM image of Figure 6.1b and HAADF image of Figure 6.1c. The spherical core@shell structure of Au rod@Titania was well retained after annealing process under 500 °C (Figure 6.1d).

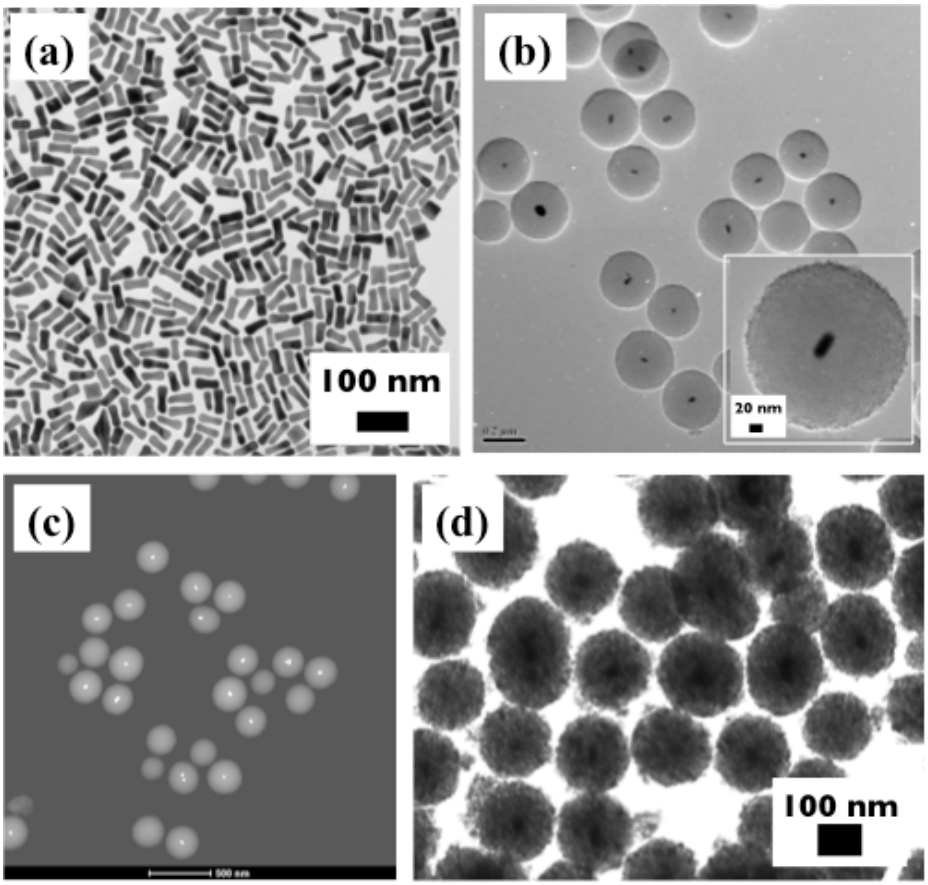

Figure 6.1. (a) TEM image of Au rod, (b) HR-TEM image of Au rod@Titania, (c) HAADF image of Au rod@Titnia and (d) TEM image of Au rod@Titnia after calcination.

`

In Figure 6.2, EDS monitoring of Au rod@Titnaia was performed with line-scanning mode. Although the atomic contribution of Ti and O atom decreased in the central area of Au rod@Titania, that of Au increased, which well indicate the core@shell structure.

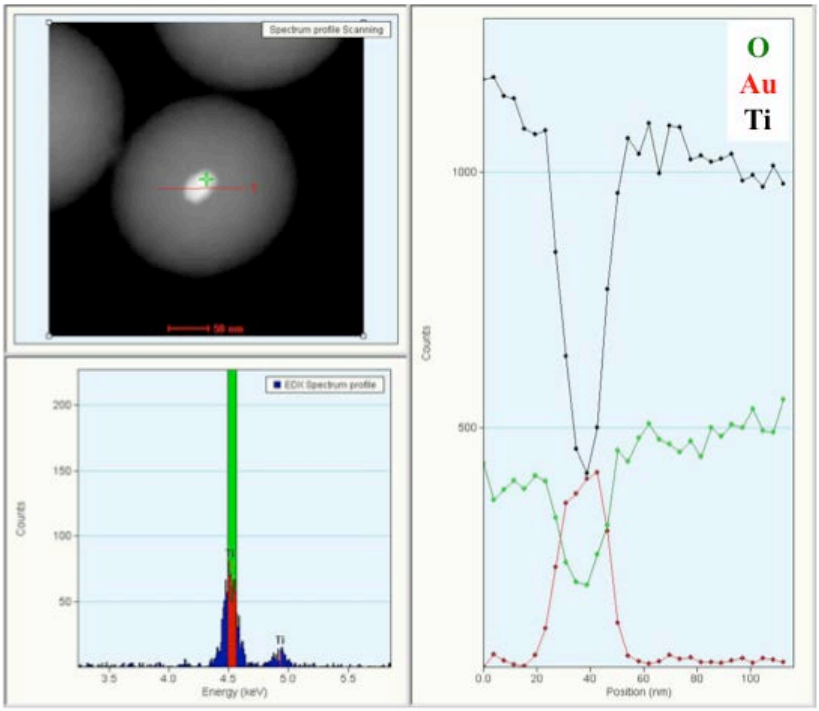

Figure 6.2. (a) HAADF image and EDS line-scanning profile of Au rod@Titania.

`

The absorption spectrum of prepared nanoparticles was monitored in Figure 6.3. First, Au rod had two absorption spectrum (wavelength of 680 nm and 520 nm) from its longitudinal and transverse plasmon band. The longitudinal absorption band of Au rod was red-shifted to have the wavelength about 700 nm due to the increased refractive index around Au rod by coating titania. More red-shift of absorption band was monitored with Au rod@Titania after calcination due to more high refractive index of anatase titania than amorphous titania.

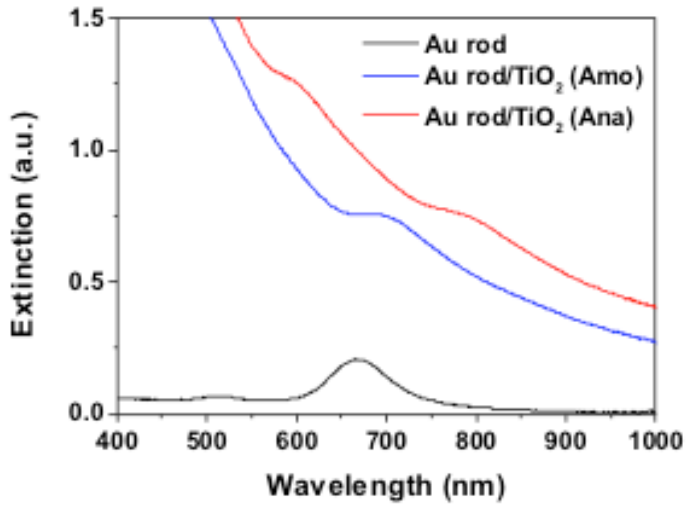

Figure 6.3. Absorption spectrum of prepared nanoparticles.

`

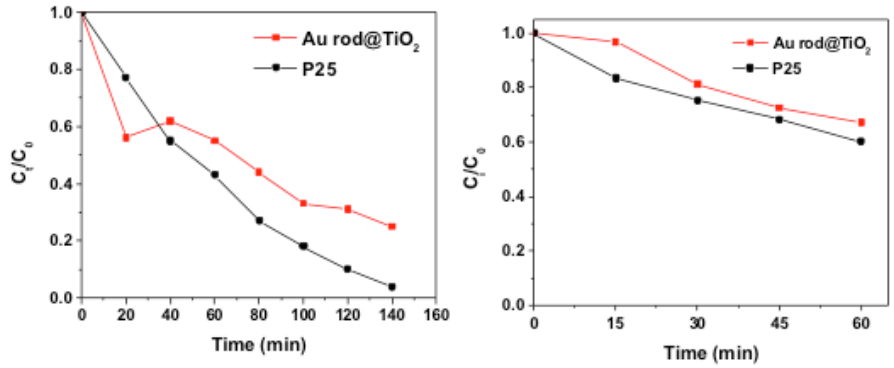

Figure 6.4. Photocatalytic degradation of MB with Au rod@Titnaia and P25 under (a) visible W-halogen lamp and (b) visible Xenon lamp (UV was cut).

The photocatalytic property of Au rod@Titnaia was studied by degradation of organic dye using MB. In Figure 6.4a, photocatalytic property of Au rod@Titania was compared under visible light (W-halogen lamp) with P25 which is about 20 nm commercial titania composed of both anatase and rutile with high photocatalytic property. But the ability of Au rod@Titania for MB degradation was similar or poor than P25 from the low surface area due to the large size and less amount of titania due to the incorporation of Au rod. The similar result was obtained under visible light from Xenon lamp (UV region under 400 nm was cut by UV filter).

To enhance the photo-catalytic property of Au rod@Titnia *via* increasing the surface area, about 100 nm of Au rod@Titania was obtained using $Ti(OBu)_4$ stabilized with ethylene glycol like chapter 1 and represented in Figure 6.5. And titania without Au rod was also prepared for the proper comparison.

`

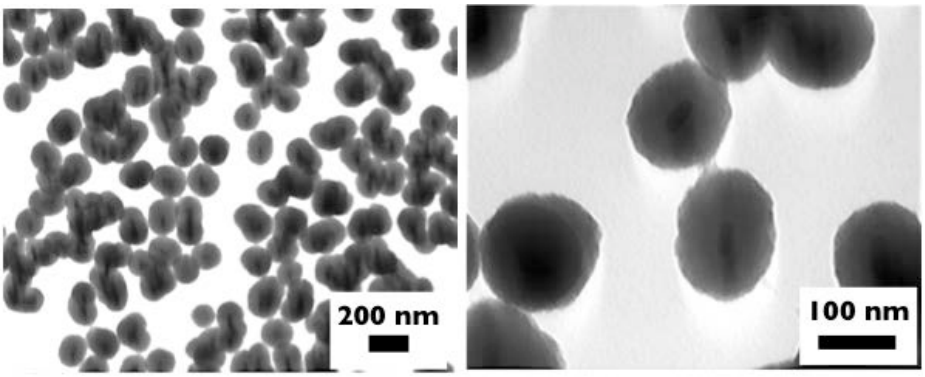

Figure 6.5. Au rod@Titania synthesis with $Ti(OBu)_4$ in ethylene glycol.

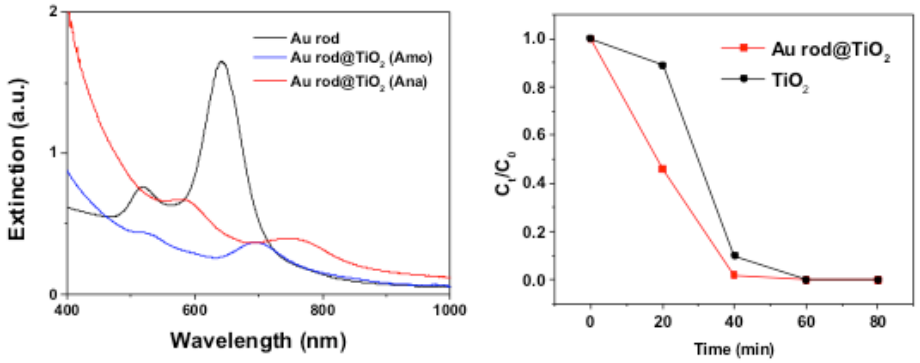

Figure 6.6. (a) Absorption spectrum and (b) photo-catalytic property of 100 nm sized Au rod@Titania.

Absorption spectrum of prepared 100 nm Au rod@Titania in Figure 6.6a was monitored and showed the similar red-shift pattern with the larger Au rod@Titania in Figure 6.3. The photo-catalytic property of 100 nm Au rod@Titania was tested under visible light from Xenon lamp and MB was more rapidly decreased with 100 nm Au rod@Titania than titania without Au rod, which seemed more powerful photo-catalytic property with Au rod.

`

Electron dynamics of Au rod@Titania To investigate electron dynamic of Au rod@Titnia under the light, TA experiment was done. Using TA, the behavior of excited electrons could be studied with pump and probe purse.

First, TA experiment was monitored under the UV light (Figure 6.7a). Both Au rod@Titania and titania without Au absorbed 850 nm of probe light after 267 nm of pump light and decayed, which shows the exited electrons in the conduction band of both nanoparticles. But in case of Au rod@Titnia, the slower decay was monitored, which was expected that the charge transfer from titania to Au rod. The similar TA experiment was done under visible light (Figure 6.8b).

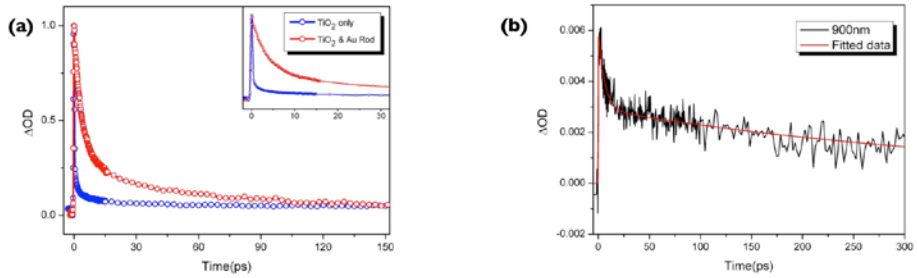

Figure 6.7. TA data of Au rod@Titnia under the wavelength of (a) pump-267, probe-850 nm and (b) pump-770 nm, probe 900 nm.

The absorbance of 900 nm probe light was monitored and decayed with Au rod@Titania under 770 nm probe light, which indicate the excited electrons in the conduction band of this structure although titania itself could not absorb the visible light. It seemed that the visible light excited the electrons in Au rod and they transferred to the conduction band of titania. The detailed life-time and schematic image of electron dynamics was presented in Figure 6.8.

`

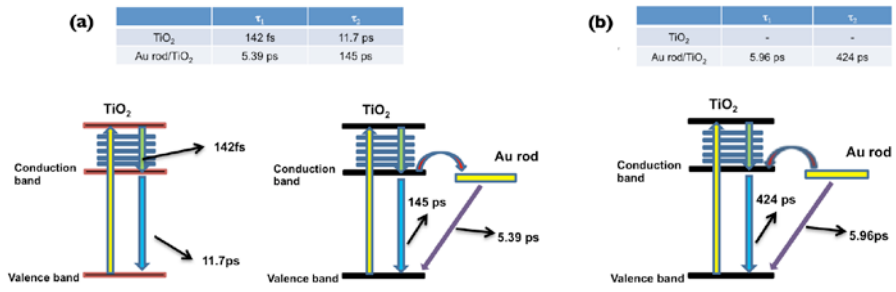

Figure 6.8. The electron life-time and schematic dynamics of Au rod@Titania and titania under (a) UV and (b) visible light.

As a result, Au rod@Titania have more powerful photo-catalytic property under visible light due to the visible light absorption and electron transfer from Au rod to titania.

6.4 Conclusions

In this chapter, Au rod@Titania nanocomposite was synthesized to study photo-catalytic property under visible light. With about 100 nm size of Au rod@Titania, more powerful photo-catalytic property than titania without Au rod was monitored by degradation of organic dye. The electron transfer from Au rod to titania under visible light was monitored with TA experiment, which seemed the major reason of enhanced photo-catalytic property of Au rod@Titania.

`

6.5 Experimental Section

Materials and Instruments Acetone, ethanol, 1-propanol and KCl were purchased from Samchun, Korea. $Ti(Bu)_4$, $Ti(OEt)_4$, ethylene glycol, Tween 20, $HAuCl_4$, CTAB, $NaBH_4$, L-ascorbic acid and methylene blue was purchased from Aldrich.

TEM image was obtained by Hitachi-7600, 100 kV and HR-TEM and EDS scanning was done with Tecnai F20, FEI.

Synthesis of Au rod Typical seed-growth method was used to prepare Au rod.[15, 17] Briefly, Au seed was obtained by reduction of $HAuCl_4$ with $NaBH_4$ in presence of CTAB. On the Au seed, $HAuCl_4$ is reduced by L-ascorbic acid anisotropically to form rod shape. In order to remove excess CTAB, Au rod was washed by centrifugation and re-dispersion using water (12,000 rpm for 10 min, twice) and re-dispersed in water.

Synthesis of 200 nm Au rod@Titania First, $Ti(OEt)_4$ (0.43 mL) is dissolved in 1-propanol (25 mL) with KCl solution (0.1 mL, 25 mg/mL). Au rod in 5 mL of water was introduced to ethanol (100 mL) following injection of prepared titania source solution. After 2 hr, Au rod@Titania was obtained after washing by centrifugation and re-dispersion.

Synthesis of 100 nm Au rod@Titania First, $Ti(OBu)_4$ (0.025 mL) is dissolved in ethylene glycol (5 mL) and stirred for 8 hr. It was poured into the acetone (125 mL) including Tween 20 (50 μL) following injection of Au rod in 0.5 mL of water. After 2 hr, Au rod@Titania was obtained after washing by centrifugation and re-dispersion.

`

Photodegration of organic dye Photo-catalyst (1 mg/mL) was stabilized with 20 ppm of MB under dark room for 30 min. The sample was obtained in terms of 30 min under the 200 W of W-halogen lamp or 100 mW/cm^2 of Xenon lamp (UV cut-off filter under the wavelength of 400 nm).

TA experiment Typical temtosecond transient absorption spectroscopy setting was used.[18] For the UV experiment, pump pulse of 267 nm, 2mW power and probe purso of 850 nm were used. For the visible experiment, pump pulse of 770 nm, 1.4 mW power and probe purse of 900 nm were used. The target sample was spin-coated on the quartz glass and dried before the experiment.

*** Contributions**

TA experiment was done by Sunjin Hwang and Prof. Seong Keun Kim in Department of Chemistry, Seoul National University.

6.6 References

[1] Hsu, W. P.; Yu, R. C.; Matijevic, E., *J. Colloid Interface Sci.* **1993**, *156*, 56-65.

[2] Kim, I.-D.; Rothschild, A.; Lee, B. H.; Kim, D. Y.; Jo, S. M.; Tuller, H. L., *Nano Lett.* **2006**, *6*, 2009-2013.

[3] Balasubramanian, B.; Kraemer, K. L.; Reding, N. A.; Skomski, R.; Ducharme, S.; Sellmyer, D. J., *Acs Nano* **2010**, *4*, 1893-1900.

`

[4] Hagfeldt, A.; Boschloo, G.; Sun, L.; Kloo, L.; Pettersson, H., *Chem. Rev.* **2010**, *110*, 6595-6663.

[5] Pan, J. H.; Dou, H.; Xiong, Z.; Xu, C.; Ma, J.; Zhao, X. S., *J. Mater. Chem.* **2010**, *20*, 4512-4528.

[6] Zhang, H.; Chen, G.; Bahnemann, D. W., *J. Mater. Chem.* **2009**, *19*, 5089-5121.

[7] Chen, C.; Ma, W.; Zhao, J., *Chem. Soc. Rev.* **2010**, *39*, 4206-4219.

[8] Papp, J.; Soled, S.; Dwight, K.; Wold, A., *Chem. Mater.* **1994**, *6*, 496-500.

[9] Serpone, N., *J. Phys. Chem. B* **2006**, *110*, 24287-24293.

[10] Tada, H.; Fujishima, M.; Kobayashi, H., *Chem. Soc. Rev.* **2011**, *40*, 4232-4243.

[11] Primo, A.; Corma, A.; Garcia, H., *Phys. Chem. Chem. Phys.* **2011**, *13*, 886-910.

[12] Zhou, X.; Liu, G.; Yu, J.; Fan, W., *J. Mater. Chem.* **2012**, *22*, 21337-21354.

[13] Seh, Z. W.; Liu, S.; Low, M.; Zhang, S.-Y.; Liu, Z.; Mlayah, A.; Han, M.-Y., *Adv. Mater.* **2012**, *24*, 2310-2314.

[14] Du, L.; Furube, A.; Yamamoto, K.; Hara, K.; Katoh, R.; Tachiya, M., *J. Phys. Chem. C* **2009**, *113*, 6454-6462.

[15] Sau, T. K.; Murphy, C. J., *Langmuir* **2004**, *20*, 6414-6420.

[16] Nikoobakht, B.; El-Sayed, M. A., *Chem. Mater.* **2003**, *15*, 1957-1962.

[17] Murphy, C. J.; San, T. K.; Gole, A. M.; Orendorff, C. J.; Gao, J. X.; Gou, L.; Hunyadi, S. E.; Li, T., *J. Phys. Chem. B* **2005**, *109*, 13857-13870.

[18] Yang, I.; Jin, S. M.; Kang, J.; Ramanathan, V.; Kim, H. M.; Suh, Y. D.; Keun, K. S., *Bull. Korean Chem. Soc.* **2011**, *32*, 3090-3093.

`

Appendix/Chapter 7.

Silver@Titania Nanocomposite Additive as both Plasmonic and Scattering Material for Dye-sensitized Solar Cells.

7.1 Abstract

In this chapter, the effect of silver-titania nanocomposite (Ag@TiO_2 about 300 nm) additive in the active layer of dye-sensitized solar cells (DSSCs) is systematically explored. The active layer including Ag@TiO_2 improves the light harvesting ability due to localized surface plasmon (LSP), scattering, and electron storage. In addition, the photo-conversion efficiency (PCE) of the DSSC devices that embedded 1 wt% Ag@TiO_2 particles are enhanced from 5.23 % to 5.35 %. The main reason of enhanced efficiency was the increase of open circuit voltage (V_{oc}) depends on increasing the weight ratio of Ag nanoparticles (Ag NPs).

`

7.2 Introduction

DSSCs, generally consisting of a mesoporous TiO_2 film, dye, electrolyte, and platinum electrode, have attracted great attention for high PCE up to 11 % and the low cost of materials and fabrication processes.[1-4] To increase short-circuit current (J_{sc}) of DSSCs, conventional approaches included the enhancing absorption of incident light, improving collection of photo-generated carriers,[5, 6] changing the thickness or morphology of the photo anode, and adding large size nanoparticles of diameter about 300 nm as light scattering materials in the photoanode.[7] There were also some efforts devoted to improve V_{oc} by developing novel electrolyte and enhancing electron lifetime in TiO_2 anode.[8, 9]

Because the entire PCE could be changed by many factors, improving light harvesting or carrier collection without affecting other factors has been considered a more effective approach for improving device performance.[10]

From this viewpoint, metal nanoparticles such as Ag and Au nanoparticles have potential for improving the performance of DSSCs for the unique capability to improve the light absorption of dye with minimal impact on other material properties.[11] Mechanisms enhancing the property of solar cells have been proposed into two major ways.[12] First, light scattering from small metal nanoparticles could increase optical path length so the absorbers in active layer of cells could use the incoming light more efficiently. Light concentration capability of metal nanoparticles is the second way. The absorption of semiconductors near metal nanoparticles could be enhanced by the strong local fields around nanoparticles and it is directly connected to the increased current of solar cells. In addition, metal nanoparticles could show electron storage effect from changing the Fermi

`

level to more negative potential.[13] However, the use of metal nanoparticles have also disadvantages of exciton recombination and charge trapping.[14-16]

In this chapter, the synthetic protocol for preparation of silver-titania nanocomposite sized about 300 nm was reported to enhace PCE of DSSCs. Taking $Ag@TiO_2$ nonocomposite in active layer with TiO_2 nanoparticles, the advantage factor of Ag could increase the PCE of DSSCs while disadvantage of Ag is compensated with the scattering effect of large size titania structure. By incorporating $Ag@TiO_2$, the V_{oc} of DSSCs was increased from 0.70 V to 0.73 V. Moreover, a large amount of $Ag@TiO_2$ (to 10%) improved V_{oc} to 0.78 V, while decrease J_{sc} to 7.75 mA/cm^2.

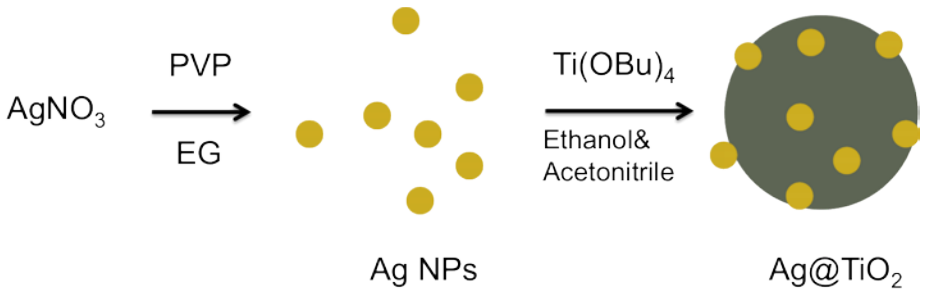

Scheme 7.1. Schematic image of the synthetic process of $Ag@TiO_2$.

7.3 Results and Discussion

The synthesis of $Ag@TiO_2$ nanocomposite is shown in Scheme 1. First, Ag NPs about 40 nm (Figure 7.1a) was prepared from reduction of silver nitrate in hot ethylene glycol with polyvinyl pyrrolidone (PVP). And $Ag@TiO_2$ nanocomposite could be obtained from hydrolysis-condensation of titanium tetrabutoxide in the mixture of ethanol and acetonitrile in presence of Ag NPs. The whole size could be controlled from about 100 nm to 300 nm by

`

the amount of titanium source and ammnonia solution (Figure 7.1b, 7.1c, and 7.1d).

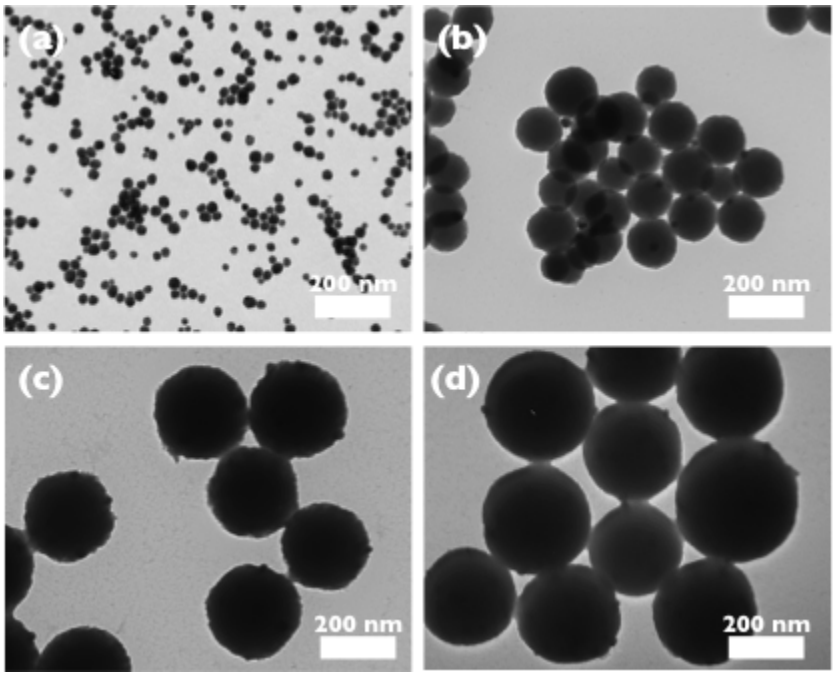

Figure 7.1. Transmittane electron microscopy (TEM) images of (a) Ag NPs and (b), (c) and (d) size-controlled Ag@TiO_2 nanocomposites.

In order to use the scattering effect of big TiO_2 NPs, Ag@TiO_2 about 300 nm was selected for the further study. The HR-TEM image and UV–vis absorption spectra of 300 nm Ag@TiO_2 was showed in Figure 7.2. The entire size seemed enough to use scattering by big size and the extinction around 420 nm indicate the light havesting ability of Ag NPs. Thus, the Ag@TiO_2 NPs were expected to improve the PCE by the scattering, LSP and electron storage effects. TiO_2 NPs which have similar size with Ag@TiO_2 were also prepared without Ag NPs for the comparison study (Figure 7.3).

`

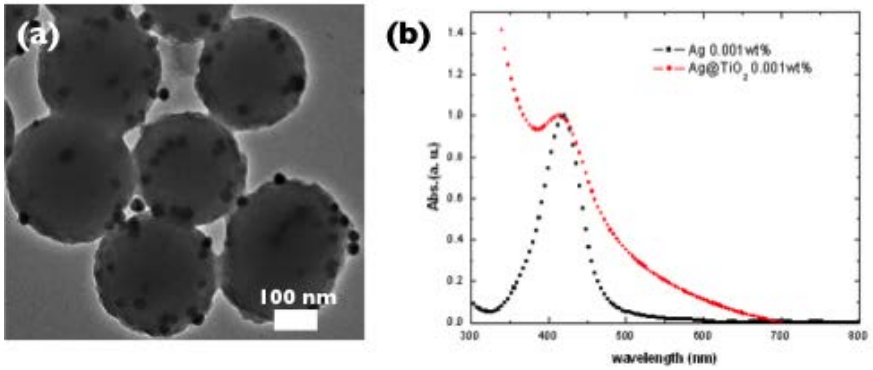

Figure 7.2. (a) The high-resolution TEM (HR-TEM) image of Ag@TiO_2 and (b) the extinction specta of Ag NPs and Ag@TiO_2.

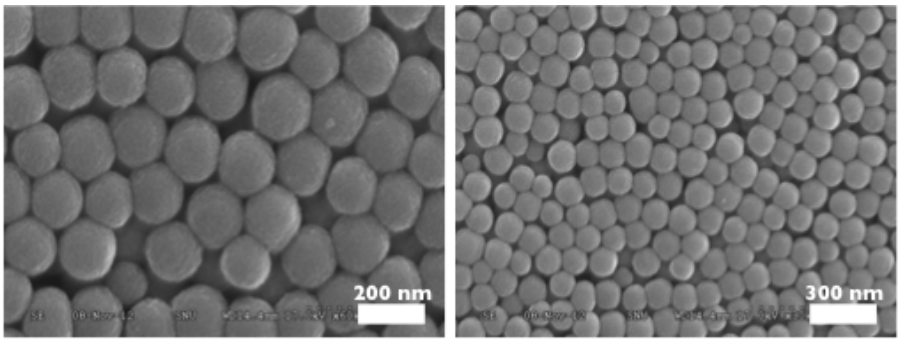

Figure 7.3. The scanning electron microscopy (SEM) images of TiO_2 NPs.

DSSCs were fabricated by using different nanoparticles Ag, Ag@TiO_2, and TiO_2 NPs with various blending ratio from 1 wt% to 10 wt%.

`

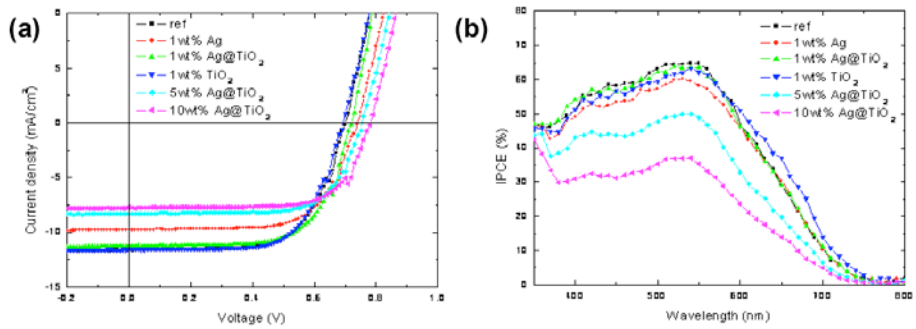

Figure 7.4. (a) The photocurrent-voltage and (b) IPCE curves of DSSC devices.

The photocurrent-voltage and incident photon to current efficiency (IPCE) curves of these devices are displayed in Figure 7.4, and the photovoltaic performances are summarized in Table 7.1. All of the photovoltaic devices embedded with Ag NPs (both Ag NPs and Ag@TiO_2) with 1 wt% concentration showed the enhanced V_{oc} at one sun intensity (100 mW/cm^2) under simulated AM 1.5 G illumination. In case of J_{sc} however, about the comparison of devices based on ref, Ag, Ag@TiO_2, and TiO_2 NP shows that J_{sc} of the photovoltaic device of 1 wt% Ag NPs (10.3 mA/cm^2) is smaller than other devices. These results are supported that Ag NPs play as a role of the electron storage as well as photo induced electron trap site in DSSCs.

However when Ag NPs was used in the formation of Ag@TiO_2, the additional scattering effect of big TiO_2 NPs seemed compensate the disadvantage of Ag NPs. Although the device based on 1 wt% TiO_2 NPs is obtained the highest J_{sc} (11.6 mA/cm^2), there is no enhancement of V_{oc}.

`

Thus, the device effciency was slightly increased in the Ag@TiO_2 and TiO_2 based DSSCs. As increase the weight ratio of Ag@TiO_2 nanoparticles to from 1 wt% to 10 wt%, the J_{sc} value is decreased but the V_{oc} is increased from 0.73 V to 0.78 V. Consequently, although the Ag@TiO_2 NPs showed the effect of electron storage by the increase of V_{oc}, additional scattering of TiO_2 was not enough to fully compensate the disadvantage of Ag NPs. Further study of using more effective TiO_2 scattering material or optimizing the ratio of Ag NPs and TiO_2 is needed to enhance the PCE of DSSSs more.

Table 7.1. The photovoltaic performance of the DSSCs.

Type of NPs	NPs ratio (wt%)	V_{oc} (V)	J_{sc} (mA/cm^2)	FF	η (%)
Non (ref)		0.71	11.00	0.67	5.23
Ag@TiO_2	1	0.73	11.10	0.66	5.35
Ag@TiO_2	5	0.75	8.57	0.70	4.50
Ag@TiO_2	10	0.78	7.75	0.71	4.29
Ag NPs	1	0.73	10.30	0.67	5.04
TiO_2	1	0.70	11.60	0.66	5.36

`

7.4 Conclusions

In this chapter, Ag@TiO_2 nanocomposite was synthesized to utilizing the PCE increasing properties of NPs in DSSCs (scattering, LSP, and charge storage of Ag NPs and scattering from large size of TiO_2 NPs). DSSCs with only Ag NPs and large sized TiO_2 were compared to investigate the property of DSSCs with Ag@TiO_2. The PCE of DDSSC was increased from 5.23 % to 5.35 % with 1 wt% of Ag@TiO_2. DSSCs with Ag@TiO_2 showed increasing V_{oc} but decreasing J_{sc} with increasing amount of Ag@TiO_2. More optimized condition is needed to get more enhanced PCE of DSSCs.

7.5 Experimental Section

Synthesis of Ag NPs First, 10 g of polyvinylpyrrolidone (PVP; 10,000 g/mol; TCI) was dissolved in 50 mL of ethylene glycol (EG; Samchun). Then, the reaction temperature was increased to 120 °C. Next, 0.8 g of $AgNO_3$ (Aldrich) was dissolved in 5 mL of ethylene glycol (Aldrich), and the mixture was added to the PVP solution. After 2 hr, the brownish dark product was purified by centrifugation to remove the excess PVP (once at 4,000 rpm for 10 min in acetone, and thrice at 17,000 rpm for 10 min in ethanol), and the final Ag NPs were dispersed in ethanol.

Synthesis of Ag@TiO_2 300 nm nanocomposite First, 9 mg of Ag NPs was dispersed in 100 mL of mixture solution of ethanol and acetonitrile (1:1 v/v). $Ti(OBu)_4$ (1 mL) was dissolved in 40 mL of mixture solution of ethanol and acetonitrile (1:1 v/v). Ammonia solution (0.65 mL) and diluted titania source (30 mL) was added to the Ag NPs solution to make composite particles. After 2 hr under room temperature, the brownish yellow product

`

was purified by centrifugation (thrice at 17,000 rpm for 10 min in ethanol), and the final Ag@TiO_2 was dispersed in ethanol. Smaller size of Ag@TiO_2 was prepared by the same method except the amount of ammonia solution (0.5 mL for 100 nm) and titania source (20 mL for both 100 nm and 200 nm). TiO_2 NPs were also prepared using the same method without Ag NPs.

Device fabrication of DSSCs Fluorine-doped tin oxide (FTO) glass plates (Pilkington, 8 Ω sq^{-1}, 2.3 mm thick) were cleaned in a detergent solution, water and isopropanol using an ultrasonic bath for 20 min, respectively. The washed FTO glass plates were immersed in an aqueous 40 mM $TiCl_4$ solution at 70 °C for 30 min. The different amounts of Ag@TiO_2 and Ag NPs in ethanol solution (Ag or Ag@TiO_2 ratio from 1 to 10 wt %) were mixed with TiO_2 paste, followed by stirring and sonicating. Then ethanol was removed by a rotary-evaporator. A transparent nanocrystalline layer was deposited on the FTO glass by a doctor blade printing method using the blended TiO_2 paste. The TiO_2 layer was gradually sintered according to a programmed procedure. The TiO_2 electrodes were treated again with $TiCl_4$ at 70 °C for 30 min and sintered at 500 °C for 30 min. After the TiO_2 electrodes were immersed in 0.3 mM N719 dye solution in ethanol, they were kept at 50 °C for 8 h in the dark. The FTO plate for the counter electrode was cleaned in an ultrasonic bath containing detergent solution, water and isopropanol. After counter electrodes were prepared by coating with a drop of H_2PtCl_6 solution (2 mg of Pt in 1 mL of ethanol) on an FTO plate followed by heating at 400 °C for 15 min, the dye-adsorbed TiO_2 electrode was attached to the counter electrode by heating with a hot-

`

melt polymer film (Surlyn 1702, 100 mm thick, DuPont). A drop of electrolyte solution (0.6 M 1,2-dimethyl-3-n-propyl-imidazolium iodide, 0.05 M iodine, 0.1 M LiI, and 0.5 M tert-butylpyridine in acetonitrile) was permeated through a hole in the counter electrode, which was driven into the cell by vacuum backfilling. Finally, the hole was sealed using a hot-melt polymer film with a cover glass (0.1 mm thick).

Characterizations The TEM images were acquired using Hitachi-7600 (Hitachi, Japan) and HR-TEM and SEM images were monitored using JEM-2100 (JEOL) and Hitachi S-4300 (Hitachi), respectively. UV-Vis spectra were recorded using a Beckman DU 650 spectrophotometer. The performance of the device was measured under AM 1.5 illumination (100 mW cm^{-2}) using a solar simulator (Peccell, 91160A) and Solar Cell IPCE Measurement System (McScience, K3100). The light intensity at each wavelength was calibrated using the standard Si solar cell as a reference. Photovoltaic performances were obtained using a source meter (Keithly 2400) connected to a computer was used to operate the device. TiO_2 paste was purchased from ENB Korea. (TTP-20N). N719 was purchased from Solaronix.

*** Contributions**

Photovoltaic cell tests were done by Dr. Woochul Lee and Prof. Jong-In Hong in Department of Chemistry, Seoul National University.

`

7.6. References

[1] O'Regan, B.; Gratzel, M., *Nature* **1991**, *353*, 737-740.

[2] Gratzel, M., *Nature* **2001**, *414*, 338-344.

[3] Grätzel, M., *J. Photochem. Photobiol. C* **2003**, *4*, 145-153.

[4] Chen, C.-Y.; Wang, M.; Li, J.-Y.; Pootrakulchote, N.; Alibabaei, L.; Ngoc-le, C.-h.; Decoppet, J.-D.; Tsai, J.-H.; Grätzel, C.; Wu, C.-G.; Zakeeruddin, S. M.; Grätzel, M., *ACS Nano* **2009**, *3*, 3103-3109.

[5] Law, M.; Greene, L. E.; Johnson, J. C.; Saykally, R.; Yang, P., *Nat. Mater.* **2005**, *4*, 455-459.

[6] Tanaka, K.; Takimiya, K.; Otsubo, T.; Kawabuchi, K.; Kajihara, S.; Harima, Y., *Chem. Lett.* **2006**, *35*, 592-593.

[7] Sauvage, F.; Chen, D.; Comte, P.; Huang, F.; Heiniger, L.-P.; Cheng, Y.-B.; Caruso, R. A.; Graetzel, M., *ACS Nano* **2010**, *4*, 4420-4425.

[8] Listorti, A.; O'Regan, B.; Durrant, J. R., *Chem. Mater.* **2011**, *23*, 3381-3399.

[9] Jang, S.-R.; Zhu, K.; Ko, M. J.; Kim, K.; Kim, C.; Park, N.-G.; Frank, A. J., *ACS Nano* **2011**, *5*, 8267-8274.

[10] Dang, X.; Yi, H.; Ham, M.-H.; Qi, J.; Yun, D. S.; Ladewski, R.; Strano, M. S.; Hammond, P. T.; Belcher, A. M., *Nat. Nanotech.* **2011**, *6*, 377-384.

[11] Wang, D. H.; Kim, D. Y.; Choi, K. W.; Seo, J. H.; Im, S. H.; Park, J. H.; Park, O. O.; Heeger, A. J., *Angew. Chem. Int. Ed.* **2011**, *50*, 5519-5523.

[12] Atwater, H. A.; Polman, A., *Nat. Mater.* **2010**, *9*, 205-213.

[13] Choi, H.; Chen, W. T.; Kamat, P. V., *ACS Nano* **2012**, *6*, 4418-4427.

[14] Topp, K.; Borchert, H.; Johnen, F.; Tunc, A. V.; Knipper, M.; von Hauff, E.; Parisi, J.; Al-Shamery, K., *J. Phys. Chem. A* **2009**, *114*, 3981-3989.

[15] Xue, M.; Li, L.; Tremolet de Villers, B. J.; Shen, H.; Zhu, J.; Yu, Z.;

`

Stieg, A. Z.; Pei, Q.; Schwartz, B. J.; Wang, K. L., *Appl. Phys. Lett.* **2011**, *98*, 253302.

[16] Salvador, M.; MacLeod, B. A.; Hess, A.; Kulkarni, A. P.; Munechika, K.; Chen, J. I. L.; Ginger, D. S., *ACS Nano* **2012**, *6*, 10024-10036.

`

Appendix/Chapter 8.

Titania Coated Hierarchical Silica Nanostructure for the High Efficient Scattering Material

8.1 Introduction

Nanostructures of several hundred nm or sub-micron have been used for scattering materials in solar-cells because light path could be lengthened by scattering effect, which enhance the short-circuit current.[1-3]

Among them, nanostructure with hierarchical structure is widely used because their high surface area for high dye absorption capacity.[4-7] However, studies on the hierarchical structures are still not well understood despite of their crucial effect on the scattering. In this chapter, titania coated hierarchical silica nanostructures was prepared to compare the scattering ability in the dye-sensitized solar cells.

`

8.2 Results and Discussion

Hierarchical silica nanostructure (HSN) was prepared as reported.[8, 9] Briefly, hierarchical silica structure could be generated in the micro-emulsion phase from water and oil by the hydrolysis and condensation of tetraethoxy silicate using CTAB as the surfactant. First, HSN about the size of 350 nm was prepared using 1-pentanol (1-PeOH) as co-solvent. The distance between hierarchical structures could be controlled by using different co-solvent because relative solubility change of surfactant in water and oil.[9, 10] In this chapter, the distance of hierarchical structure was increased when the more amount of 1-PeOH was used (Figure 8.1) Increasing amount of co-solvent could control the solubility of surfactant in water and oil with the same way of using co-solvent with longer alkyl chain; increasing the hydrophobicity. For the further study, HSN having the narrow hierarchical structure distance (Figure 8.1a, N-HSN) and wide distance (Figrue 8.1d, W-HSN) was selected.

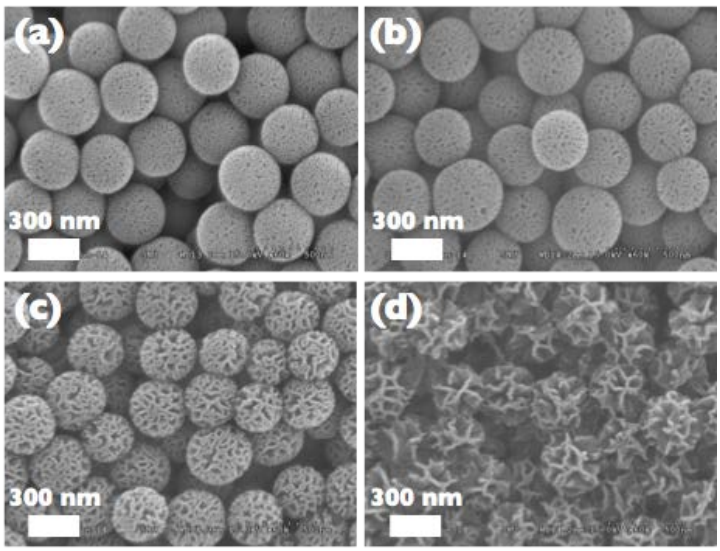

Figure 8.1. (a) TEM images of HSN by using 1-PeOH of (a) 0.16 mL, (b) 0.33 mL, (c) 0.65 mL, and (d) 1.3 mL.

`

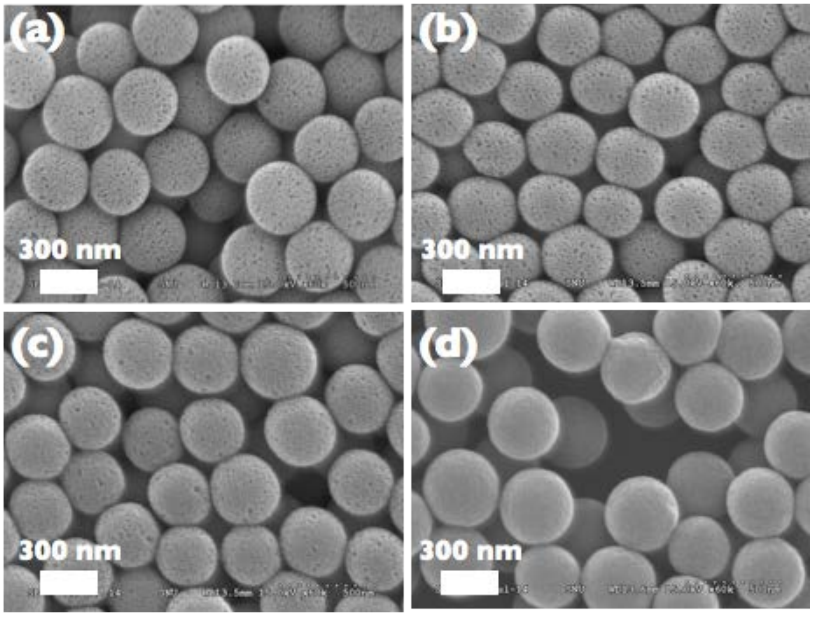

Figure 8.2. (a) FT-SEM image of (a) HSN and titania coated HSN using (b) 0.5 mL, (c) 1.0 mL, and (d) 2.0 mL of TB.

Titania was coated on the N-HSN in the mixed solvent of ethanol and acetonitrile. Titanium butoxide was hydrolyzed and condensed on the HSN with the ammonia solution in mixed solvent. The degree of titania coating was monitored in Figure 8.2 with the increasing amount of titania source (diluted titanium butoxide, TB). In the use of 2 mL of TB, hierarchical nanostructure of HSN was disappeared with too much coated titania. In order to use the hierarchical structure, 1 mL of TB was used in the following experiments. Titania coating process of N-HSN and W-HSN was monitored by TEM in Figure 8.3.

`

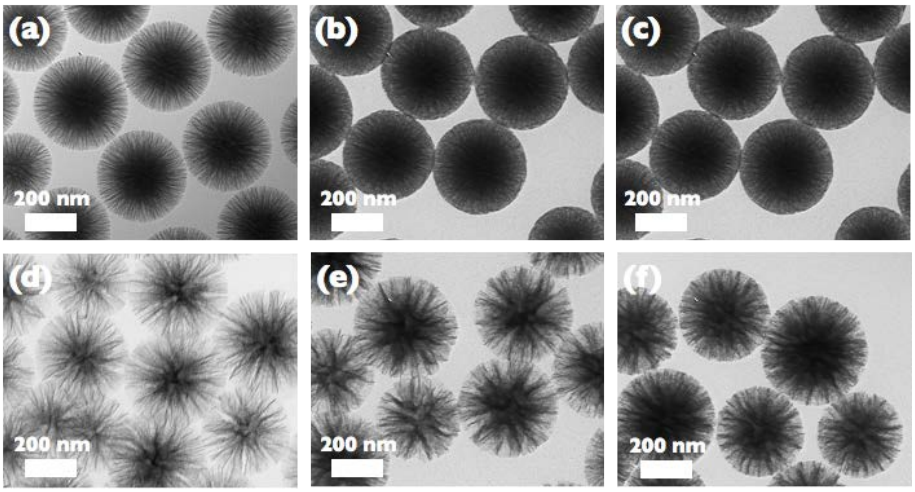

Figure 8.3. TEM images of (a) N-HSN, (b) N-HST, (c) annealed N-HST, (d) W-HSN, (e) W-HST, and (f) annealed W-HST.

TEM images of Figure 8.3a and 8.3d show well developed hierarchical structure of HSTs and titania coating was clearly shown in darken image of Figure 8.3b and 8.3e. Titania coated structure was stained their own structure after calcination process under 600 ºC for 4 hr (Figure 8.3c and 8.3f).

For the comparison of scattering effect of HST with other structures, various spherical particles about 350 nm were prepared. Silica@Titania (ST) and Titania@Titania (TT) was prepared by seed-growth method using silica and titania core and had similar size with N-HST and W-HST.

Prepared scattering materials retained their own structure after calcination shown in Figure 8.5.

`

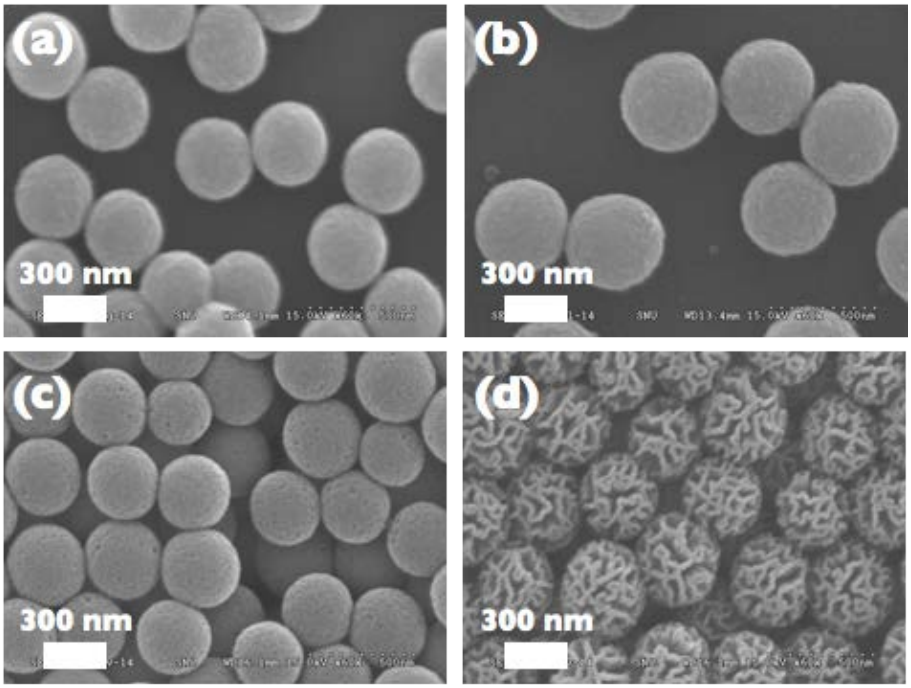

Figure 8.4. FE-SEM images of (a) ST, (b) TT, (c) N-HST, and (d) W-HST.

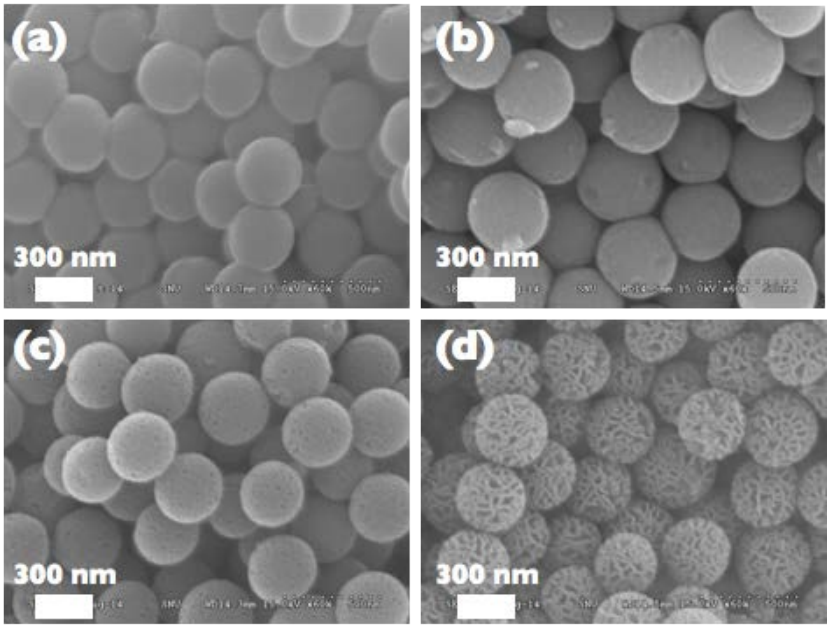

Figure 8.5. FE-SEM images of (a) ST, (b) TT, (c) N-HST, and (d) W-HST after calcination.

`

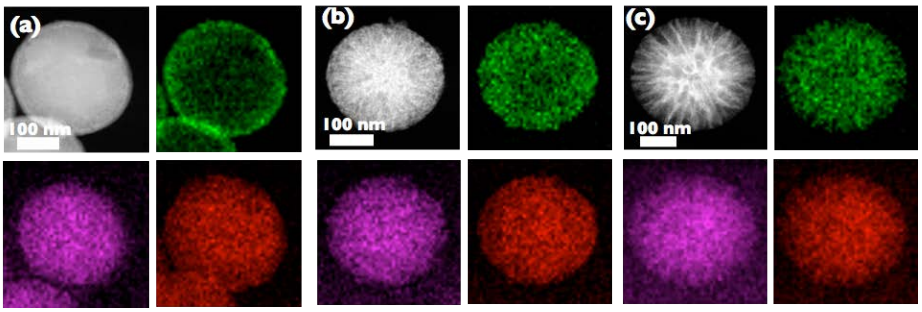

Figure 8.6. HAADF and EDS mapping images of (a) ST, (b) N-HST, and (c) W-HST after calcination (green –Ti, purple – Si, and red – O).

The atomic distribution of scattering material composed of silica and titania were monitored by EDS mapping (Figure 8.6). EDS mapping of ST shows green Ti atom in the shell and purple Si in the core. In case of HSTs, Ti atoms are well dispersed on the hierarchical silica structures showing successfully coating of titania.

The formation of titania on the scattering materials was confirmed by XRD in Figure 8.7. All the scattering materials have anatase crystal phase (JCPDS File No. 21-1272), which indicate the presence of titania.

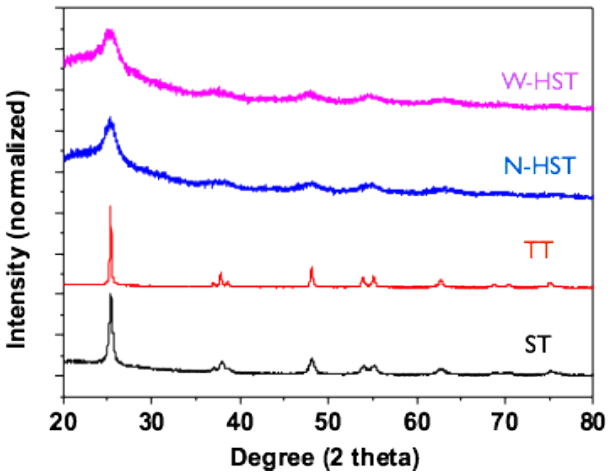

Figure 8.7. XRD data of scattering materials.

`

To compare the dye adsorption capacity of scattering materials the absorbance of N719 dye was monitored in remnant solution or after adsorption/desorption experiment. First, the remnant solution of N719 dye in ethanol was compared (Figure 8.8a). The remnant solution after removing P25 (commercial titania about 20 nm) showed the lowest absorption, which indicates the highest absorption capacity due to their small size with high surface area. But the remnant solution of ST and TT showed the similar adsorption with N719 solution itself, which indicate very low adsorption capacity for their large size with low surface area.

Although their large particle size and having silica content which could not bind with dye, the remnant solution of HSTs showed low absorbance due to the high surface area of HSTs (BET surface area of 418 m^2/g for N-HST and 416 m^2/g for W-HST). The dye adsorption capacity of scattering materials was also confirmed by detaching and measuare the absorbance of N719 dye and the similar result was obtained in Figure 8.8b.

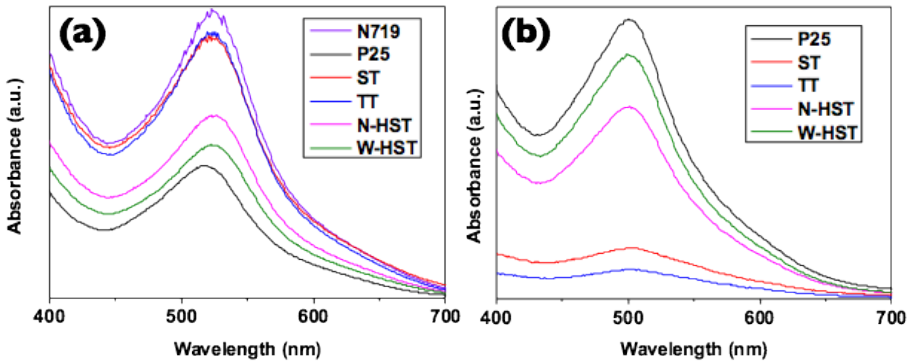

Figure 8.8. Absorption spectra of (a) remnant solution of N719 dye in ethanol after removing scattering materials and (b) detached N719 dye in 1 M of KOH solution.

`

8.3 Conclusions

In this chapter, titnia coated hierarchical silica structure were prepared to compare their scattering ability in solar-cells. Hierarchical silica structure could be controlled their hierarchical structure by changing the amount of co-solvent. Titania coated hierarchical structures were confirmed by SEM, TEM, HR-TEM, EDS, XRD, and Raman. Their dye adsorption capacity was compared with other structures such as silica@titania and titania@titania. The outstanding scattering and high dye adsorption is expected by using prepared hierarchical silica@titania structure in this chapter.

`

8.4 Experimental Section

Materials and Instruments Tetraethyl orthosilicate (TEOS) was purchased by TCI and hexadecyltrimethylammonium bromide (CTAB), 1-pentanol, and titanium butoxide ($Ti(OBu)_4$), ethanol, and acetonitrile were purchased from Aldrich. Urea, cyclohexane, hydrochloric acid (HCl), and ammonia solution was purchased from Samchun and all the chemicals were used without further purification.

The FE-SEM and TEM images were acquired using Hitachi S-4300 (Hitachi) and Hitachi-7600 (Hitachi), respectively. More detailed images and information about the atomic distributions in HTNPs were obtained using TEM with a higher accelerating voltage (Tecnai F20, FEI, 200 kV) and an energy dispersive spectroscopy (EDS) system. The absorbance was measured using a UV-Vis spectrometer (Sinco, S-3100).

Synthesis of HSNs HSNs were obtained in the microemulsion system by using the reported method.[8, 9] First, 1 g of CTAB 600 g of urea were dissolved in 30 mL of water. To this solution, 1-PeOH (0.16 mL for N-HSN and 1.3 mL for W-HSN) in 30 mL of cyclohexane were added with vigorous stirring. After 30 min of stirring under room temperature, the reaction temperature was raised to 70 °C for 16 hr. The white product was washed with ethanol by 3 times centrifugation (13,000 rpm, 10 min) and re-dispersion and dispersed in ethanol. To remove CTAB, 10 % (v/v to ethanol) of HCl was injected and stirred for overnight. The white product was purified by centrifugation and dispersed in ethanol for titnaia coating.

Synthesis of HSTs First, 200 mg of HST (N-HST or W-HST) was dispersed in 200 mL of mixture solution of ethanol and acetonitrile (1:1 v/v)

`

and 2 mL of ammonia solution was added. $Ti(OBu)_4$ (0.5 mL) was dissolved in 20 mL of mixture solution of ethanol and acetonitrile (1:1 v/v) and this solution was injected to the HST dispersed solution. After 2 hr under room temperature, the white product was purified by centrifugation (thrice at 13,000 rpm for 10 min in ethanol).

Synthesis of ST and TT ST and TT were prepared by seed growth method. First, silica core was prepared by using stober method. 1.2 mL of TEOS was dissolved in mixed alcohol solution of 1-PrOH and 1-BuOH (v/v) following the addition of ammonia solution (6 mL) and water (2 mL). After 6 hr, the white product was purified by centrifugation and re-dispersion and dispersed in ethanol. To introduce titania shell on the silica core, 200 mg of silica was dispersed in the mixed solution of ethanol and acetonitrile (200 mL, 1:1 v/v) with ammonia solution (2 mL). $Ti(OBu)_4$ (0.5 mL) in mixed solution of ethanol and acetonitrile (20 mL, 1:1 v/v) was added to the silica dispersed solution and stirred for 2 hr. The white product of ST was purified by centrifugation and re-dispersion and dispersed in ethanol.

Titania core was prepared in the mixed solution of ethanol and acetonitrile (1:1 v/v). $Ti(OBu)_4$ (1.5 mL) in the mixed solution of ethanol and acetonitrile (60 mL, 1:1 v/v) was added to the mixed solution of ethanol and acetonitrile (200 mL, 1:1 v/v) with ammonia solution (2 mL). After 2 hr, the white product of titania (50 mL) was extracted and ammonia solution (0.5 mL) and $Ti(OBu)_4$ (1.0 mL) in the mixed solution of ethanol and acetonitrile (40 mL, 1:1 v/v) was added to increase the size of titania. After 2 hr, the white product was purified by centrifugation and re-dispersion and dispersed in ethanol.

\

`

8.5 References

[1] Galvez, F. E.; Kemppainen, E.; Miguez, H. n.; Halme, J., *J. Phys. Chem. C* **2012**, *116*, 11426-11433.

[2] Zhang, Q.; Myers, D.; Lan, J.; Jenekhe, S. A.; Cao, G., *Phys. Chem. Chem. Phys.* **2012**, *14*, 14982-14998.

[3] Hagfeldt, A.; Boschloo, G.; Sun, L.; Kloo, L.; Pettersson, H., *Chem. Rev.* **2010**, *110*, 6595-6663.

[4] Wu, W.-Q.; Xu, Y.-F.; Rao, H.-S.; Su, C.-Y.; Kuang, D.-B., *Nanoscale* **2013**, *5*, 4362-4369.

[5] Gao, X.-D.; Li, X.-M.; Gan, X.-Y.; Wu, Y.-Q.; Zheng, R.-K.; Wang, C.-L.; Gu, Z.-Y.; He, P., *J. Mater. Chem.* **2012**, *22*, 18930-18938.

[6] Lv, F.; Xiao, S.; Zhu, J.; Li, H., *RSC Adv.* **2014**, *4*, 36206-36211.

[7] Zhu, G.; Pan, L.; Yang, J.; Liu, X.; Sun, H.; Sun, Z., *J. Mater. Chem.* **2012**, *22*, 24326-24329.

[8] Polshettiwar, V.; Cha, D.; Zhang, X.; Basset, J. M., *Angew. Chem. Int. Ed.* **2010**, *49*, 9652-9656.

[9] Moon, D.-S.; Lee, J.-K., *Langmuir* **2012**, *28*, 12341-12347.

[10] Kahlweit, M.; Strey, R.; Busse, G., *J. Phys. Chem.* **1990**, *94*, 3881-3894.

`

Appendix/Chapter 9.

Synthesis of Micron Sized Flower-like Hierarchical Iron Oxide from Primary Nanoparticles and Their Morphology Control

9.1 Introduction

Metal oxide nanoparticles have been used for adsorbent and photo-catalyst to remove various pollutants in the water and air for their powerful property with high surface area.[1, 2] However, extracting and reusing metal oxide in nanoscale are very challenging for their small size and low weight. Therefore, micron sized hierarchical structures have been widely researched these days due to their high surface area in spite of their large size.

After Wan *et al*. reported the preparation of 3D flower-like hierarchical iron oxide nanostructures (FIOs),[3] many researchers have studied the synthesis and application of FIO. In a typical synthetic method, iron source like iron halide salt, base like urea and surfactants like long alkyl halide salt in ethylene glycol (EG) are refluxed at high temperature about 200 °C in autoclave, so called solvothermal method.[4-7] However, the reaction in this system has some disadvantages of small scale, not in safe, and using harmful surfactants.

In this chapter, FIOs are prepared without any surfactant and autoclave reaction. Using pre-obtained primary nanoparticles, monodispersed FIOs could be obtained in the simple reflux reaction. The obtained FIOs simply transform their morphology via hydrolysis reaction, which are systemically investigated in this chapter.

`

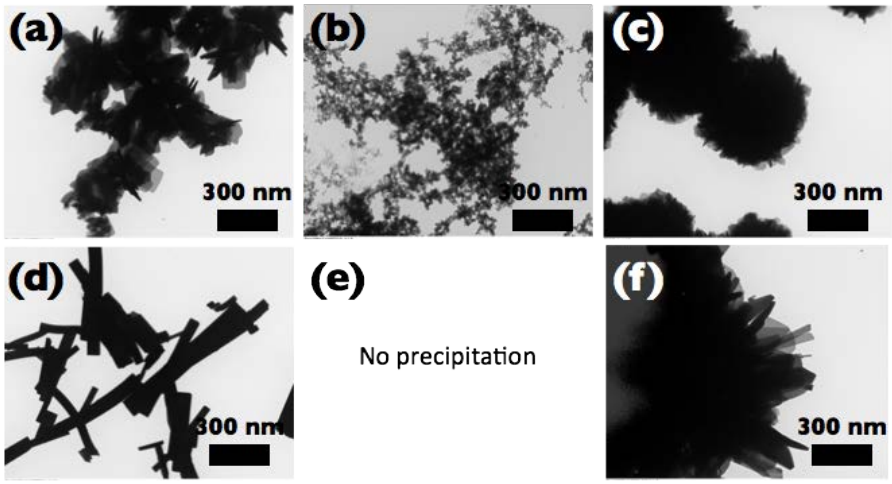

Figure 9.1. TEM images of the products under the amount of reactants in 50 mL of EG under mild reaction condition.

	a	b	c	d	e	f
$FeCl_3 \cdot 6H_2O$	30	60	120	250	750	300
NaOAc	100	100	100	100	100	500

Table 9.1. The amount of reactants used in Figure 9.1

9.2. Results and Discussion

Synthesis flower-like particles in mild condition The formation mechanism of FIOs was expected as follows; making primary nanoparticles by coordination of Fe and EG and their aggregation into the flower like morphology.[3] The preparation of FIOs in mild condition was tried. Iron chloride hexahydrate was used as an iron source and sodium acetate was used as a base in EG solvent. Any surfactant was not used and autoclave reactor

`

was also used.

Although various experiments by changing the amount of reactants, mono-dispersed hierarchical structure was rarely found and the color of products was yellow-green, differ from dark-green as reported. Irregular hierarchical structures in Figure 9.1 indicate some part of precursor could be transformed from primary particle. It could be expected that the formation of FIOs is limited due to the reduced reactivity in the mild condition especially at the formation of primary particles.

To start from primary particles in mild condition, primary particles including iron source was prepared by simple precipitation method. It was already shown that titania nanoparticles could be obtained in the mixed solvent of ethanol and acetonitrile with ammonia solution in this thesis of chapter 4.

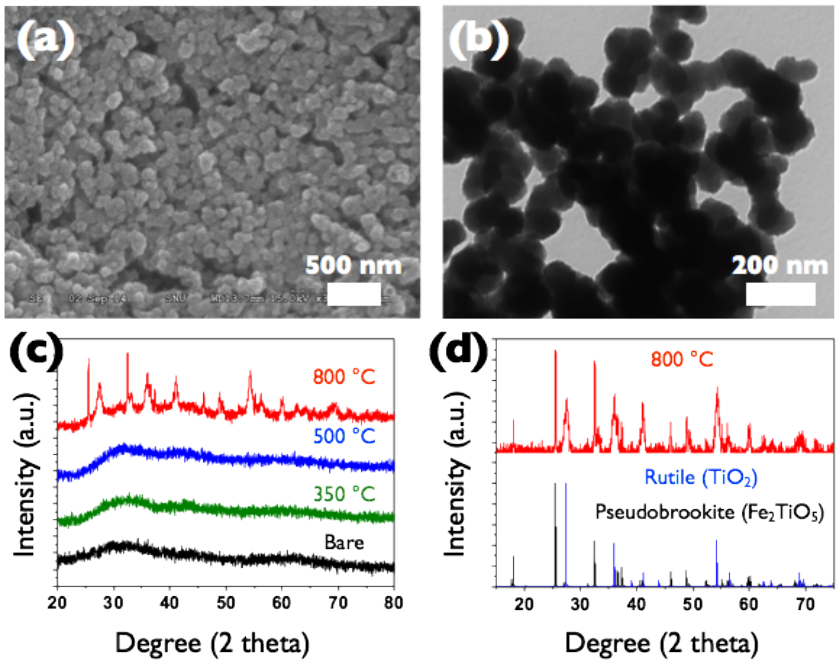

Figure 9.2. (a) FE-SEM image, (b) TEM image, and (c) and (d) XRD patterns of p-FIOs.

`

When Fe source was co-used with Ti source, brown-yellow solid product was obtained as ~100 nm nanoparticles (FE-SEM and TEM images of Figure 9.2a and 9.2b).

To confirm the obtained primary particles for FIOs (p-FIOs), XRD patterns were monitored after calcination at various temperatures (Figure 9.2c). As-prepared p-FIOs and the annealed p-FIOs at 350 °C and 500 °C were did not showed any peaks in XRD, indicating the amorphous phase. The p-FIOs in the well-dispersed solid-solution of (Fe,Ti) oxide could be expected because any crystal peaks of anatase TiO_2 or hematite Fe_2O_3 were not found. However, p-FIOs annealed at 800 °C showed lots of peaks in XRD and could be assigned to mixed crystal of psedobrookite of Fe_2TiO_5 and rutile of TiO_2.

Using as-prepared p-FIOs as iron source, preparation of FIOs was tested with NaOAc in EG solvent without autoclave. Brown-yellow p-FIOs turned to dark-green gradually with the increasing reaction time until 120 min (Figure 9.2).

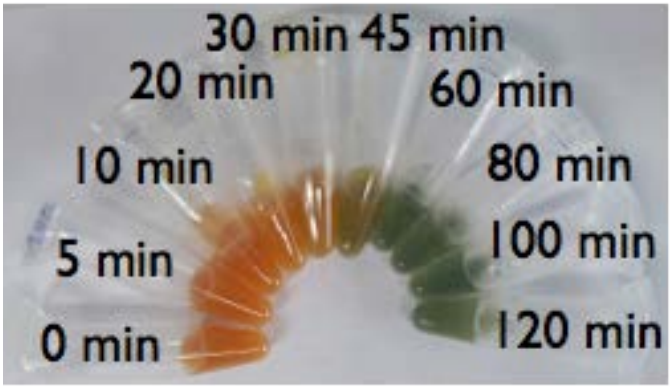

Figure 9.3. Photograph of color change with the reaction time of preparing FIOs with p-FIOs.

`

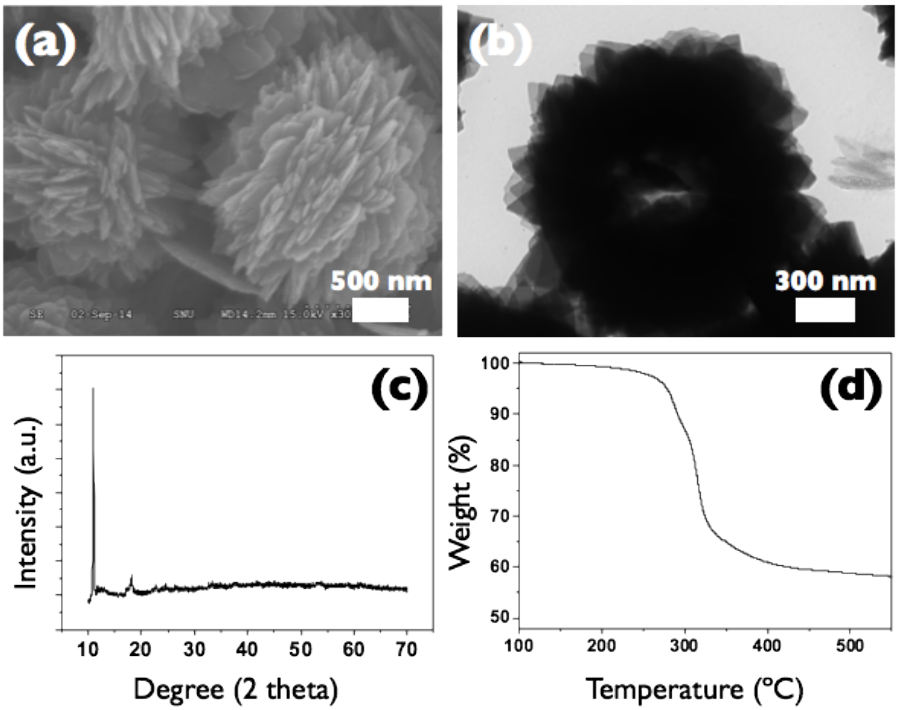

Figure 9.4. (a) FE-SEM image, (b) TEM image, (c) XRD pattern, and (d) TGA data of flower like particles.

The obtained product was washed with ethanol and monitored by using FE-SEM and TEM (Figure 9.4a and 9.4b). Micron-sized particles composed of hierarchical nanostructure were well developed in flower like particles synthesized from p-FIOs.

XRD patterns of flower like particles show the intense peak around 10 °, which is the representative peak of metal-glycolate complexes (Figure 9.4c).[7,8]

From the atomic composition of flow-like particles by ICP-AES (Fe:Ti=97:3) and EDS in SEM (Fe:Ti=96:4), the major metal component of flow-like particles is expected to Fe ion.

`

The existence of glycol unit in flower like particles was also confirmed by TGA experiment in Figure 9.4d. The remained weight (about 58 wt%) after TGA experiment in N_2 gas had similar value with the reported flower like particles having glycol units. Because it was reported and confirmed that flower like complex get magnetite (Fe_3O_4) in the annealing condition with N_2, the following equation could be expected and compared with TGA data.

$$Fe_3(OCH_2CH_2O)_4 \rightarrow Fe_3O_4$$

, where the mass of particles reduced from Calc. 100 wt% to Calc. 57 wt%. This value is very similar with TGA data, which confirms the Fe-glycolate state of flower-like particles.

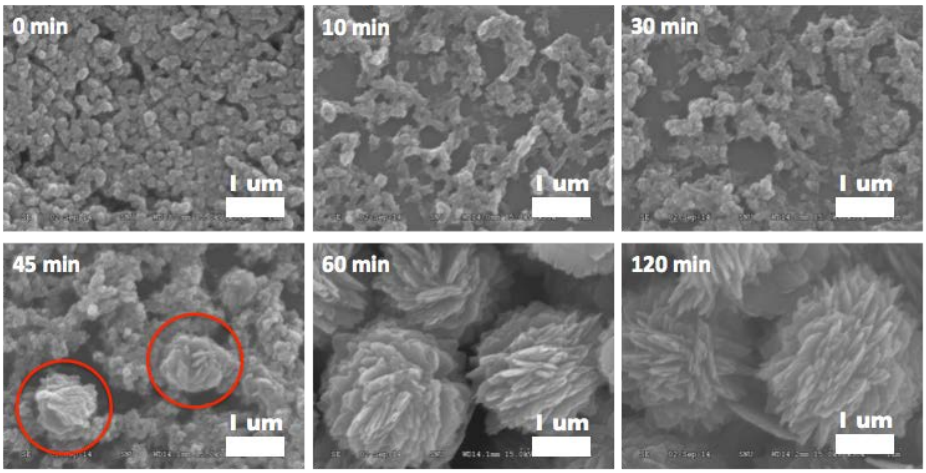

Figure 9.5. FE-SEM images of time-dependent formation of flower-like particles.

`

To investigate the formation mechanism of flower-like particles, time-dependent FE-SEM images were obtained in Figure 9.5. The p-FIOs were slightly dissolved until 30 min of reaction time and the formation of flower-like particles was detected at 45 min of reaction time. From the atomic composition of final flower-like particles as mentioned, the dissolved part is expected to mainly Ti components. The particle size growth could be monitored until 120 min of reaction time to have micron size.

The dissolution of p-FIOs in EG was further studied. The solubility of p-FIOs in ethanol (EtOH) and EG was tested by stirring particles in two solvents during overnight. The photographs of Figure 9.6 shows high solubility of p-FIOs in EG than EtOH. After overnight stirring, p-FIOs in EG were clear and transparent (Figure 9.6a) and any precipitation was obtained after centrifugation in Figure 9.6b. Although colorless solution was obtained after ethanol solvent was removed, dark-brown solution was obtained after EG was removed, which indicated the existence of solvated species.

The dark-brown solution from p-FIOs in EG was monitored by TEM (Figure 9.7d. The partially dissolved particle could be found and the remained part was expected to mainly Fe from atomic composition monitoring as mentioned before.

The dissolved Ti component after the synthesis of flower-like particles was confirmed by preparing the titania nanoparticles. After removing flower-like particles by using centrifugation, the remnant solution was injected to acetone solvent to make white spherical particles.

`

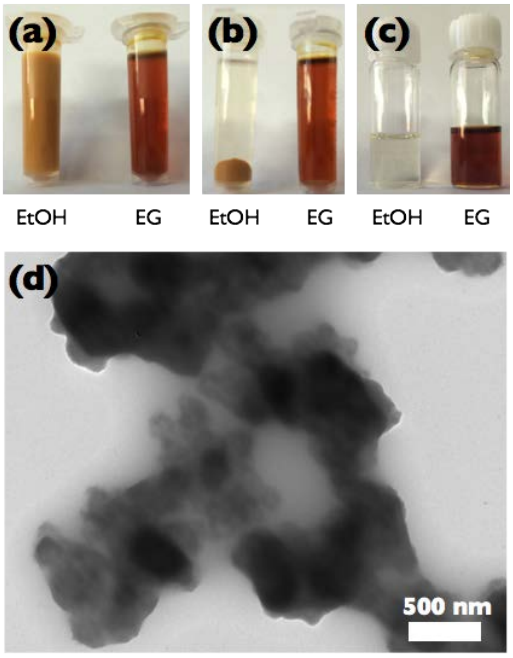

Figure 9.6. Photographs of (a) p-FIOs in EtOH and in EG, (b) after centrifugation in EtOH and EG, remnant solution in EtOH and EG, and TEM image of p-FIOs in EG.

It was reported and showed in the chapter 2 of this thesis that the spherical titania nanoparticles could be obtained using titania source stabilized by EG. The FE-SEM image of as-prepared particles and anatase peaks of annealed particles (at 500 °C) from XRD patterns (Figure 9.7) showed the prepared particle was titania, which indicated that the major part of remnant solution was Ti component.

`

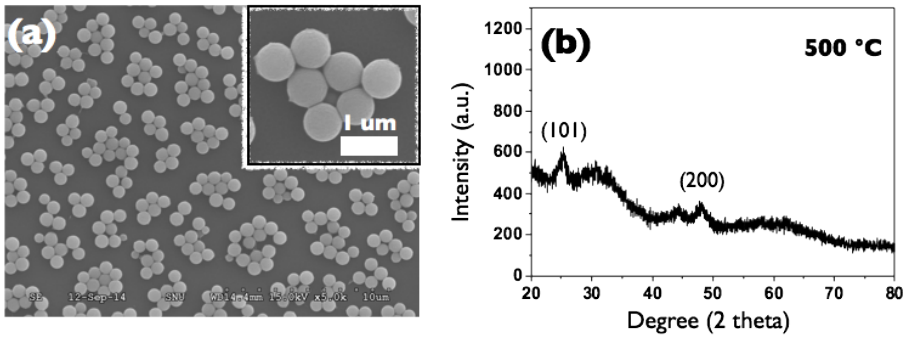

Figure 9.7. FE-SEM image and (b) XRD patterns of prepared titania particles.

Morphology control via hydrolysis Prepared flower-like particles were changed in their color from dark-green to red in a few minutes with the excess amount of water. In the image of FE-SEM in Figure 9.8a, the morphology of red product was similar with dark-green flower-like particles. However, TEM image of Figure 9.8b shows the generation of very tiny pore in the leaves of flower-like structures. The XRD patterns of red product showed almost non-crystalline structure without intense peak of flower-like particles. From the red color and crystallnity of product, the generation of FeO(OH) from $Fe_3(OCH_2CH_2O)_4$ was expected *via* hydrolysis (Figure 9.8c).[9]

To investigate the hydrolysis of flower-like particles, NMR experiment was performed. Flower-like particles were stirred in MeOD and D_2O to monitor whether any reaction would occur. The color of particle was changed not in MeOD but in D_2O. The remnant solution without particles was monitored by ^1H NMR (Figure 9.9a). It showed the existence of EG as the peak of 3.6 ppm, which indicate the glycolate unit was replaced with D_2O. However, any exchange was possible in MeOD without D_2O (Figure 9.9b).

`

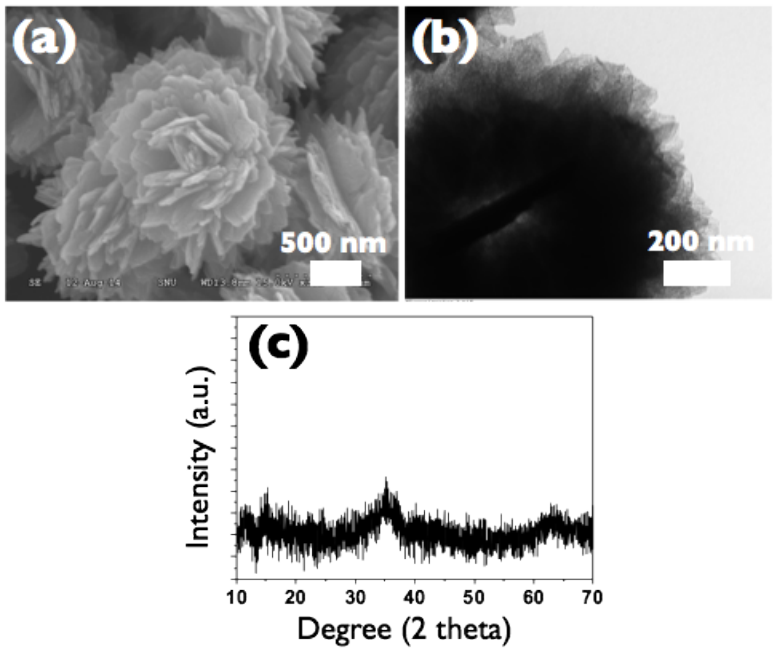

Figure 9.8. (a) FE-SEM image, (b) TEM image, and (c) XRD pattern of prepared hydrolyzed flower-like particles.

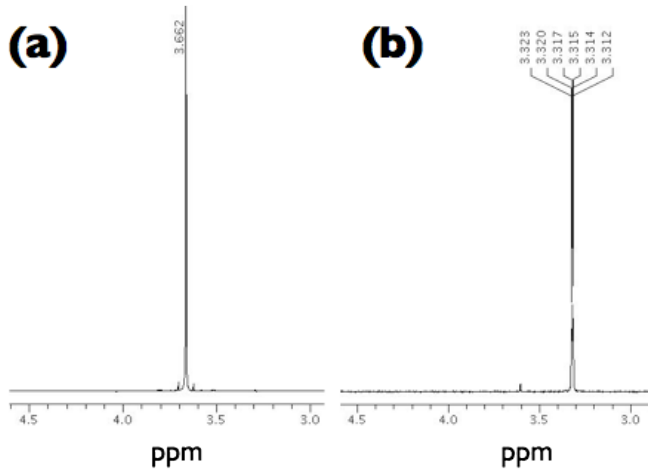

Figure 9.9. The ^{1}H NMR spectrum of solutions after removing flower-like particles in (a) D_2O and (b) MeOD.

`

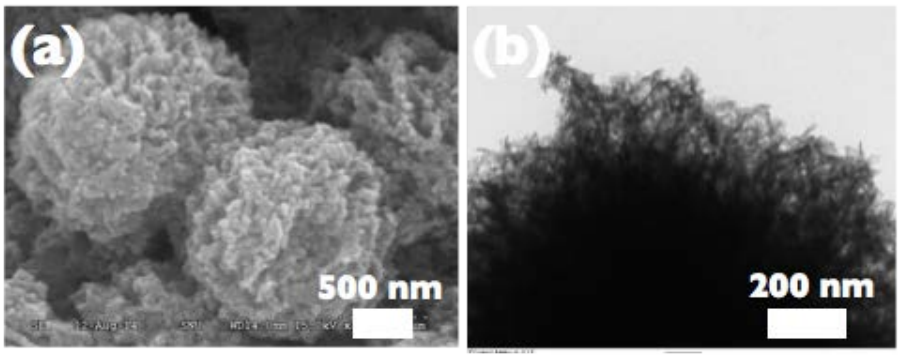

Figure 9.10. (a) FE-SEM and (b) TEM image of flower-like particles stirred in ammonia solution.

When flow-like particles were stirred in ammonia solution, red product was obtained with different morphology in a few seconds. FE-SEM and TEM image of the product showed still hierarchical but without inside part of leaves structure (Figure 9.10). Hollow-like structure could result from rapid hydrolysis of Fe-glycolate. Because the reaction start the outside part of leaves structure, rapid condensation into outer region could make hollow leaves structures like kirkendall effect.[10]

The chemical structure of hydrolysed flower-like particles was expected with TGA experiment (Figure 9.11). The remained weight percent after TGA experiment were 90 wt% and 91 wt% from water and ammonia solvent, respectively. In case of FeO(OH), it transforms to Fe_2O_3 of hematite, which change their weight percent from Calc. 100 wt% to Calc. 89 wt%. The similar weight change indicate the hydrolysed flower-like particles have the structure of FeO(OH).

`

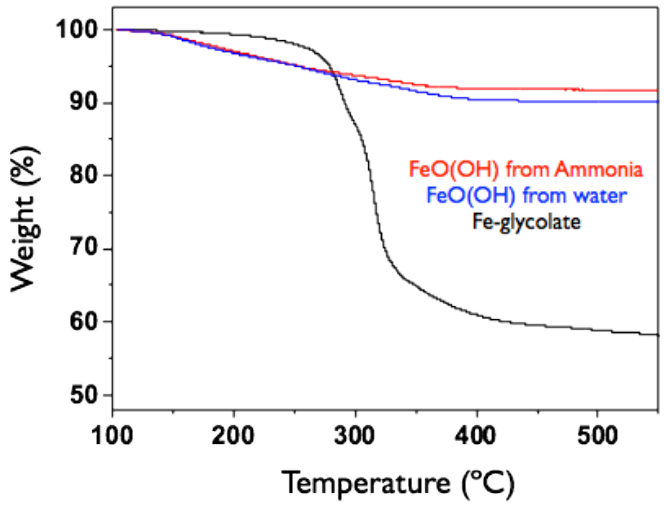

Figure 9.11. TGA experiments of flower-like particles.

The crystal phase of flower-like particles was transformed to magnetite. Flower-like particles of Fe-glycolate could easily get magnetite in the calcination process under Ar because ethylene glycol group have reduction power to reduce some part of Fe^{3+} to Fe^{2+}. However, hydrolysed flower-like particles need reducing agent to get magnetite phase. In this chapter, hydrolysed flower-like particles were mixed with $NaBH_4$ as a reducing agent. The generation of reactive hydride or hydrogen from $NaBH_4$ under high temperature is expected as the reason of powerful reducing power in this reaction condition.[11, 12]

The obtained particles showed the black color and were represented as the FE-SEM image in Figure 9.12. Three flower-like particles remained their own structure. The magnetite crystal phase of reduced flower-like particles was monitored by XRD in Figure 9.13 (denoted as m-FIOs). Using the Scherrer equation and XRD patterns, the crystal size of m-FIOs from Fe-gly could be expected to have the largest size and that of m-FIOs from water have similar or less size. The m-FIOs from ammonia solution had the smallest crystalline

`

size.

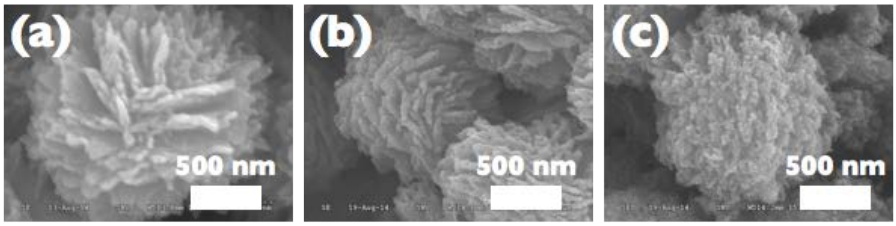

Figure 9.12. (a) FE-SEM image of reduced flower-like particles from (a) Fe-gly, (b) flower-like particles hydrolysed with water, and (c) flower-like particles hydrolysed with ammonia solution.

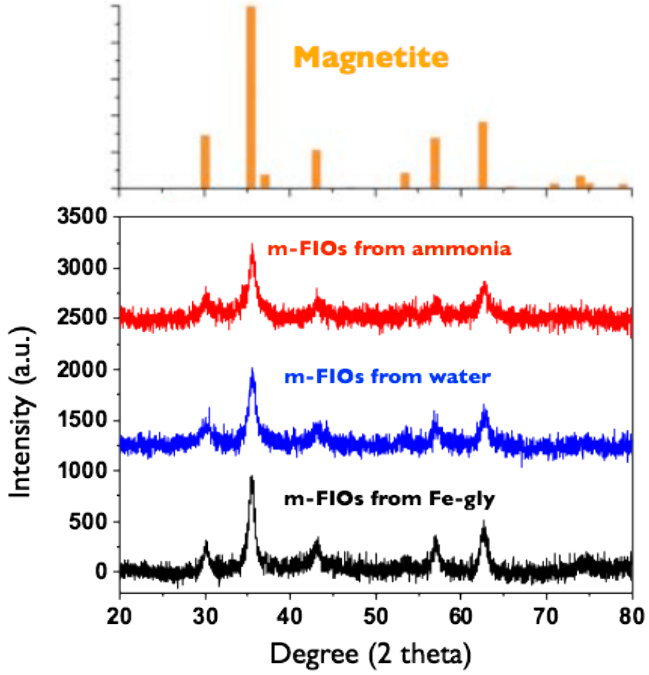

Figure 9.13. XRD patterns of m-FIOs.

`

Finally, the magnetic property of m-FIOs was compared with a magnetic property measurement system at 300 K in the applied field changing from -7 kOe to 7 kOe. The m-FIOs form Fe-gly had the similar Ms value with the reported flower-like particles.[6] The *Ms* values decreased in the following order; m-FIOs from Fe-gly, m-FIOs from water, and m-FIOs from ammonia. It could results from the decreasing crystal size of m-FIOs.[13]

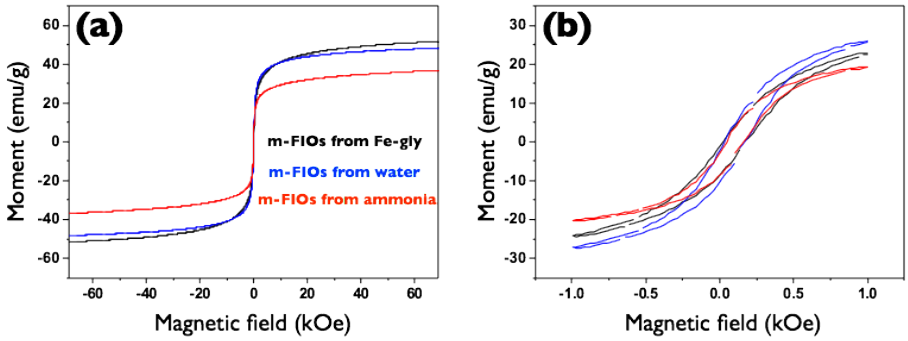

Figure 9.14. (a) Magnetic hysteresis curves in room temperature for m-FIOs and (b) magnified low-field region.

`

9.3 Conclusions

Flower-like particles of iron oxide was prepared via self-assembly of primary particles in EG with the mild condition. Primary particles of Fe,Ti oxide nanoparticles were used for the preparation of mono-dispersed flower-like particles without harsh condition. Prepared flower-like particles had Fe-glycolate sturucture, which could be hydrolysed to have FeO(OH) structure. The transformation was confirmed by ^{1}H NMR, and the morphology could be controlled using ammonia solution. Prepared flower-like particles could also be transformed to have magnetite phase after proper calcination conditions. Finally, the magnetic properties of flower-like particles were investigated.

9.4. Experimental Section

Materials and Instruments Titanium tetrabutoxide, ferric chloride hexahydrate, sodium borohydride, anhydrous ethanol, and acecetonitrile were purchased from Aldrich. Urea, sodium acetate, and ethylene glycol were purchased from Samchun, Korea. All solvents and reagents used in this chapter were commercially available and used as received.

The sizes and morphologies of products were analyzed by using field-emission scanning electron microscopy (FE-SEM, Hitachi S-4300, 4.2 kV) and transmission electron microscopy (TEM, Hitachi-7600, 100 kV). The atomic component was confirmed by using inductively coupled plasma atomic emission spectrometry (ICP-AES, Optima-4300 DV) installed at the National Center for Inter-university Research Facilities (NCIRF) at Seoul National University. Thermogravimetric analysis (TGA) was performed using an SDT Q600 (TA Instruments Inc.). The samples for TGA were preheated at 100 °C for 30 min and then the temperature was raised to 550 °C at 10 °C/min in nitrogen. The crystallinity of the samples was evaluated by powder X-ray

`

diffraction (XRD) analysis on a Bruker New D8 Advanced Diffractometer with Cu K radiation (λ = 1.5418 Å). The scanning rate was 0.02 ° per second and the range was from 10 to 70 °. The magnetic properties of m-FIOs were obtained using Physical Property Measurement System (PPMS-14).

Primary particles for FIOs Titanium butoxide (1.0 mL) and ferric chloride hexahydrate (500 mg) were diluted in a mixture of solvent of absolute ethanol and acetonitrile (1:1 v/v, V_{tot} = 40 mL) and poured into the mixture of absolute ethanol and acetonitrile (1:1 v/v, V_{tot} = 400 mL). This turned to the yellow-milky colloids, and after a reaction for 2 hr, the products were purified and washed with water and ethanol using centrifugation/re-dispersion (17,000 rpm, 10 min, 3 repetitions). The obtained Fe,Ti composite oxide nanoparticles were dispersed in EG for further reaction.

Flower-like particles Prepared primary nanoparticles were dispersed in EG (50 mL) with NaOAc (200 mg). The reaction temperature was raised to 200 °C and stirred for 2 hr. The dark-green product was purified by centrifugation and re-dispersion (4,000 rpm, 10 min, and 3 times) using ethanol.

Hydrolysis of flow-like particles Flower-like particles was stirred in the excess amount of water or ammonia solution over 6 hr. The red product was purified by centrifugation and re-dispersion (4,000 rpm, 10 min, and 3 times) using ethanol.

Calcination to prepare m-FIOs Flower-like particles from Fe-gly were annealed at 450 °C for 3 hr under Ar. Flower-like particle from water and ammonia solution were mixed with the same amount of NaBH4. The mixed solid was annealed at 300 °C for 30 min under Ar. All annealed particles were tuned their color to black after calcination.

`

9.5. References

[1] Saharan, P.; Chaudhary, G. R.; Mehta, S. K.; Umar, A., *J. Nanosci. Nanotech.* **2014**, *14*, 627-643.

[2] Saha, B.; Das, S.; Saikia, J.; Das, G., *J. Phys. Chem. C* **2011**, *115*, 8024-8033.

[3] Zhong, L. S.; Hu, J. S.; Liang, H. P.; Cao, A. M.; Song, W. G.; Wan, L. J., *Adv. Mater.* **2006**, *18*, 2426-2431.

[4] Gao, Q.; Zhao, A.; Gan, Z.; Tao, W.; Li, D.; Zhang, M.; Guo, H.; Wang, D.; Sun, H.; Mao, R.; Liu, E., *CrystEngComm* **2012**, *14*, 4834-4842.

[5] Jin, S.; Deng, H.; Long, D.; Liu, X.; Zhan, L.; Liang, X.; Qiao, W.; Ling, L., *J. Power Sources* **2011**, *196*, 3887-3893.

[6] Xu, J.-S.; Zhu, Y.-J.; Chen, F., *J. Solid State Chem.* **2013**, *199*, 204-211.

[7] Zhang, J.-J.; Chen, Y.-L.; Sun, Y.-F.; Huang, T.; Yu, A.-S., *RSC Adv.* **2013**, *3*, 20639-20646.

[8] Jiang, X. C.; Wang, Y. L.; Herricks, T.; Xia, Y. N., *J. Mater. Chem.* **2004**, *14*, 695-703.

[9] Cha, J.; Lee, J. S.; Yoon, S. J.; Kim, Y. K.; Lee, J.-K., *RSC Adv.* **2013**, *3*, 3631-3637.

[10] Fan, H. J.; Gösele, U.; Zacharias, M., *Small* **2007**, *3*, 1660-1671.

[11] Tan, H.; Zhao, Z.; Niu, M.; Mao, C.; Cao, D.; Cheng, D.; Feng, P.; Sun, Z., *Nanoscale* **2014**, *6*, 10216-10223.

[12] Tan, H.; Zhao, Z.; Zhu, W.-b.; Coker, E. N.; Li, B.; Zheng, M.; Yu, W.; Fan, H.; Sun, Z., *ACS Appl. Mater. Interfaces* **2014**, *6*, 19184-19190.

[13] Choi, J.; Cha, J.; Lee, J.-K., *RSC Adv.* **2013**, *3*, 8365-8371.

`

Korean Abstract

TiO_2 는 비교적 인체에 무해하고 쉽게 구할 수 있음에도 페인트, 광촉매, 태양전지, 배터리 등의 분야에서 뛰어난 특성을 보이기 때문에 높은 응용 가능성을 가진 재료로 각광받고 있다. TiO_2 나노 입자의 특성은 그 크기 및 형태에 따라 달라지기 때문에, 응용 가능성을 높이기 위해서는 이것의 크기 및 형태를 원하는 대로 조절하는 것이 필요하다.

본 논문에서는 TiO_2 기반의 나노입자들을 합성하고 그 구조적 특성을 실질적인 응용을 통해 알아보았다. 먼저 비교적 간단한 방법들을 이용하여 구형의 TiO_2 나노 입자를 합성하고, 그 크기를 약 60 nm 에서 300 nm 까지 조절하였다. TiO_2 나노 입자의 크기별 특성을 알아보기 위해 리튬 이온 전지로 응용해 봄과 동시에, 그에 대한 전기화학적 분석을 진행하였다. 또한 간단한 방법으로 속이 빈 구조의 TiO_2 나노 입자를 합성할 수 있었다. 이 방법을 이용하여 Ti와 Sn가 함께 존재하는 혼합 산화물을 쉽게 합성할 수 있었다. 또한 TiO_2 껍질 안에 별도로 합성한 산화 철 나노 입자 알맹이와 빈 공간이 존재하도록 알맹이@빈공간@TiO_2 껍질 나노 구조를 합성할 수 있었다. 이렇게 합성된 혼합 나노 입자들 역시 그 구조적 특징을 리튬 이온 전지 응용을 통해 알아보았고, 그에 따른 여러 가지 전기화학적 특성 분석이 진행되었다.

주요 핵심어: TiO_2, 나노 입자, 전기화학적 특성, 리튬 이온 전지

학번: 2009-20313